COO-2245-54TR

DEPARTMENTS OF NUCLEAR AND MECHANICAL ENGINEERING
MASSACHUSETTS INSTITUTE OF TECHNOLOGY
Cambridge, Massachusetts 02139

December, 1977

MIXING EXPERIMENTS IN AN ALTERNATING WIRE WRAPPED ASSEMBLY

by

C. Chiu
N.E. Todreas
W.M. Rohsenow

ERDA Research and Development
Contract E(11-1)-2245
U.S. Energy Research and Development Administration

DISCLAIMER

Reports and Papers Published under
MIT Coolant Mixing in LMFBR Rod Bundles Project

A. Quarterly Progress Reports (Available from National Technical Information Service, U.S. Department of Commerce, Springfield, VA 22151)

COO-2245-1	Period June 1, 1972 - November 30, 1972
COO-2245-2	Period December 1, 1972 - February 28, 1973
COO-2245-3	Period March 1, 1973 - May 31, 1973
COO-2245-6	Period June 1, 1973 - August 31, 1973
COO-2245-7	Period September 1, 1973 - November 30, 1973
COO-2245-8	Period December 1, 1973 - February 28, 1974
COO-2245-10	Period March 1, 1974 - May 31, 1974
COO-2245-13	Period June 1, 1974 - August 31, 1974
COO-2245-14	Period September 1, 1974 - November 31, 1974
COO-2245-15	Period December 1, 1974 - February 28, 1975
COO-2245-23	Period March 1, 1975 - May 31, 1975
COO-2245-25	Period June 1, 1975 - August 31, 1975
COO-2245-26	Period September 1, 1975 - November 30, 1975
COO-2245-28	Period December 1, 1975 - February 29, 1976
COO-2245-30	Period March 1, 1976 - May 31, 1976
COO-2245-31	Period June 1, 1976 - August 31, 1976
COO-2245-34	Period September 1, 1976 - November 30, 1976
COO-2245-38	Period December 1, 1976 - February 28, 1977
COO-2245-50	Period March 1, 1977 - May 31, 1977
COO-2245-53	Period June 1, 1977 - August 31, 1977
COO-2245-60	Period September 1, 1977 - November 30, 1977
COO-2245-63	Period December 1, 1977 - February 28, 1978

Reports Issued Under This Contract

B. Topical Reports (Available from National Technical Information Service, U.S. Department of Commerce, Springfield, VA 22151)

E. Khan and N. Todreas, "A Review of Recent Analytical and Experimental Studies Applicable to LMFBR Fuel and Blanket Assembly Design," COO-2245-4TR, MIT, Sept. 1973.

E. Khan, W. Rohsenow, A. Sonin and N. Todreas, "A Simplified Approach for Predicting Temperature Distribution in Wire Wrapped Assemblies," COO-2245-5TR, MIT, Sept. 1973.

T. Eaton and N. Todreas, "Instrumentation Methods for Interchannel Coolant Mixing Studies in Wire-Wrap Spaced Nuclear Fuel Assemblies," COO-2245-9TR, MIT, June 1974.

Y.B. Chen, K. Ip, N.E. Todreas, "Velocity Measurements in Edge Subchannels of Wire Wrapped LMFBR Fuel Assemblies," COO-2245-11TR, MIT, September 1974.

E. Khan, N. Todreas, W. Rohsenow, A.A. Sonin, "Analysis of Mixing Data Relevant to Wire-Wrapped Fuel Assembly Thermal-Hydraulic Design," COO-2245-12TR, MIT, September 1974.

E. Khan, W. Rohsenow, A. Sonin, N. Todreas, "A Porous Body Model for Predicting Temperature Distributions in Wire Wrapped Fuel and Blanket Assemblies of a LMFBR," COO-2245-16TR, MIT, March 1975.

E. Khan, W.M. Rohsenow, A. Sonin, N. Todreas, "Input Parameters to the ENERGY Code (To be used with the ENERGY Code Manual) COO-2245-17TR, MIT, May 1975.

E. Khan, W. Rohsenow, A. Sonin, N. Todreas, "Manual for ENERGY Codes I, II, III," COO-2245-18TR, MIT, May 1975

E. Khan, W. Rohsenow, A. Sonin, N. Todreas, "Manual for ENERGY Codes I, II, III Computer Programs," COO-2245-18TR Revision 1, MIT, July 1976.

P. Carajilescov and N. Todreas, "Experimental and Analytical Study of Axial Turbulent Flows in an Interior Subchannel of a Bare Rod Bundle," COO-2245-19TR, MIT.

B. Chen and N. Todreas, "Prediction of Coolant Temperature Field in a Breeder Reactor Including Interassembly Heat Transfer," COO-2245-20TR, MIT, May 1975.

B. Chen and N. Todreas, "Prediction of Coolant Temperature Field in a Breeder Reactor Inlcuding Interassembly Heat Transfer," COO-2245-20TR Revision 1, MIT, December 1976.

F. Carre and N. Todreas, "Development of Input Data to ENERGY Code for Analysis of Reactor Fuel Bundles," COO-2245-21TR, MIT, May 1975.

Reports Issued Under This Contract

B. Topical Reports, Continued

H. Ninokata and N.E. Todreas, "Turbulent Momentum Exchange Coefficients for Reactor Fuel Bundle Analysis," COO-2245-22TR, MIT, June 1975.

R. Anoba and N. Todreas, "Coolant Mixing in LMFBR Rod Bundles and Outlet Plenum Mixing Transients," COO-2245-24TR, August 1975.

B. Bosy, "Fabrication Details for Wire Wrapped Fuel Assembly Components," COO-2245-27TR, MIT, November 1975.

Ralph G. Bennett and Michael W. Golay, "Interferometric Investigation of Turbulently Fluctuating Temperature in an LMFBR Outlet Plenum Geometry," COO-2245-29TR, MIT, June 1976.

N.E. Todreas, "Analysis Methods for LMFBR Wire Wrapped Bundles," COO-2245-32TR, MIT, November 1976.

K.L. Basehore and N.E. Todreas, "Development of Stability Criteria and an Interassembly Conduction Model for the Thermal-Hydraulics Code SUPERENERGY," COO-2245-33TR, MIT December 1976.

Robert Masterson and Neil E. Todreas, "Analysis of the Feasibility of Implementing an Implicit Temporal Differencing Scheme in the SUPERENERGY Code," COO-2245-35TR, MIT, February 1977.

S. Glazer, C. Chiu and N. Todreas, "Collection and Evaluation of Salt Mixing Data with the Real Time Data Acquisition System," COO-2245-36TR, MIT, April 1977.

B. Mikic, E.U. Khan and N.E. Todreas "An Approximate Method for Predicting Temperature Distribution in Wire Wrapped Fuel Assemblies of a LMFBR," COO-2245-37TR, MIT, April 1977.

C. Chiu and N. Todreas, "Development of a Technique for Subchannel Flow Rate Measurements in LMFBR Wire Wrapped Assemblies," COO-2245-39TR, July 1977

C. Chiu and N. Todreas, "WARD Blanket Assembly Pre-Test Predictions by SUPERENERGY," COO-2245-40TR, July 1977

C. Chiu and N. Todreas, "Flow Split Measurements in LMFBR Blanket Assemblies," COO-2245-41TR, April 1978.

C. Chiu and N. Todreas, "Pressure Drop Measurements in LMFBR Blanket Assemblies," COO-2245-42TR, April, 1977.

Reports Issued Under This Contract

B. Topical Reports, Continued

C. Chiu and N. Todreas, "Mixing Experiments in LMFBR Wire Wrapped Blanket Assemblies, "COO-2245-43TR, April 1978.

Yi Bin Chen and Michael W. Golay, "Coolant Mixing in the LMFBR Outlet Plenum," COO-2245-44TR, June 1977.

J. Kelly and N. Todreas, "Turbulent Interchange in Triangular Array Bare Rod Bundles," COO-2245-45TR, July 1977

K.L. Basehore and N.E. Todreas, "Assessment of the Need to Incorporate a Variable Swirl Flow Model into the ENERGY Code," COO-2245-46TR, July 1977.

K.L. Basehore and N. Todreas, "Analysis of the Thermal-Hydraulic Behavior in the CRBR Secondary Control Assembly, Including Interassembly Heat Transfer Effects," COO-2245-47TR, July 1977.

J.G. Bartzis and N.E. Todreas, "Hydrodynamic Behavior of a Bare Rod Bundle," COO-2245-48TR, June 1977.

M.R. Fakori-Monazah and N.E. Todreas, "Measurement and Analysis of Flow Wall Shear Stress in an Interior Subchannel of Triangular Array Rods," COO-2245-49TR, August 1977.

A.S. Hanson and N.E. Todreas, "Fluid Mixing Studies in an Hexagonal 61-Pin, Wire-Wrapped Rod Bundle," COO-2245-51TR, August 1977.

S. Glazer, N. Todreas, W. Rohsenow, and A. Sonin, "TRANSENERGY S,M - Computer Codes for Coolant Temperature Prediction in LMFBR Cores During Transient Events," COO-2245-52TR, January 1977.

C. Chiu, W.M. Rohsenow and N.E. Todreas, "Mixing Experiments in an Alternating Wire Wrapped Assembly," COO-2245-54TR, MIT, April, 1977.

C. Chiu, W.M. Rohsenow and N.E. Todreas, "Turbulent Sweeping Flow Mixing Model for Wire Wrapped LMFBR Assemblies," COO-2245-55TR, MIT, April 1978.

C. Chiu, W.M. Rohsenow and N.E. Todreas, "Flow Split Model For LMFBR Wire Wrapped Assemblies, COO-2245-56TR, MIT, April, 1978.

Reports Issued Under This Contract

B. Topical Reports, Continued

K. Basehore and N.E. Todreas, "SUPERENERGY: Multiassembly Thermal-Hydraulic LMFBR Code," to be issued as topical report COO-2245-57TR, Department of Nuclear Engineering, MIT.

C-N. Wong and L. Wolf, "A 3-D Slug Flow Heat Transfer Analysis of Coupled Coolant Cells in Finite LMFBR Bundles," COO-2245-58TR, MIT, February 1978.

Roohallah Karimi and L. Wolf, "Two Dimensional Structural Analysis of Reactor Fuel Element Claddings due to Local Effects, COO-2245-59TR, MIT, April 1978.

Vincent Manno and Michael Golay, "Measurement of Heat and Momentum Eddy Diffusivities in Recirculating LMFBR Outlet Plenum Flows," COO-2245-61TR, MIT, April, 1978.

Hafeez Khan, Chong Chiu and Neil Todreas, "Laboratory Manual for Salt Mixing Test in Rod Bundles," to be issued as topical report COO-2245-62TR, Department of Nuclear Engineering, MIT.

Reports Issued under this Contract

C. Papers and Summaries

Yi Bin Chen, Ka-Lam Ip, Neil E. Todreas, "Velocity Measurements in Edge Channels of Wire-Wrapped LMFBR Fuel Assemblies," American Nuclear Society Transactions Vol. 19, 1974, pp. 323-324.

P. Carajilescov, N. Todreas, "Experimental and Analytical Study of Axial Turbulent Flows in an Interior Subchannel of a Bare Rod Bundle," J. of Heat Transfer, Vol. 98, No. 2, May 1976, pp. 262-268 (Included as Appendix to Quarterly Progress Report, COO-2245-15).

E. Khan, W. Rohsenow, A. Sonin, N. Todreas, "A Porous Body Model for Predicting Temperature Distribution in Wire-Wrapped Fuel Rod Assemblies," Nuclear Engineering and Design, 35 (1975) 1-12.

E. Khan, W. Rohsenow, A. Sonin, N. Todreas, "A Porous Body Model for Predicting Temperature Distribution in Wire-Wrapped Rod Assemblies Operating in Combined Forced and Free Convection," Nuclear Engineering and Design, 35 (1975) 199-211.

Ralph G. Bennett and Michael W. Golay, "Development of an Optical Method for Measurement of Temperature Fluctuation in Turbulent Flows," American Nuclear Society Transactions, Vol. 22, 1975, p. 581.

B. Chen and N. Todreas, "Prediction of the Coolant Temperature Field in a Breeder Reactor Including Interassembly Heat Transfer," Nuclear Engineering and Design 35, (1975) 423-440 (Included as Appendix to Quarterly Progress Report, COO-2245-23).

R. Bennett and M.W. Golay, "Interferometric Investigation of Turbulently Fluctuating Temperature in an LMFBR Outlet Plenum Geometry," Accepted for the ASME Winter Annual Meeting, Dec., 1976, (Included as Appendix in Quarterly Progress Report, COO-2245-30).

B.B. Mikic, E.U. Khan, N.E. Todreas, "An Approximate Method for Predicting Temperature Distribution in Wire Wrapped Fuel Assemblies of a Liquid Metal Fast Breeder Reactor," Mech. Res. Comm., Vol. 3, 353-360 (1976).

Reports Issued Under this Contract

C. Papers and Summaries (Continued)

L. Wolf, R. Karimi, J.Y. Kim, C.N. Wong, M.K, Yeung "2-D Thermoelastic Analysis of LMFBR Fuel Rod Claddings," Paper C4/d,4th International Conf. Structural Mechanics in Reactor Technology, San Francisco, August 1977.

M. Yeung, L. Wolf, "Effective Conduction Mixing Lengths for Subchannel Analysis of Finite Hexagonal LMFBR Bundles," ANS Meeting, New York, June 1977.

C. Chiu and N. Todreas,"Flow Split Measurements In An LMFBR Radial Blanket Assembly," ANS Meeting, New York, June 1977.

J.K. Kim and L. Wolf, "Laminar Mixed Convection Heat Transfer in Finite Hexagonal Bundles," ANL Winter Meeting, San Francisco, Nov. 27 - Dec. 2, 1977.

NOTICE

Printed in the United States of America
Available from

National Technical Information Service
U.S. Department of Commerce
5285 Port Royal Road
Springfield, VA 22161

Price: Printed Copy ; Microfiche $3.00

ABSTRACT

The salt injection experiment was performed in an alternating wire-wrapped, triangular-array bundle to study the coolant mixing behavior pertaining to alternating wrapped wires.

Results show that the coolant mixing is much enhanced in the subchannels for this type of bundle compared to the in-phase wire-wrapped bundle currently used in the LMFBR design. A strong interaction between the coolants in the edge and the interior subchannels at four assembly faces (where the alternating wires give 180° out-of-phase configuration) has also been observed.

After calibrating the input parameters for the sweeping flow of the COBRA-IIIC/MIT code against this experimental data, the code is employed to predict the coolant temperatures for a skew-powered alternating wire-wrapped blanket assembly. Comparing the code results with the SUPERENERGY code predicted coolant temperature data for an in-phase wrapped assembly under identical operating conditions, it is observed that the hot spot temperature for the alternating wire-wrapped assembly is less than that for the in-phase wire-wrapped bundle by 5% (normalized to the hot spot axial temperature rise).

ACKNOWLEDGEMENTS

The authors would like to express their sincere gratitude to the undergraduate assistants Jim Hawley, David Liu and Michael Mitsock for their tireless assistance in data acquisition.

Mr. Ray Johnson and Mr. J.A. Caloggero are thanked for their assistance and advice on the construction of the experimental apparatus and instruments.

The authors also wish to thank Mr. Mike Corradini and Ms. Jacqueline Humbert for their editing and proofreading of this report.

Thanks are also due to Malka Grinkorn and Ginny O'Keefe for their typing.

Sponsorship of this work through the Energy Research and Development Administration is also acknowledged.

NOMENCLATURE

C_1	Swirl flow parameter, input to SUPERENERGY code
c_i	Salt concentration for subchannel i (gram-salt/lbm-water)
c_o	Effective salt concentration of the injection subchannel at the injection position (gram-salt/lbm-water)
c_i^*	Dimensionless salt concentration, defined as c_i/c_o
m_i	Subchannel flow rate for subchannel i (lbm/hr)
m_o	Injection subchannel flow rate (lbm/hr)
$\overline{W_{ij}}$	Average sweeping flow from subchannel i to subchannel j over one wire wrap lead length (lbm/hr-ft)
ε_1^*	Effective enhanced eddy diffusivity, input to SUPERENERGY code

TABLE OF CONTENTS

List of Figures

List of Figures

List of Tables

CHAPTER 1

INTRODUCTION

The current wire wrap configuration in LMFBR assemblies (EBR-I, FFTF, and CRBR) is counterclockwise and in-phase, as shown in Fig. (1-1). The simplicity of construction and the satisfactory coolant mixing capability make this wire wrap configuration attractive. Nevertheless, a severe duct temperature gradient and a severe coolant temperature gradient caused by the high power skew are inherent in the assemblies close to the fuel-blanket interface. This suggests an investigation into other wire wrap configurations which might alleviate this temperature gradient as a contributor to duct and fuel pin bowing behavior.

A preliminary study with a series of the dye injection experiments of different wire wrap configurations has been performed at WARD (Ref. 1) Results indicated that the alternating wire wrap configuration proposed by C.E. Ockert (Ref. 2) in July, 1975 (as illustrated in Fig. (1-2), may enhance the cross assembly coolant flow, either potentially decreasing the hot spot coolant temperature or alleviating the crossflat duct temperature difference in a high power skew assembly. However, the study by WARD is not detailed enough to draw any conclusion on the above two aspects. There is, therefore, an incentive to further explore the flow characteristics of the alternating wire wrap configuration by performing a series of salt injection tests with saline

solution injected at different subchannels and different depths from the bundle exit. The results of these operations are discussed and analyzed in this report. Additionally, a qualitative comparison of the salt mixing capability of this alternating wire wrap configuration and the conventional in-phase wire wrap configuration is made to assess the advantages associated with the alternating wire-wrap thermal-hydraulic design application.

The computer code COBRA-IIIC/MIT (Ref. 3) was used in this study and was calibrated against the experimental data. It should be noted that due to the simplicity of the wire-wrap model used to construct the code, it does not predict the salt concentration maps well. Consequently, no attempt has been made in this report to utilize the code to quantitatively assess the detailed coolant mixing behavior of this alternating wire wrap assembly. Nevertheless, we made a sample computer run for an alternating wire wrapped skewed power generating assembly to demonstrate, in a conservative way, its overall mixing capability relative to that of a normal, in-phase wire wrapped-assembly.

CHAPTER 2

EQUIPMENT SETUP

The hydraulic test loop used in this experiment is the same as that used for the CRBR blanket mock-up test (Ref. 4). The geometric characteristics of the test section are kept the same as the CRBR blanket mock-up. Only the wire wrap configuration is modified from the 4 inch lead in-phase configuration to the configuration illustrated in Fig. (1-2a) The key geometric parameters of the test bundle are listed in Table (2-1).

It should be noted that the wire wrapped configuration at the bundle exit plane of our experimental mock-up differs from that originally proposed by Mr. Ockert. His original design requires that every wire terminate in a position at the bundle exit plane in such a way as to lie on the normal to one of the six faces. The wires in our experimental mock-up, on the other hand, terminate at the exit plane in such a way as to be located at the nine o'clock position of each rod. (Refer to Fig.(1-2a)). The difference between these two configurations will result in different wire intervals (i.e., the distance between the axial locations at which two opposing and adjacent wires cross the subchannel gap) in his and our designs. Figs.(2-1) and (2-2) illustrate the gap wire intervals in Ockert's bundle and in our bundle for two different types of gaps between the interior and edge subchannels. It is clear from these figures that the gap wire intervals of the

opposing wires in Ockert's bundle are alternatively 1/3 and 2/3 of the wire lead length for both kinds of gaps; and that those in our bundle are alternatively 1/6 and 5/6 of the lead length in the gaps depicted in Fig. (2-1) and alternatively 1/2 and 1/2 of the wire lead length in the gaps depicted in Fig.(2-2). Since the sweeping flow diverted by one wire from subchannel to subchannel is believed to be independent of the wire intervals (experimental data for the in-phase wire wrapped assembly fluid mixing summarized in Ref. (5) has demonstrated this point), the difference in the wire wrapped configurations in this respect and under this assumption would not cause large differences in the basic sweeping flow behavior of either bundle (his or ours). Even if this were not so, we will show that the total sweeping flow from one subchannel to another over one wire lead length for both bundles will nevertheless remain the same. This is mainly because the two different wire intervals are axially alternating in nature. Therefore, if the sweeping flow through the gap were decreased in the shorter gap wire interval, then the sweeping flow would be correspondingly enhanced in the longer gap wire interval. Therefore, these two effects would cancel each other out and make the total sweeping flow over one wire lead length remain the same for both bundles.

The salt injection system and data acquisition system are utilized as discussed in Ref. (6). The saline solution is injected at a pre-selected subchannel and depth from the bundle exit while the water is flowing through the bundle. The salt concentration ($\frac{\text{gram-salt}}{\text{lbm-water}}$) for each subchannel is detected

at the bundle exit by utilizing the on-line microprocessor system developed in reference (6). This data can be consequently reduced to a dimensionless form by dividing the exit region salt concentration levels for each subchannel by the initial subchannel salt concentration, c_o, at the injection position. c_o is evaluated from the following formula

$$c_o \equiv \frac{\Sigma c_i m_i}{m_o}$$

where $c_i \equiv$ salt concentration of subchannel i at the bundle exit

$m_i \equiv$ axial average subchannel flow rate of subchannel i

$m_o \equiv$ subchannel flow rate at the injection position of the injection subchannel.

(where m_i is derived from the flow-split data of a separate experiment (Ref. 7)).

The experimental results discussed in this report can be expressed either in the dimensionless form or nondimensionless form ($\frac{\text{mg-salt}}{\text{lbm-water}}$). However, since the dimensionless salt concentration is independent of the amount and the concentration of the saline solution injected, only the dimensionless salt concentration maps are used in the subsequent discussion.

It should be noted that the subchannel geometric characteristics, such as subchannel area, hydraulic equivalent diameter and wetted perimeter, for three different types of subchannels, i.e., interior, edge and corner, are determined under the assumption that the bundle tolerance is equally distributed between two fuel rods and the rod and the bundle wall[4]. Under this assump-

tion, the subchannel geometric characteristics are:

Interior Subchannel

Area = 0.0251 inch^2

Hydraulic diameter = 0.1196 inch

Edge Subchannel

Area = 0.0525 inch^2

Hydraulic diameter = 0.153 inch

Corner Subchannel

Area = 0.0133 inch^2

Hydraulic diameter = 0.0874 inch

The pressure drop data and the flow split data[4], which are subsequently used in conjunction with the pressure drop data in the determination of the subchannel friction factor, are measured at different times with several intermediate disassembly and assembly of the bundles. Use of the above geometric characteristics to reduce all the experimental data is based on the assumption that the tolerance remains equally distributed throughout the entire experiment. This assumption is essentially true when the bundle total tolerance is relative small and all the edge rods are likely to be pushed against the duct wall by a cluster of the interior rods which are more or less bowed through the fabrication and handling process.

The locations of the pressure taps are chosen such that the effect of the dynamic head in the static pressure drop determination can be eliminated. This is accomplished by setting the distance between two pressure tap instrumentation planes by a multiple of the wire lead length. Therefore, the dynamic head effect on the pressure drop reading can be cancelled out when the pressure drop reading is obtained as a difference between two static pressure readings at two elevations.

The range of the Reynolds number over which the pressure drop data were taken is limited by the pump capacity at the high R_e end and by the accuracy of the static pressure gauge at the low R_e end. The specifications of the instruments we used in this experiment are listed below:

(1) Main flow meter (Fisher Porter Co. Model No. B3565-7-3-GD-BSY), 0 ~ 200 GPM.

(2) Flow meter installed on the by-pass flow loop (Fisher Porter Co., Model 10A3567A), 0 ~ 37 GPM.

(3) Pump-Motor Sets (Bell and Gossett Co., Catalog No. 2-1/2A 7AB, 1510 Type B), 300 GPM @ 180 ft.

(4) Pressure Gauge - Two ITT Barton gauges (Series No. 277-57466 and 277-57467); ranges from 0 to 150 inches of H_2O and 0 to 400 inches H_2O. One ACCO Helicoid Gauge; 0 to 150 psi; accuracy $\pm$ 1/4 of 1%.

CHAPTER 3

EXPERIMENTAL RESULTS

Three injection subchannels were chosen in this work, as shown in Fig. (3-1). The salt transport mode differs for the subchannels around each injection subchannel. For instance, the wire wraps tend to diffuse the saline solution to the peripheral interior subchannels when the saline solution is injected at a center subchannel (subchannel 1 in Fig. (3-1)). On the other hand, the saline solution injected at subchannels 2 and 3 is either diverted deeply into the interior subchannel by the 180° out-of-phase wire wrap configuration or diverted to the downstream region of the swirl flow by the in-phase wire wrap configuration.

Test runs with these injection subchannels were performed at different Reynolds numbers and injection depths. The dimensionless salt concentration for these test runs are documented in Appendix A. The identification number of these test runs is tabulated in Tables (3-1), (3-2), (3-3), and (3-4). Table (3-1) tabulates all the test runs at a given injection depth, but with different Reynolds numbers. Tables (3-2), (3-3), and (3-4) tabulate all the test runs at a certain Reynolds number, but at different injection depths for injection subchannels 1, 2, and 3 respectively. The depths at which the saline solution is injected for these three subchannels are larger than two leads so that the salt distribution development versus axial length can be clearly observed.

Experimental error involved in the determination of the dimensionless salt concentration for each subchannel has been analyzed in Ref. (8). This error is engendered by the uncertainties of the salt concentration measurement and the flow split parameters, which is used to reduce the salt concentration data to its dimensionless form. The analysis showed that the maximum expected errors are 5.1% and 25% for the magnitude of the dimensionless salt concentration data for saline solution injected at center and edge subchannels, respectively.

CHAPTER 4

INTERPRETATION OF EXPERIMENTAL DATA

Because of the unusual salt distribution patterns, as observed from the experimental results documented in Appendix A, a brief interpretation of these experimental results is useful to aid understanding of the salt mixing mechanism. This section is divided into three sub-groups corresponding to three different kinds of salt distribution patterns. The first kind of salt injection pattern is associated with injection subchannel 1. The second and third kinds of injection patterns are associated with injection subchannels 2 and 3 respectively.

4.1 Experimental Data of Injection Subchannel 1

As figures (A-1) to (A-5) show, the salt distribution pattern is relatively independent of the Reynolds number. This indicates that the sweep flow diverted by the wire wraps is proportional to R_e for $R_e > 4367$, the lowest R_e under investigation. This feature can be proved by resorting to the salt transport equation as follows:

$$\frac{\partial c_i^*}{\partial \chi} = \sum_j \frac{\overline{w_{ij}}}{m_i} \left(c_i^* - c_j^* \right) \quad \text{for subchannel } i \qquad (4\text{-}1)$$

where c_i^* = dimensionless salt concentration for subchannel i

$\overline{w_{ij}}$ = average sweeping flow over a lead

m_i = subchannel flow rate

Since the salt distribution map is independent of R_e, the dimensionless salt concentrations c_i^* and c_j^* and the net salt transport, $\frac{\partial c_i^*}{\partial \chi}$, between subchannels must be independent of R_e. This then leads to the parameter $\frac{\bar{W}_{ij}}{m_i}$ being independent of R_e and, in turn, $\overline{W_{ij}}$ being proportional to m_i. Since the subchannel flow rate m_i is linearly proportional to the bundle R_e, we thus have demonstrated that the sweeping flow will be proportional to the bundle's Reynolds number if the dimensionless salt concentration map is independent of the bundle R_e.

Another interesting characteristic of these figures is that the salt diffusion in the interior subchannels is not enhanced in the expected direction (marked by the dotted arrows) along which the wire wraps tend to divert the saline flow. (Refer to Fig. (4-1) for the relationship between this expected preferred flow direction and the wire wrap configurations.) This effect is mainly due to the fact that the enhanced flows in the adjacent strips of subchannels move in opposite directions. Thus the saline solution is prevented from penetrating too far along the preferred directions due to fluid mixing between these strips. Figure (4-2) demonstrates this effect by a series of graphs which simulate the salt mixing process between and along the strips. In Fig. (4-2), a cluster of subchannels with alternating enhanced directions are employed. Initially, the saline solution is completely

confined in subchannel 4,4 (i.e., the subchannel which lies in column 4 and strip 4 as shown in Fig. (4-2a). After a step forward downstream the saline solution in subchannel 4,4 is partially diverted to subchannel 3,4 and mixed with subchannels 4,3 and 4,5 as shown in Fig. (4-2b).

The diversion and mixing processes in turn will result in the salt distribution pattern shown in Fig. (4-2c). Here, it is clear that the saline solution is not restricted to moving along strip 4, but rather diffuses into the adjacent strips. This diffusion prevents the saline solution from penetrating too far along the preferred flow direction into the low salt concentration region.

4.2 Experimental Data of Injection Subchannel 2

Injection subchannel 2 is one of the edge subchannels for which the out-of-phase wire wraps tend to divert the edge subchannel flow into the interior suchannels. Almost all the saline solution injected into this subchannel is diverted into the interior subchannels, as shown in Figs. (A-6) to (A-10).

The spider shape salt distribution pattern is mainly due to the alternating directions of the enhanced flow strips. The legs of the salt configuration occur in the subchannel strips with the enhanced flow directions toward the injection subchannel. This is because the saline solution which exists in these coolant strips tends to move toward the injection subchannel and thus accumulates around the high salt concentration region. On the other hand, the saline solution in the

subchannel strips with the preferred flow direction toward the center of the bundle is diverted and smeared into the low concentration region. As a result, the saline solution accumulates in the strips with the enhanced flow toward the injection subchannel, and the low concentration solution exists in the strips with the preferred flow toward the center of the bundle.

4.3 Experimental Data of Injection Subchannel 3

Injection subchannel 3 is one of the edge subchannels in which the in-phase wire wraps tend to divert the saline solution into the neighborine edge subchannels. This transport mechanism is somewhat similar to the swirl flow mixing in the normal in-phase wire wrapped assembly.

Figures (A-11) to (A-15) show the saline solution distribution maps for different Reynolds numbers with respect to the salt injection subchannel 3. From these graphs, we can see that the salt distribution seems to be independent of the Reynolds number for this injection subchannel. The direct proportionality of the diversion crossflow for the subchannels can be directly derived from this fact.

The saline solution injected into this subchannel is mostly swept into the subchannels located in the regions on both sides of the injection subchannel. In the downstream region of the swirl flow (located on the right hand side of the injection subchannel), the saline solution is transferred into the edge subchannels by the preferred flow directed there.

However, in the upstream region of the swirl flow (located on the left side of the injection subchannel), the saline solution penetrates into the neighboring interior subchannel because of the strong edge-interior mixing interaction induced by the 180° out-of-phase wire wraps.

CHAPTER 5

COMPARISON OF THE DEVELOPMENT OF SALT CONCENTRATION PATTERNS BETWEEN ALTERNATING WIRE-WRAPPED ASSEMBLY AND IN-PHASE WIRE-WRAPPED ASSEMBLY

The salt concentration distribution develops in the direction of fluid flow starting from the position of saline solution injection. For instance, at the level of the injection, the saline solution is largely confined to the injection subchannel; however, in the downstream regions, the saline solution has diffused into the subchannels around the injection subchannel. By studying the development of salt concentration maps, the behavior and capability of the coolant mixing mechanism can be clearly understood. Accordingly, experimental salt concentration data at different injection depths with respect to three injection subchannels were taken. It is worth noting that the experiments were performed by varying the injection depths and monitoring the salt concentrations for each subchannel at the bundle exit. This is in contrast to varying the salt concentration measurement plane with a fixed injection depth. A difference between salt concentration development patterns is expected for these two measurement schemes over the first lead because the wire orientations with respect to the injection location will generally differ. However, the development patterns will be similar if the distance between the injection position and the measurement position is larger than one wire-wrap lead length.

The main objective of this chapter is to study the salt concentration development patterns of an alternating wire wrap assembly by comparing the experimental results of such an assembly with the results predicted by SUPERENERGY/DRV (Ref. 6) for such an in-phase wire wrapped assembly under the same experimental operating conditions. This discussion is presented in the next three sections for three different salt concentration patterns corresponding to three injection subchannels.

5.1 Development of Salt Concentration Maps of Injection Subchannel 1

The experimental data corresponding to injection subchannel 1 (dimensionless salt concentration) are illustrated in Figs. (A-16) to (A-32) with respect to different injection depths. The coverage between highest and lowest injection depth is more than two wrap leads. These figures are reported here in a different way than they were in Figs. (A-1) to (A-5); the map has been rotated 60° clockwise. The rotation can be observed by comparing the directions of the enhanced flow between the two sets of figures, i.e., (A-1) to (A-5) and (A-17) to (A-33), respectively. The difference of the shapes of the 0.5 dimensionless salt concentration isothermal contour between the two sets of figures is simply due to the rotation of the printout scheme.

The crossflat dimensionless salt concentrations at two different injection depths are plotted in Fig. (5-1) to illustrate the development of a one dimensional salt

concentration contour (crossflat along the preferred flow depth) vs. the axial length (injection depth). From this figure, it is clear that the salt solution at the center region diffuses into the peripheral low salt concentration region as the injection depth increases. This feature reveals that the alternating wire wraps perform the same function in the diffusion of the salt as do the in-phase wire wraps.

To compare the saline solution mixing effectiveness of the alternating wire wraps with that of the in-phase wire wraps, the computer code SUPERENERGY/DRV is used. With this code we predicted the dimensionless salt concentration for each subchannel of an in-phase wire wrapped assembly to have identical bundle geometric and operational parameters to those of the alternating wire-wrapped assembly. The code input mixing parameters ε_1^* (in-phase) and C_1 are obtained experimentally for the 61-pin blanket mock-up (Ref. 5-2), i.e., $\varepsilon_1^* = 0.35$ and $C_1 = 0.375$, again using the same geometric parameters as those of the alternating assembly mock-up. The results of the code prediction are documented in Appendix B. The crossflat one-dimensional salt concentrations predicted by SUPERENERGY/DRV for the in-phase assembly are plotted at the injection depths of 16 and 23.5 inches in Fig. (5-2). Comparing Figs (5-2) and (5-1), it can be observed that the dimensionless salt concentrations for the center interior subchannels are much higher than those of the alternating wire-wrapped assembly. In addition, the salt concentrations for the edge subchannels are lower than those of the alternating wire-wrapped assembly. This implies that the alternating wire wraps have better salt

(or heat) mixing capabilities than those of the in-phase wire wraps. These differences between the mixing capabilities of the two types of assemblies can be characterized by an effective value of ε_1^* (call it ε_{1A}^*) for in-phase assemblies. This effective value is the one which gives the smallest difference between the salt concentration levels for the in-phase wire wrapped assembly (predicted by SUPERENERGY/DRV) and the alternating wire wrapped assembly along a crossflat line for a certain injection depth and bundle Reynolds number. Thus the physical meaning of the parameter ε_{1A}^* is an artificial enhanced eddy diffusivity (for the in-phase wire wrapped assembly), which can produce the same coolant mixing effectiveness of the in-phase wire wraps as that of the alternating wire wraps.

This ε_{1A}^*, which has been evaluated by calibrating the code SUPERENERGY against the salt concentration data at injection depth 16 inches and R_e = 9134, is 2.56 times higher than ε_1^* (in-phase) obtained experimentally from the 61 pin in-phase mock-up. The salt concentration distribution pattern of an in-phase wire wrapped assembly at $\varepsilon_1^* = \varepsilon_{1A}^*$ is compared against the experimental data, as Fig. (5-3) shows. This figure indicates that the ε_{1A}^* of the in-phase wire wrap assembly can provide a similar salt concentration to the experimental salt concentration profile obtained in the alternating wire wrapped assembly.

From the above discussion, we can then conclude that:

1) The saline solution around the interior subchannel is diffused (or diverted) into the peripheral low

concentration region; and

2) The mixing capability of the alternating wire wraps is much more effective than that of the in-phase wire wraps.

5.2 Development of Salt Concentration Maps of Injection Subchannel 2

The experimental data corresponding to injection subchannel 2 (dimensionless salt concentrations) are illustrated in Figs. (A-35) to (A-48), at the different injection depths reported in Table 3-3. At the injection depth 13.5 inches (as illustrated in Fig. (A-35)), the saline solution has been well diverted into the interior subchannels. This indicates that a strong edge-interior coolant mixing takes place at the edge subchannels which have the 180° out-of-phase wire wraps.

As the injection depth increases, the saline solution tends to penetrate deep into the interior subchannels through the process of the preferred flow. At the injection depth 25 inches, as Fig. (A-48) illustrates, the highly concentrated saline solution almost reaches the edge subchannels on the other side of the bundle.

The salt concentration patterns in the in-phase wire wrapped assembly corresponding to the same injection subchannel and the same injection depths employed in this task are predicted by SUPERENERGY/DRV, and reported in Appendix B in Figs. (B-18) to (B-39). As these figures show, most of the saline solution is kept in the edge subchannels. In addition, the major transport process transferring the saline solution along

the assembly duct wall is the swirl flow in the edge subchannels. This transport process is totally different from the one that causes the diversion of the saline solution in the alternating wire wrapped assembly.

The salt concentration maps for the two assemblies are compared side by side in Fig. (5-4) at three different injection depths. In this figure, we can observe the following:

1) More saline solution is transferred to the half of the assembly in which the injection did not take place (i.e., the half of the assembly which does not include the injection rod, as illustrated in Fig. (11)), in the alternating wire wrap assembly than in the in-phase assembly, at a given injection depth.
2) The saline solution is totally transferred into the interior subchannels in the alternating assembly and is accumulated around the edge subchannels in the in-phase assembly.

To quantitatively evaluate the mixing capability of these wire wrap assemblies, we evaluated over a two lead length distance the total dimensionless salt concentrations transferred to the half of the assembly in which the injection did not take place. This can be done by measuring the extra salt which crosses the imaginary dotted line (as shown in Fig. (5-5)) at the center of the assembly for the two different injection depths. (Refer to Figs. (5-4a) and (5-4c)). The results

indicate that the ratio of the dimensionless salt transfer in the alternating wire wrapped assembly to that of the in-phase wire wrapped assembly is 1.89. This number indicates that the coolant mixing capability of the alternating wire wraps to divert the saline solution from one side of the bundle to the other side of the bundle is about two times more effective than that of in-phase wire wraps. It must be remembered that the above conclusion only holds when the injection subchannel has 180° out-of-phase wire wraps (i.e., for injection subchannel 2 vs. 3).

5.3 Development of Salt Concentration Patterns of Injection Subchannel 3

The experimental data corresponding to injection subchannel 3 (dimensionless salt concentrations) are illustrated in Figs. (A-50) to (A-72). The injection depths under investigation are from 13.5 to 27.0 inches as shown in Table(3-4).At the injection depth 13.5 inches, when the saline solution reaches the bundle exit plane, it has already been diverted into the edge subchannels located on the two sides of the injection face. The swirl flow induced by the in-phase wire wraps around the injection subchannel transfer the saline solution into the downstream edge subchannels. The saline solution existing in the axially upstream edge subchannels is transported there by the preferred flow, which diverts it from the interior subchannel to the upstream edge subchannels. As the injection depth increases, the saline solution in the edge subchannels tends to be re-diffused into

the interior subchannels, by the preferred flow mixing process. By comparing the dimensionless salt concentration maps of the alternating wire wrapped assembly to those of the in-phase wire wrapped assembly at this particular injection subchannel (as shown in Fig.(5-6)), it is clear that the saline solution does not penetrate into the low concentration region in the alternating wire wrapped assembly as effectively as it does in the in-phase wire wrap assembly. This feature is in contrast to what has been discussed (Sect. (5.2)) for injection subchannel 2.

The quantitative comparison of the coolant mixing capability of these two kinds of assemblies can be done by measuring between two wire wrap leads the amount of dimensionless salt concentration transferred into the non-injected half of the assembly for each kind of assembly. Results show that there is three times more salt penetrating into the non-injected half of the in-phase assembly than into the non-injected half of the alternating assembly.

CHAPTER 6

PREDICTION OF SUBCHANNEL TEMPERATURES IN A HEATED ALTERNATING WIRE WRAPPED ASSEMBLY

The discussion so far has been based on the saline solution mixing experimental data. The effect of this particular coolant mixing pattern on the subchannel coolant temperatures in a heated assembly should be investigated in order to assess its application in the LMFBR design.

In general, there are three methods to predict the coolant temperatures in a heated assembly from salt concentration experimental data. The first method is to inject the saline solution at all the positions axially along all the subchannels. With the injected saline solution simulating the heat added to the subchannel coolant, one can superimpose the salt concentration patterns at the bundle exist corresponding to all the injection positions and yield equivalent coolant temperatures (at the bundle exit) with all the fuel pins heated. The second method is in the principle the same as the first, but it reduces the experimental data needed, by identifying a small number of injection subchannels which are sufficient to model all the types of subchannels existing in the bundle.

The third method is to calibrate the related input parameters of a code which has a built-in sweep flow physical model for each wire across each gap against the experimental data. The coolant temperatures are calculated by the code

with the calibrated input parameter. This method is more indirect than the other two because the temperature prediction relies on a computer code in which some physical models are still in question.

In this task, the third method is employed to predict the coolant temperatures of a skewed power heated bundle. The reasons for discarding the first and second methods are as follows:

1) The first method is much more laborious than the third method. By the first method, about 400 man-days are needed , at a rough estimate, to accomplish this task compared to 30 man-days by the third method.

2) The second method is also much more laborious than the third method. We know that the salt distribution pattern at the bundle exit plane differs depending on which injection subchannel is used. However, if the bundle is axially cut in half, the salt distribution pattern resulting from a salt concentration injection at any one injection subchannel is identical to the salt distribution pattern that would result from an injection at the symmetrical subchannel. Therefore, the second method permits measurement of the salt distribution patterns in only one-half of the assembly, i.e., that part of the assembly which includes the injection

rods. (See Fig. (5-5) for the location of this half of the assembly.) This method would thus involve 200 man-days of work to accomplish the coolant temperature prediction of a heated assembly.

The computer code COBRA-IIIC/MIT (Ref. 3) is employed here to predict the subchannel coolant temperatures in a heated alternating wire-wrapped assembly. This computer code employs physical models identical to those used in COBRA-IIIC (Ref. 2), but a different numerical scheme to solve the conservation equations. The input "DUR" in the code is calibrated against the dimensionless salt concentration data corresponding to the injection subchannel 1 (center interior subchannel). There are two reasons for calibrating the code against only the interior subchannel data. Not only did the developer of the code suggest that a constant effective fraction of lead length be employed for any gap throughout the assembly; but also that the mixing data we took do not provide enough information to calibrate the sweeping flow input parameters for two different kinds of edge subchannel gaps, i.e., the gaps through which pass the 180° out-of-phase wires, and the gaps through which pass the in-phase wires. The prediction results with this calibrated input "DUR" are then compared with the coolant temperature results predicted by SUPERENERGY (Ref. 9), of an in-phase wire wrapped assembly under the same thermal-hydraulic operational conditions. The details of the comparison are

discussed in Sect. (6.2)

The first section of this chapter, Sect. (6.1), is devoted to the calibration of the computer code and the discussion on the validity of the code in the alternating wire-wrap assembly thermal-hydraulic calculations.

6.1 Calibration of Computer Code

The dimensionless salt concentration data corresponding to injection subchannel 1 and injection depth 16 inches, as illustrated in Fig. (A-2), is used to calibrate the input parameter "DUR" of COBRA-IIIC/MIT. This parameter governs the magnitude of total sweep flow diverted by the wire wrap crossing the subchannel gap. The relationship between the total sweep flow and the parameter "DUR" is presented as follows (Eq. (32), Ref. (3)):

$$W_{TOTAL} = W_{FORCE}\,\Delta X = \pi p\left(\frac{P-D}{A_i}\right) * DUR * m_i$$

where

W_{TOTAL} = total sweep flow caused by the wire wrap crossing the gap between subchannel i and its surrounding subchannel (lbm/hr).

W_{FORCE} = diversion cross-flow per unit length over the axial increment ΔX.

ΔX = axial increment (node); specified by the user.

A_i = subchannel area

$P-D$ = gap width

p = rod pitch

m_i = subchannel flow rate (lbm/hr)

The physical meaning of this parameter, DUR, is that is represents the effective fraction of a lead over which a constant sweep flow is diverted from one subchannel to another.

The least mean square technique is employed in the calibration. This technique requires that the optimum input parameter "DUR" corresponds to the minimum value of the following parameter LMS:

$$LMS = \sum_{i=\text{subchannel}}^{N} \left(c_i^* - T_i^*\right)^2$$

where c_i^* ≡ dimensionless salt concentration

T_i^* ≡ dimensionless temperature, defined as

$$\frac{T_i - T_{in}}{T_o - T_{in}}$$

T_o is the inlet temperature of the hot water injection channel

i ≡ subchannel identification number

N ≡ all subchannels in bundle

The value of LMS as a function of the sweep flow input parameter, DUR, in the code calibration, is illustrated in Fig. (6-1). From this figure, it is clear that the optimum value of the sweep flow input parameter is 0.19. With this calibrated input parameter, the dimensionless temperatures are computed by the code. The results are illustrated in Figs. (6-2), (6-3), and (6-4). Figure (6-2) is the dimensionless salt mixing results with the saline solution injected at the

center interior subchannel. Figs. (6-3) and (6-4) show the dimensionless temperature results with the saline solution injected at injection subchannels 2 and 3 (as defined in Fig. (4-1), respectively. Comparing these COBRA predicted results with the experimental data as illustrated in Figs. (6-5), (6-6), and (6-7), the following facts can be observed:

1) Injection subchannel 1:

The code predicts that the saline solution will be transported more effectively in the direction of enhanced flow than does the experimental data.

The dimensionless salt concentrations are distributed more uniformly than predicted by COBRA using calibrated sweep flow input parameter. In other words, the code underestimates the coolant mixing capability of the alternating wire wrap due to its inherent deficiency.

2) Injection subchannel 2:

The code underestimates the cooling mixing capability with the saline solution injected at this particular subchannel. (This can be observed by comparing Fig. (6-3) with Fig. (6-6).

3) Injection subchannel 3:

The code predicts that the saline solution penetrates into the interior subchannels which are close to the injection subchannel, with a preponderance of the salt in downstream (with respect

to the local swirl flow), subchannels. The experimental data shows a large portion of the injected saline solution is swept into the downstream edge subchannels but does not penetrate radially into the interior subchannels.

The code underestimates the coolant mixing capability since the experimental data, as illustrated in Fig. (6-7) shows that the saline solution can be transported very deeply into the low concentration region (downstream edge subchannels).

From the above observations, we can conclude that the COBRA code cannot predict exactly the coolant mixing process inherent in an alternating wire wrapped assembly. The code tends to underestimate the cooling mixing capability, due to the inherent deficiency in its sweep model. It is employed nevertheless since is considerably quicker to use than the other two methods, keeping in mind that it will conservatively predict the coolant temperatures in a heated alternating wire wrapped assembly. The word "conservatively" means that the predicted coolant temperatures may possess more adverse features, such as high hot spot coolant temperature and larger duct wall temperature differential, than realistically occur.

6.2 Comparison of Subchannel Coolant Temperatures Between Alternating Wire Wrapped Assembly and In-Phase Wire Wrapped Assembly

In order to compare the coolant mixing effect on the duct wall temperature gradients between these two different types of assemblies, a severe power skewed operational condition is analyzed in the code calculation. The input radial power factors for all the fuel rods, as input data to the code, are illustrated in Fig. (6-8). These values are the same as those of one of the outer blanket assemblies in CRBR (Ref. 10). This power skew is supposed to be the highest among all the CRBR fuel and blanket assemblies.

The operational conditions and geometric characteristics of the model assembly used in the calculation are listed in Table 6-1.

The subchannel coolant temperatures of the alternating wire wrapped assembly, under the aforementioned operational condition, are predicted by COBRA-IIIC with the input sweep flow mixing coefficient, "DUR", equal to 0.19. Meanwhile, the coolant temperatures of the in-phase wire wrapped assembly are predicted by SUPERENERGY with its input mixing parameters calibrated by the experimental salt concentration results (that is, the mock-up with the same geometric characteristics used in the code calculation). The cross-assembly coolant temperatures in a line of maximum power skew of these two different assemblies are illustrated in Fig.(6-9); the peripheral subchannel coolant temperatures are illustrated

in Fig. (6-10). These coolant temperatures are plotted corresponding to the assembly mid-plane, which is 22.5 inches from the assembly inlet with a 45 inch heated length. The primary reasons for not calculating the coolant temperature at the bundle exit, i.e., at 45 inches from the bundle inlet, are as follows:

1) Long computer running time and limited core storage space prevent the calculation. The 22.5 inch case with 0.5 inch axial interval already requires 700K core storage (where 900K is the limit of the computer facility we used) and a very long running time. It is not practical (even if it were possible), to run a 45 inch case to obtain the exit temperature information.

2) The hot spot temperature difference between the alternating wire wrapped assembly and the in-phase wire wrapped assembly is almost linearly proportional to the subchannel axial length. This characteristic has been observed from the computer results with the subchannel length less than 22.5 inches. It is thus reasonable to deduce the hot spot temperature difference at the bundle exit plane from the results we obtain at the assembly mid-plane.

As can be observed in Fig.(6-9), the coolant temperatures around the assembly hot spot for the alternating wire wrapped assembly is less than those for the in-phase wire wrapped assembly. This is due to the strong coolant mixing effects between the interior subchannels, and between the edge

subchannels and interior subchannels. As a consequence, the coolant temperatures of the edge subchannels, in both hot and cold sides, increase due to this enhanced mixing. The hot spot coolant temperature of the alternating wire wrapped assembly, however, is 6 to 7°F lower than that of the in-phase wire wrapped assembly. This leads to approximately a 12 to 14°F hot spot temperature decrease at the exit plane of the alternating wire wrapped assembly. This is 5% of the total hot subchannel axial temperature rise.

Figure (6-10) illustrates the peripheral subchannel coolant temperatures on six faces of the assemblies. Faces 1 and 6 are hot faces while faces 3 and 4 are cold faces. As can be observed in this figure, the shapes of the temperature of these two types of assemblies are quite different. This is because there is a lack of lateral swirl flow causing face-to-face coolant mixing in the alternating wire wrapped assembly. As a result, the edge subchannel temperatures of each face resemble the coolant temperatures of the neighboring interior subchannels. The difference between the maximum and minimum peripheral coolant temperatures for the two assemblies, however, remains small. This means that the net duct deflection caused by the differential thermal expansion will be approximately the same. It is worth noting that the temperature gradients on faces 2 and 5 of the alternating wire wrapped assembly are greater than those encountered in the in-phase wire wrapped assembly. This may result in higher thermal stress on these two faces.

6.3 Discussion of Predicted Results

The 5% hot spot coolant temperature decrease of the alternating wire wrapped bundle at the bundle exit compared to that of the in-phase wire wrapped assembly is a conservative estimate. The temperature differences between the edge and the interior subchannels of the downstream half of the axial assembly is larger than those of the upstream half. The enhanced mixing phenomenon between the edge and interior subchannels in the alternating wire wrapped assembly can lower the hot spot temperature more in the downstream half of the assembly than in the upstream half of the assembly. Using the 6-7°F difference of the hot spot temperature at the bundle mid-plane between these two assemblies to estimate an actual hot spot temperature difference of 12-14°F at the bundle exit is conservative. In other words, the predicted hot spot temperature difference between these two assemblies at the bundle exit plane may be larger than the 14°F estimated in the previous section.

In addition, the code COBRA-IIIC always underestimates the coolant mixing capability in areas around the three types of injection subchannels, as mentioned in Chapter 3. Therefore, it is expected that the actual hot spot temperature decrease, compared to that of the in-phase wire wrapped assembly, may be larger than the amount discussed above.

The peripheral temperature span, i.e., between the maximum and minimum peripheral coolant temperatures, is expected to be less sensitive to the assembly's capability

of enhanced edge-interior coolant mixing. The reason is that as the mixing capability between the edge and interior subchannels increases, the edge coolant temperatures of both the cold and hot sides will be increased by convection of more hot fluid from the interior subchannels. Thus, the peripheral temperature span for an actual heated alternating wire wrapped assembly will not be too different from that which we have predicted here.

CHAPTER 7

GENERAL CONCLUSIONS

Given the discussion and analysis of the previous sections, the design application of the alternating wire wrapped assembly in the LMFBR can now be presented. The advantages and disadvantages of the alternating wire wrapped assembly, compared to the in-phase wire wrapped assembly, can be classified in the following three subgroups:

1) Coolant Mixing

The alternating wire wrapped assembly provides more effective coolant mixing in the interior subchannels and between the edge and interior subchannels. This results in a lower hot spot temperature (5% difference) than that in the in-phase wire wrapped assembly.

2) Duct Wall Structural Integrity

Since the maximum and minimum peripheral coolant temperatures for an alternating wire wrapped assembly and an in-phase wire wrapped assembly are about the same, the total duct wall radial deflections due to thermal bowing for each will be about the same. However, the average temperature difference between the hot faces, i.e., faces 1 and 6 (refer to Fig. (1-2) for the face identification number), and the cold faces, i.e., faces 3 and 4, is larger than that of

the in-phase wire wrapped assembly, as illustrated in Fig. (6-10).

3) Fuel Pin Integrity

Since the coolant temperatures for the interior subchannels of the alternating wire wrapped assembly are lower in magnitude than those of the interior subchannels of the in-phase wire wrapped assembly, both the thermal induced and irradiation induced bowings of the fuel rods will be less severe than that occurring in the in-phase wire wrapped assembly. The numerical magnitudes of these effects have been conservatively estimated using the COBRA IIIC/MIT code. The sweep flow model in this code is not formulated to effectively deal with the alternating wire wrap configuration. Because of the exploratory nature of this investigation, and the modest performance gains associated with this configuration, it was not deemed worthwhile at this time to reformulate an effective sweep flow model.

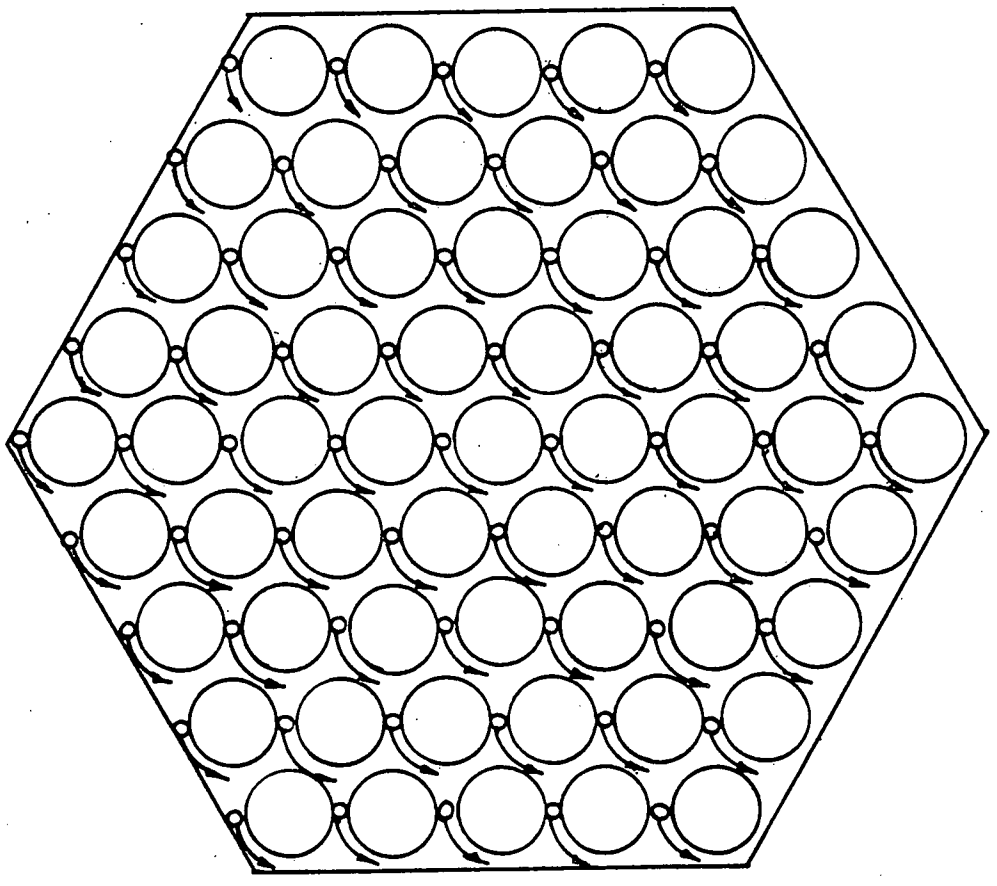

-- Fuel Pin and Wire Wrap (With Counter-Clockwise Direction)

FIGURE 1-1 In-Phase Wire Wrap Configuration

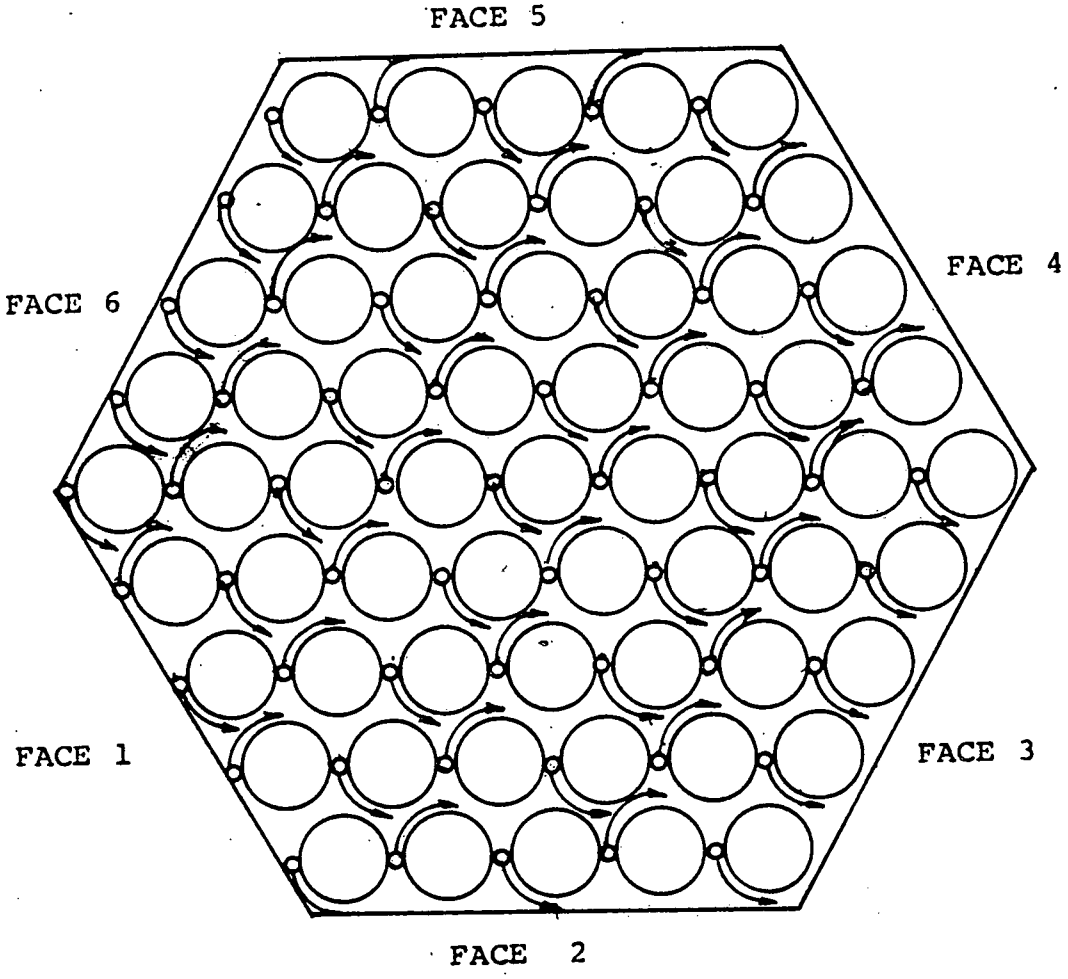

- Fuel pin and wire wrap (wire wrap twisting direction is indicated by arrow)

FIGURE 1-2a Alternating Wire Wrap Configuration (Bundle Exit Plane, Mock-up)

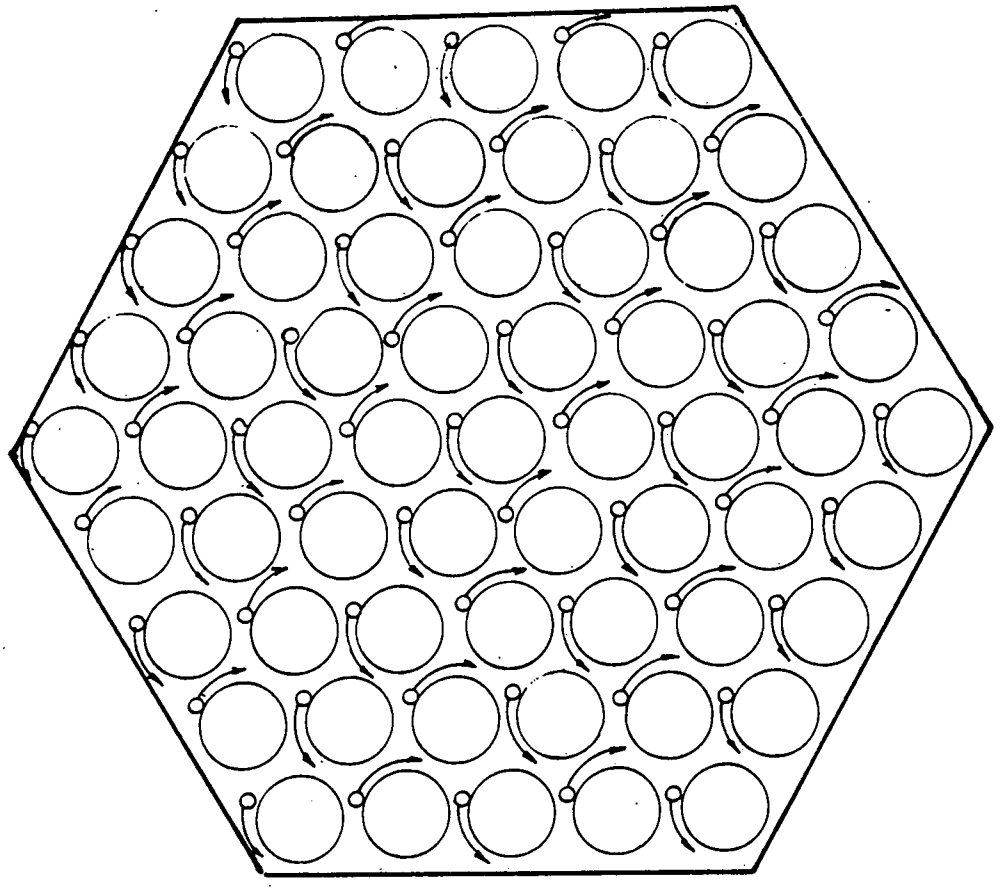

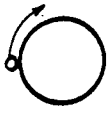 - Fuel pin and wire wrap (wire wrap twisting direction is indicated by arrow)

FIGURE 1-2b Alternating Wire Wrap Configuration (Bundle Exit Plane - Eckert's Bundle)

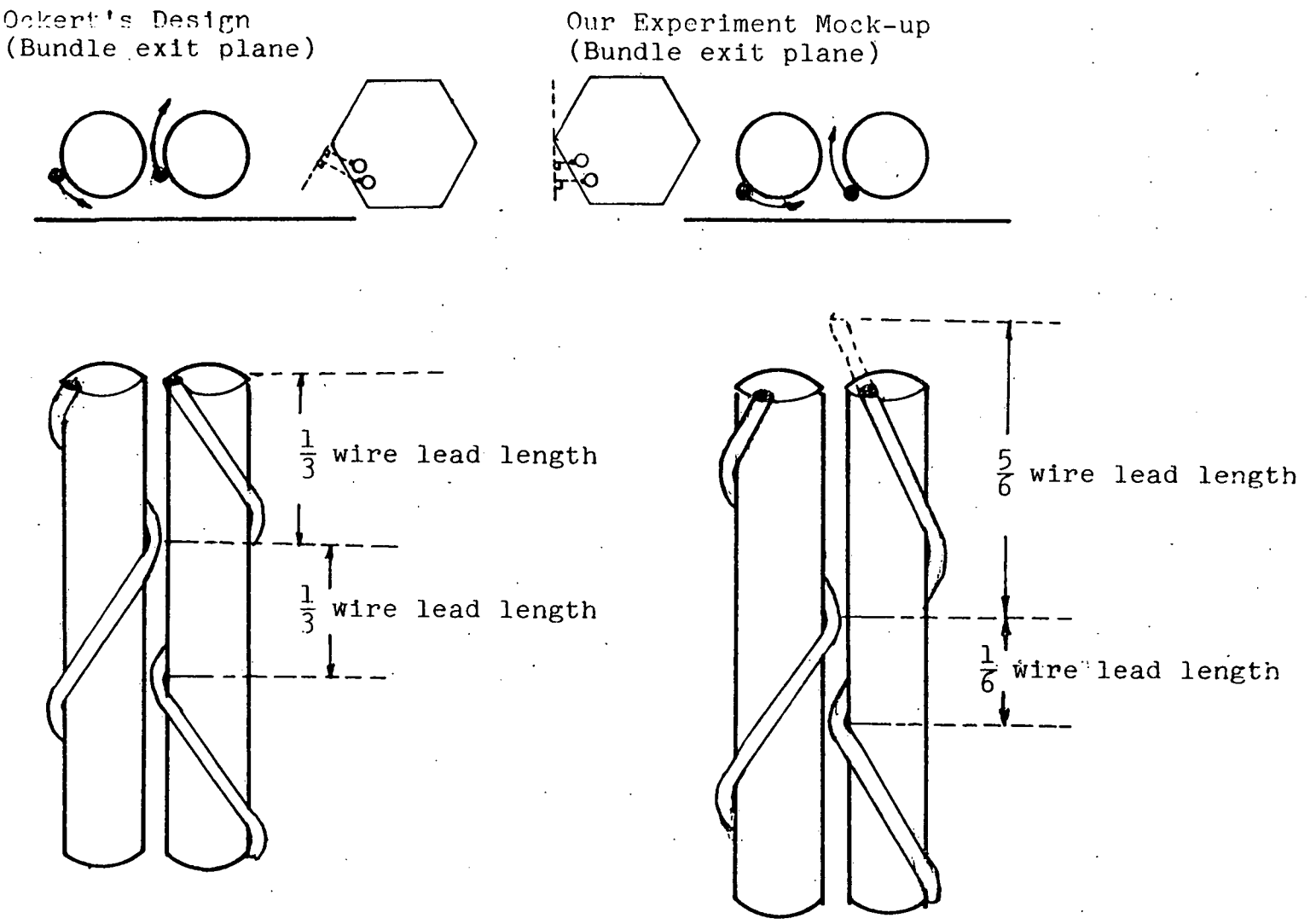

FIGURE 2-1 Wire Intervals in Gaps between Interior and Edge Subchannels (Type 1)

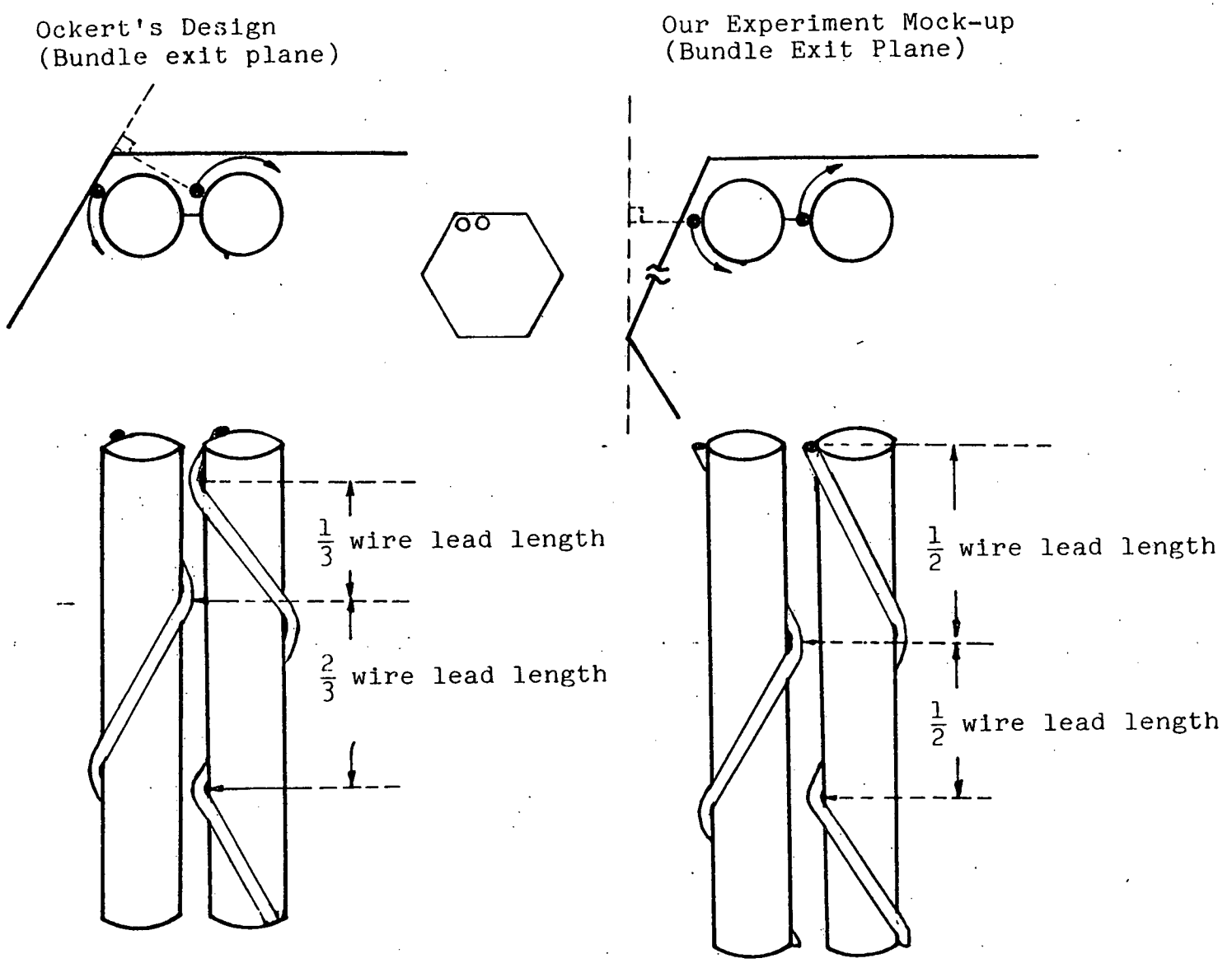

FIGURE 2-2 Wire Intervals in Gaps between Interior and Edge Subchannels (Type 2)

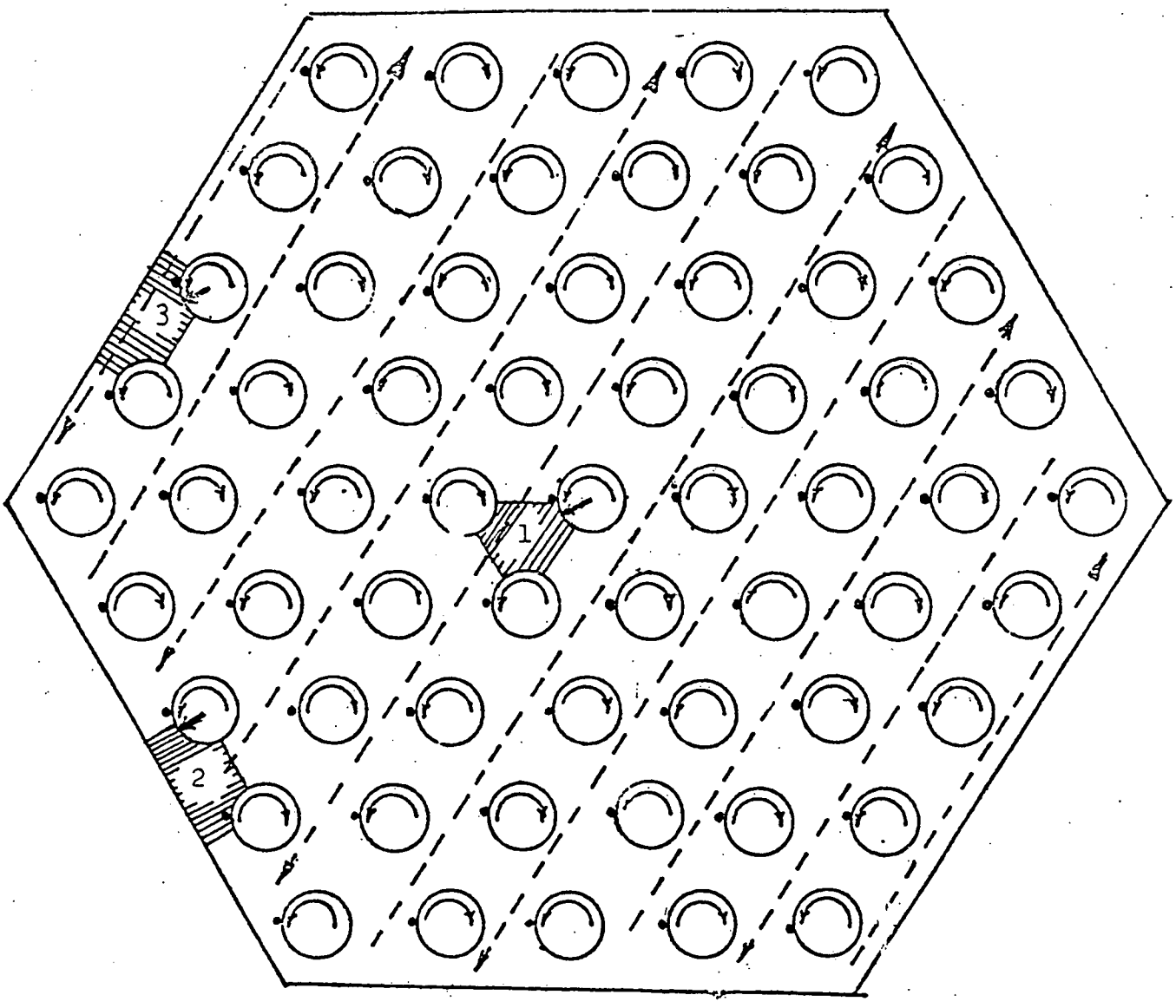

FIGURE 4-1 Injection Positions in the Alternate Wire Wrap Bundle

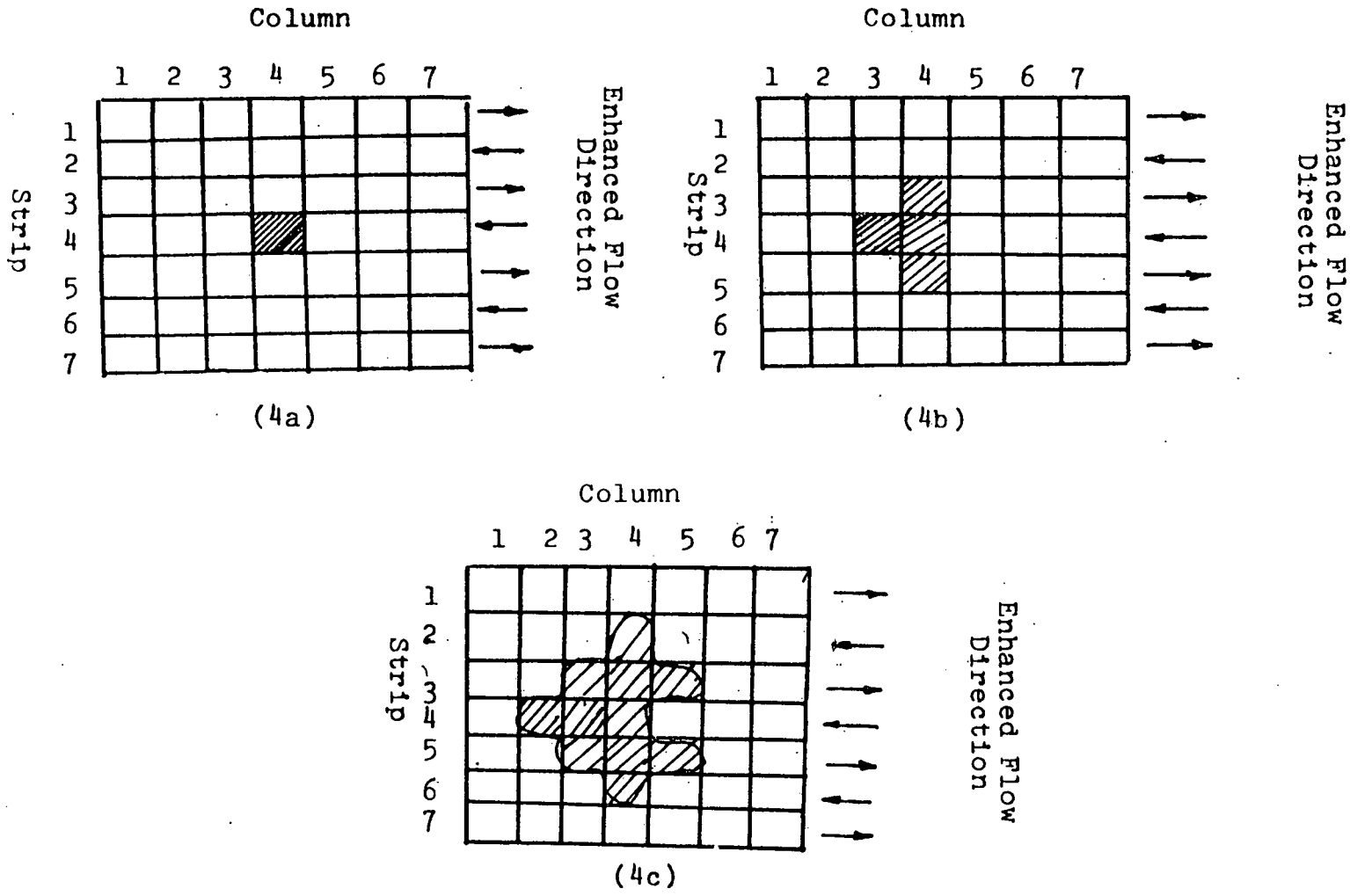

FIGURE 4-2 Salt Transport Mechanism in the Alternating Wire Wrapped Assembly

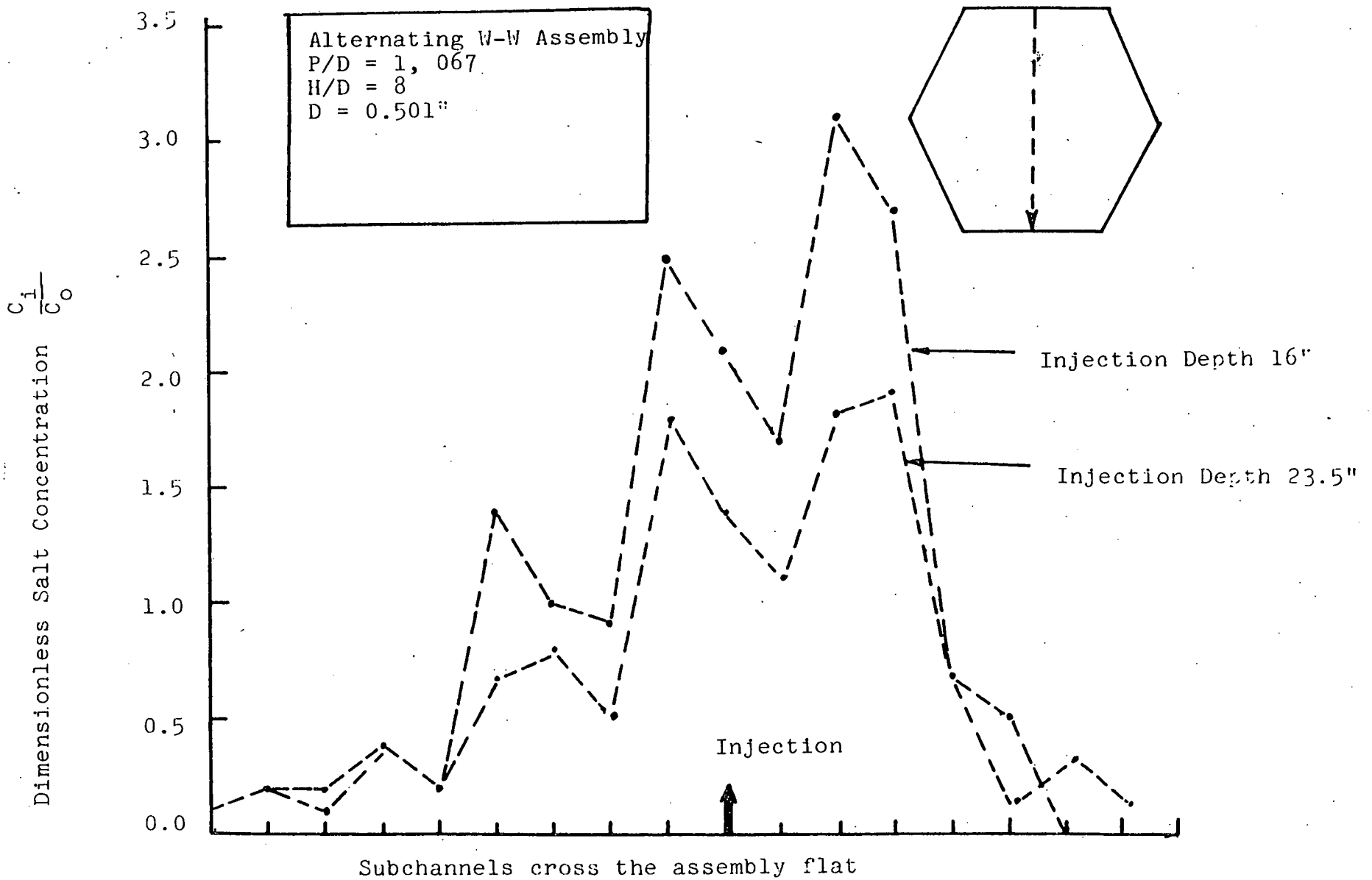

FIGURE 5-1 Salt Distribution Pattern versus Injection Depth of Alternating Wire Wrapped Assembly

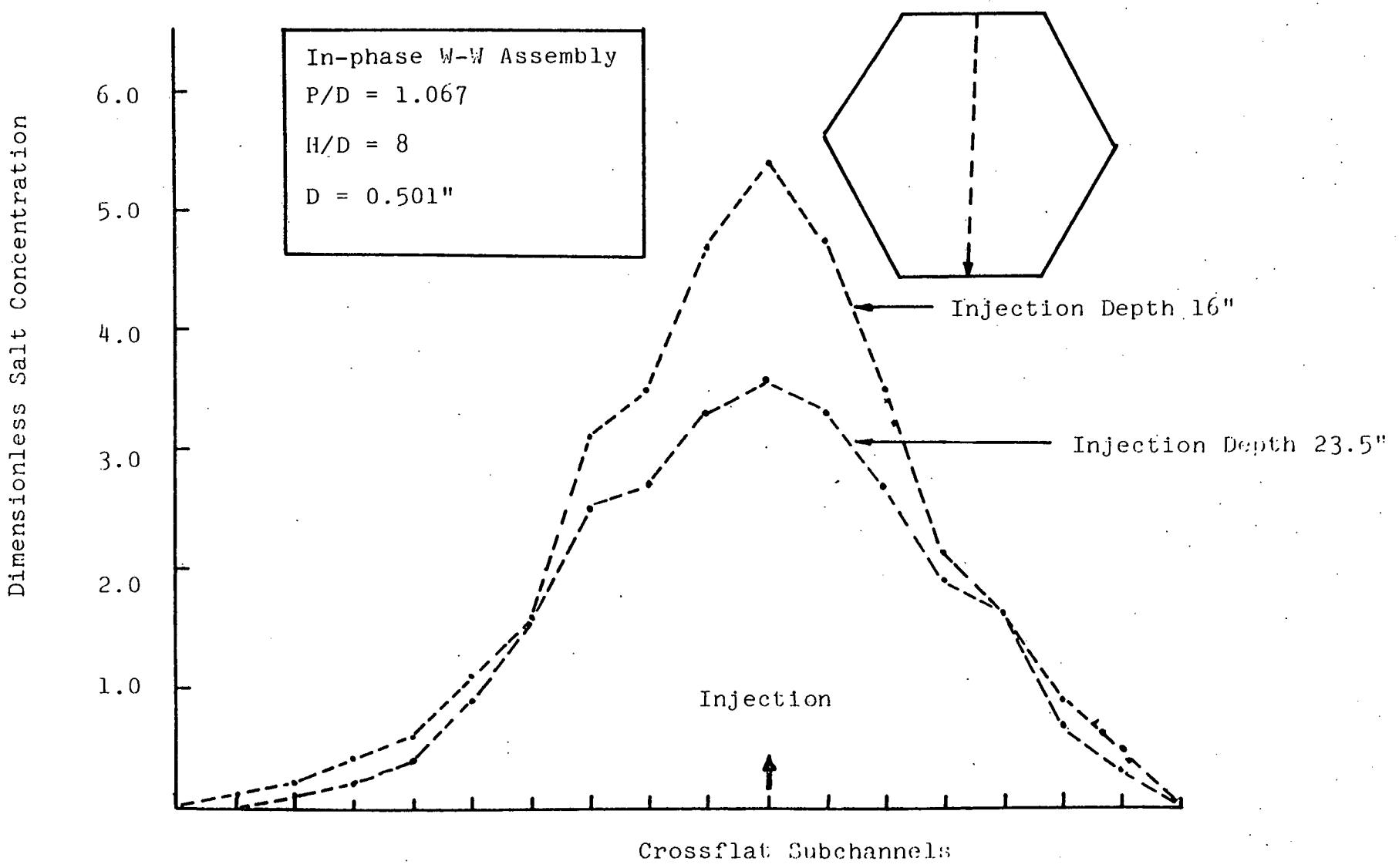

FIGURE 5-2 Salt Distribution Pattern versus Injection Depth of In-Phase Wire Wrapped Assembly

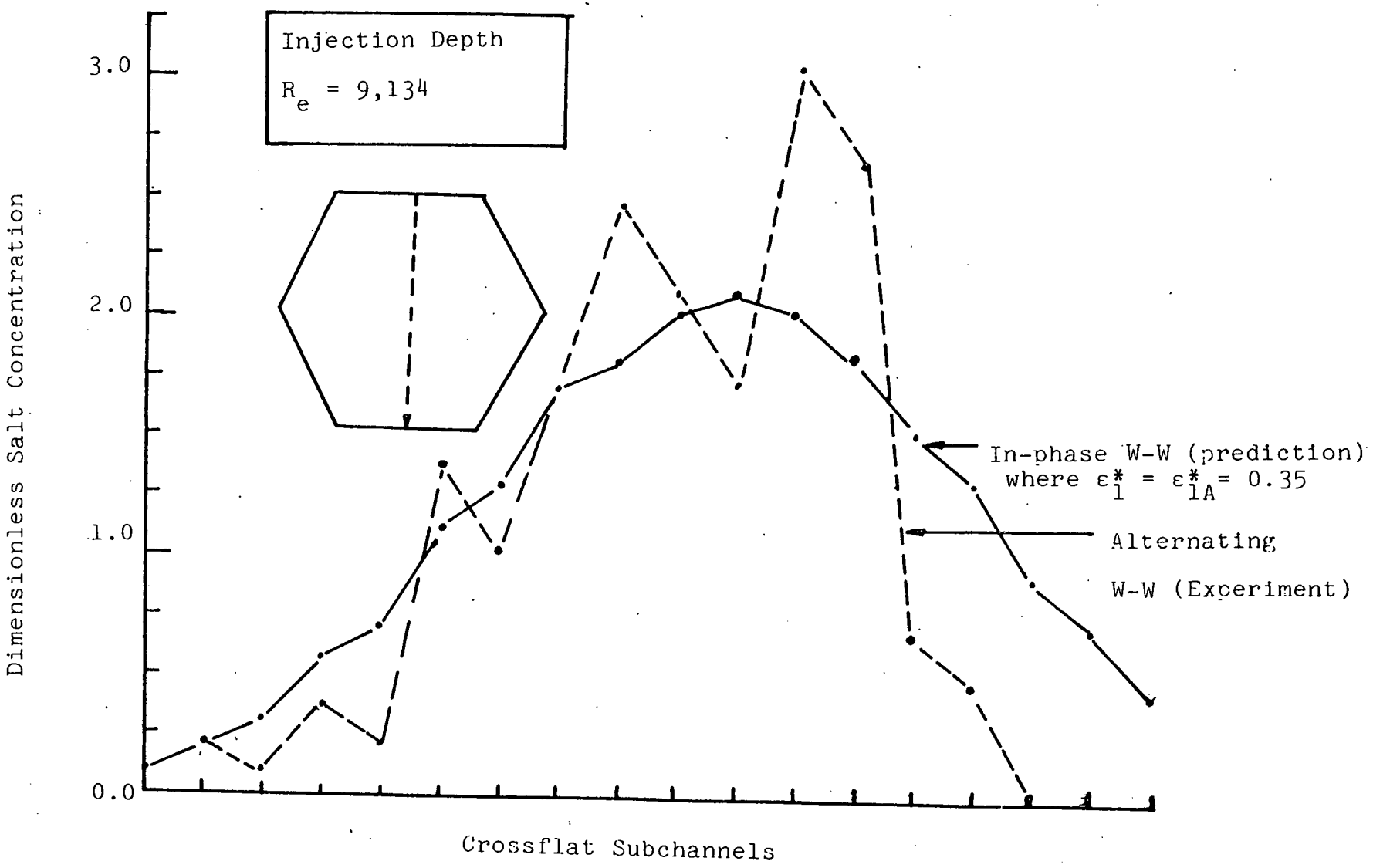

FIGURE 5-3 Comparison Between Salt Distribution Patterns of In-Phase and Alternating Wire Wrapped Assemblies

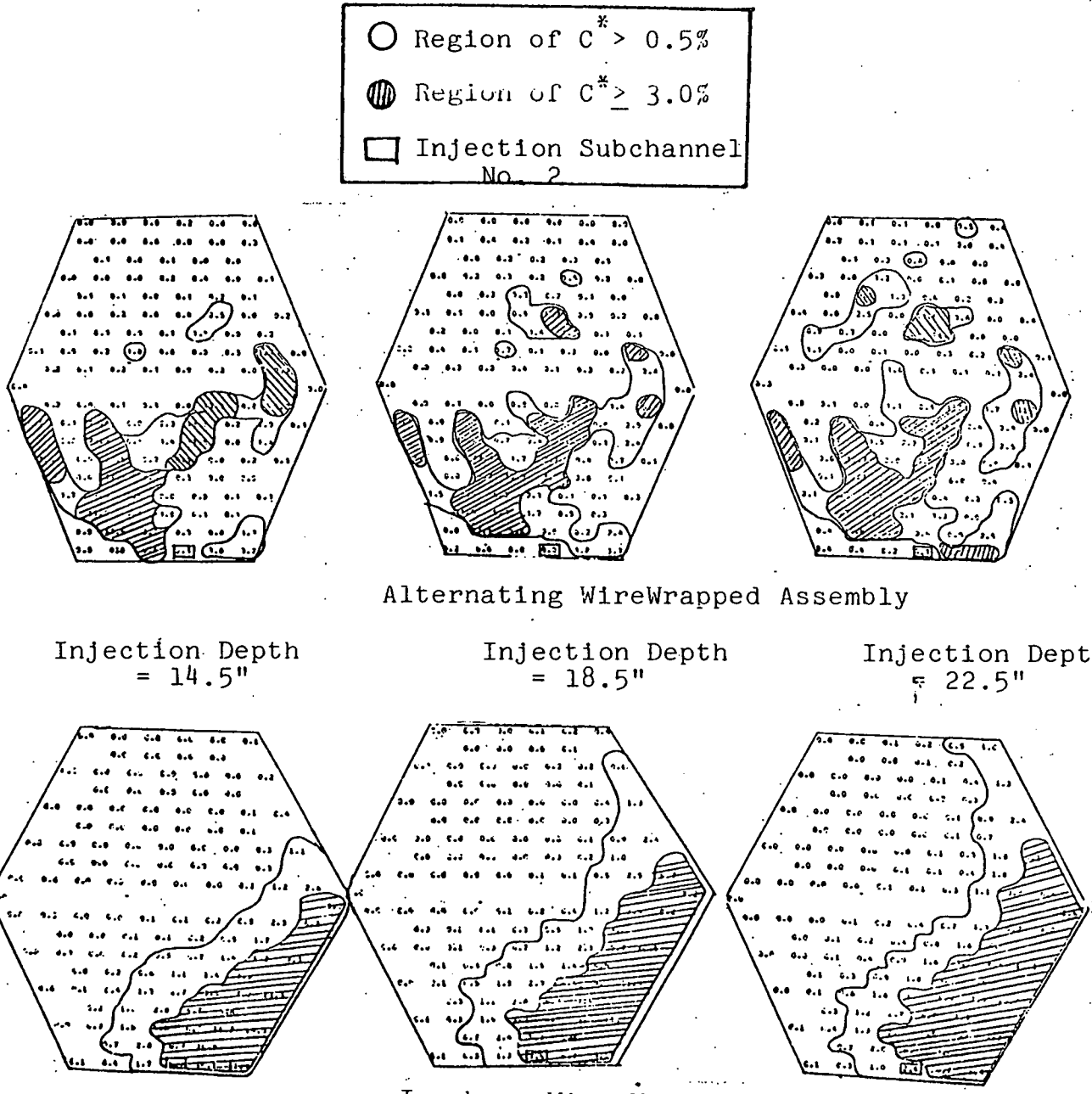

FIGURE 5-4 Development of Dimensionless Salt Concentration Pattern Versus Injection Depth (Injection Subchannel No. 2).

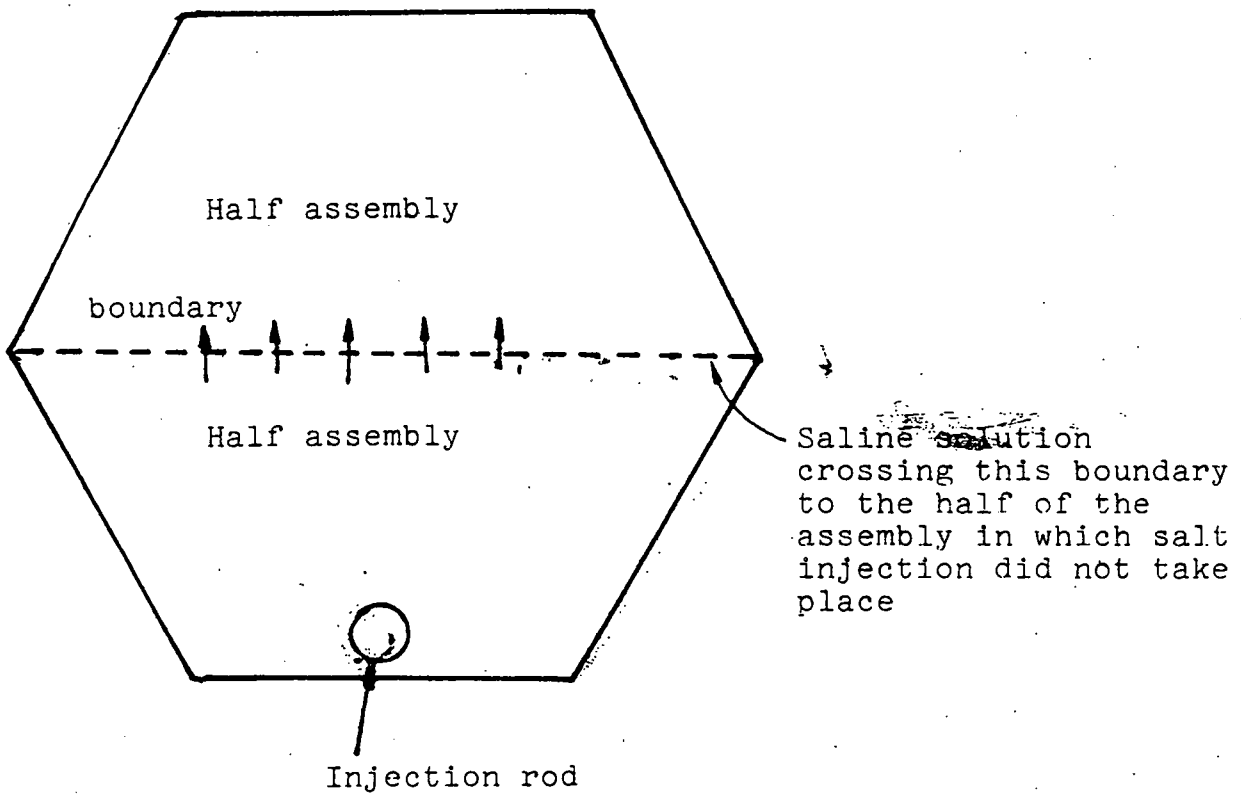

FIGURE 5-5 Configuration of Half of the Assembly in Which the Salt Injection did not Take Place

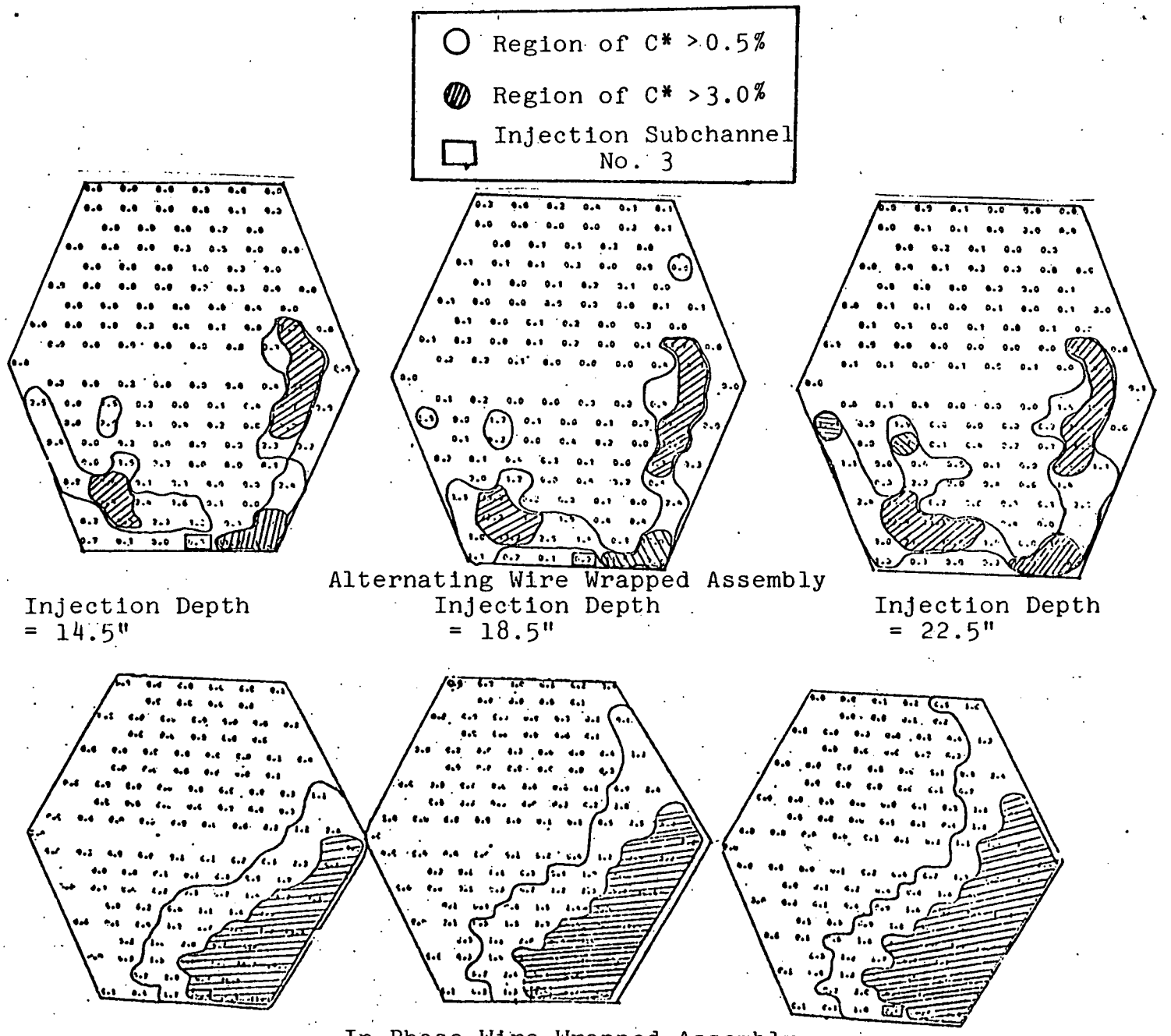

FIGURE 5-6 Development of Dimensionless Salt Concentration Pattern Versus Injection Depth (Injection Subchannel No. 3)

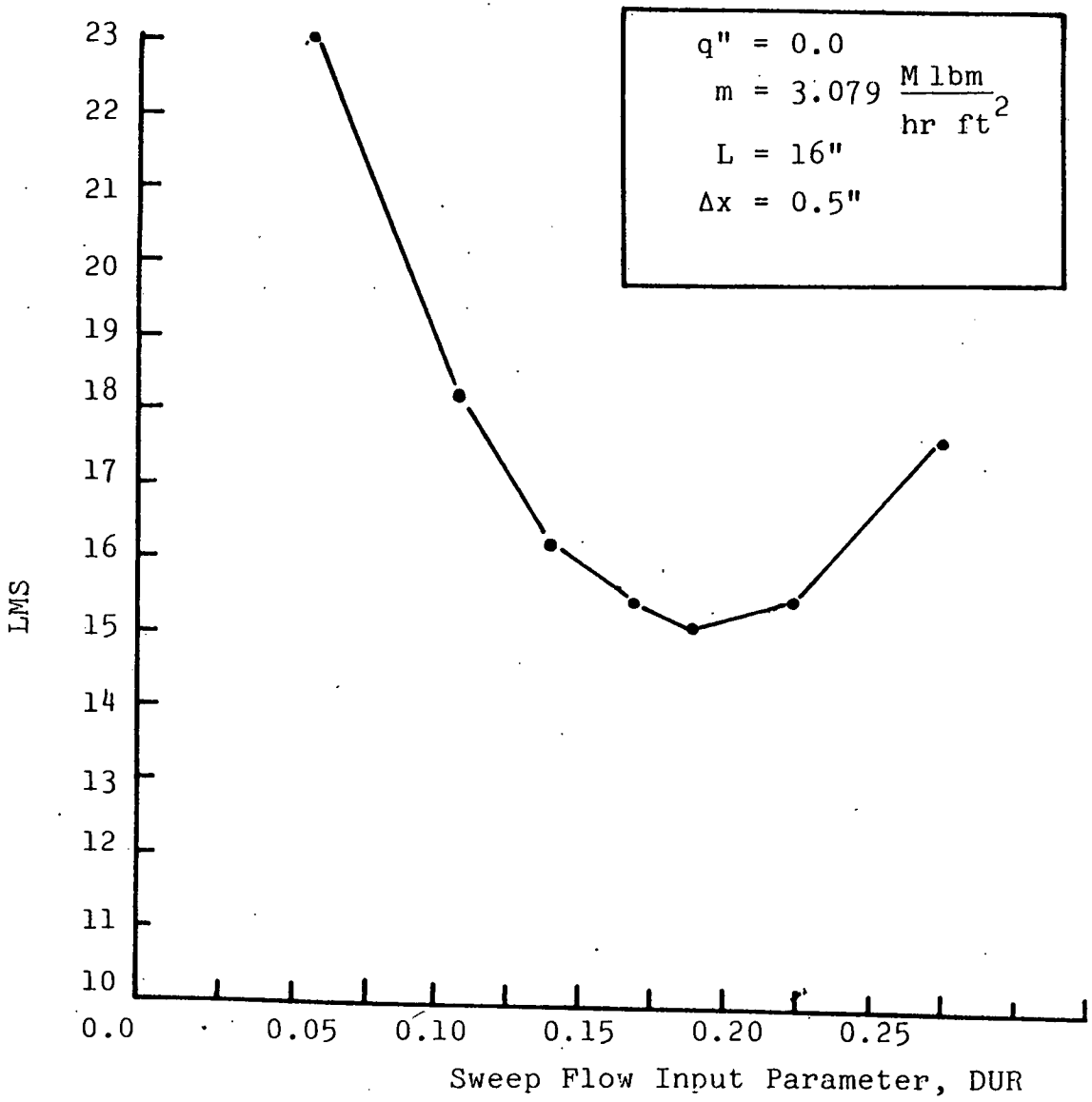

FIGURE 6-1 COBRA-III C Sweep Flow Input Parameter Calibration Curve

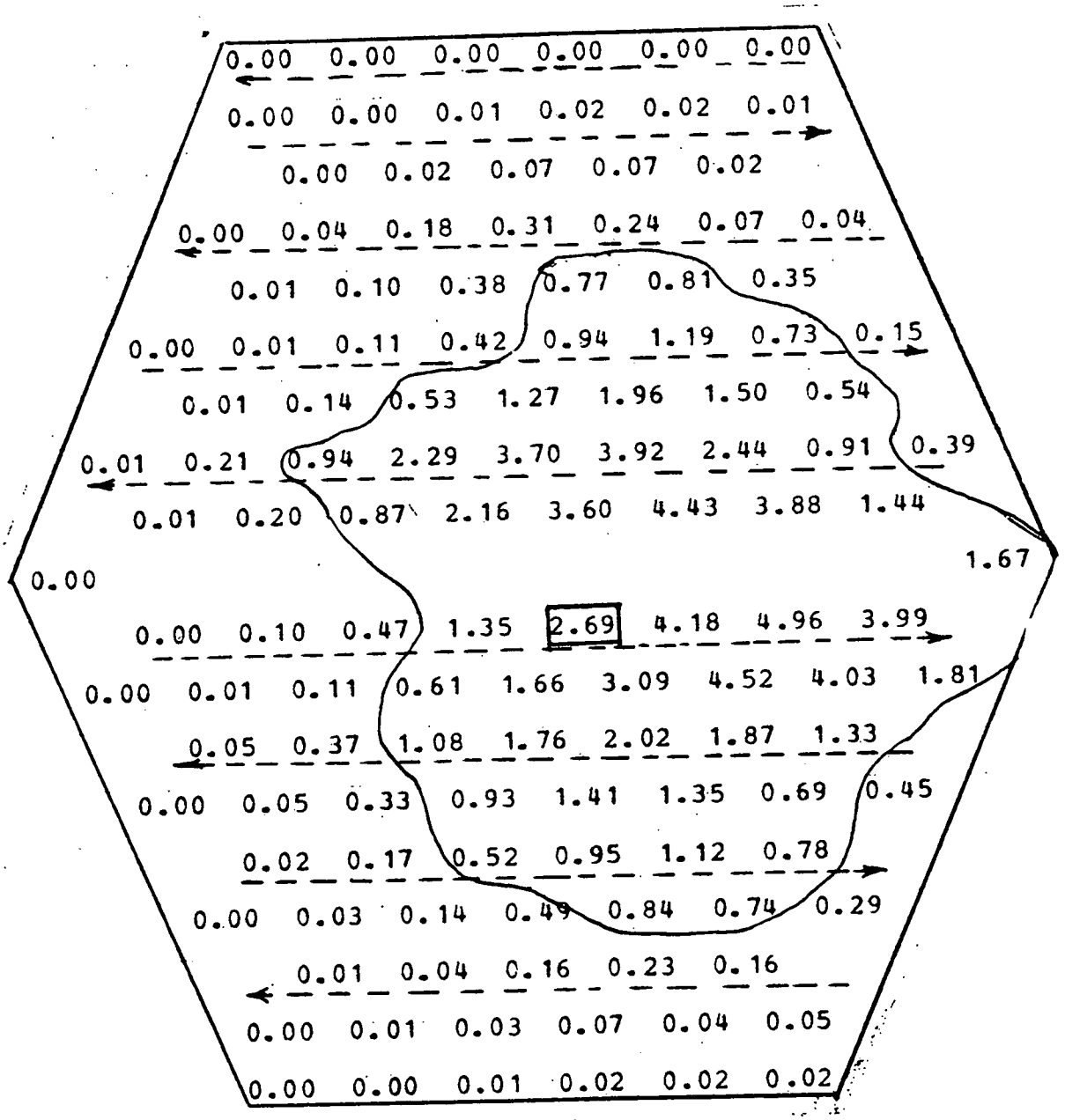

FIGURE 6-2 Dimensionless Salt Concentration Distribution Predicted by COBRA-IIIC/MIT (with Salt Injection at Injection Subchannel No. 1)

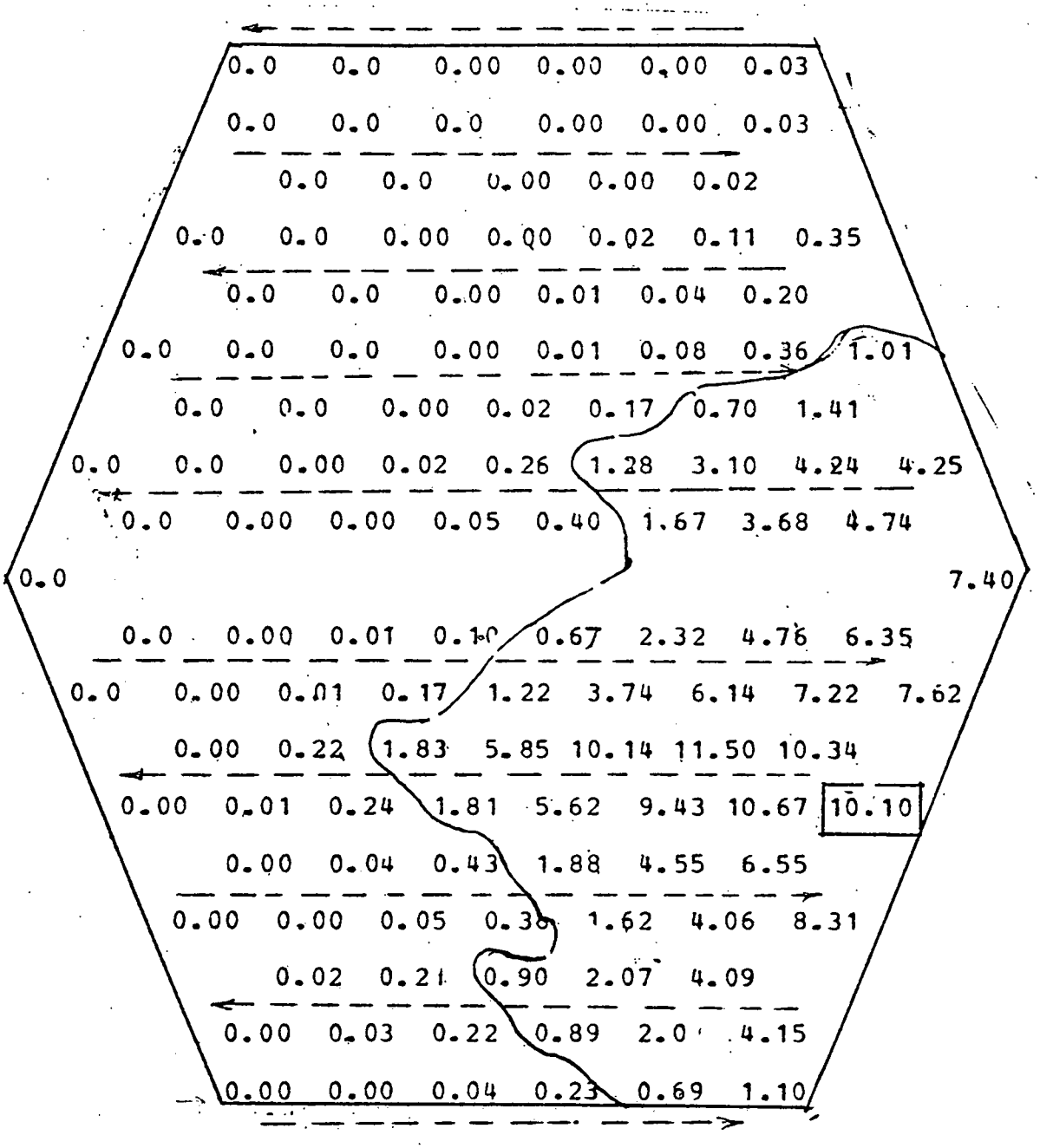

FIGURE 6-3 Dimensionless Salt Concentration Distribution Predicted by COBRA-IIIC/MIT (with Salt Injected at Injection Subchannel No. 2)

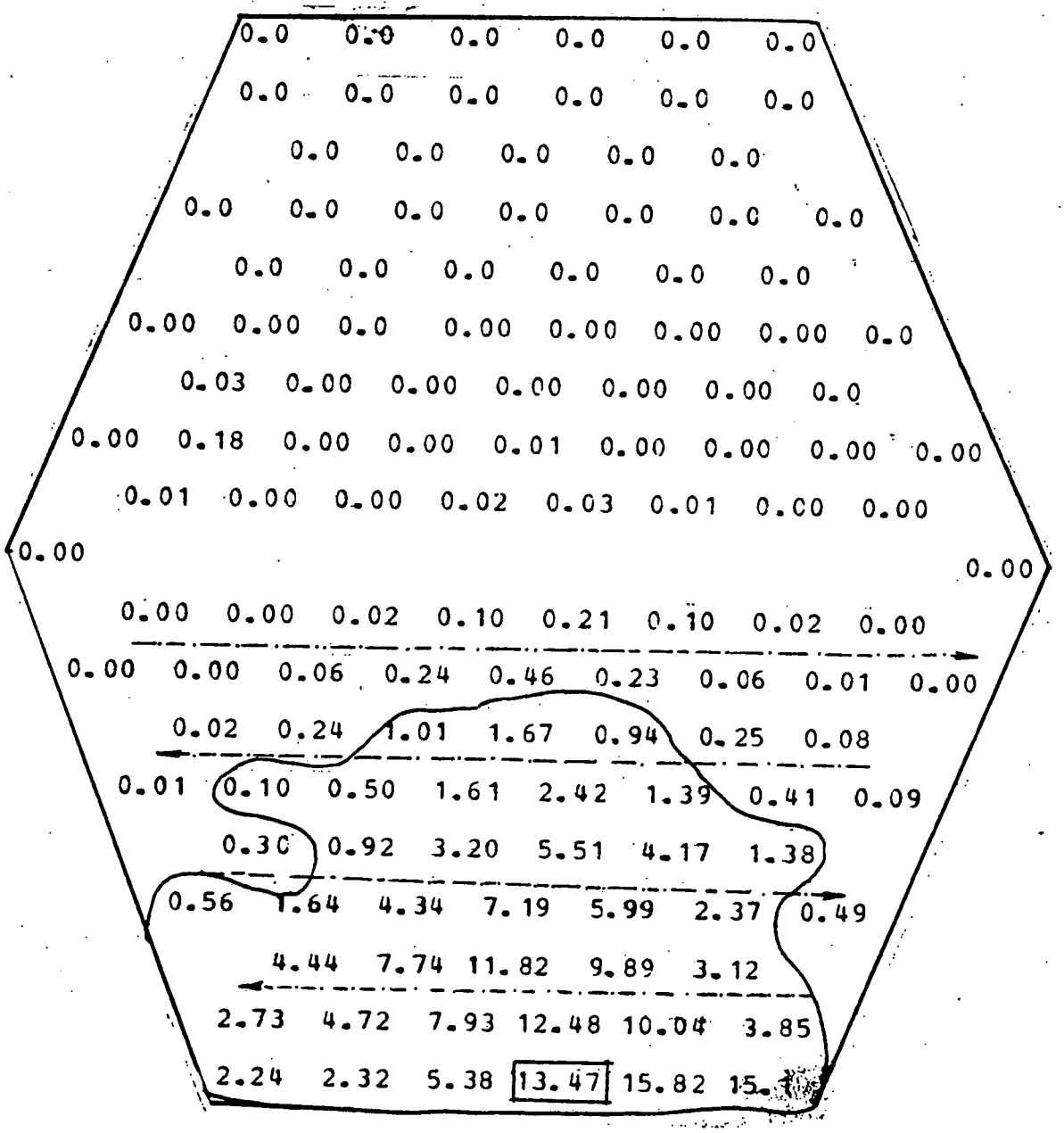

FIGURE 6-4 Dimensionless Salt Concentration Distribution Predicted by COBRA-IIIC/MIT (with Salt Injected at Injection Subchannel No. 3)

SALT CONCENTRATION DISTRIBUTION MAP:

DIMENSIONLESS RATIO OF SALT CONCENTRATION*0.01
MIN16.01
BUNDLE R.E. : 9981
AXIAL LEVEL (IN.) : 16.00
INJ. SUBCHANNEL : 6
MASSBALANCE RATIO : 0.973

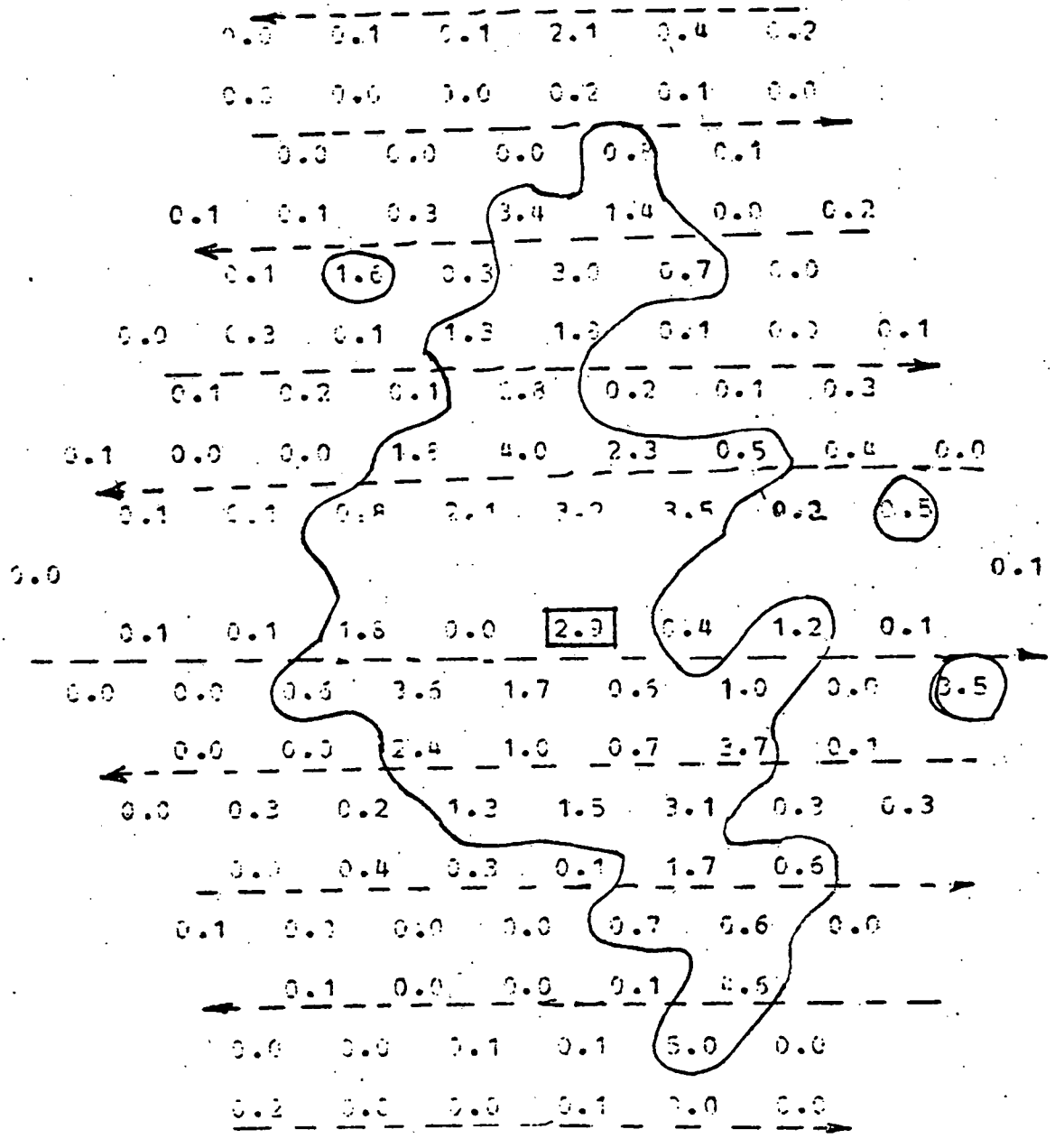

FIGURE 6-5 Dimensionless Salt Concentration Map (Injection Subchannel No. 1)

SALT CONCENTRATION DISTRIBUTION MAP:

DIMENSIONLESS RATIOS OF SALT CONCENTRATION*0.01
MIX80.01
BUNDLE R.E. : 9885
AXIAL LEVEL (IN.) : 21.50
INJ. SUBCHANNEL : 120
MASSBALANCE RATIO : 0.922

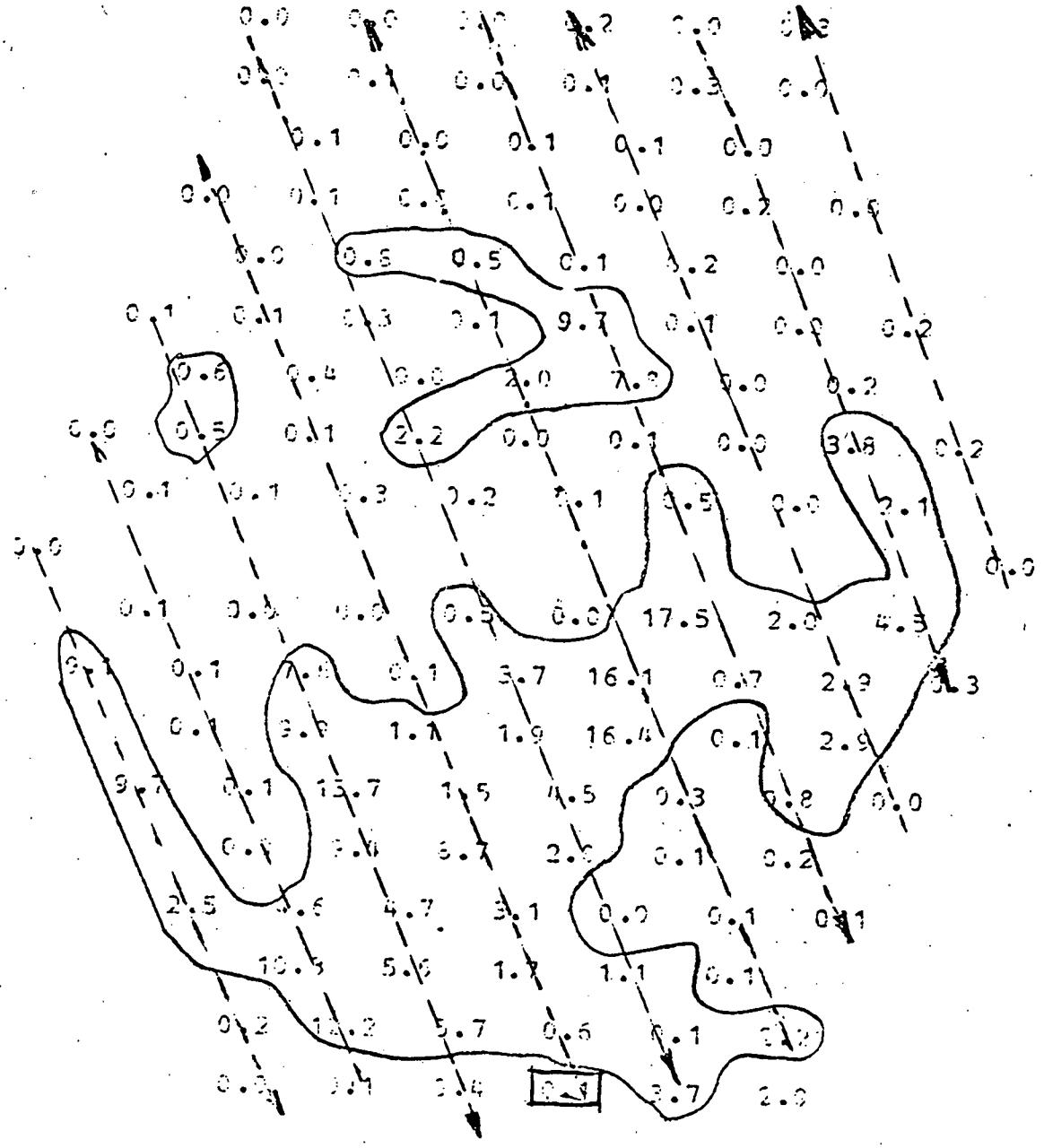

FIGURE 6-6 Dimensionless Salt Concentration Distribution (Injection Subchannel No. 2)

SALT CONCENTRATION DISTRIBUTION MAP:

DIMENSIONLESS RATIOS OF SALT CONCENTRATION*0.01
MIX22.01
BUNDLE R.E. : 9981
AXIAL LEVEL (IN.) : 20.5
INJ. SUBCHANNEL : 120
MASSBALANCE RATIO : 0.987

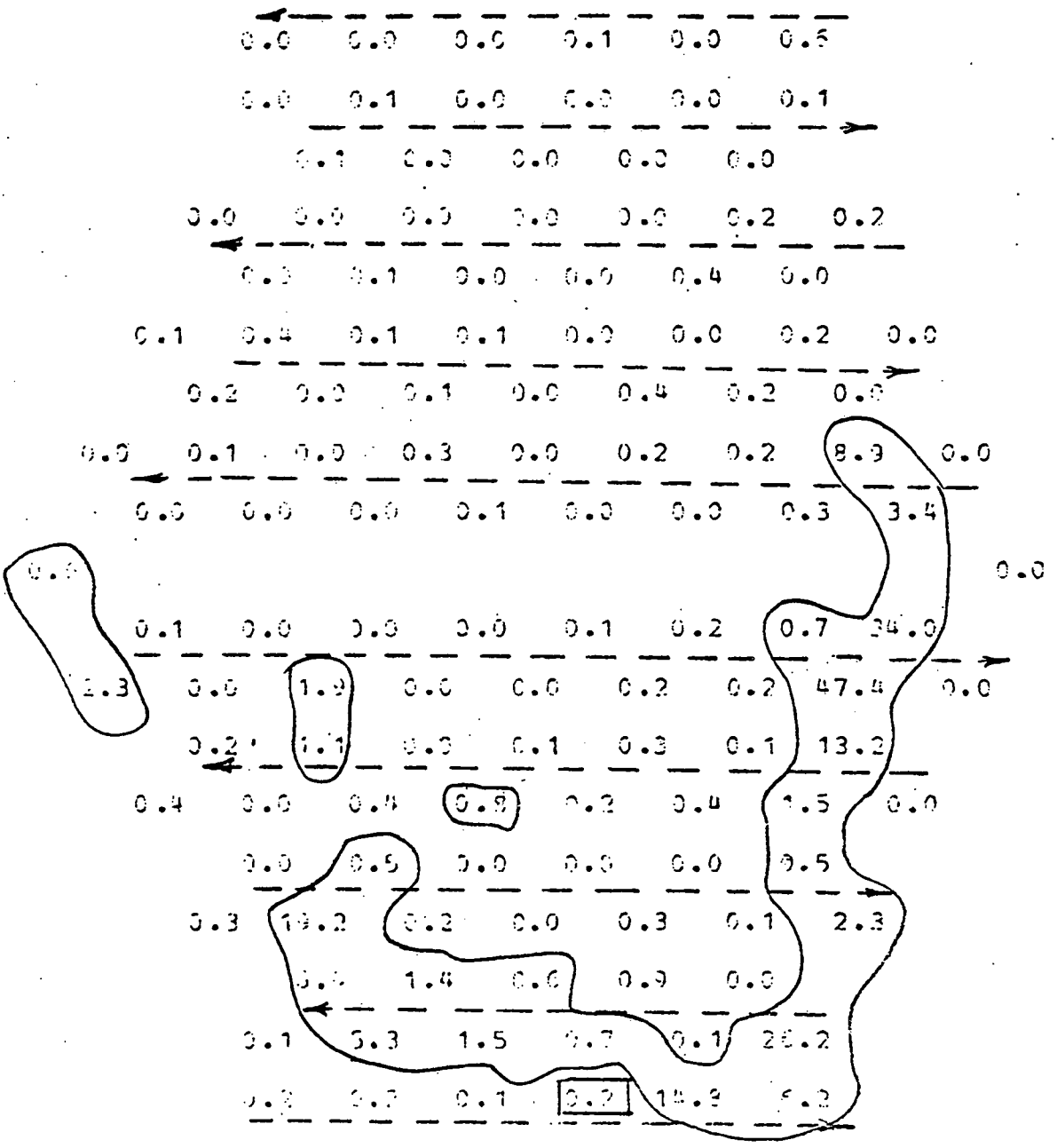

FIGURE 6-7 Dimensionless Salt Concentration Distribution (Injection Subchannel No. 3)

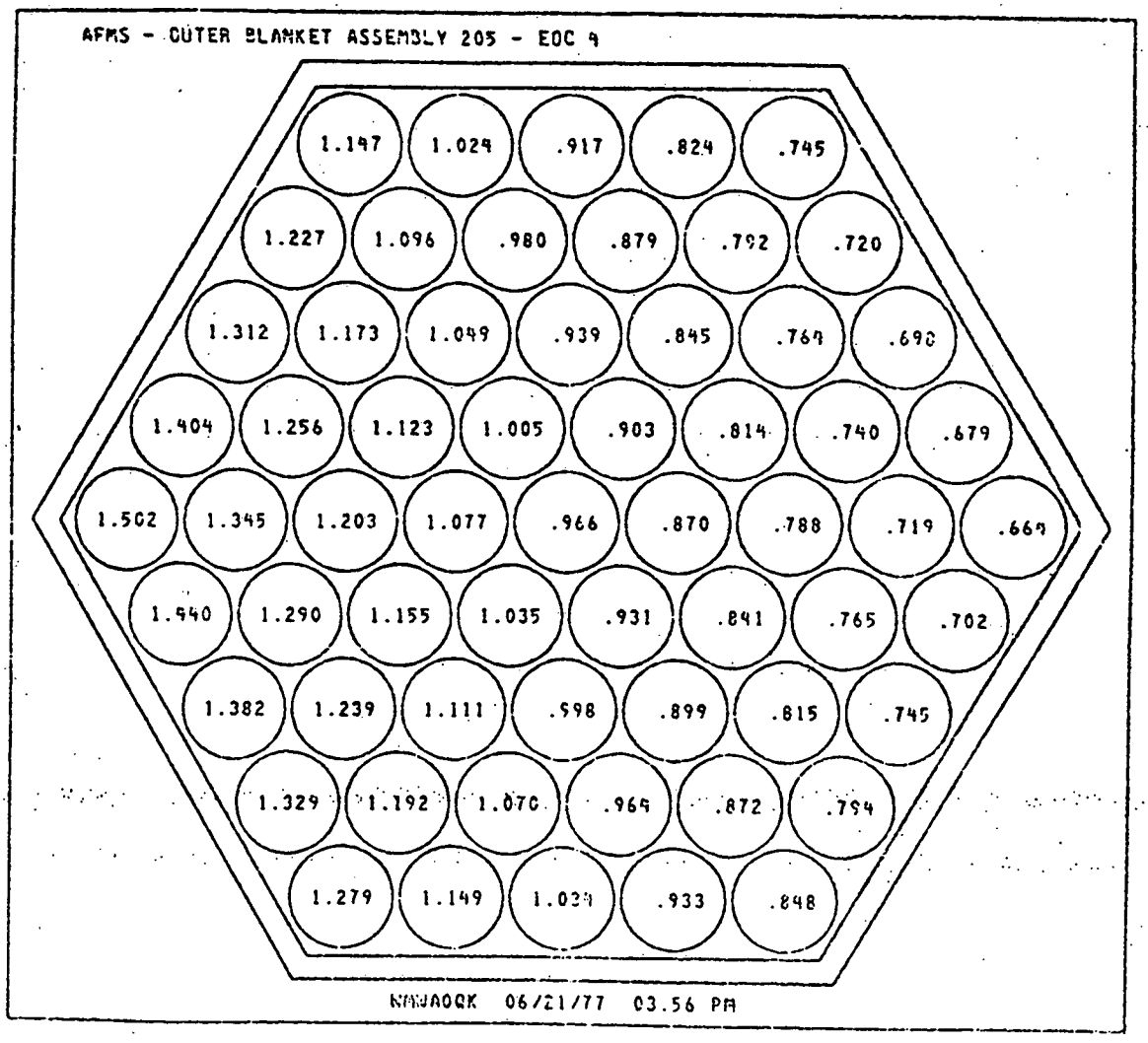

FIGURE 6-8 Radial Power Factors Used in the Code Sample Calculation

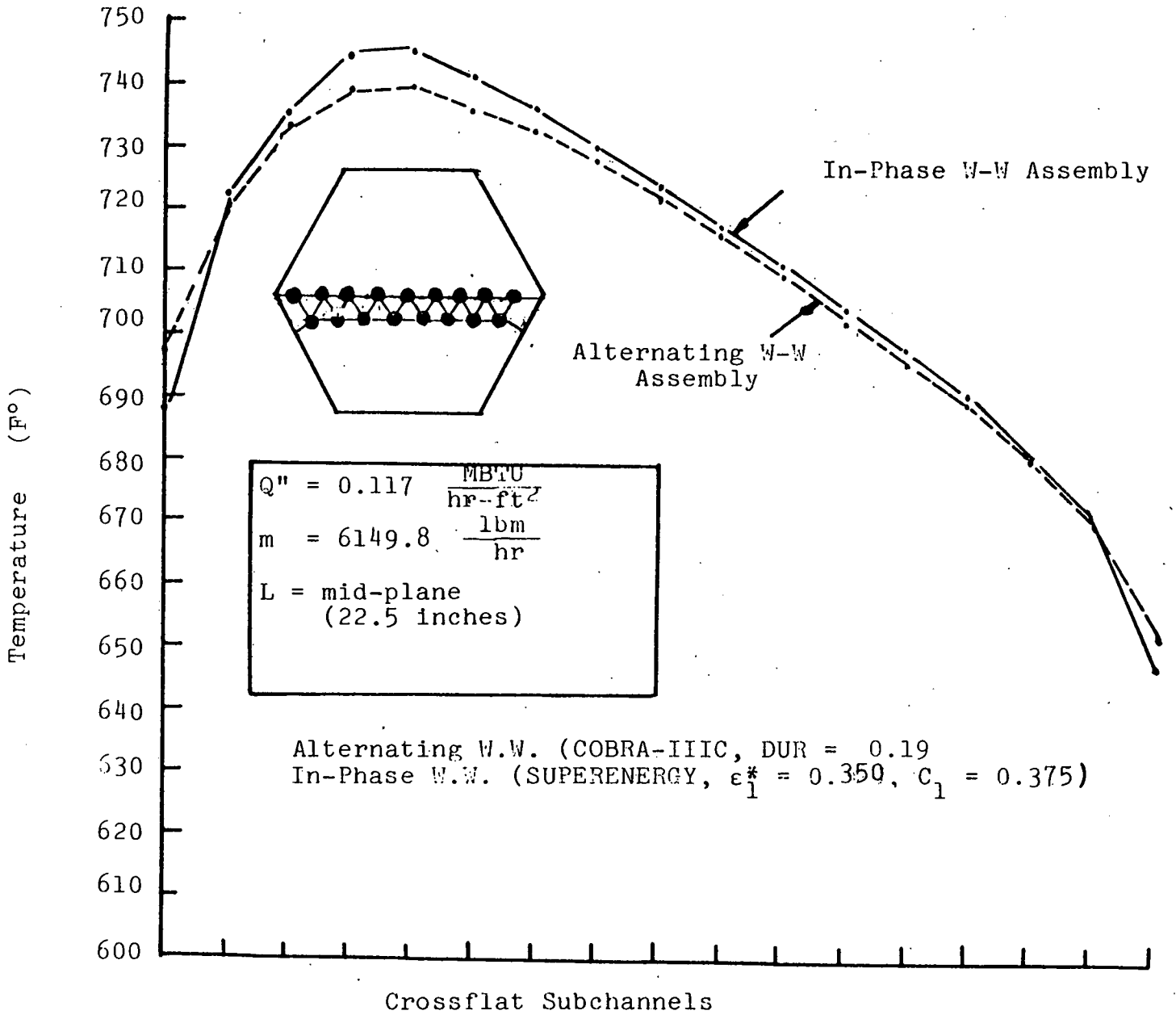

FIGURE 6-9 Cross-assembly (along a Line with Maximum Power Skew) Coolant Temperatures

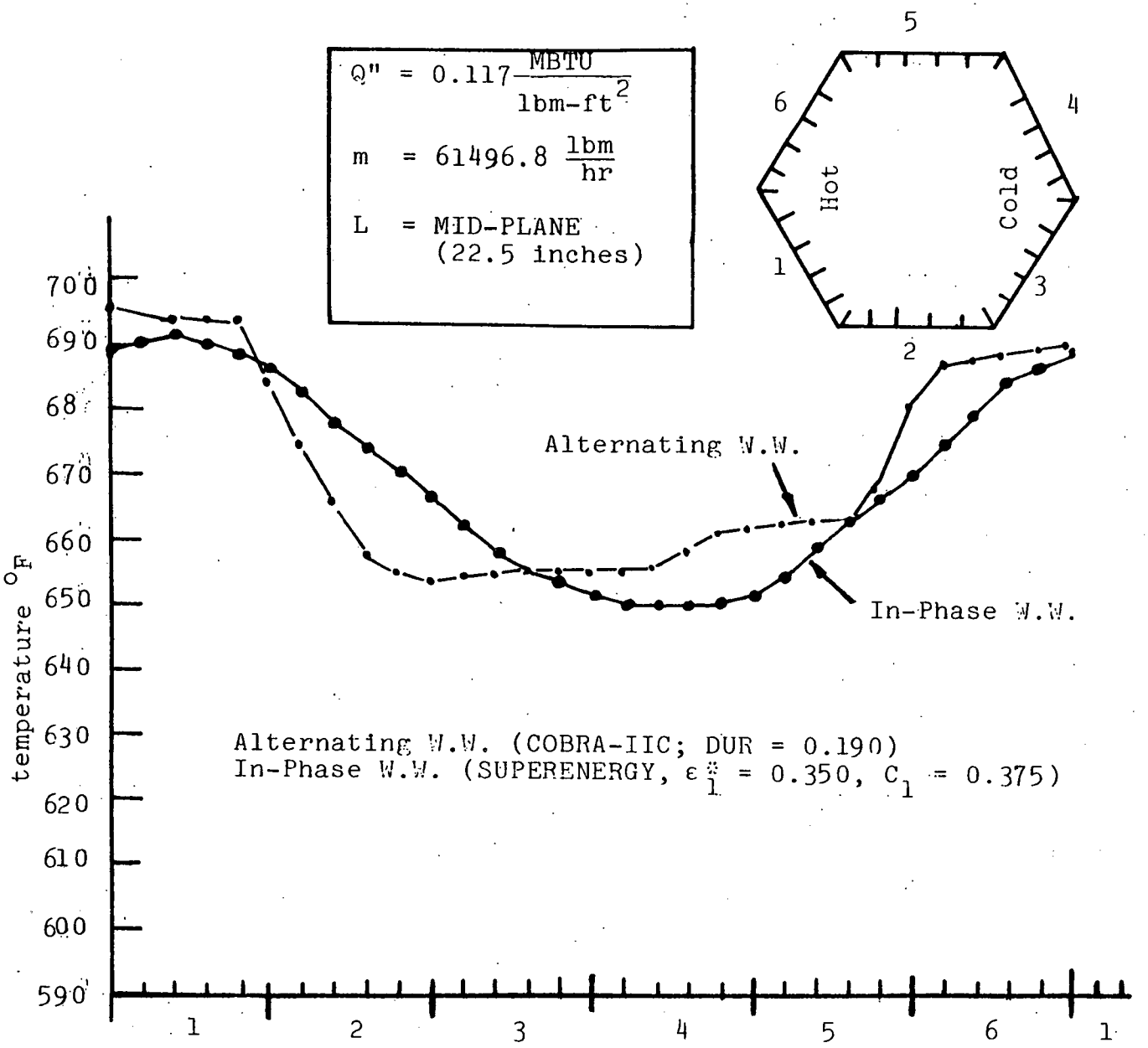

FIGURE 6-10 Peripheral Coolant Temperatures

TABLE 2-1

Test Section Geometric Parameters

Wire wrap lead	4 inch
Rod diameter	0.50 inches
Wire diameter	0.0314 inches
Bundle length	5 foot
Flat to flat distance (as-built)	4.275 inch
Flat to flat tolerance	0.022 inch

TABLE 3-1

Test Runs at a Given Injection Depth and Different Reynolds Numbers

INJECTION SUBCHANNEL No. 1			INJECTION SUBCHANNEL No. 2			INJECTION SUBCHANNEL No. 3		
Test Run No.	R_e	Injection Depth	Test Run No.	R_e	Injection Depth	Test Run No.	R_e	Injection Depth
1	12,164	16"	6	12,164	20.5"	11	12,164	21.5"
2	9,981	16"	7	9,981	20.5"	12	9.981	21.5"
3	8,109	16"	8	8,109	20.5"	13	8,109	21.5"
4	6,238	16"	9	6,238	20.5"	14	6,238	21.5"
5	4,367	16"	10	4,367	20.5"	15	4,867	21.5"

TABLE 3-2

Test Runs at Re = 9134 and Different Injection Depths for Injection Subchannel 2

INJECTION SUBCHANNEL 1

$R_e \equiv 9134$

Injection Depth ≡ Variable

Test Run No.	INJECTION DEPTH	Test Run No.	INJECTION DEPTH
16	16.0"	24	20.5"
17	16.5"	25	21.0"
18	17.0"	26	22.0"
19	17.5"	27	22.5"
20	18.0"	28	23.0"
21	19.0"	29	23.5"
22	19.5"	30	24.5"
23	20.0"	31	25.5"
		32	26.5"

TABLE 3-3

Test Runs at Re = 9134 and Different Injection Depths for Injection Subchannel 2

INJECTION SUBCHANNEL 2
$R_e \equiv$ 9134
INJECTION DEPTH ≡ VARIABLE

Test Run No.	Injection Depth	Test Run No.	Injection Depth
33	13.5"	40	19.0"
34	14.5'	41	19.5"
35	15.5"	42	20.0"
36	16.5"	43	23.0"
37	17.5"	44	23.5"
38	18.0"	45	24.0"
39	18.5"	46	25.0"

TABLE 3-4

Test Runs at Re = 8822 and Different Injection Depths for Injection Subchannel 3

INJECTION SUBCHANNEL 3 $R_e \equiv 8822$ Injection Depth ≡ Variable

Test Run No.	INJECTION DEPTH	Test Run No	INJECTION DEPTH
47	13.5"	58	19.5"
48	14.0"	59	20.0"
49	14.5"	60	20.5"
50	15.0"	61	21.0"
51	15.5"	62	21.5"
52	16.0"	63	22.0"
53	16.5"	64	22.5"
54	17.5"	65	23.0"
55	18.0"	66	24.0"
56	18.5"	67	25.0"
57	19.0"	68	26.0"
		69	27.0"

TABLE 6-1

Bundle Geometric Characteristics and Operational Conditions in Code Calculation

Geometric characteristics:		
wire wrap lead	4	inch
rod diameter	0.50	inch
wire diameter	0.0314	inch
bundle length	22.5	inch
flat to flat distance	4.275	inch
Operational conditions:		
average rod heat flux	0.117	$\frac{\text{MBTU}}{\text{hr ft}^2}$
total bundle flow rate	6149.8	$\frac{\text{lbm}}{\text{hr}}$
axial power profile	flat	
radial power factor	as illustrated in Fig. 20	

APPENDIX A

Dimensionless Salt Concentration Data

In this appendix, the dimensionless salt concentration experimental data are presented. Section A.1 contains the dimensionless salt distribution maps for three injection subchannels at a series of different Reynolds Numbers. Section A.2 contains the dimensionless salt distribution maps for the interior injection subchannel, injection subchannel No. 1, and a given Reynolds Number, but at a series of injection depths. Sections A.3 and A.4 contain the dimensionless salt distribution maps for the injection subchannels No. 2 and No. 3 respectively. The data presented in these two sections are at a given Reynolds Number and a series of injection depths.

The 0.5 dimensionless salt concentration contours are plotted on all the maps to aid the understanding of the salt distribution. In addition, the enhanced flow paths are marked on all the maps presented in this Appendix to illustrate the orientation of the data with respect to the enhanced flow directions. The injection subchannel is marked as a box on each map.

APPENDIX A.1

DIMENSIONLESS SALT CONCENTRATION MAPS AT DIFFERENT REYNOLDS NUMBERS FOR THREE INJECTION SUBCHANNELS

SALT CONCENTRATION DISTRIBUTION MAP:

DIMENSIONLESS RATIO OF SALT CONCENTRATION*0.01
MIX21.01
BUNDLE R.E. : 4357
AXIAL LEVEL (IN.) : 16.00
INJ. SUBCHANNEL : 6
MASSBALANCE RATIO : 0.972

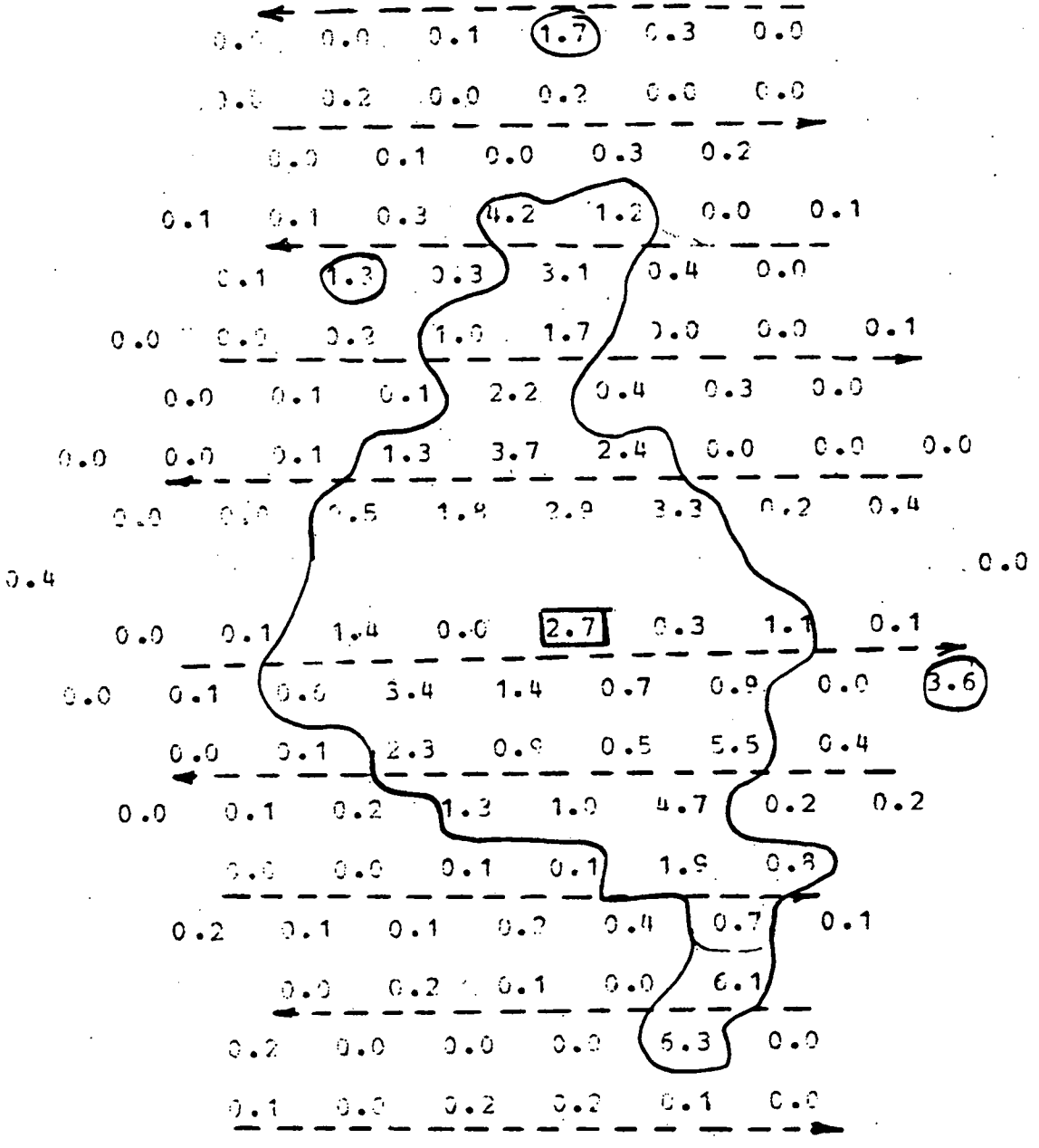

Figure A.1

SALT CONCENTRATION DISTRIBUTION MAP:

DIMENSIONLESS RATIOS OF SALT CONCENTRATION*0.01
MIX20.01
BUNDLE R.E. : 6238
AXIAL LEVEL (IN.) : 16.00
INJ. SUBCHANNEL : 6
MASSBALANCE RATIO : 0.977

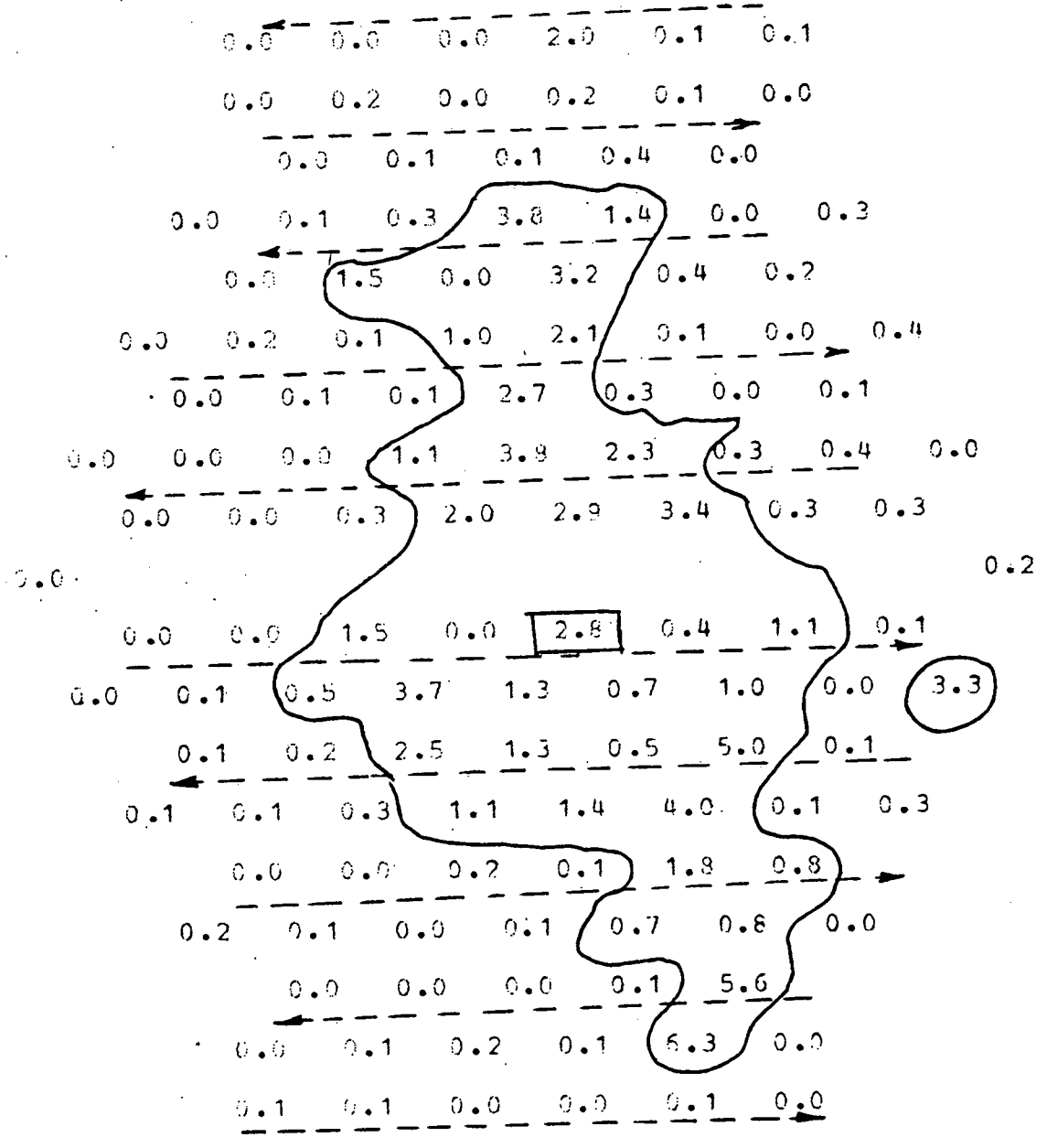

Figure A.2

SALT CONCENTRATION DISTRIBUTION MAP:

DIMENSIONLESS RATIOS OF SALT CONCENTRATION*0.01
MIX19.01
BUNDLE R.E. : 8109
AXIAL LEVEL (IN.) : 19.00
INJ. SUBCHANNEL : 6
MASSBALANCE RATIO : .984

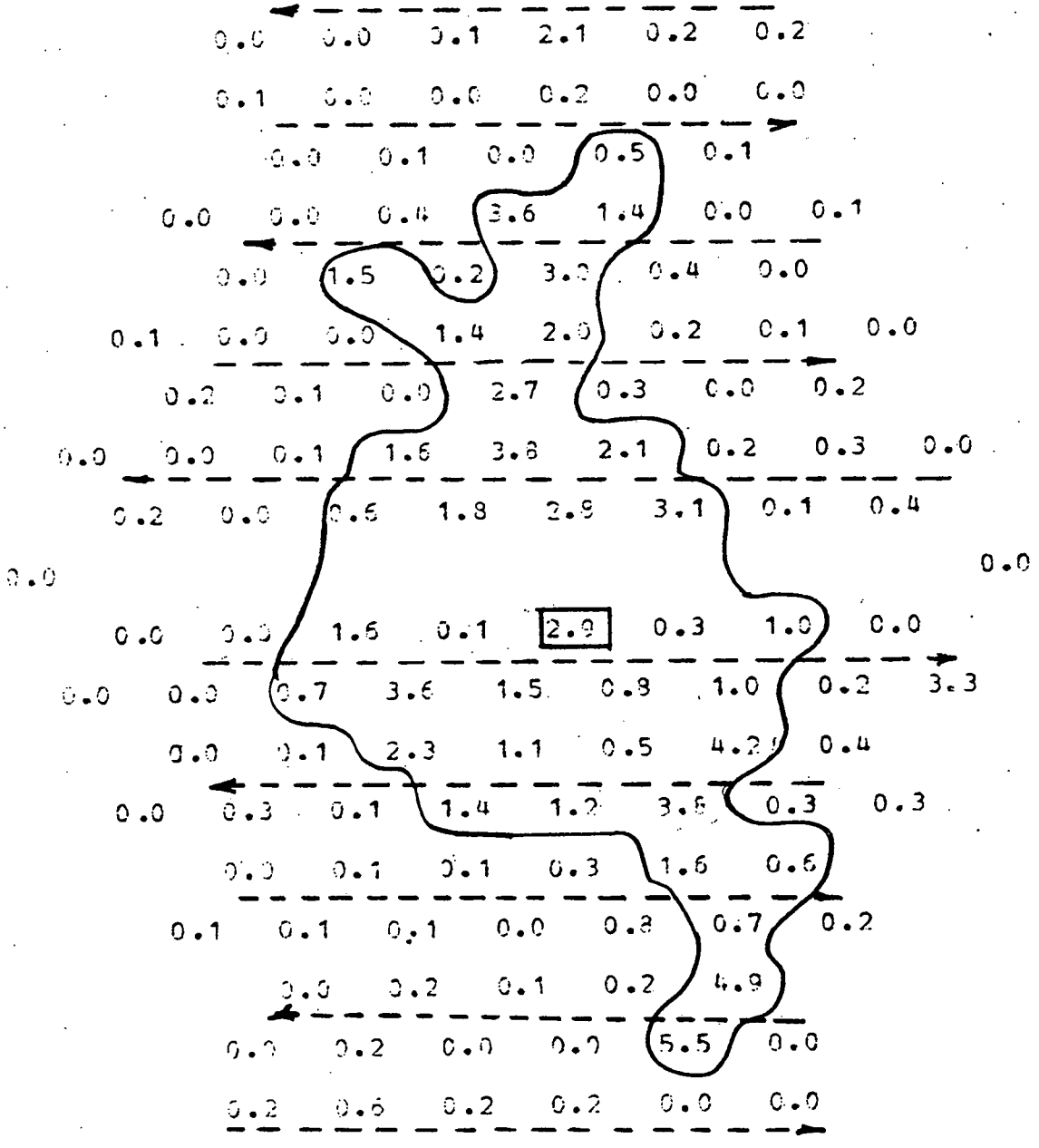

Figure A.3

SALT CONCENTRATION DISTRIBUTION MAP:

DIMENSIONLESS RATIO OF SALT CONCENTRATION*0.01
MIX18.01
BUNDLE R.E. : 9981
AXIAL LEVEL (IN.) : 18.00
INJ. SUBCHANNEL : 6
MASSBALANCE RATIO : 0.973

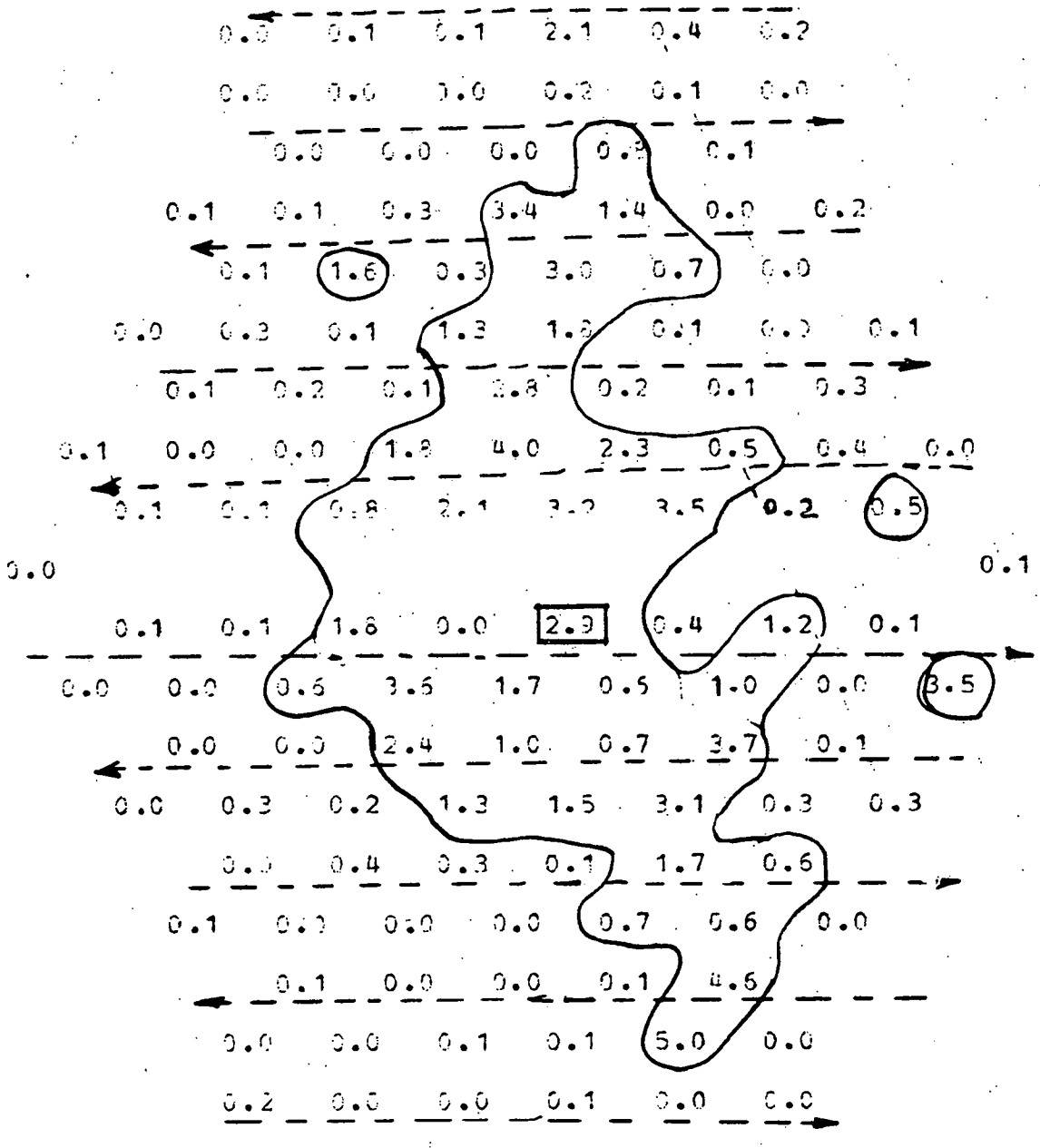

Figure A.4 Dimensionless Salt Concentration Map with Injection Channel No. 1

SALT CONCENTRATION DISTRIBUTION MAP:

DIMENSIONLESS RATIOS OF SALT CONCENTRATION*0.01
MIX17.01
BUNDLE R.E. : 12164
AXIAL LEVEL (IN.) : 16.00
INJ. SUBCHANNEL : 6
MASSBALANCE RATIO : 0.921

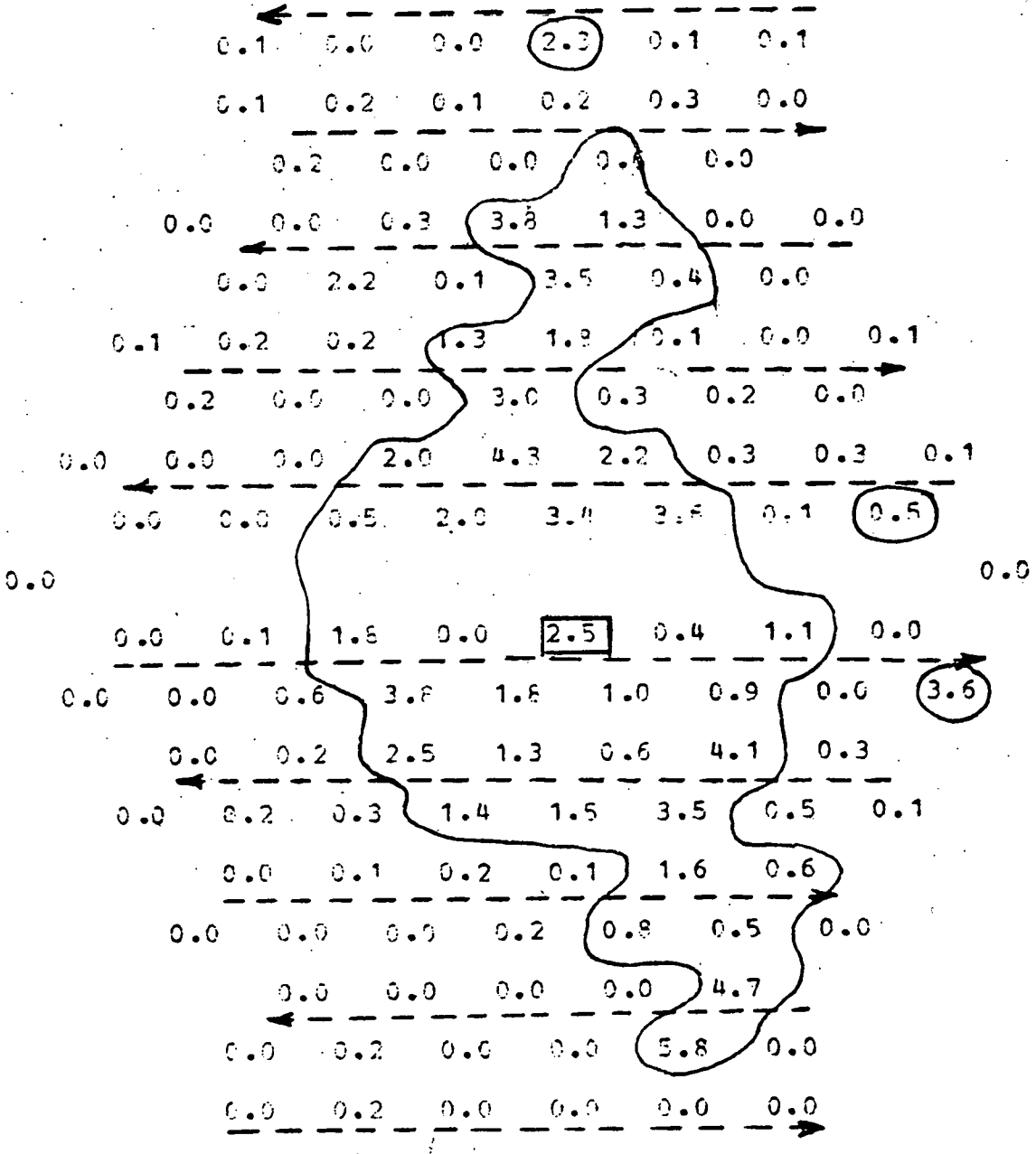

Figure A.5

SALT CONCENTRATION DISTRIBUTION MAP:

DIMENSIONLESS RATION OF SALT CONCENTRATION*0.01
MIX33.01
BUNDLE R.E. : 4335
AXIAL LEVEL (IN.) : 21.50
INJ. SUBCHANNEL : 120
MASSBALANCE RATIO : 0.86%

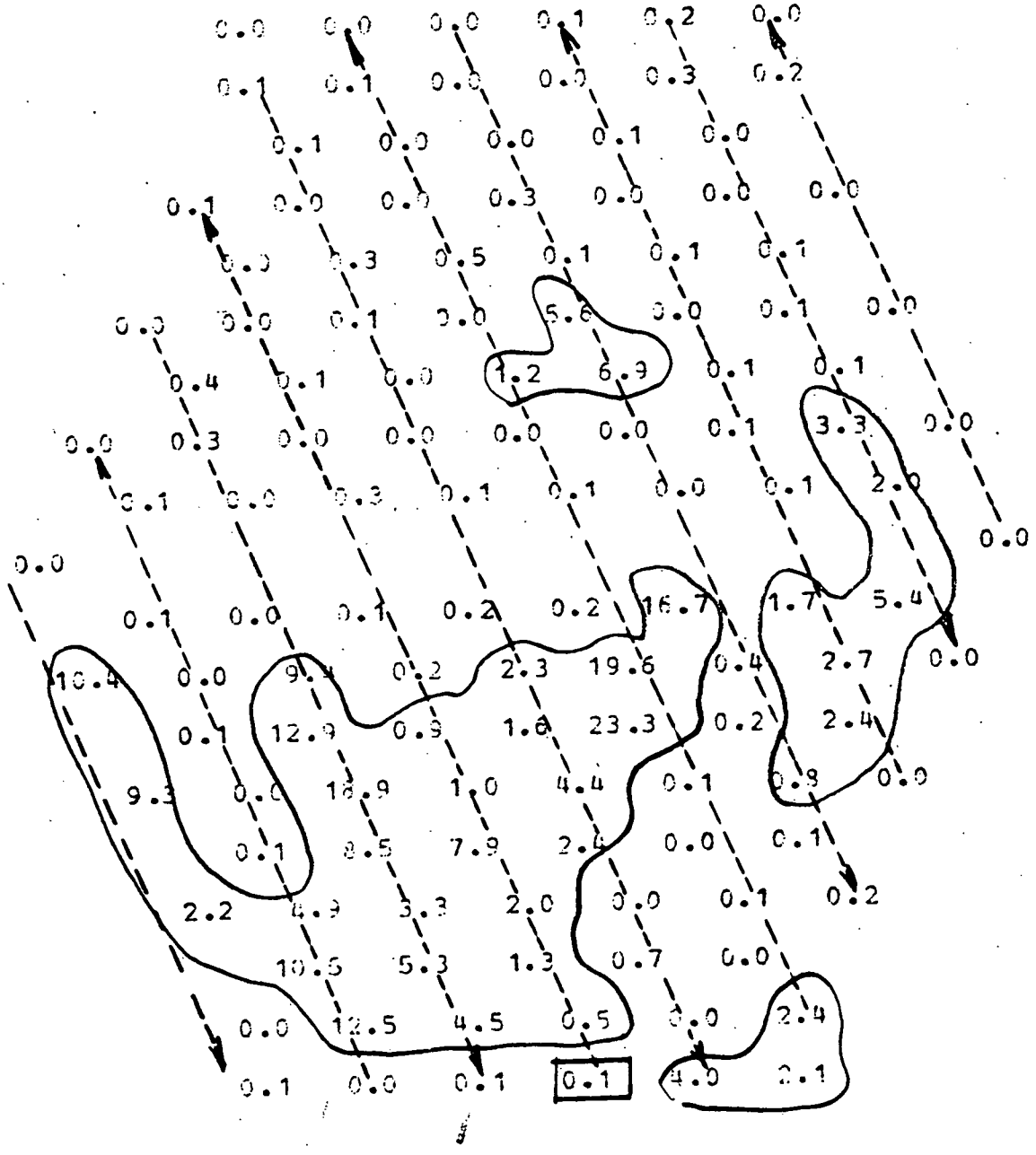

Figure A.6

SALT CONCENTRATION DISTRIBUTION MAP:

DIMENSIONLESS RATIOS OF SALT CONCENTRATION*0.01
MIX32.01
BUNDLE R.E. : 6178
AXIAL LEVEL (IN.) : 21.50
INJ. SUBCHANNEL : 120
MASSBALANCE RATIO : 0.861

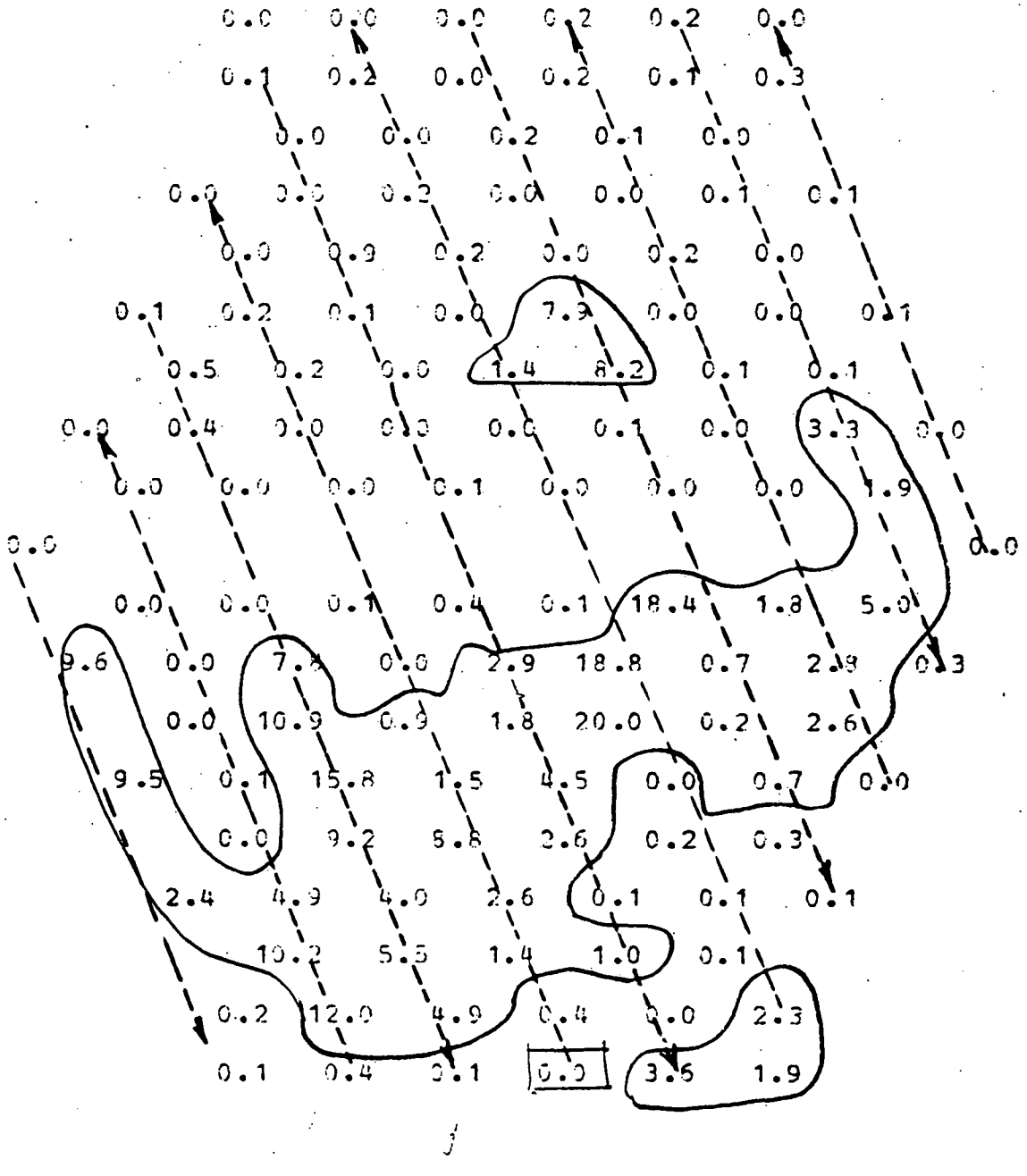

Figure A.7

SALT CONCENTRATION DISTRIBUTION MAP:

DIMENSIONLESS RATIOS OF SALT CONCENTRATION*0.01
MIX31.01
BUNDLE R.E. : 8031
AXIAL LEVEL (IN.) : 21.50
INJ. SUBCHANNEL : 120
MASSBALANCE RATIO : 0.910

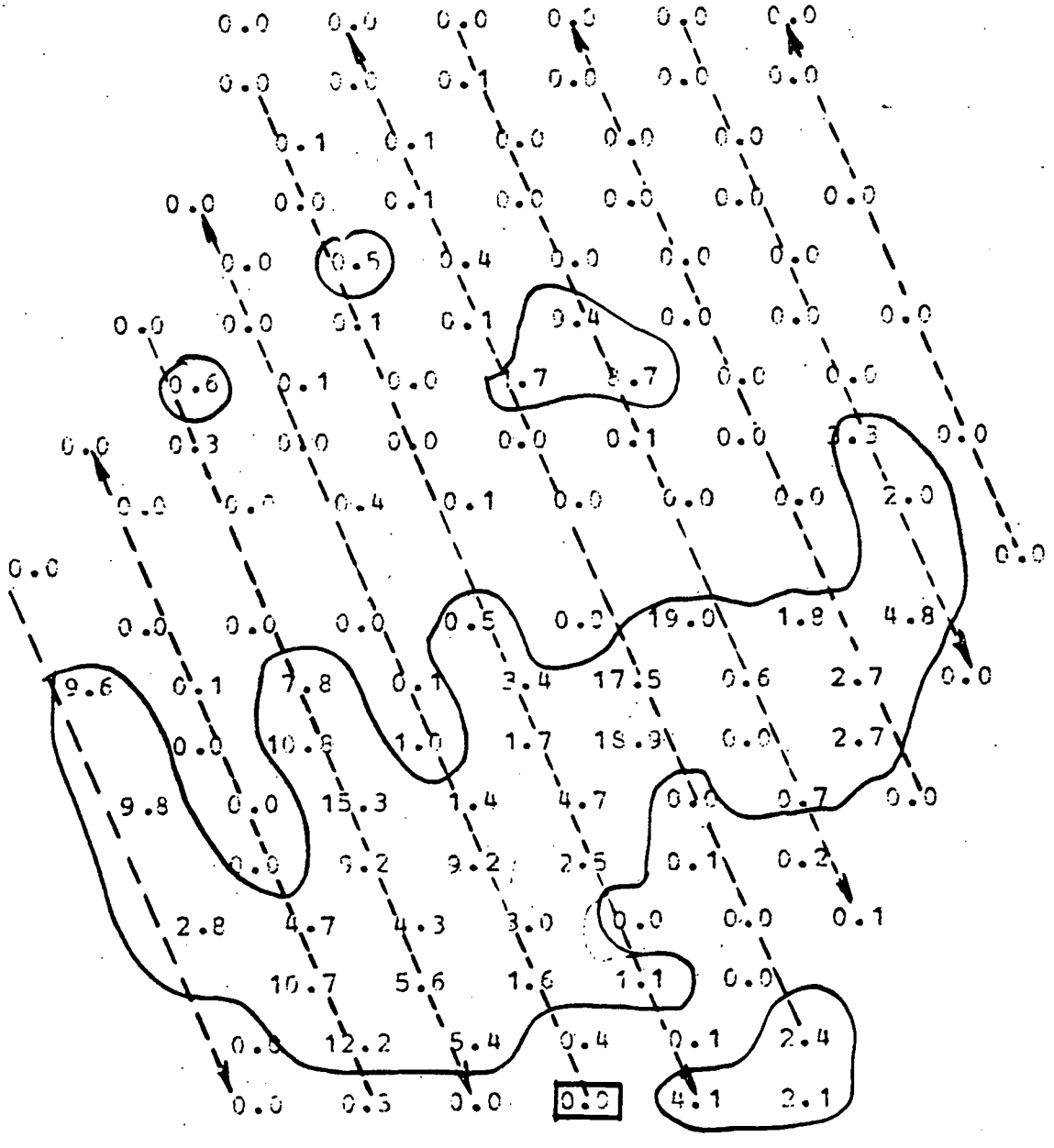

Figure A.8

SALT CONCENTRATION DISTRIBUTION MAP:

DIMENSIONLESS RATIOS OF SALT CONCENTRATION*0.01
MIX29.01
BUNDLE B.E. :12047
AXIAL LEVEL (IN.) : 21.30
INJ. SUBCHANNEL : 120
MASSBALANCE RATIO : 0.909

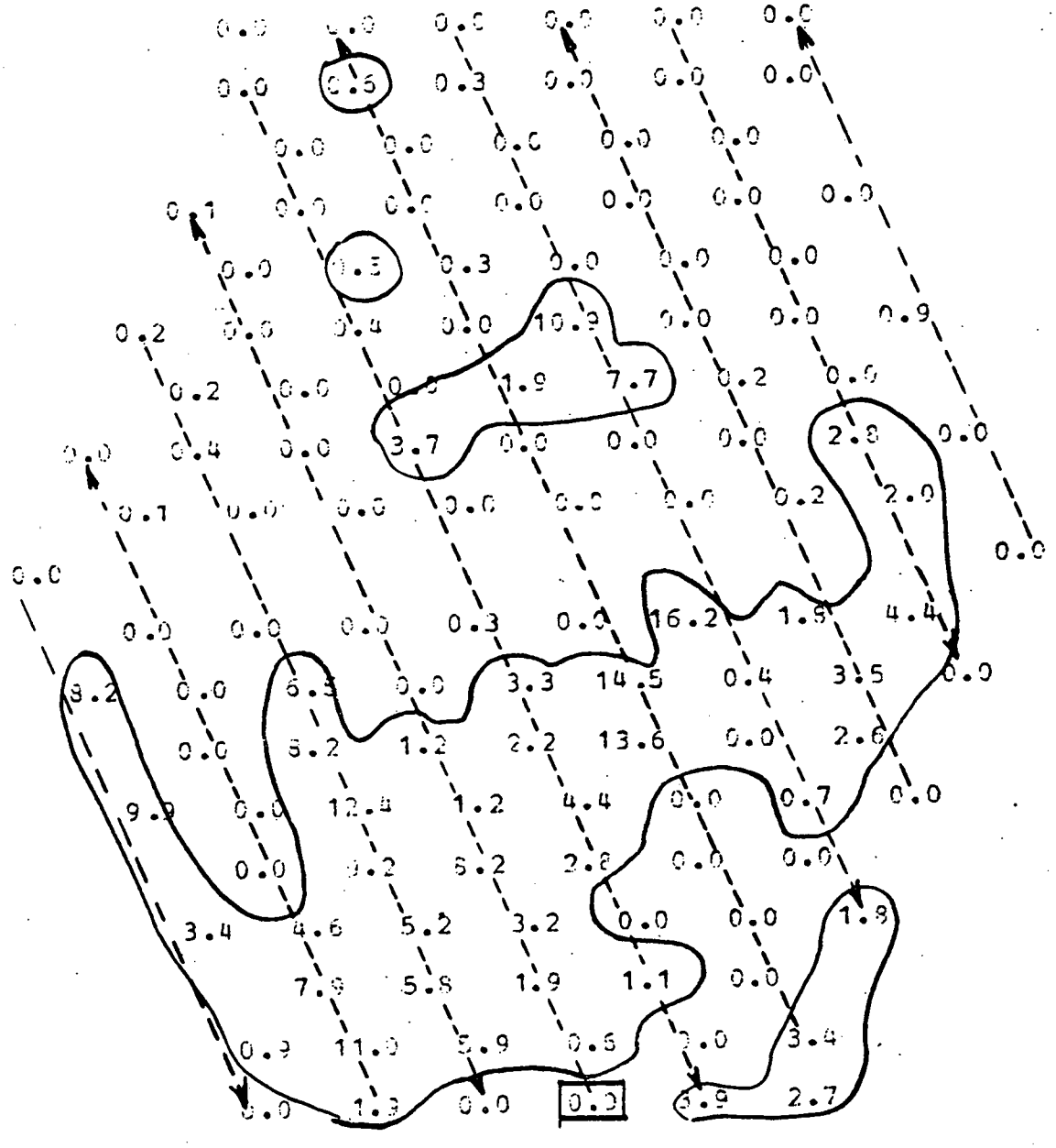

Figure A.9

SALT CONCENTRATION DISTRIBUTION MAP:

DIMENSIONLESS RATIO OF SALT CONCENTRATION*0.01
MIX30.01
BUNDLE R.E. : 9885
AXIAL LEVEL (IN.) : 21.50
INJ. SUBCHANNEL : 120
MASSBALANCE RATIO : 0.922

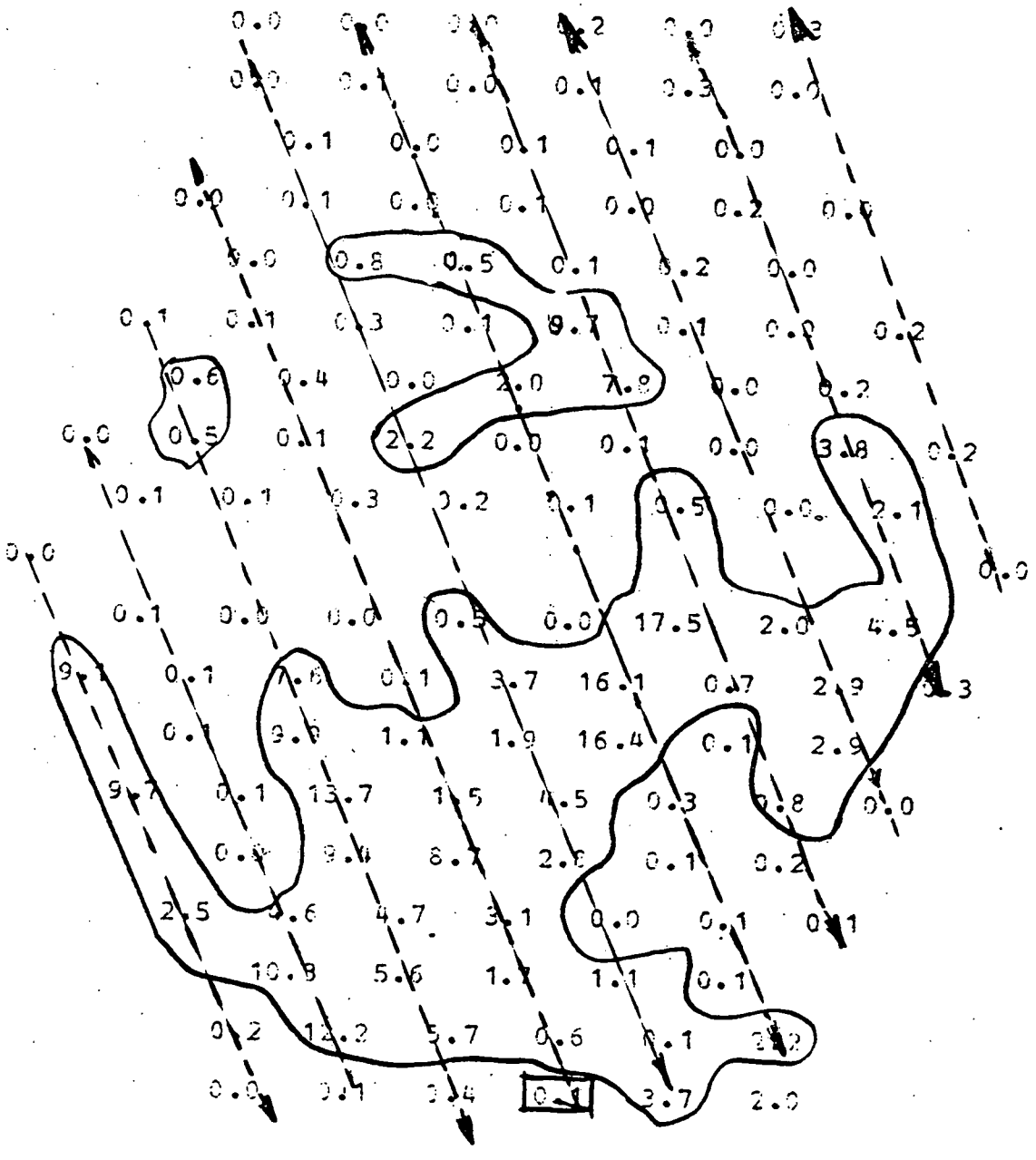

Figure A.10 Dimensionless Salt Concentration Map with Injection Channel No. 2

SALT CONCENTRATION DISTRIBUTION MAP:

DIMENSIONLESS RATIOS OF SALT CONCENTRATION*0.01
MIX26.01
BUNDLE R.E. : 4367
AXIAL LEVEL (IN.) : 2.00
INJ. SUBCHANNEL : 120
MASSBALANCE RATIO : 0.980

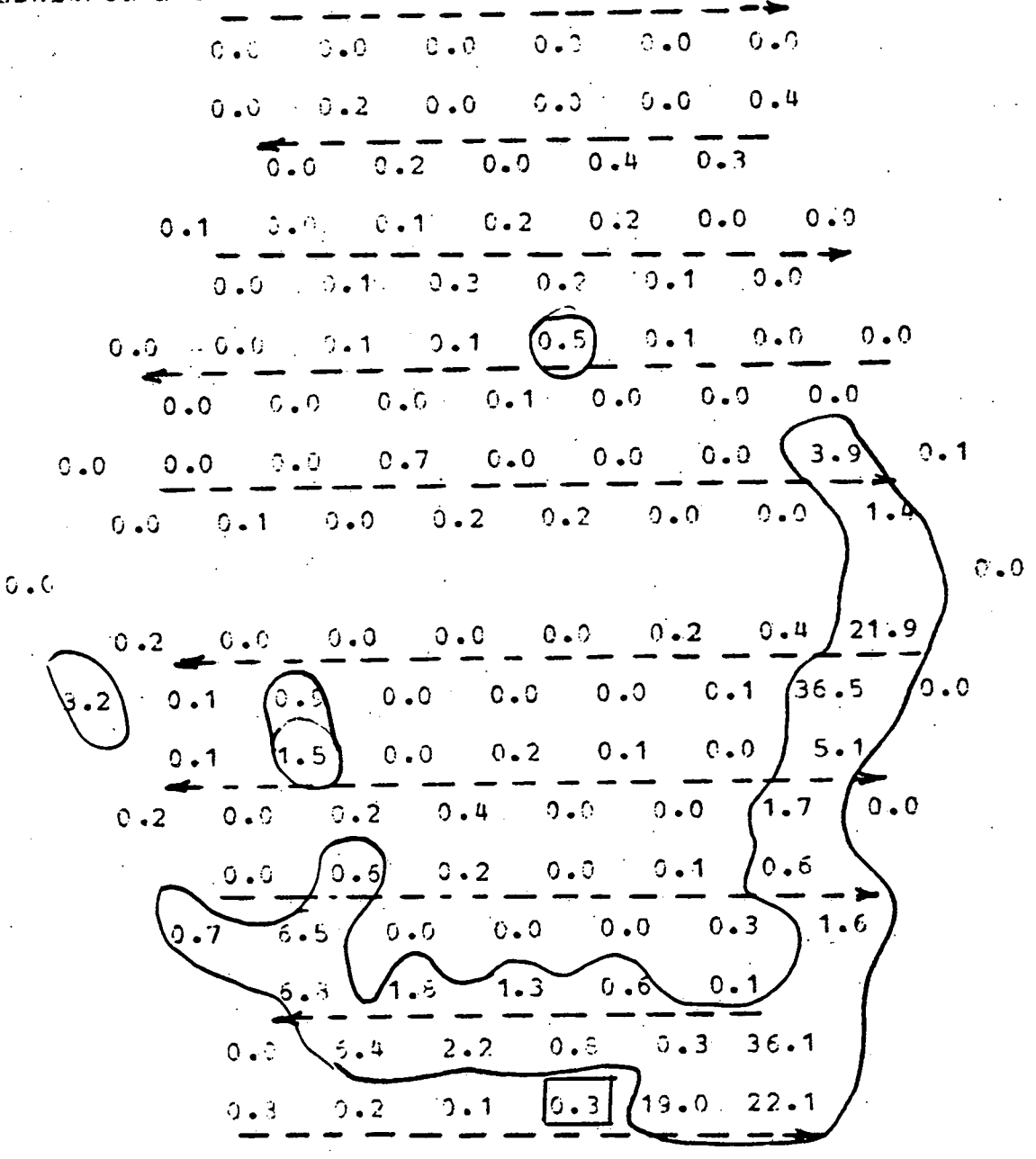

Figure A.11

SALT CONCENTRATION DISTRIBUTION MAP:

DIMENSIONLESS RATIOS OF SALT CONCENTRATION*0.01
MIX25.01
BUNDLE R.E. : 6238
AXIAL LEVEL (IN.) : 2.00
INJ. SUBCHANNEL : 120
MASSBALANCE RATIO : 0.910

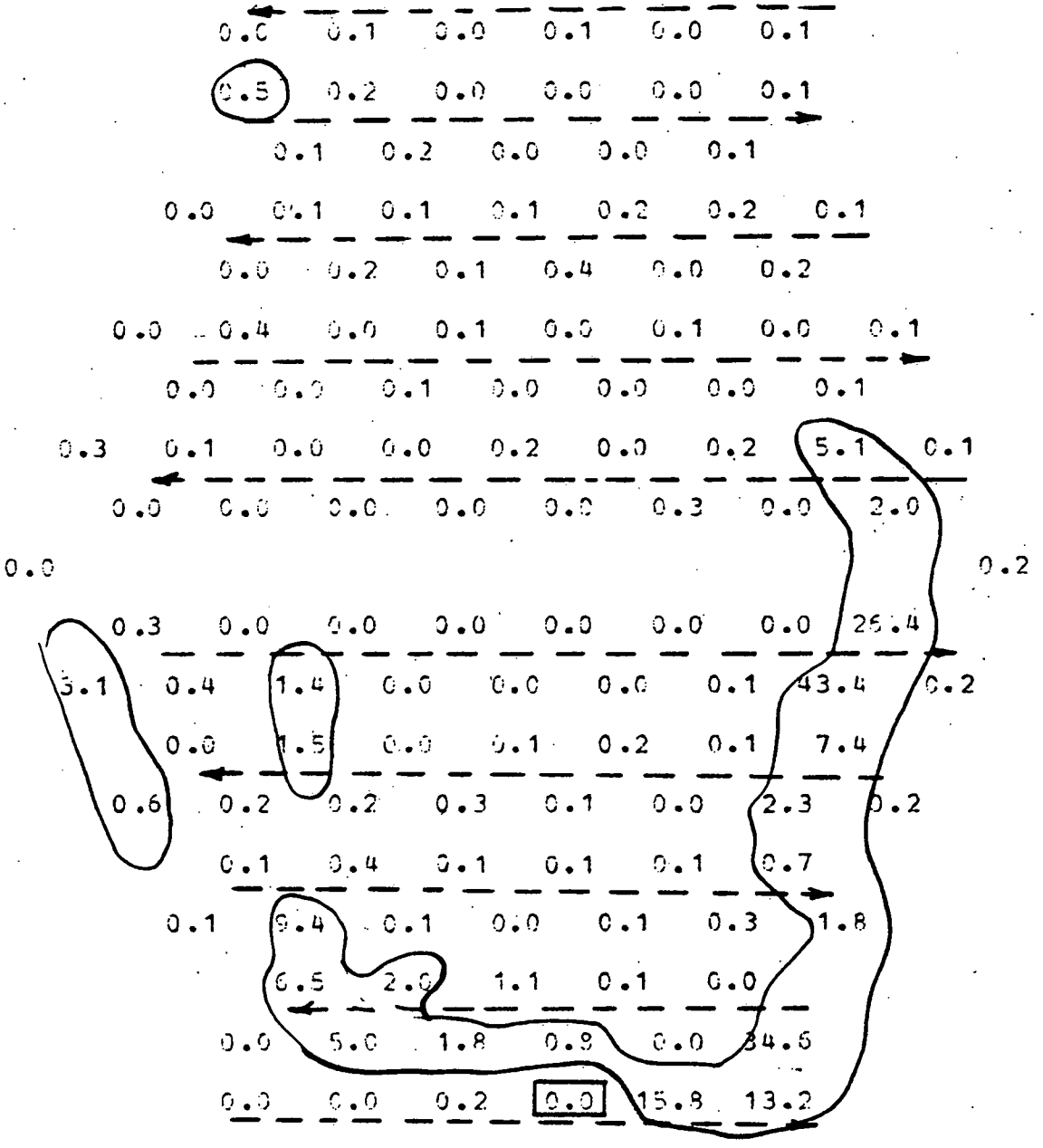

Figure A.12

SALT CONCENTRATION DISTRIBUTION MAP:

DIMENSIONLESS RATIO OF SALT CONCENTRATION*0.01
MIX24.01
BUNDLE R.E. : 8109
AXIAL LEVEL (IN.) : 3.00
INJ. SUBCHANNEL : 120
MASSBALANCE RATIO : 0.981

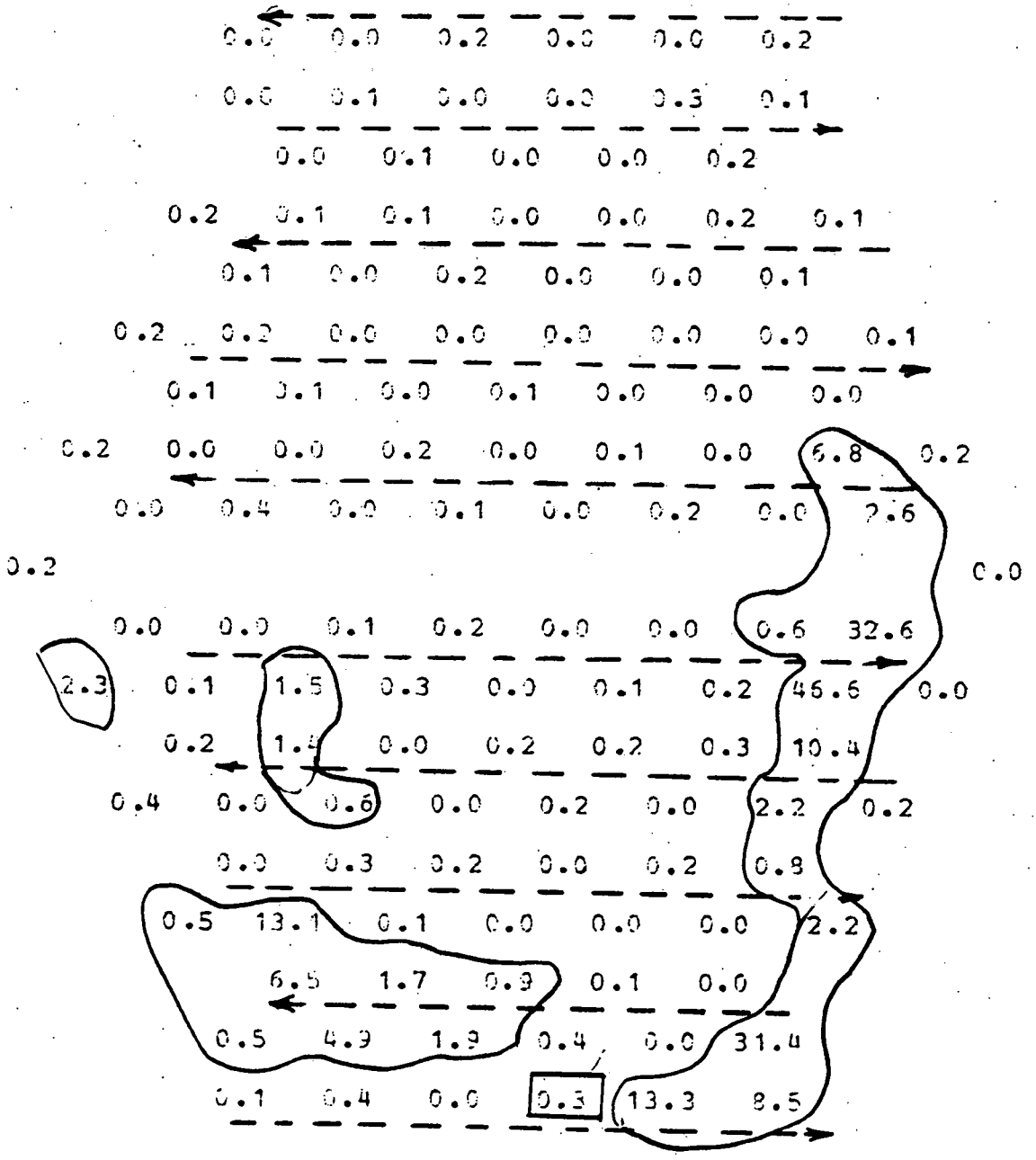

Figure A.13

SALT CONCENTRATION DISTRIBUTION MAP:

DIMENSIONLESS RATIOS OF SALT CONCENTRATION*0.01
MIX22.01
BUNDLE R.E. : 3981
AXIAL LEVEL (IN.) : 7.00
INJ. SUBCHANNEL : 120
MASSBALANCE RATIO : 0.997

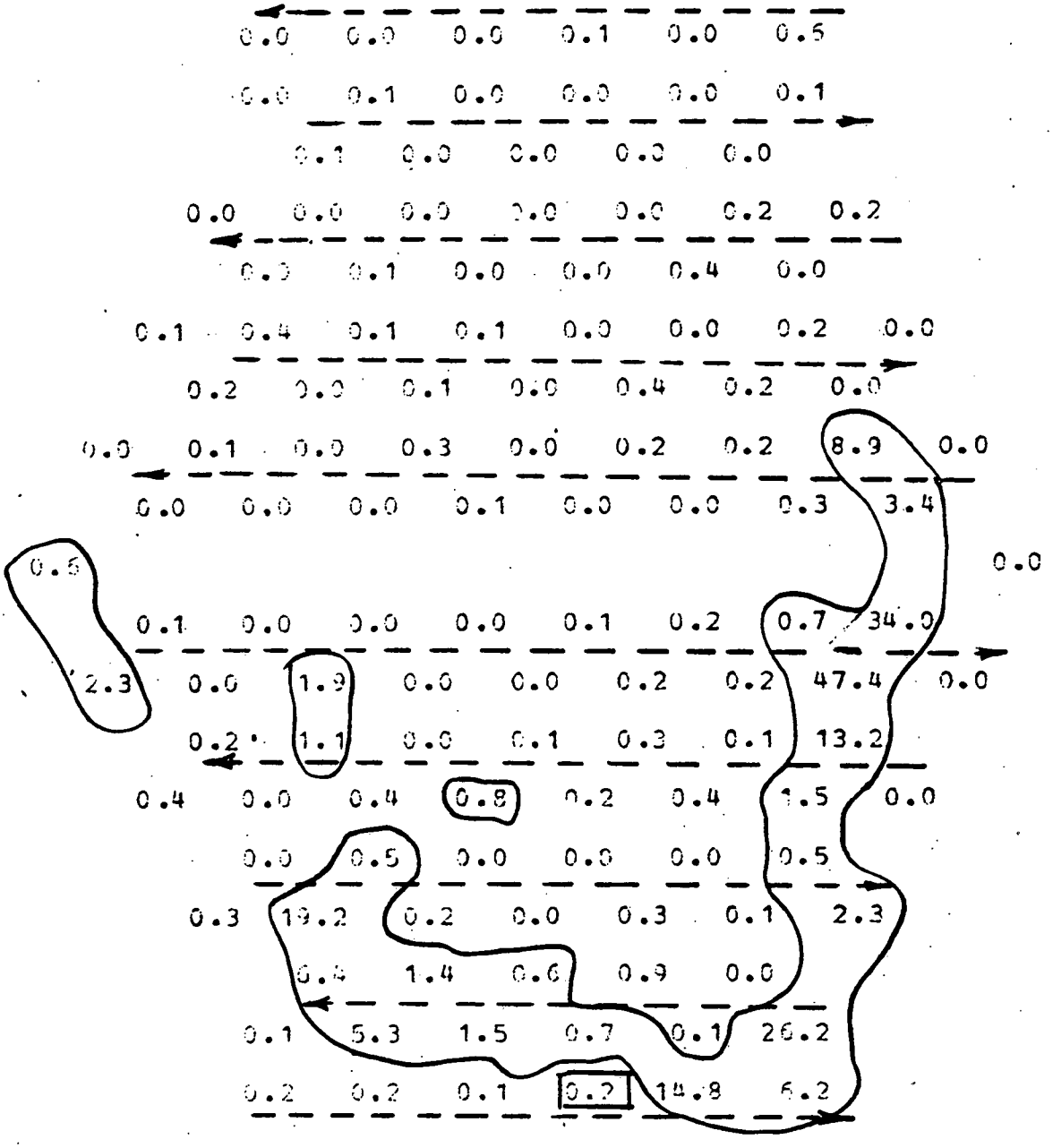

Figure A.14

SALT CONCENTRATION DISTRIBUTION MAP:

DIMENSIONLESS RATIOS OF SALT CONCENTRATION*0.01
MIN23.01
BUNDLE R.B. : 12164
AXIAL LEVEL (IN.) : 3.00
INJ. SUBCHANNEL : 120
MASSBALANCE RATIO : 0.985

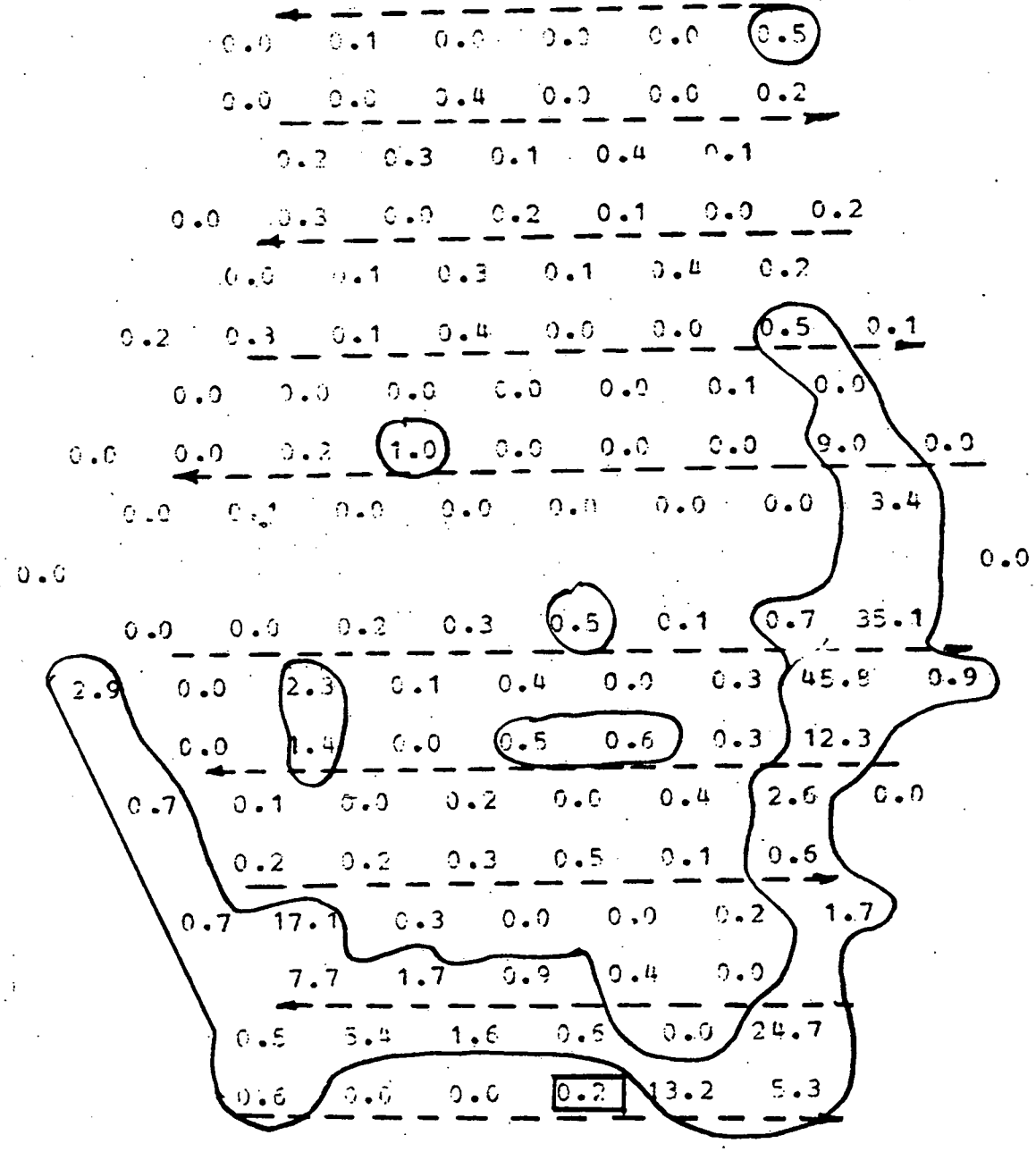

Figure A.15

APPENDIX A.2

DIMENSIONLESS SALT CONCENTRATION MAPS AT DIFFERENT INJECTION DEPTHS FOR INJECTION SUBCHANNEL NO. 1

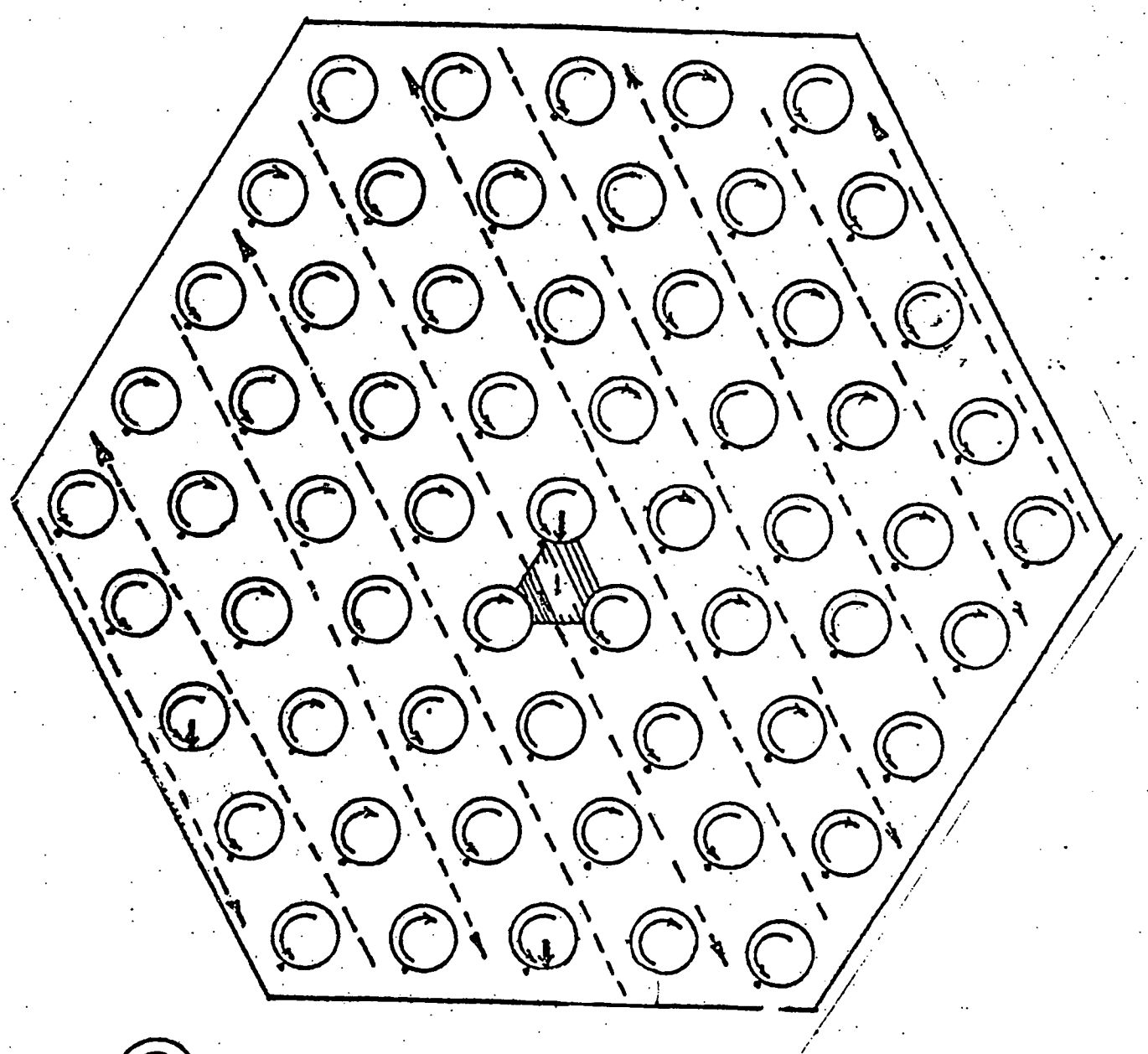

Fuel Pin and Wire Wrap Direction

Flow Preferable Path

Injection Channel

Figure 16 Injection Positions in the Alternate Wire Wrap Bundle

SALT CONCENTRATION DISTRIBUTION MAP:

DIMENSIONLESS RATIOS OF SALT CONCENTRATION*0.01
MIX01.01
BUNDLE R.E. : 9134
AXIAL LEVEL (IN.) : 16.00
INJ. SUBCHANNEL : 6
FLOW SPLITS :
X1= 0.8650 X2= 1.2800 X3= 1.2800
MASSBALANCE RATIO : 0.976

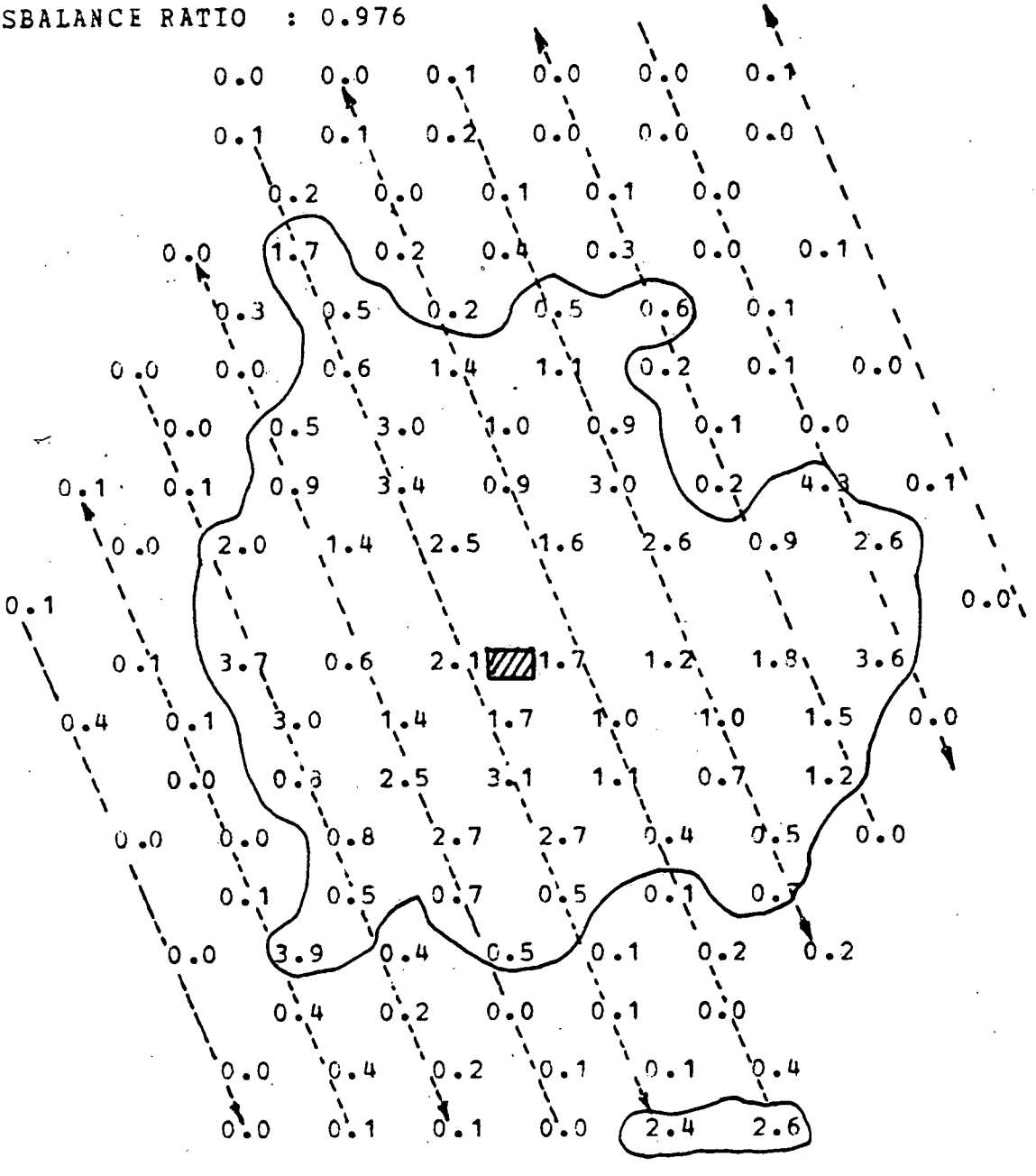

Figure A.17

SALT CONCENTRATION DISTRIBUTION MAP:

DIMENSIONLESS RATIOS OF SALT CONCENTRATION*0.01
MIX01.02
BUNDLE R.E. : 9134
AXIAL LEVEL (IN.) : 16.50
INJ. SUBCHANNEL : 6
FLOW SPLITS :
X1= 0.8650 X2= 1.2800 X3= 1.2800
MASSBALANCE RATIO : 0.999

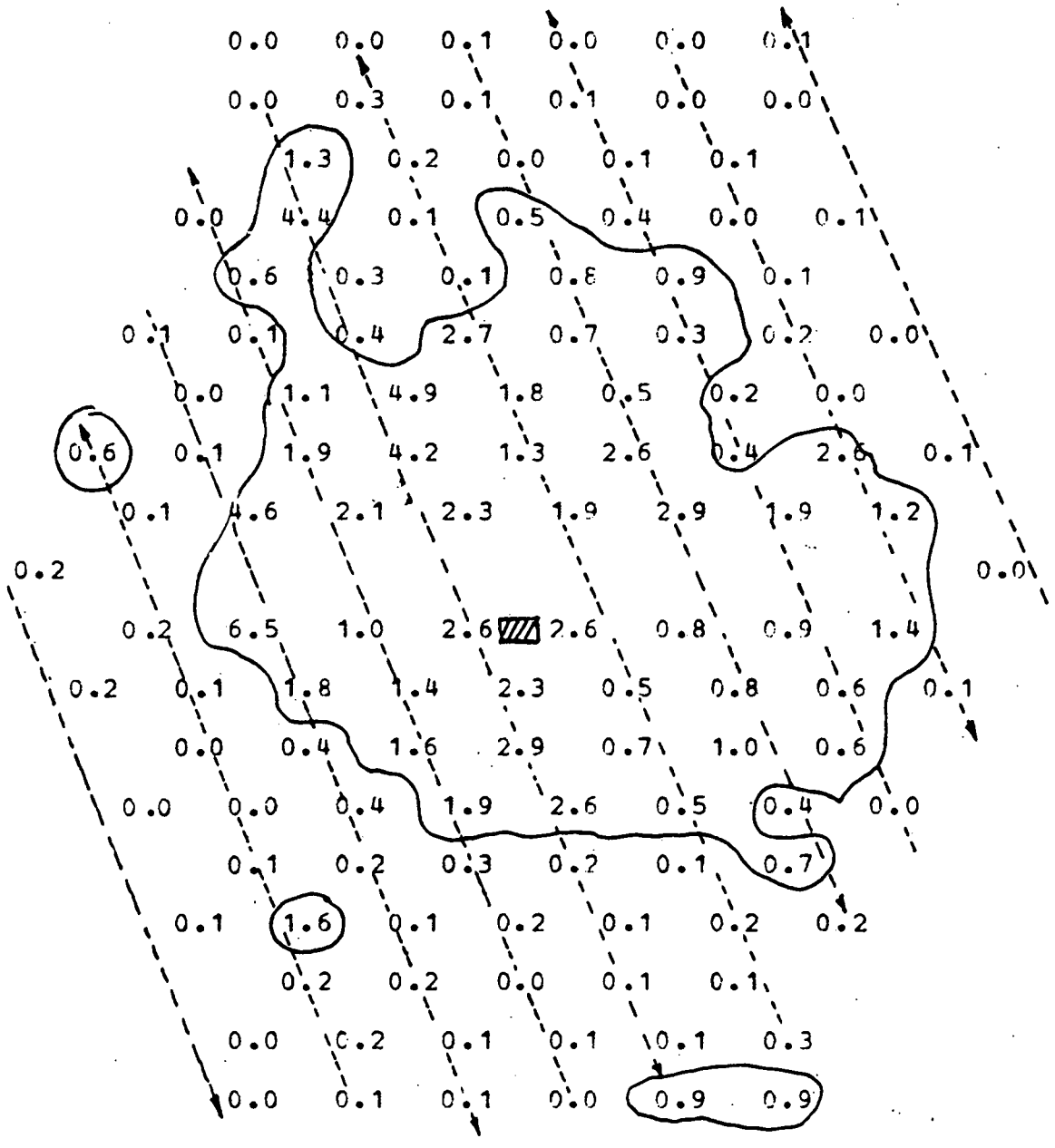

Figure A.18

SALT CONCENTRATION DISTRIBUTION MAP:

DIMENSIONLESS RATIOS OF SALT CONCENTRATION*C.01.
MIX01.03
BUNDLE R.E. : 9134
AXIAL LEVEL (IN.) : 17.00
INJ. SUBCHANNEL : 6
FLOW SPLITS :
X1= 0.8650 X2= 1.2800 X3= 1.2800
MASSBALANCE RATIO : 1.004

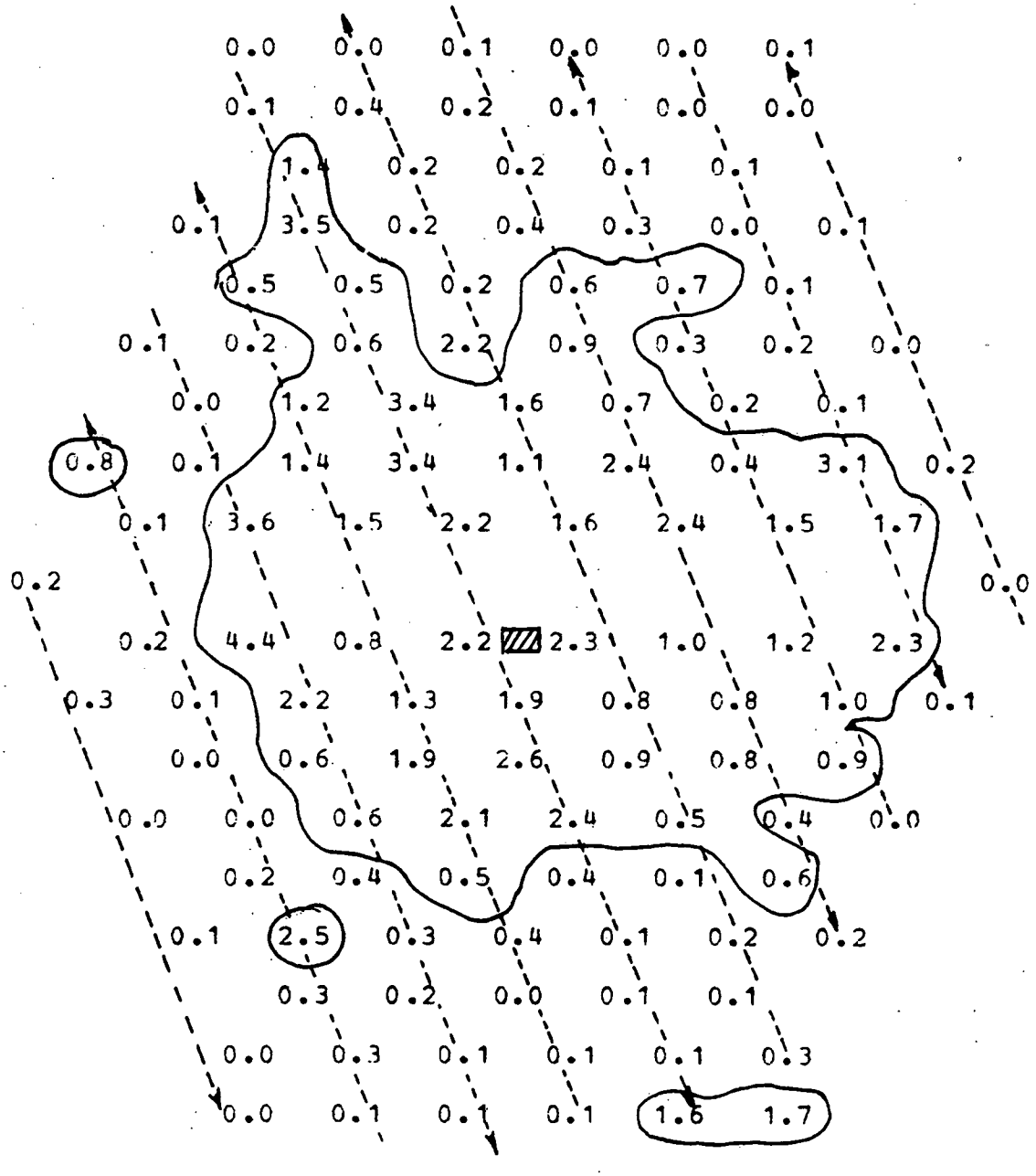

Figure A.19

SALT CONCENTRATION DISTRIBUTION MAP:

DIMENSIONLESS RATIOS OF SALT CONCENTRATION*0.01
MIX01.04
BUNDLE R.E. : 9134
AXIAL LEVEL (IN.) : 17.50
INJ. SUBCHANNEL : 6
FLOW SPLITS :
X1= 0.8650 X2= 1.2800 X3= 1.2800
MASSBALANCE RATIO : 1.045

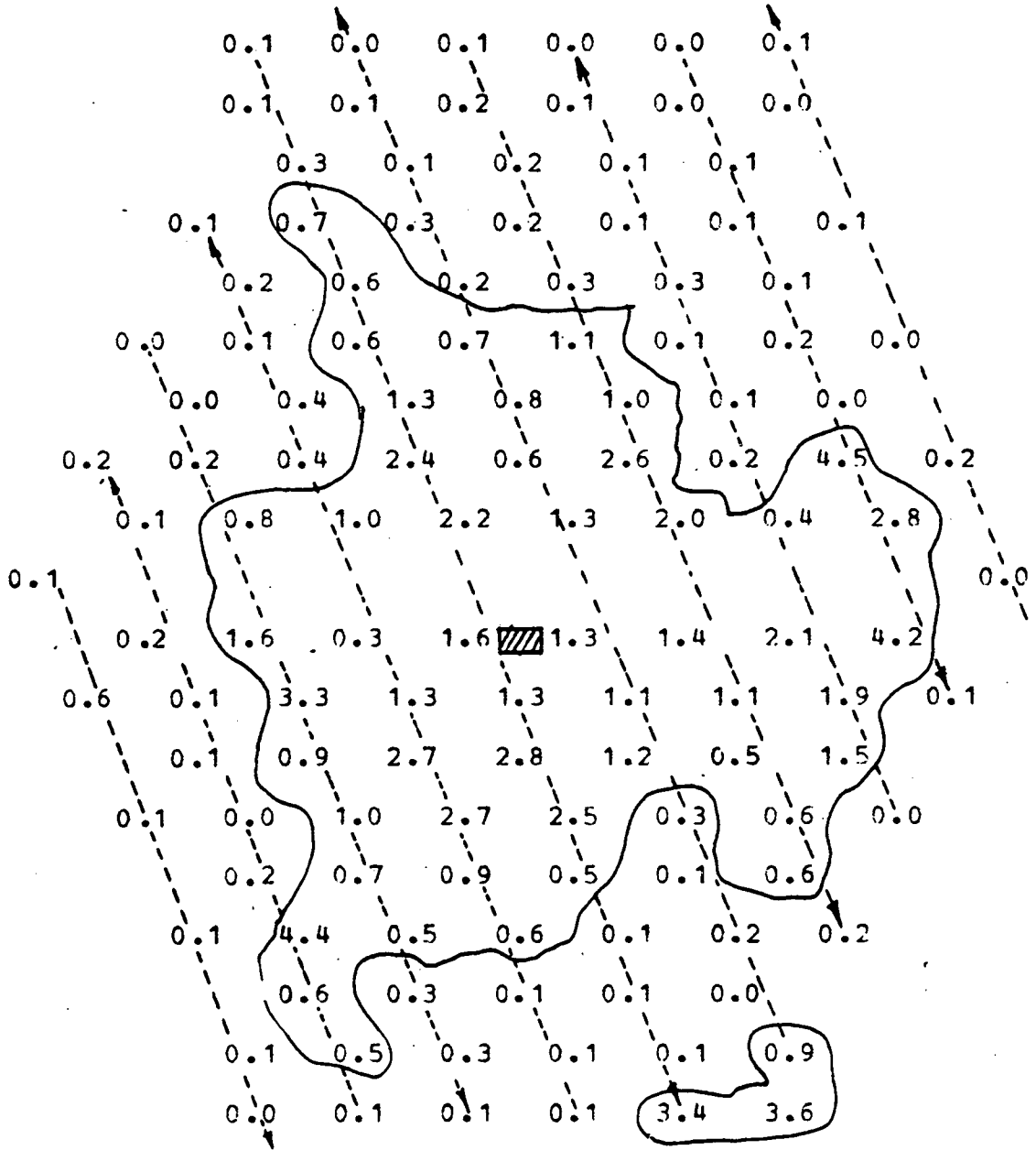

Figure A.20

SALT CONCENTRATION DISTRIBUTION MAP:

DIMENSIONLESS RATIOS OF SALT CONCENTRATION*0.01
MIX01.05
BUNDLE R.E. : 9134
AXIAL LEVEL (IN.) : 18.00
INJ. SUBCHANNEL : 6
FLOW SPLITS :
X1= 0.8650 X2= 1.2800 X3= 1.2800
MASSBALANCE RATIO : 1.091

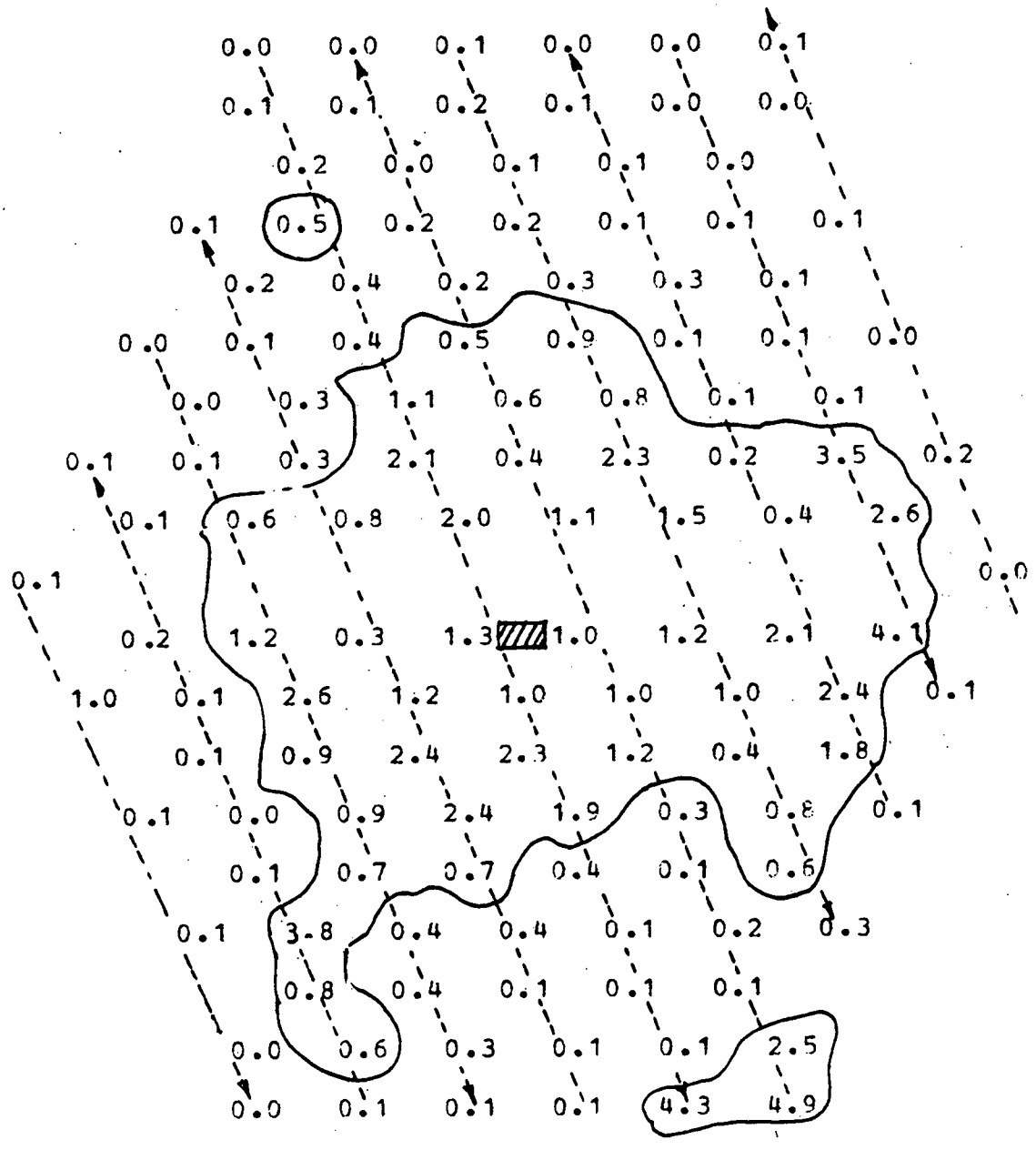

Figure A.21

SALT CONCENTRATION DISTRIBUTION MAP:

DIMENSIONLESS RATIOS OF SALT CONCENTRATION*0.01
MIX01.06
BUNDLE R.E. : 9134
AXIAL LEVEL (IN.) : 19.00
INJ. SUBCHANNEL : 6
FLOW SPLITS :
X1= 0.8650 X2= 1.2800 X3= 1.2800
MASSBALANCE RATIO : 1.116

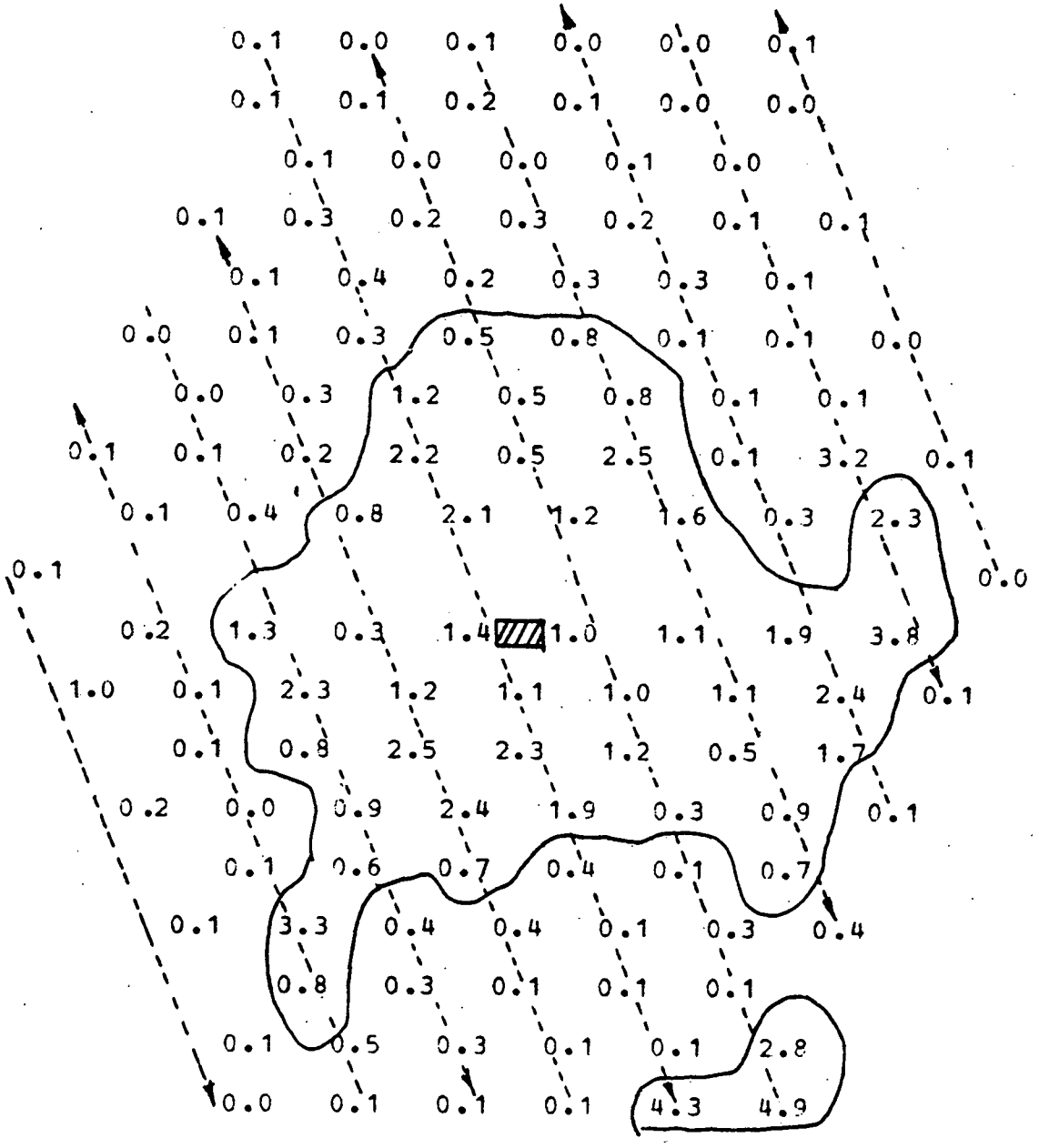

Figure A.22

SALT CONCENTRATION DISTRIBUTION MAP:

DIMENSIONLESS RATIOS OF SALT CONCENTRATION*0.01
MIX01.07
BUNDLE R.E. : 9134
AXIAL LEVEI (IN.) : 19.5
INJ. SUBCHANNEL : 6
FLOW SPLITS :
X1= 0.8650 X2= 1.2800 X3= 1.2800
MASSBALANCE RATIO : 1.119

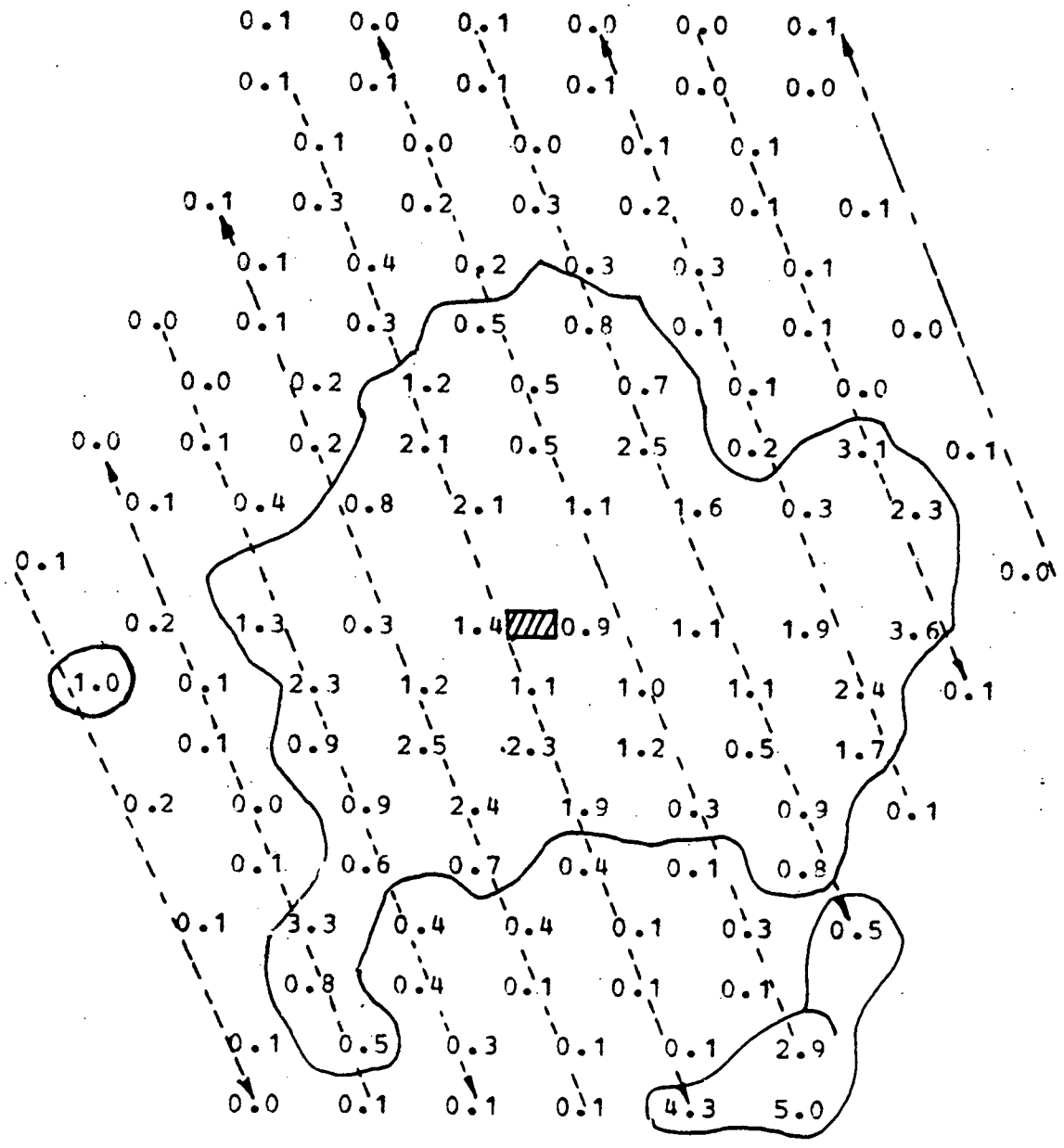

Figure A.23

SALT CONCENTRATION DISTRIBUTION MAP:

DIMENSIONLESS RATIOS OF SALT CONCENTRATION*0.01
MIX01.08
BUNDLE R.E. : 9134
AXIAL LEVEL (IN.) : 20.0
INJ. SUBCHANNEL : 6
FLOW SPLITS :
X1= 0.8650 X2= 1.2800 X3= 1.2800
MASSBALANCE RATIO : 1.102

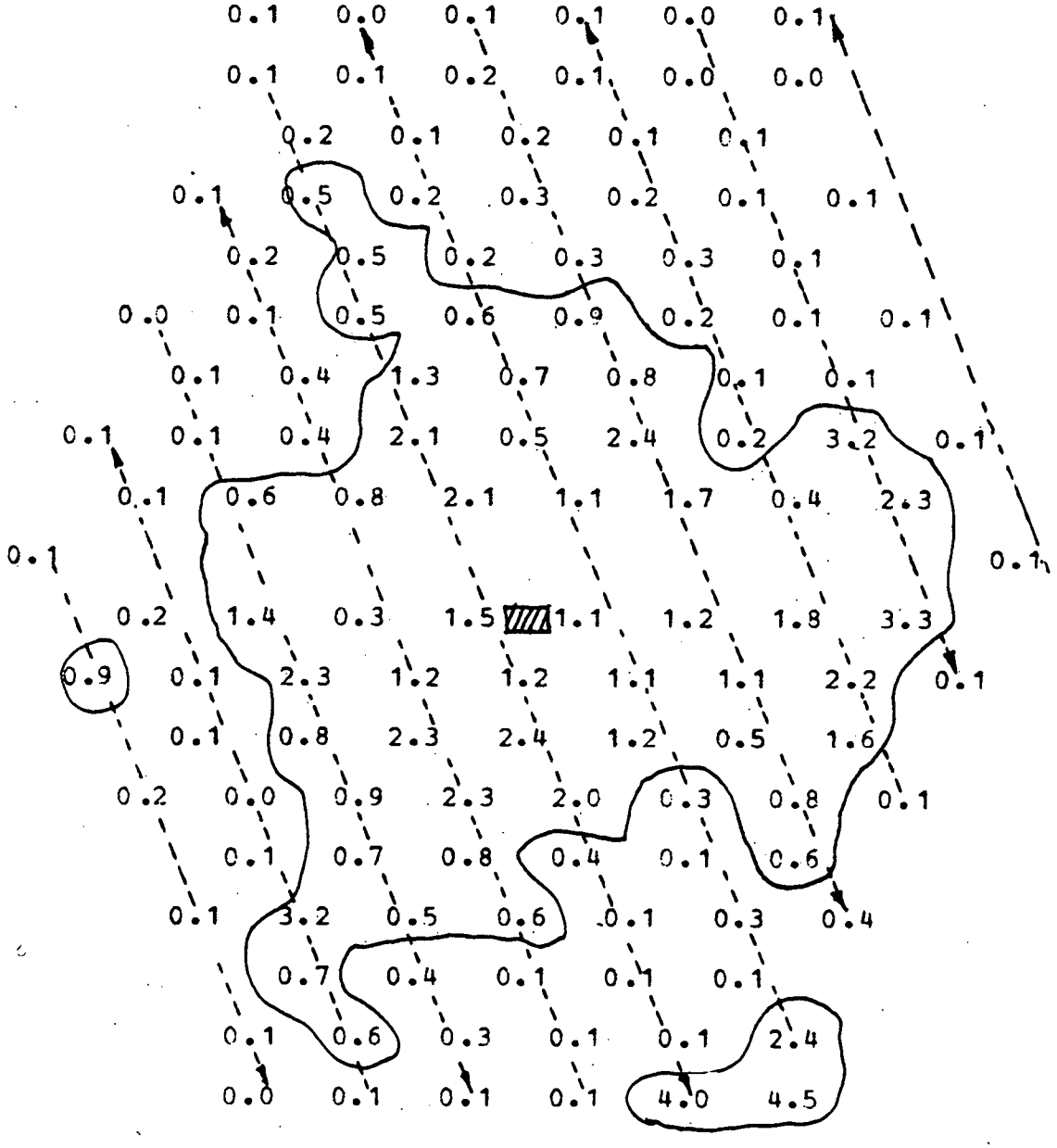

Figure A.24

SALT CONCENTRATION DISTRIBUTION MAP:

DIMENSIONLESS RATIOS OF SALT CONCENTRATION*0.01
MIX01.09
BUNDLE R.E. : 9134
AXIAL LEVEL (IN.) : 20.5
INJ. SUBCHANNEL : 6
FLOW SPLITS :
X1= 0.8650 X2= 1.2800 X3= 1.2800
MASSBALANCE RATIO : 1.100

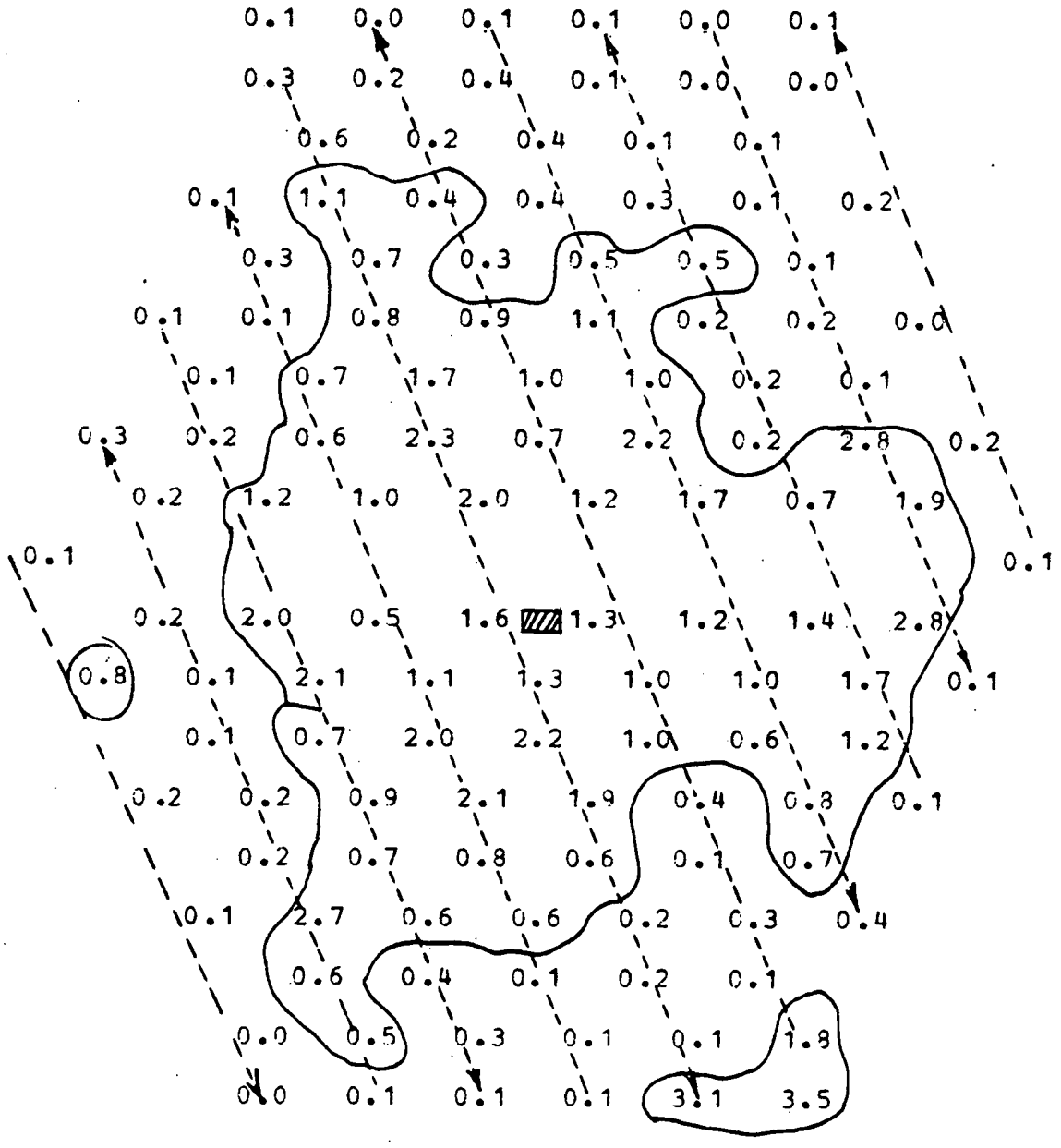

Figure A.25

SALT CONCENTRATION DISTRIBUTION MAP:

DIMENSIONLESS RATIOS OF SALT CONCENTRATION*0.01
MIX01.10
BUNDLE R.E. : 9134
AXIAL LEVEL (IN.) : 21.0
INJ. SUBCHANNEL : 6
FLOW SPLITS :
X1= 0.8650 X2= 1.2800 X3= 1.2800
MASSBALANCE RATIO : 1.112

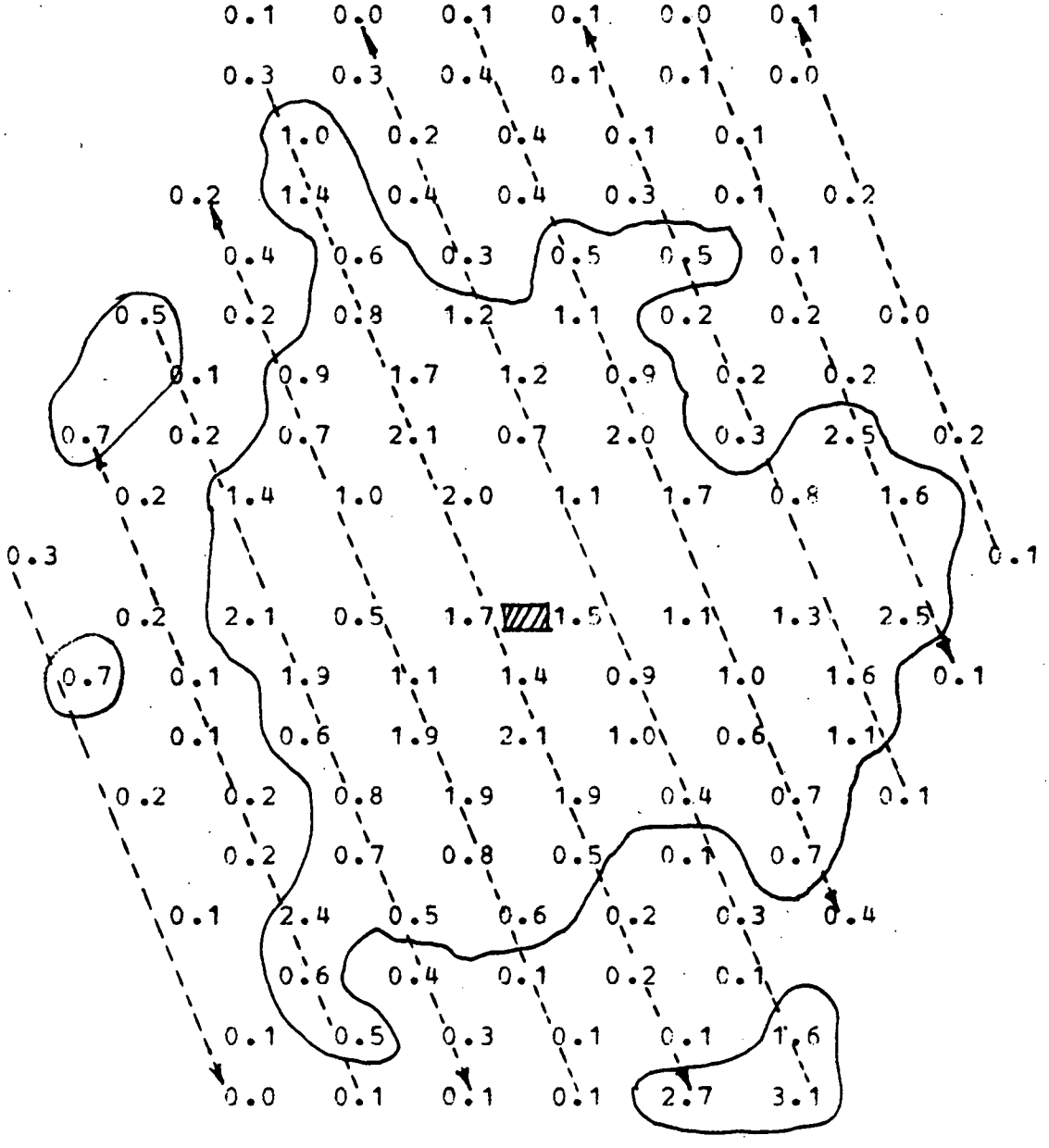

Figure A.26

SALT CONCENTRATION DISTRIBUTION MAP:

DIMENSIONLESS RATIOS OF SALT CONCENTRATION*0.01
MIX01.11
BUNDLE R.E. : 9134
AXIAL LEVEL (IN.) : 22.00
INJ. SUBCHANNEL : 6
FLOW SPLITS :
X1= 0.8650 X2= 1.2800 X3= 1.2800
MASSBALANCE RATIO : 1.128

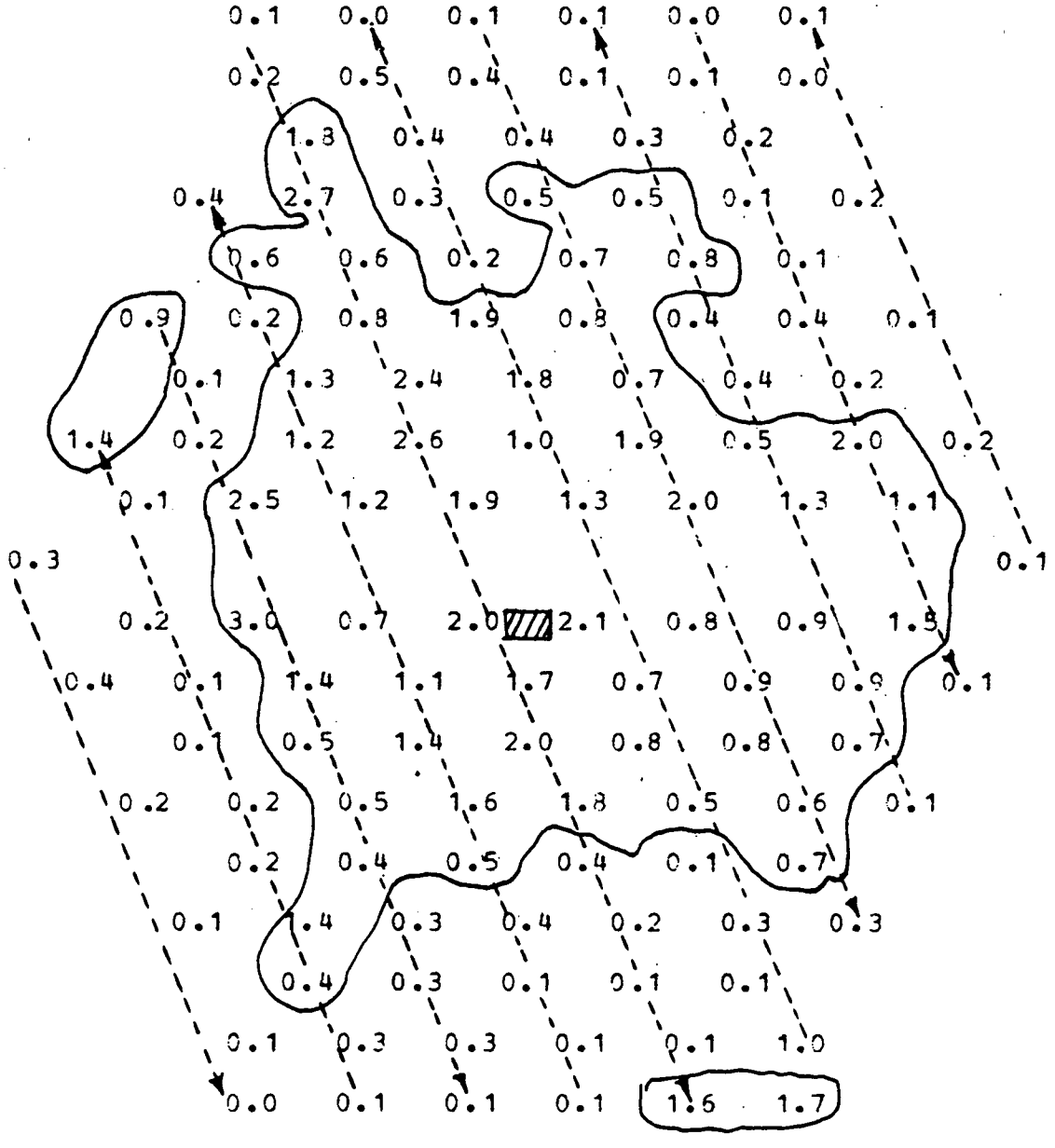

Figure A.27

SALT CONCENTRATION DISTRIBUTION MAP:

DIMENSIONLESS RATIOS OF SALT CONCENTRATION*0.01
MIX01.12
BUNDLE R.E. : 9134
AXIAL LEVEL (IN.) : 22.5
INJ. SUBCHANNEL : 6
FLOW SPLITS :
X1= 0.8650 X2= 1.2800 X3= 1.2800
MASSBALANCE RATIO : 1.152

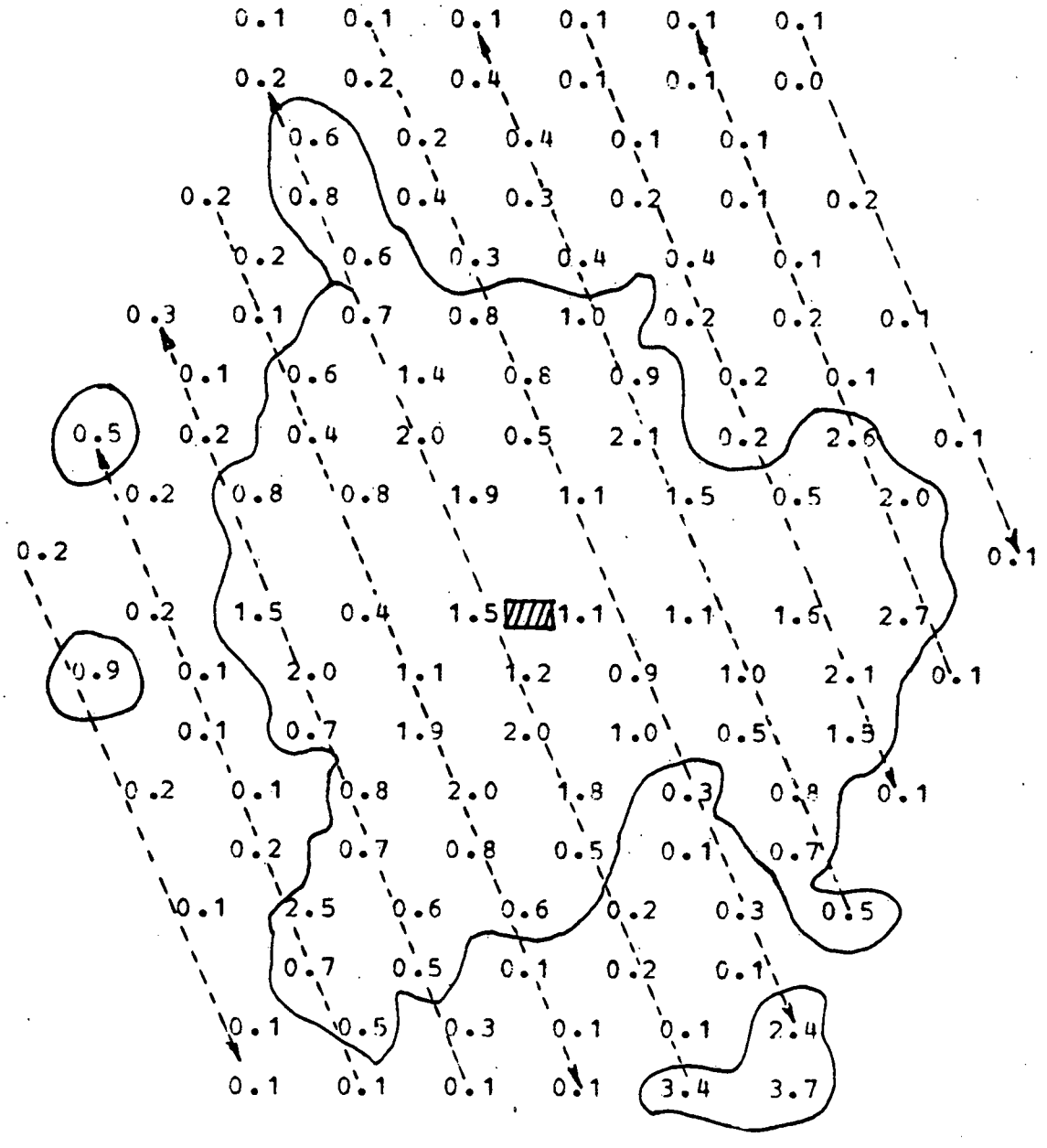

Figure A.28

SALT CONCENTRATION DISTRIBUTION MAP:

DIMENSIONLESS RATIOS OF SALT CONCENTRATION*0.01
MIX01.13
BUNDLE R.E. : 9134
AXIAL LEVEL (IN.) : 23.00
INJ. SUBCHANNEL : 6
FLOW SPLITS :
X1= 0.8650 X2= 1.2800 X3= 1.2800
MASSBALANCE RATIO : 1.160

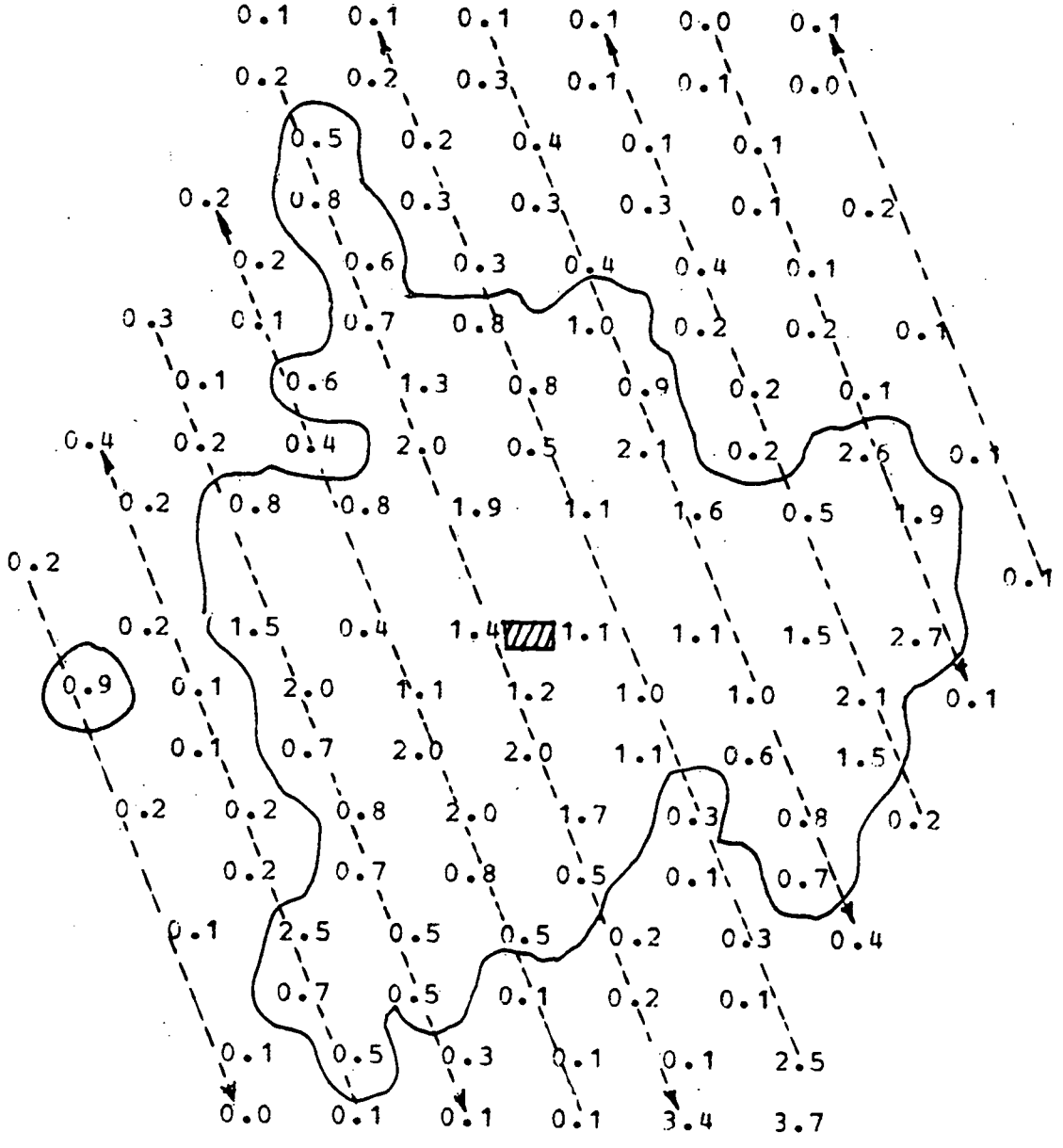

Figure A.29

SALT CONCENTRATION DISTRIBUTION MAP:

DIMENSIONLESS RATIOS OF SALT CONCENTRATION*0.01
MIX01.14
BUNDLE R.E. : 9134
AXIAL LEVEL (IN.) : 23.5
INJ. SUBCHANNEL : 6
FLOW SPLITS :
X1= 0.8650 X2= 1.2800 X3= 1.2800
MASSBALANCE RATIO : 1.190

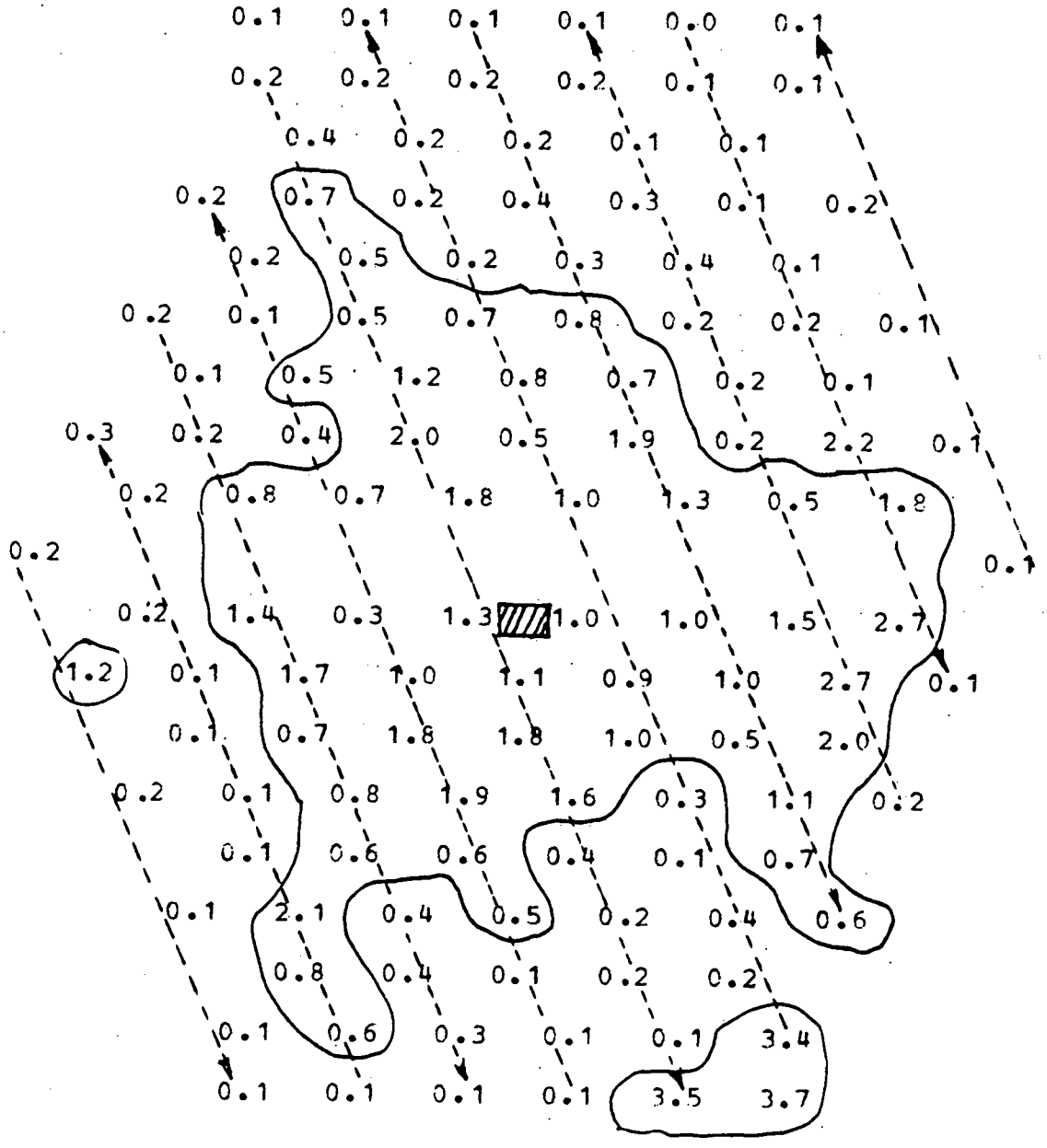

Figure A.30

SALT CONCENTRATION DISTRIBUTION MAP:

DIMENSIONLESS RATIOS OF SALT CONCENTRATION*0.01
MIX01.15
BUNDLE R.E. : 9134
AXIAL LEVEL (IN.) : 24.5
INJ. SUBCHANNEL : 6
FLOW SPLITS :
X1= 0.8650 X2= 1.2800 X3= 1.2800
MASSBALANCE RATIO : 1.168

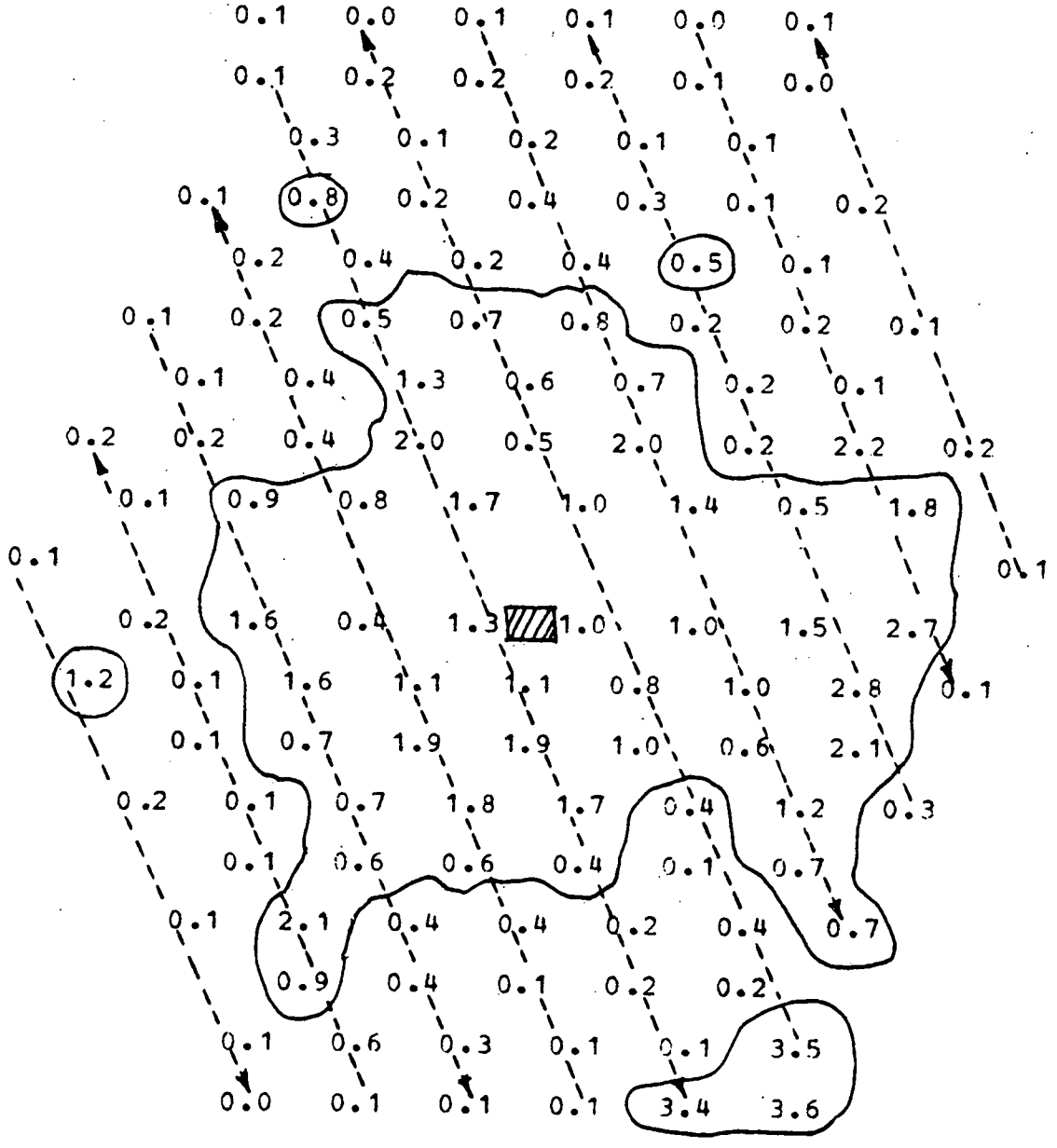

Figure A.31

SALT CONCENTRATION DISTRIBUTION MAP:

DIMENSIONLESS RATIOS OF SALT CONCENTRATION*0.01
MIX01.16
BUNDLE R.E. : 9134
AXIAL LEVEL (IN.) : 25.5
INJ. SUBCHANNEL : 6
FLOW SPLITS :
X1= 0.8650 X2= 1.2800 X3= 1.2800
MASSBALANCE RATIO : 1.169

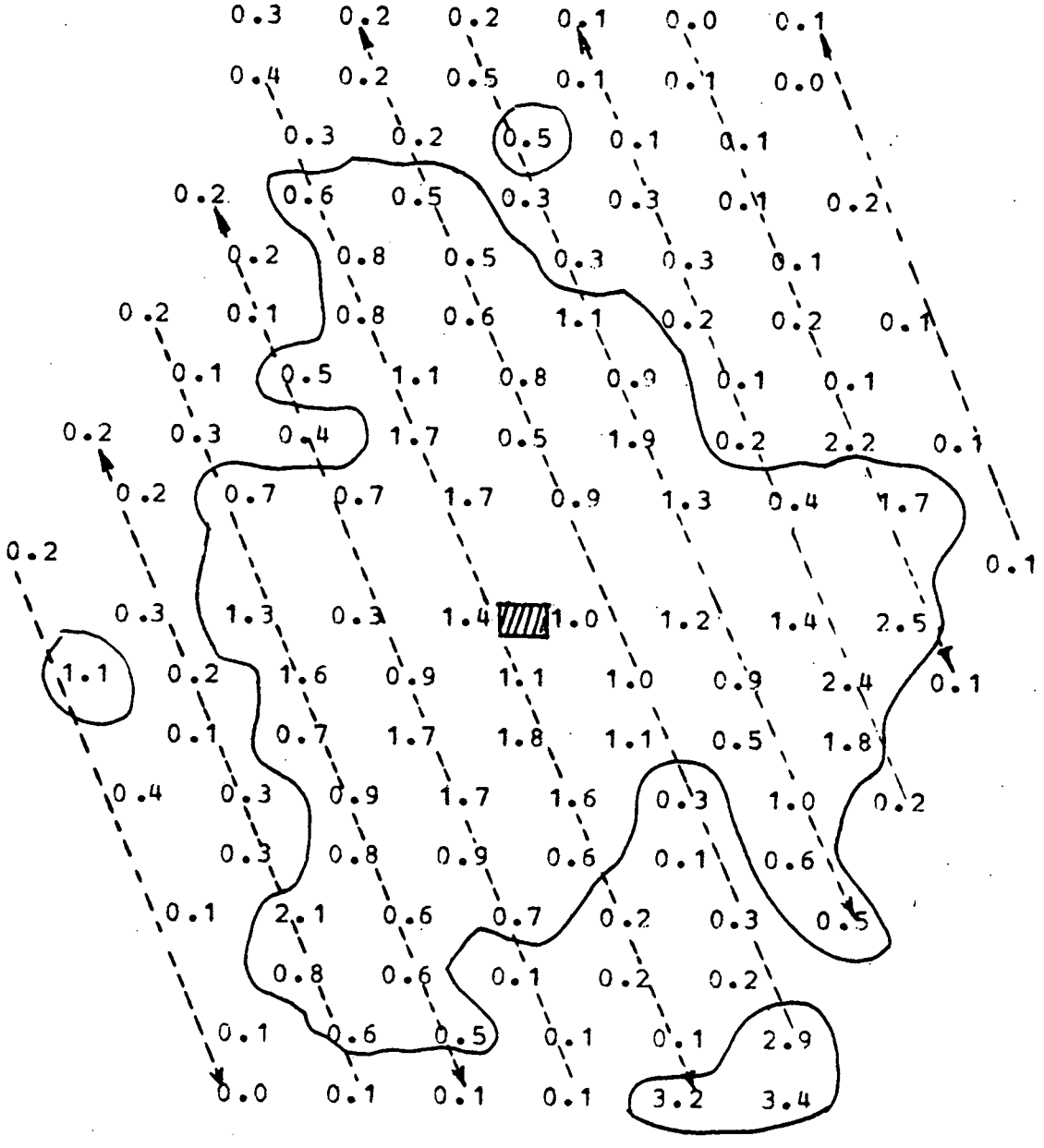

Figure A.32

SALT CONCENTRATION DISTRIBUTION MAP:

DIMENSIONLESS RATIOS OF SALT CONCENTRATION*0.01
MIX01.17
BUNDLE R.E. : 9134
AXIAL LEVEL (IN.) : 26.5 26.5
INJ. SUBCHANNEL : 6
FLOW SPLITS :
X1= 0.8650 X2= 1.2800 X3= 1.2800
MASSBALANCE RATIO : 1.171

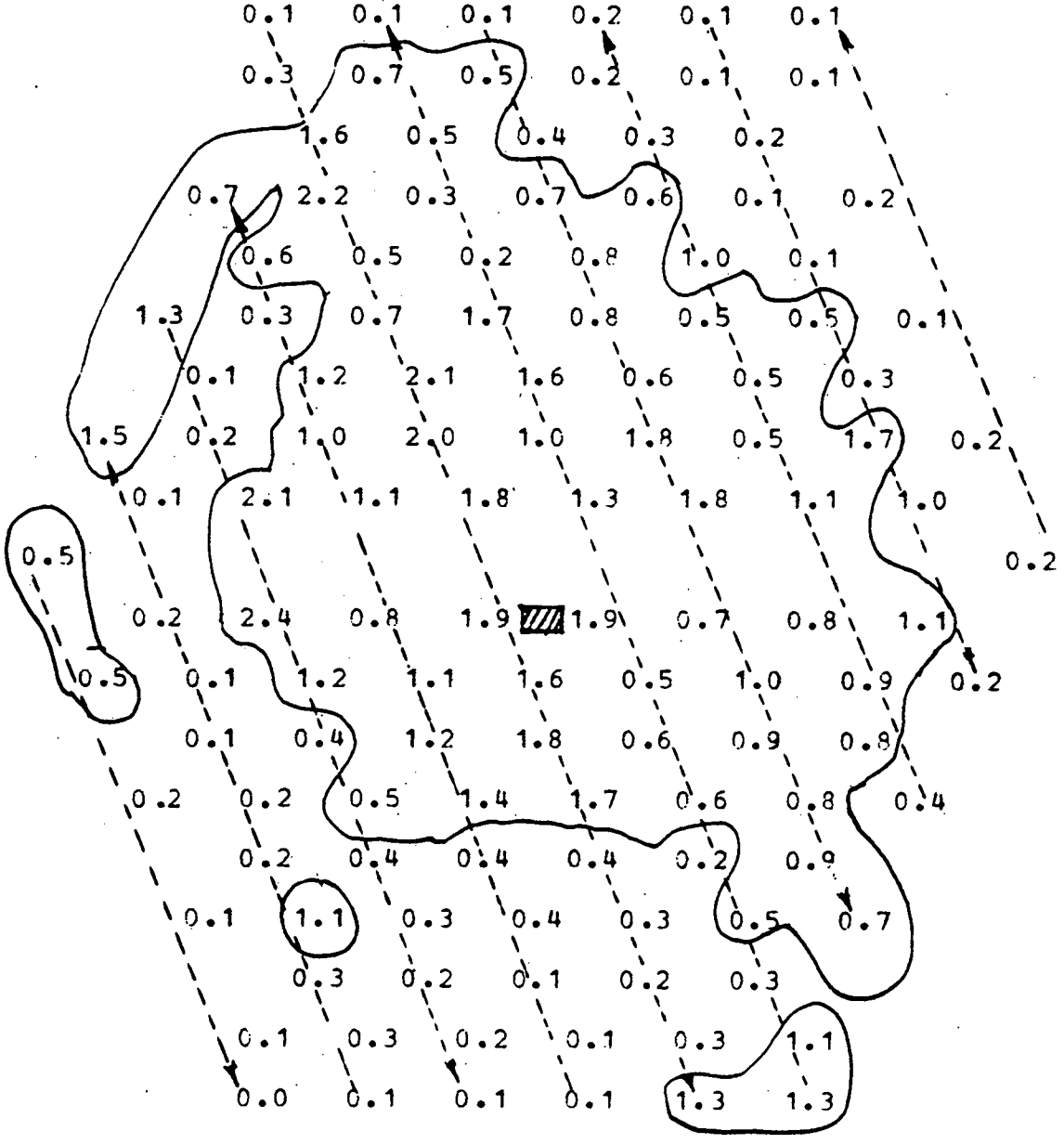

Figure A.33

APPENDIX A.3

DIMENSIONLESS SALT CONCENTRATION MAPS AT DIFFERENT INJECTION DEPTHS FOR INJECTION SUBCHANNEL NO. 2

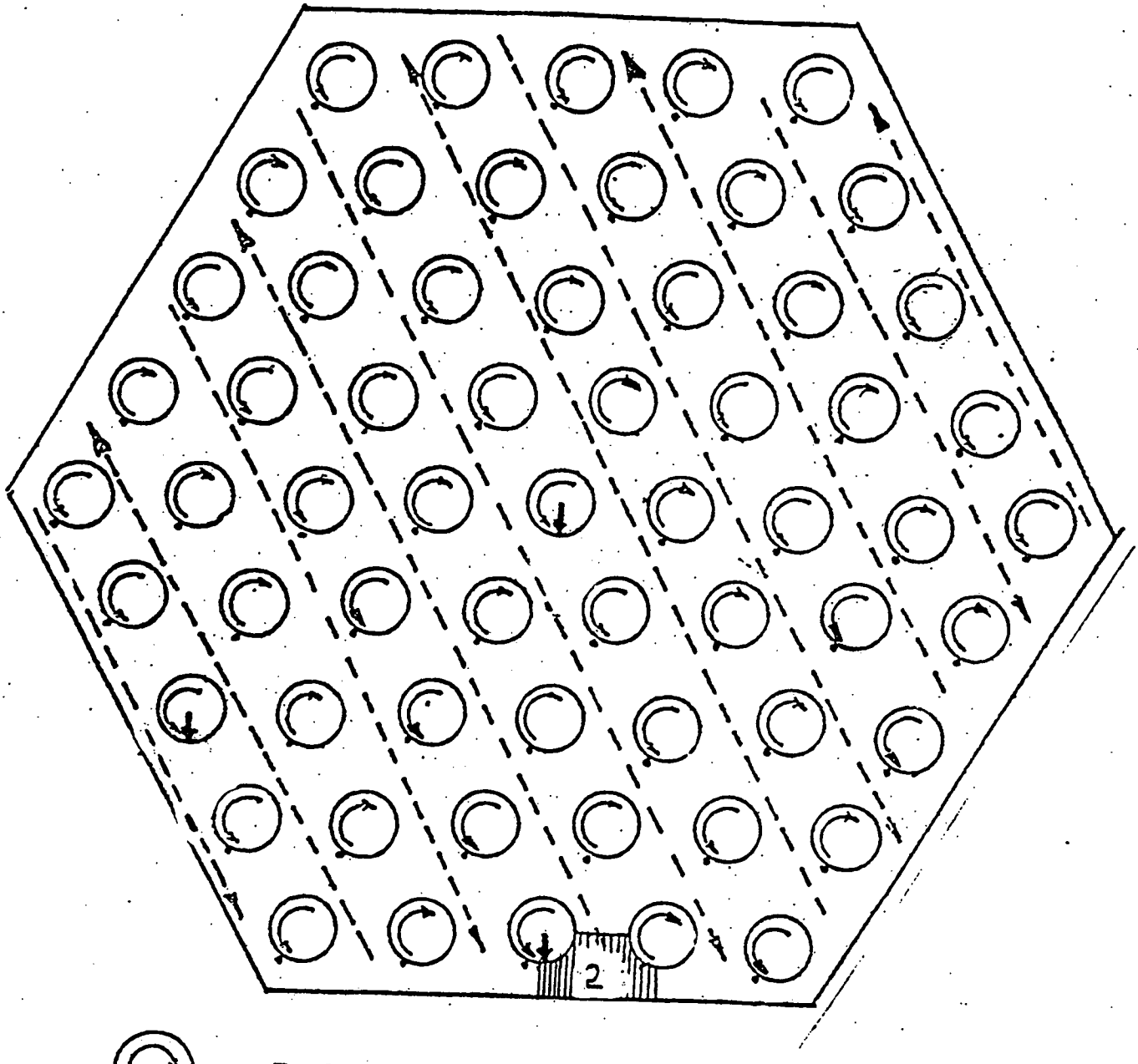

Fuel Pin and Wire Wrap Direction

Flow Preferable Path

Injection Channel

Figure 34 Injection Positions in the Alternate Wire Wrap Bundle

SALT CONCENTRATION DISTRIBUTION MAP:

DIMENSIONLESS RATIOS OF SALT CONCENTRATION*0.01
MIX07.03
BUNDLE R.E. : 9134
AXIAL LEVEI (IN.) : 13.5
INJ. SUBCHANNEL : 120
FLOW SPLITS :
X1= 0.8650 X2= 1.2800 X3= 1.2800
MASSBALANCE RATIO : 0.870

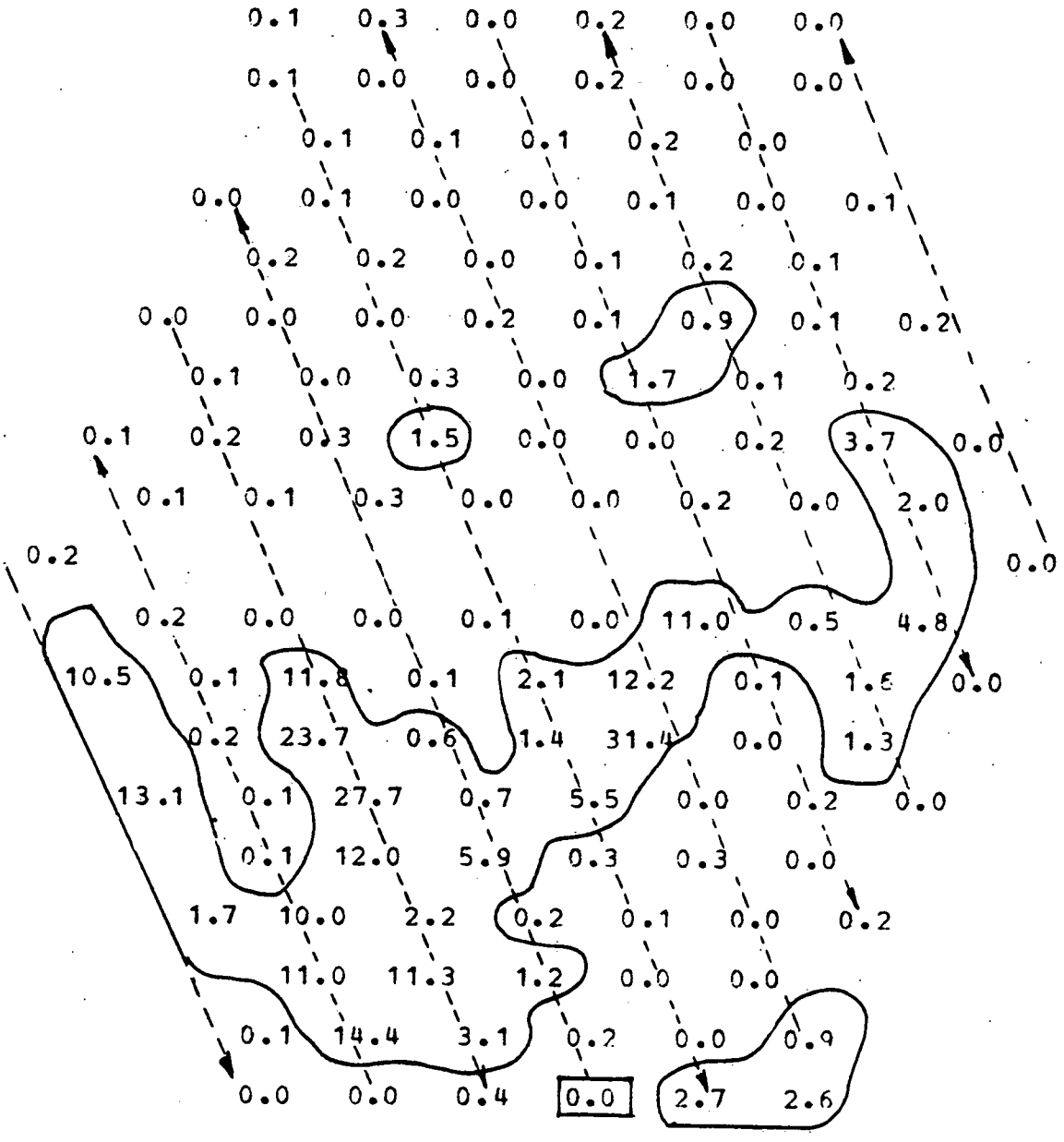

Figure A.35

SALT CONCENTRATION DISTRIBUTION MAP:

DIMENSIONLESS RATIOS OF SALT CONCENTRATION*0.01
MIX07.02
BUNDLE R.E. : 9134
AXIAL LEVEI (IN.) : 14.5
INJ. SUBCHANNEL : 120
FLOW SPLITS :
X1= 0.8650 X2= 1.2800 X3= 1.2800
MASSBALANCE RATIO : 0.873

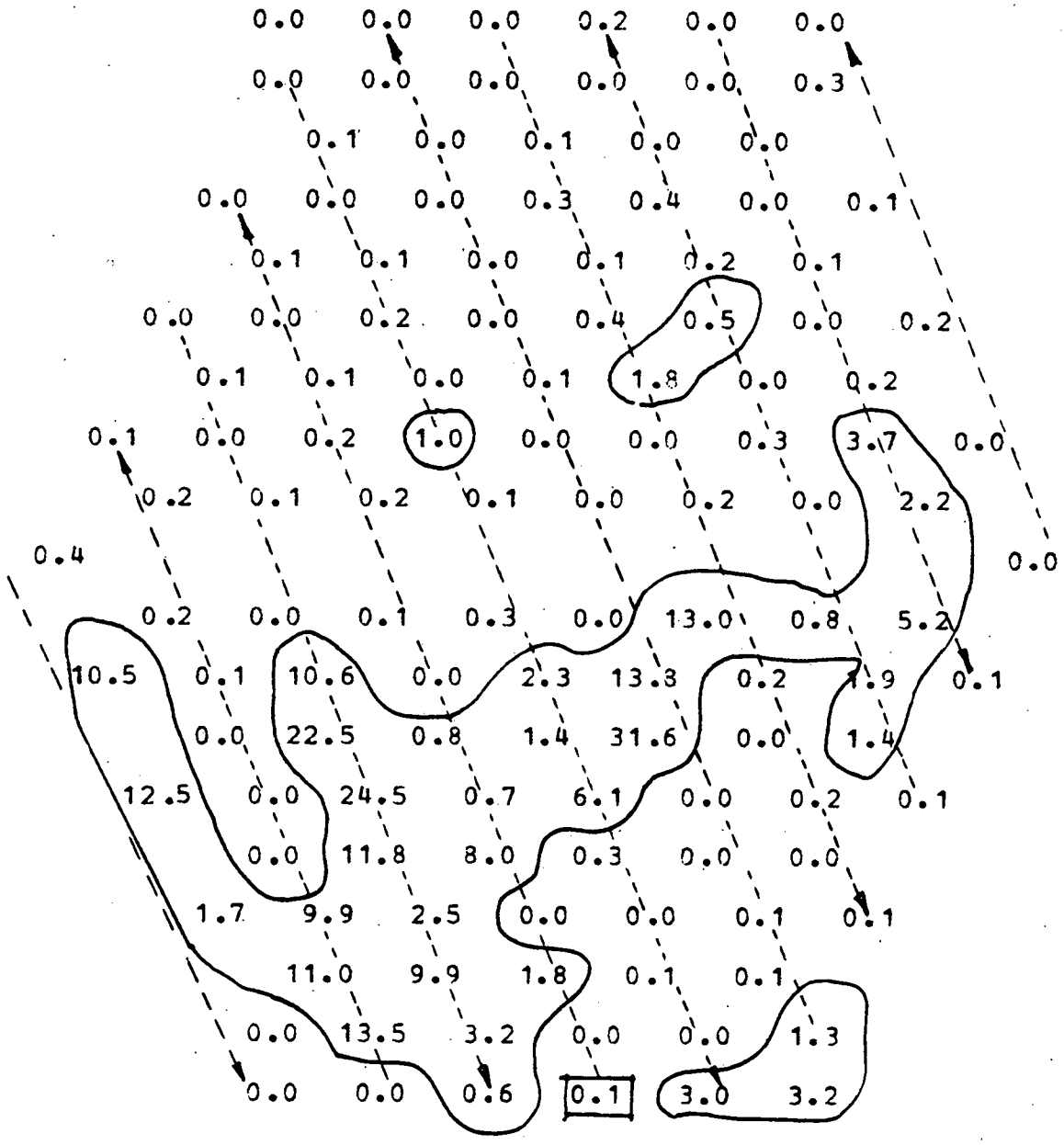

Figure A.36

SALT CONCENTRATION DISTRIBUTION MAP:

DIMENSIONLESS RATIOS OF SALT CONCENTRATION*0.01
MIX07.01
BUNDLE R.E. : 9134
AXIAL LEVEI (IN.) : 15.5
INJ. SUBCHANNEL : 120
FLOW SPLITS :
X1= 0.8650 X2= 1.2800 X3= 1.2800
MASSBALANCE RATIO : 0.879

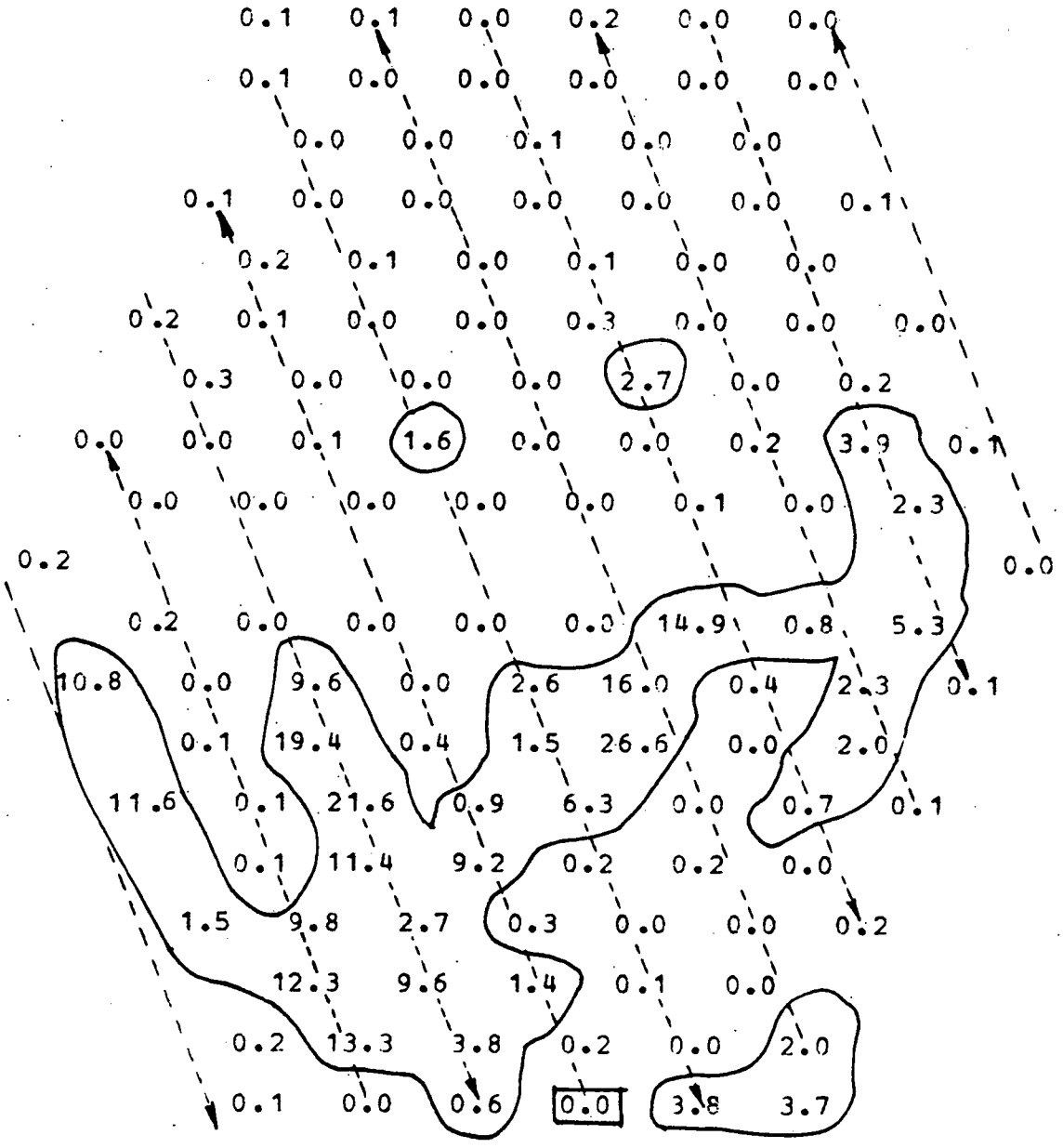

Figure A.37

SALT CONCENTRATION DISTRIBUTION MAP:

DIMENSIONLESS RATIOS OF SALT CONCENTRATION*0.01
MIX06.03
BUNDLE R.E. : 9134
AXIAL LEVEI (IN.) : 16.5
INJ. SUBCHANNEL : 120
FLOW SPLITS :
X1= 0.8650 X2= 1.2800 X3= 1.2800
MASSBALANCE RATIO : 0.908

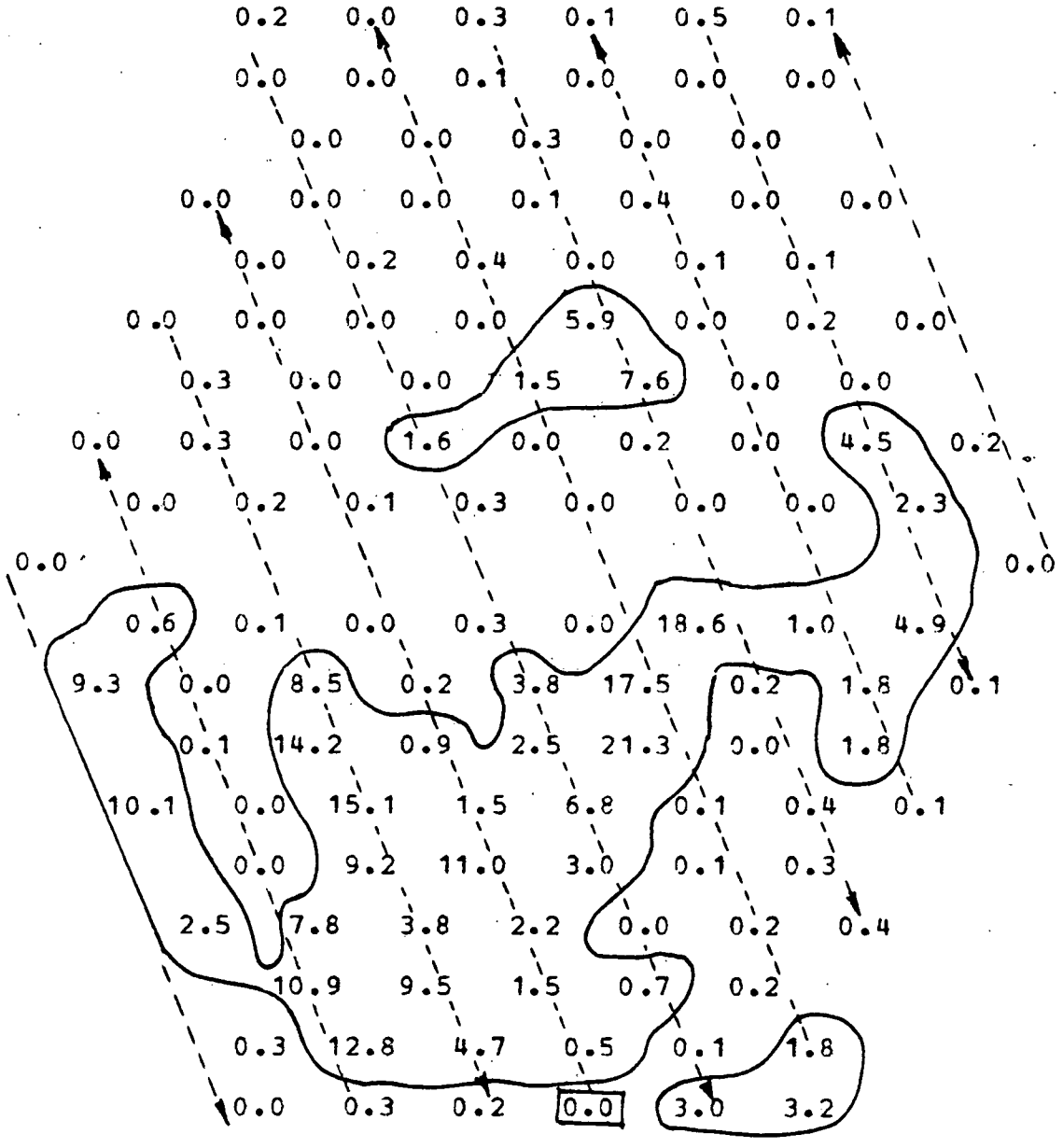

Figure A.38

SALT CONCENTRATION DISTRIBUTION MAP:

DIMENSIONLESS RATIOS OF SALT CONCENTRATION*0.01
MIX06.02
BUNDLE R.E. : 9134
AXIAL LEVEI (IN.) : 17.5
INJ. SUBCHANNEL : 120
FLOW SPLITS :
X1= 0.8650 X2= 1.2800 X3= 1.2800
MASSBALANCE RATIO : 0.898

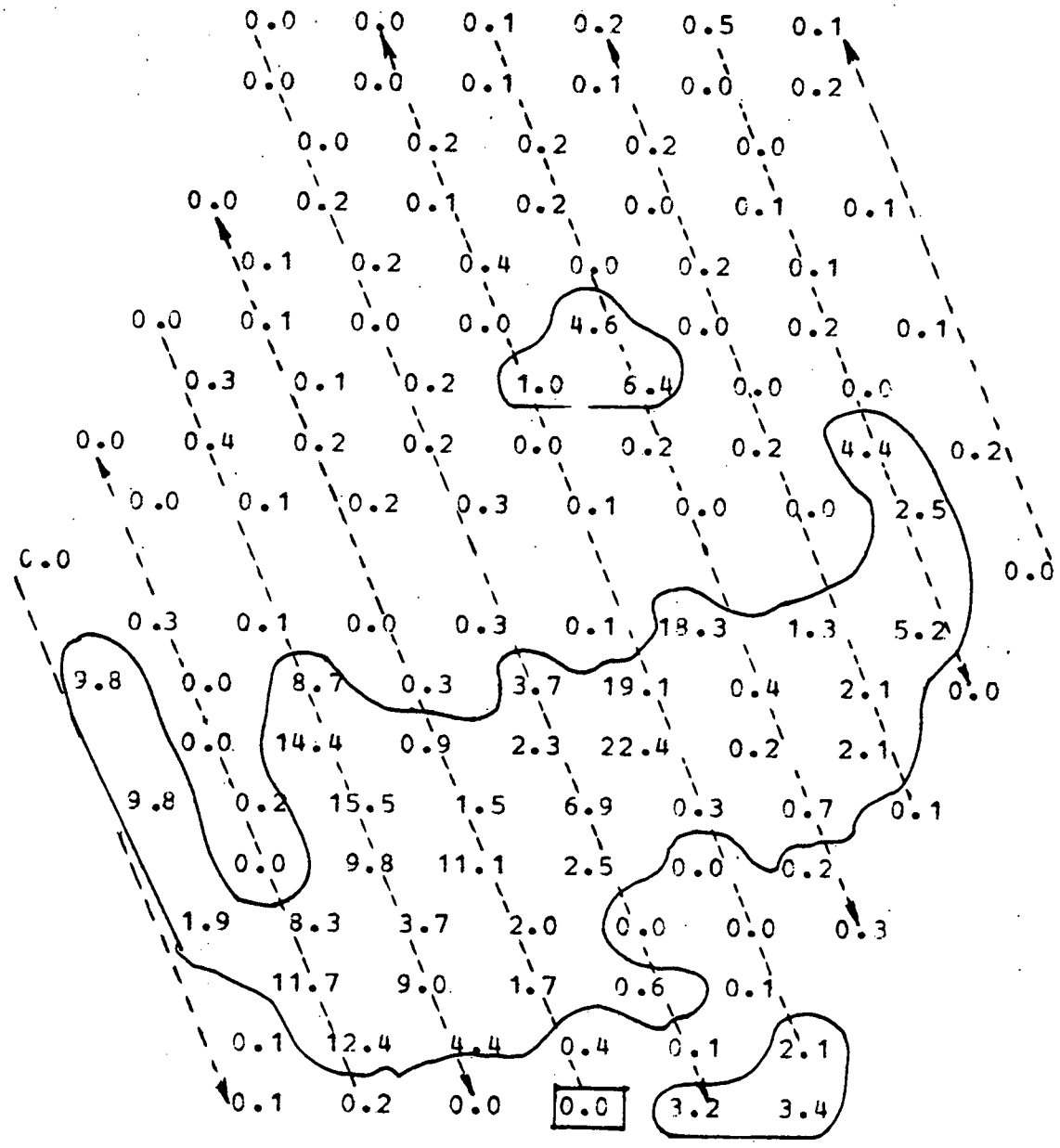

Figure A.39

SALT CONCENTRATION DISTRIBUTION MAP:

DIMENSIONLESS RATIOS OF SALT CONCENTRATION*0.01
MIX06.01
BUNDLE R.E. : 9134
AXIAL LEVEL (IN.) : 18.00
INJ. SUBCHANNEL : 120
FLOW SPLITS :
X1= 0.8650 X2= 1.2800 X3= 1.2800
MASSBALANCE RATIO : 0.878

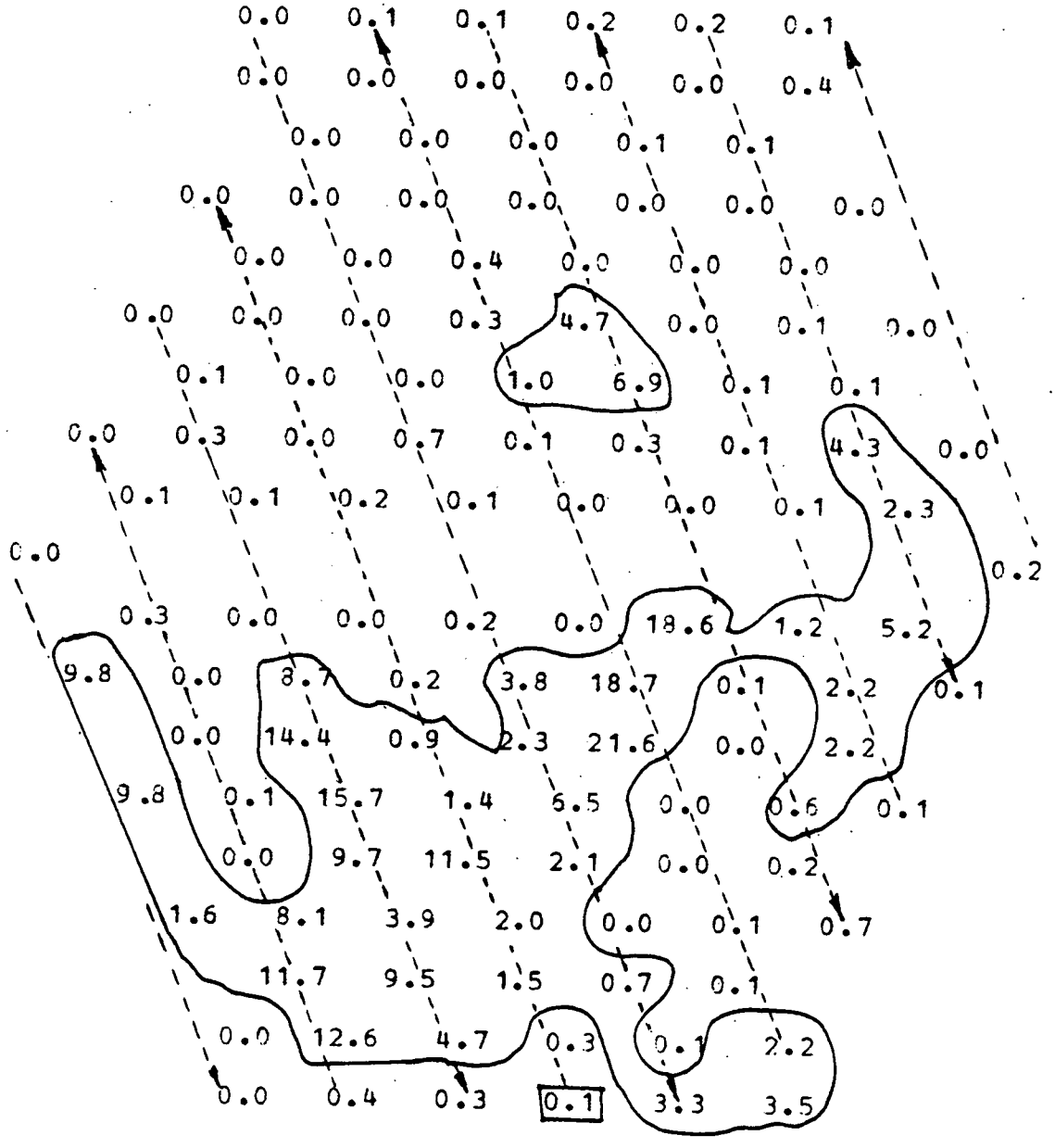

Figure A.40

SALT CONCENTRATION DISTRIBUTION MAP:

DIMENSIONLESS RATIOS OF SALT CONCENTRATION*0.01
MIX05.03
BUNDLE R.E. : 9134
AXIAL LEVEL (IN.) : 18.5
INJ. SUBCHANNEL : 120
FLOW SPLITS :
X1= 0.8650 X2= 1.2800 X3= 1.2800
MASSBALANCE RATIO : 0.888

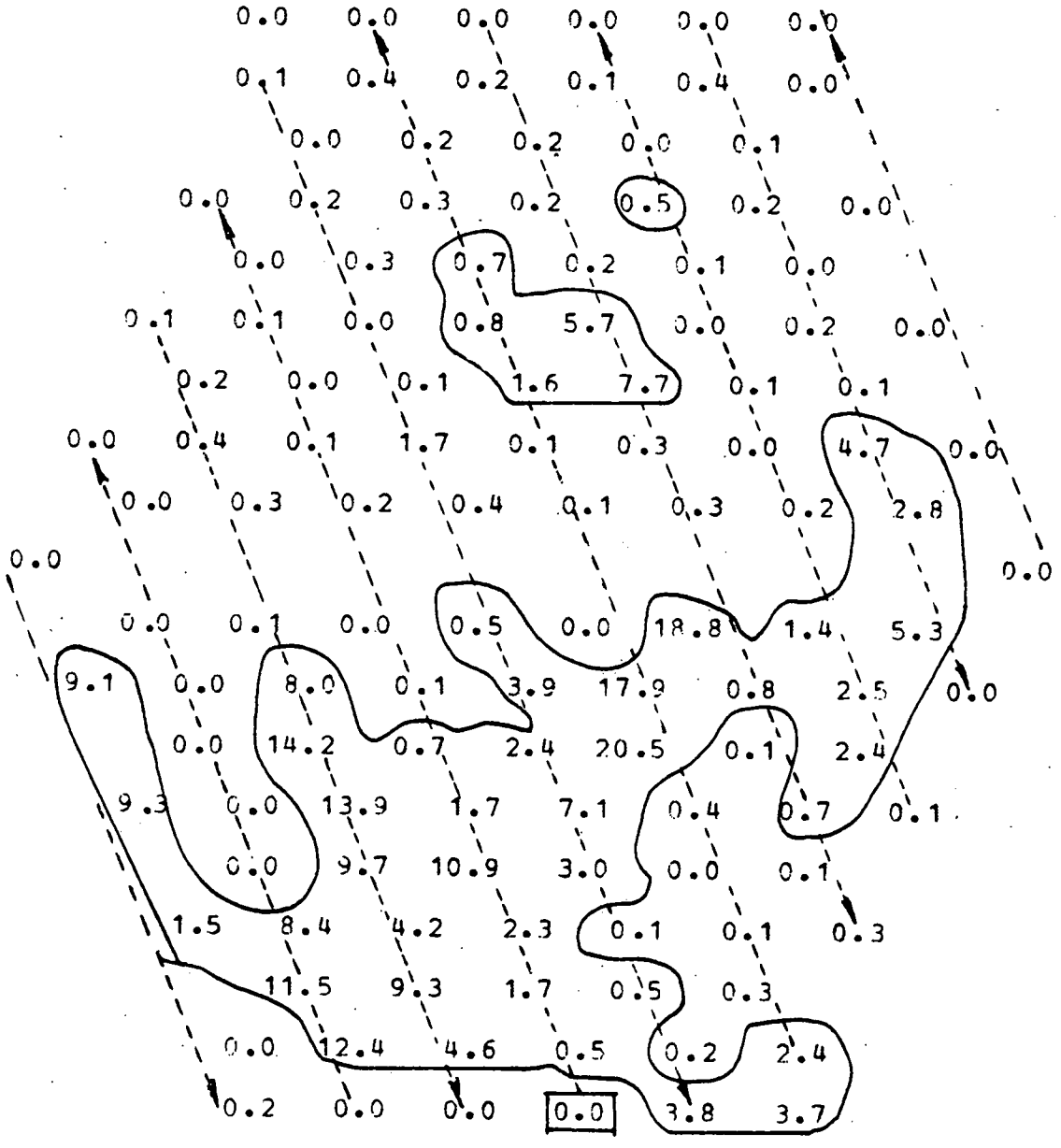

Figure A.41

SALT CONCENTRATION DISTRIBUTION MAP:

DIMENSIONLESS RATIOS OF SALT CONCENTRATION*0.01
MIX05.02
BUNDLE R.E. : 9134
AXIAL LEVEL (IN.) : 19.0
INJ. SUBCHANNEL : 120
FLOW SPLITS :
X1= 0.8650 X2= 1.2800 X3= 1.2800
MASSBALANCE RATIO : 0.900

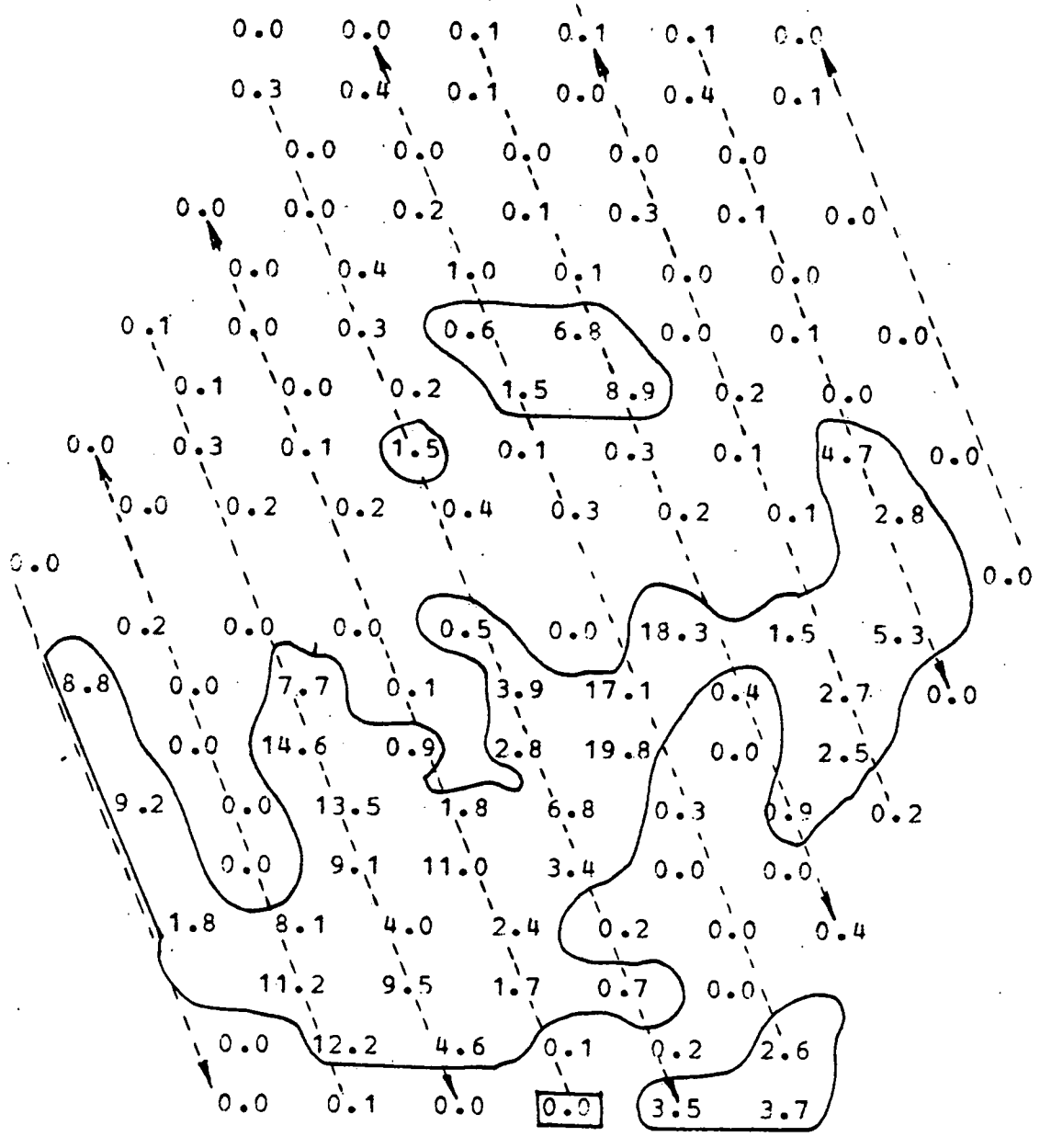

Figure A.42

SALT CONCENTRATION DISTRIBUTION MAP:

DIMENSIONLESS RATIOS OF SALT CONCENTRATION*0.01
MIX05.01
BUNDLE R.E. : 9134
AXIAL LEVEI (IN.) : 19.5
INJ. SUBCHANNEL : 120
FLOW SPLITS :
X1= 0.8650 X2= 1.2800 X3= 1.2800
MASSBALANCE RATIO : 0.892

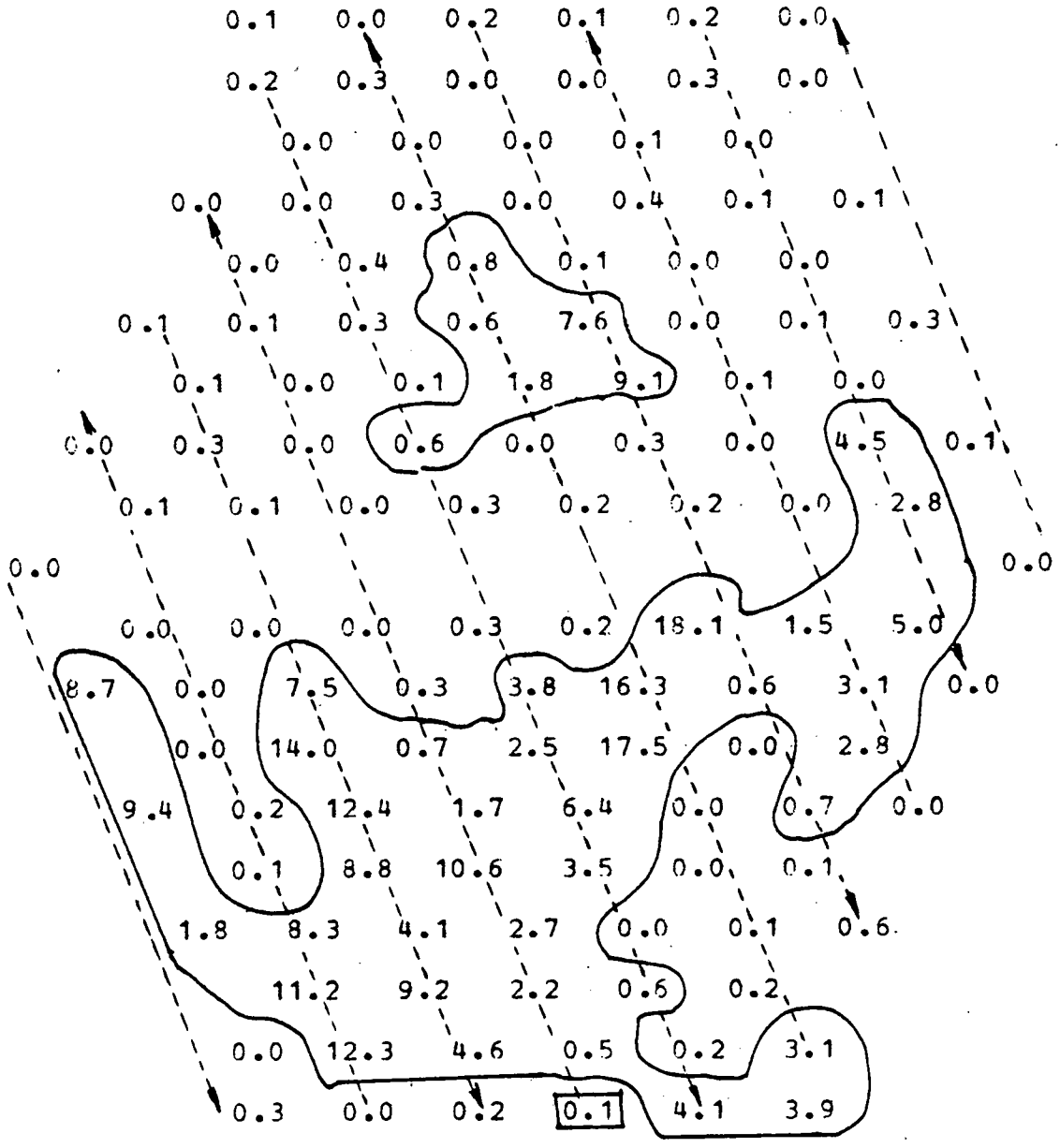

Figure A.43

SALT CONCENTRATION DISTRIBUTION MAP:

DIMENSIONLESS RATIOS OF SALT CONCENTRATION*0.01
MIX04.03
BUNDLE R.E. : 9134
AXIAL LEVEI (IN.) : 20.0
INJ. SUBCHANNEL : 120
FLOW SPLITS :
X1= 0.8650 X2= 1.2800 X3= 1.2800
MASSBALANCE RATIO : 0.935

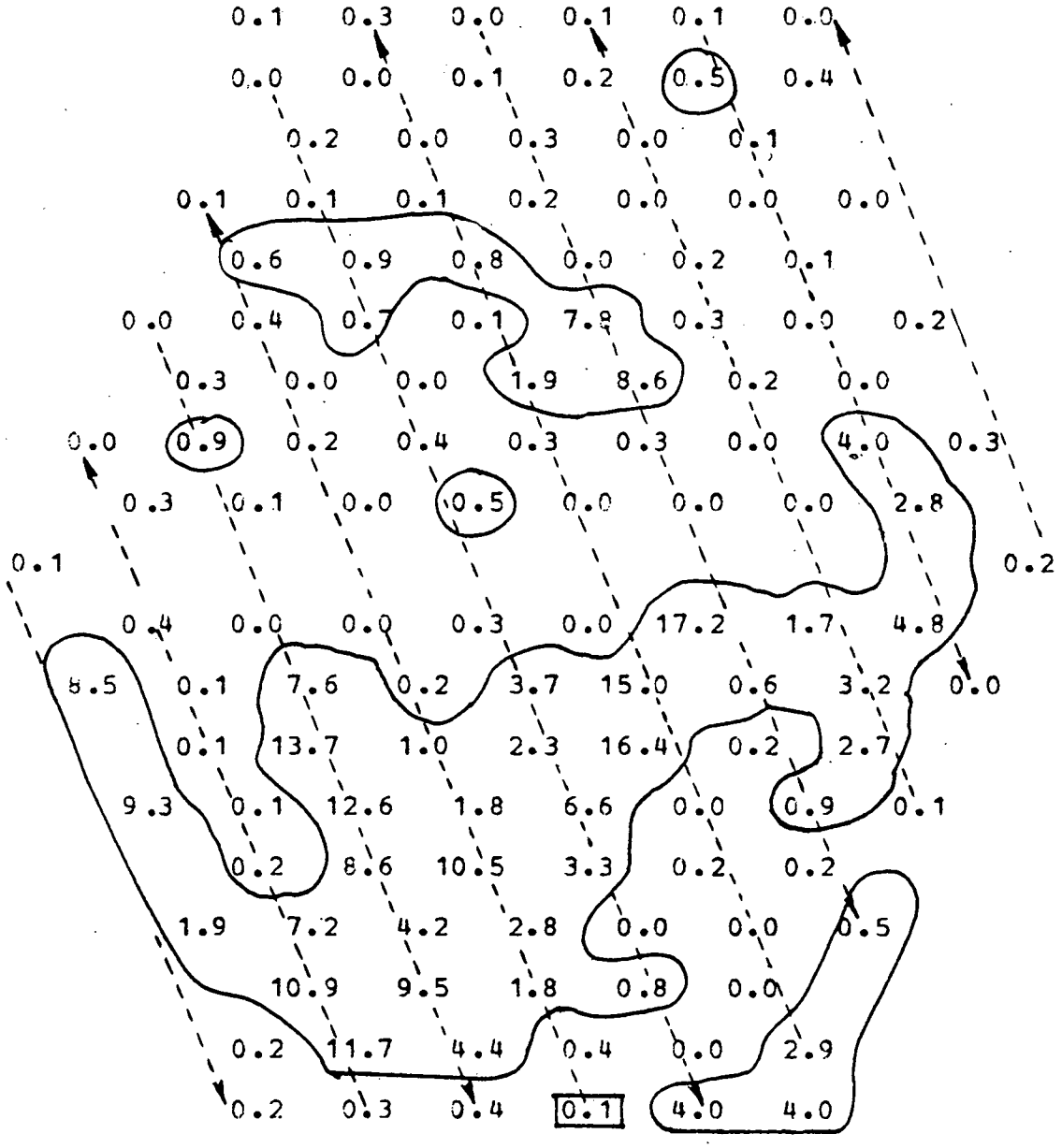

Figure A.44

SALT CONCENTRATION DISTRIBUTION MAP:

DIMENSIONLESS RATIOS OF SALT CONCENTRATION*0.01
MIX03.01
BUNDLE R.E. : 9134
AXIAL LEVEL (IN.) : 23.00
INJ. SUBCHANNEL : 120
FLOW SPLITS :
X1= 0.8650 X2= 1.2800 X3= 1.2800
MASSBALANCE RATIO : 0.922

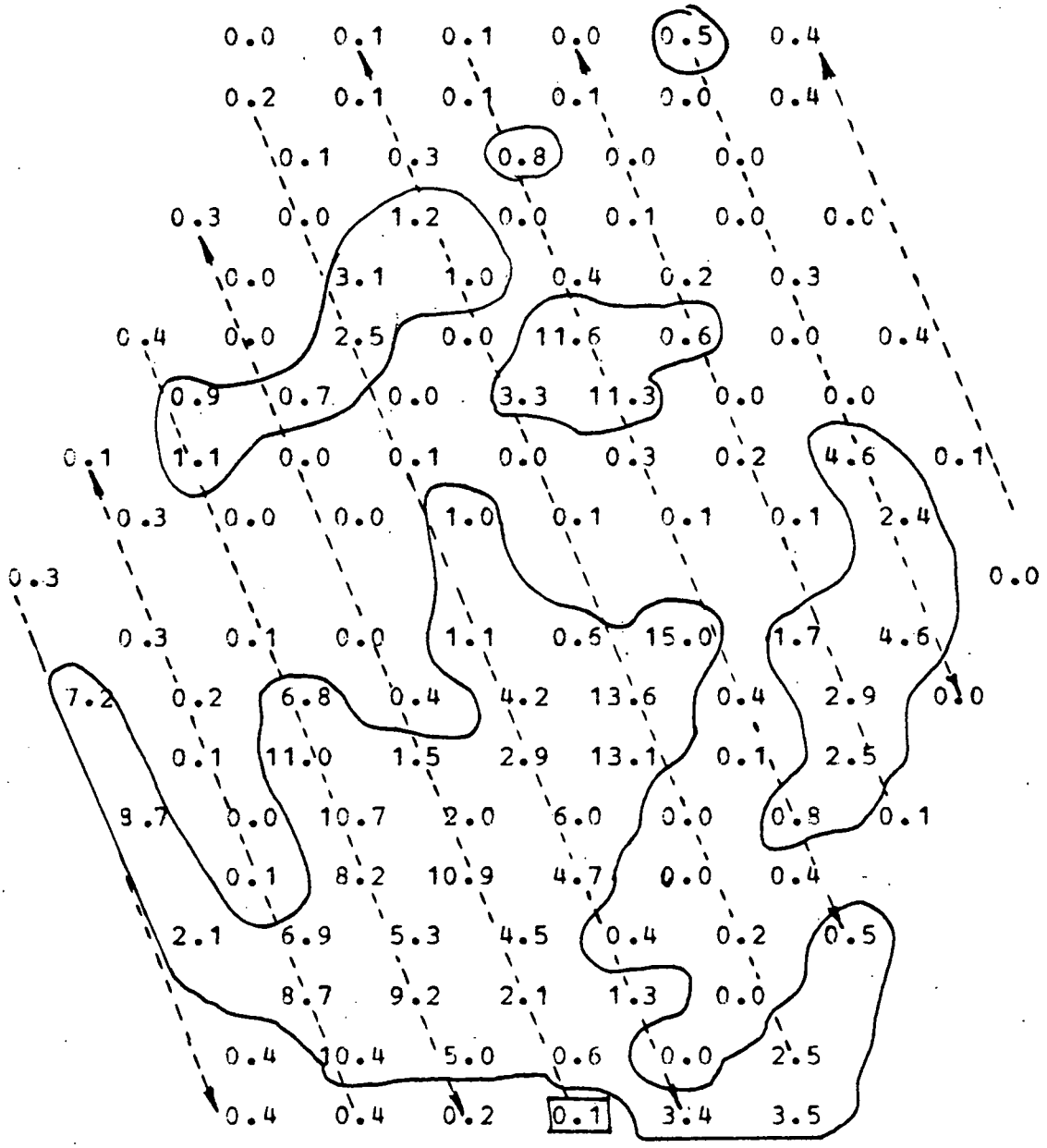

Figure A.45

SALT CONCENTRATION DISTRIBUTION MAP:

DIMENSIONLESS RATIOS OF SALT CONCENTRATION*0.01
MIX03.02
BUNDLE R.E. : 9134
AXIAL LEVEL (IN.) : 23.50
INJ. SUBCHANNEL : 120
FLOW SPLITS :
X1= 0.8650 X2= 1.2800 X3= 1.2800
MASSBALANCE RATIO : 0.954

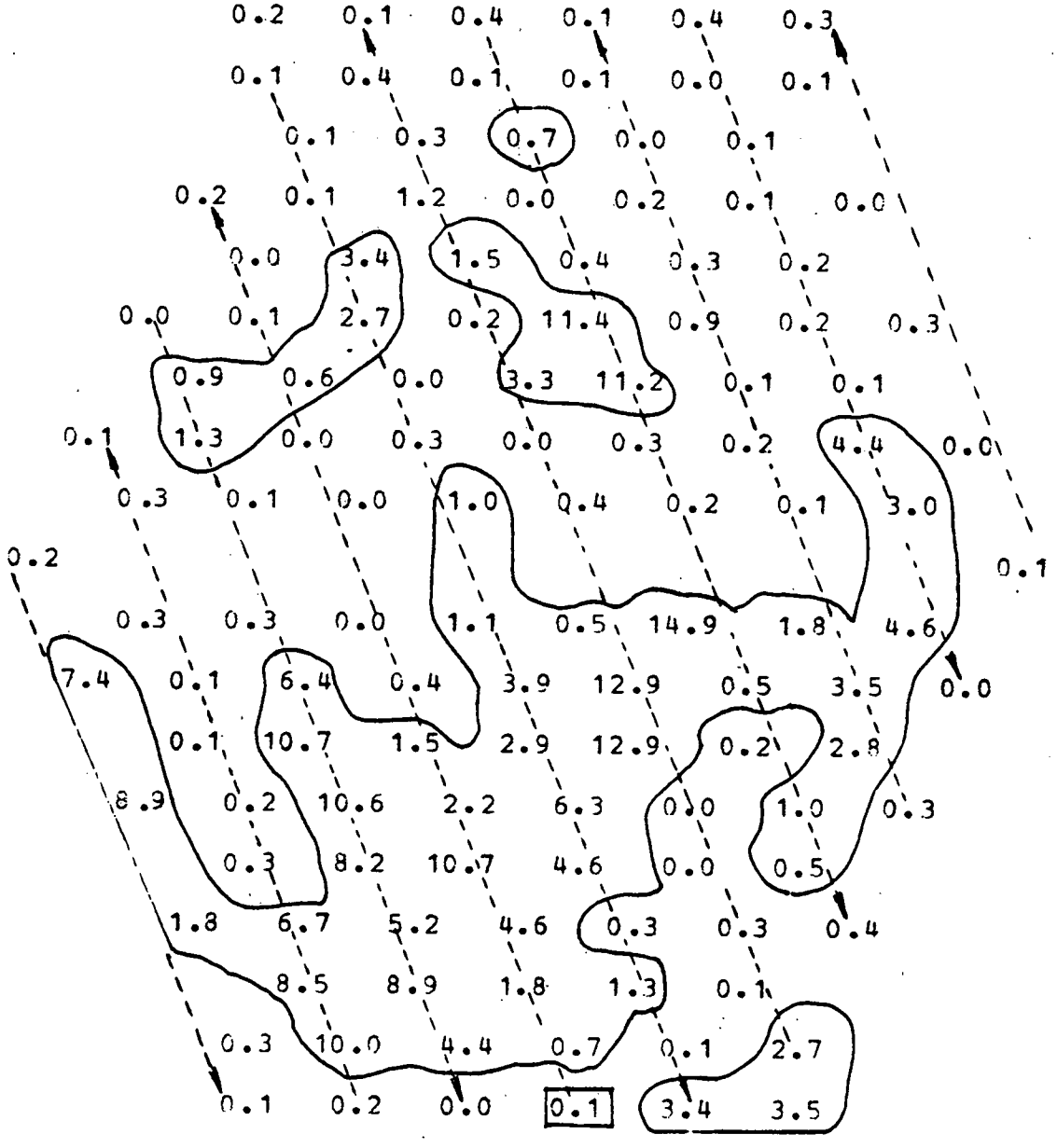

Figure A.46

SALT CONCENTRATION DISTRIBUTION MAP:

DIMENSIONLESS RATIOS OF SALT CONCENTRATION*0.01
MIX03.03
BUNDLE R.E. : 9134
AXIAL LEVEL (IN.) : 24.00
INJ. SUBCHANNEL : 120
FLOW SPLITS :
X1= 0.8650 X2= 1.2800 X3= 1.2800
MASSBALANCE RATIO : 0.942

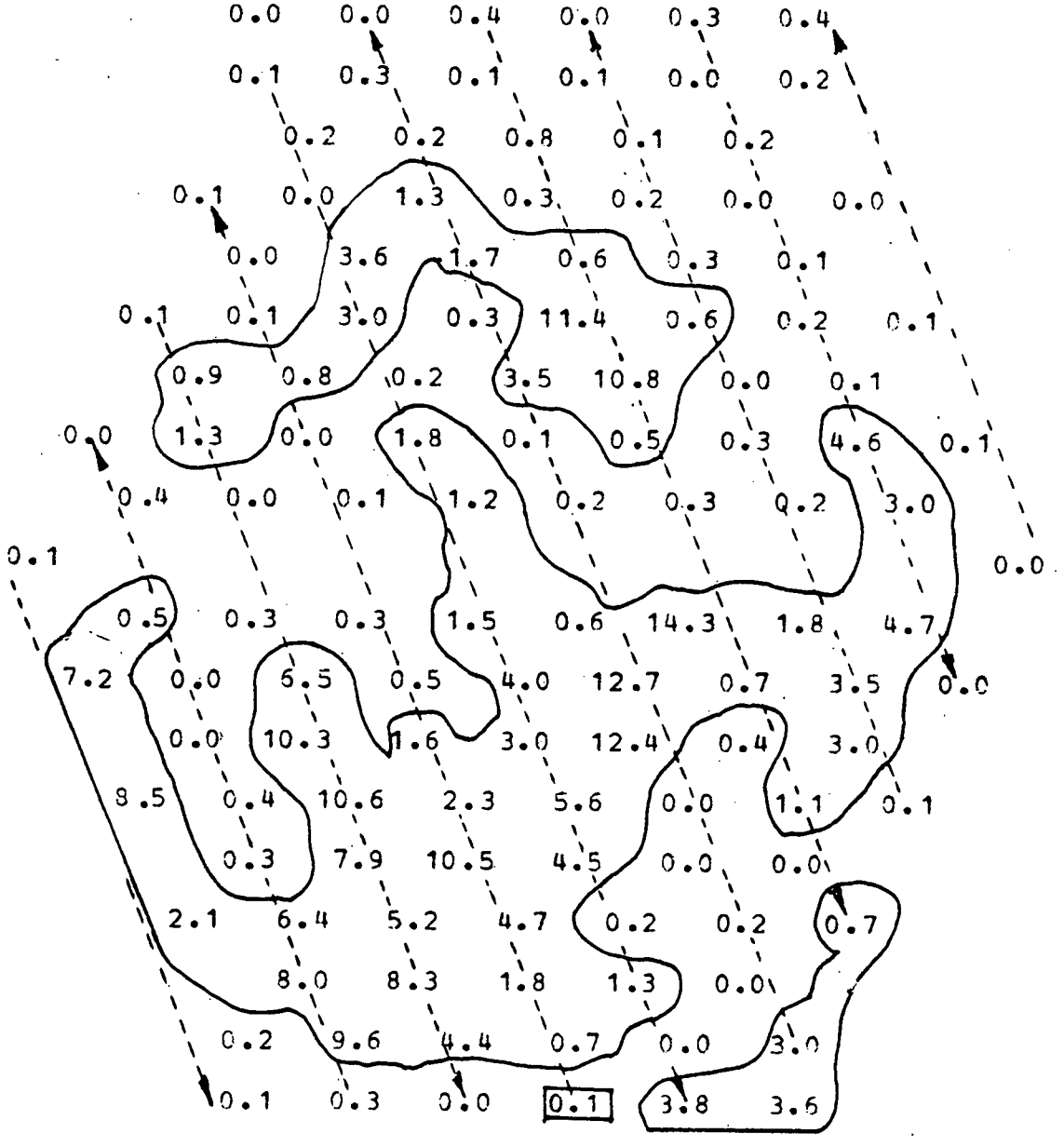

Figure A.47

SALT CONCENTRATION DISTRIBUTION MAP:

DIMENSIONLESS RATIOS OF SALT CONCENTRATION*0.01
MIX04.02
BUNDLE R.E. : 9134
AXIAL LEVEI (IN.) : 25.00
INJ. SUBCHANNEL : 120
FLOW SPLITS :
X1= 0.8650 X2= 1.2800 X3= 1.2800
MASSBALANCE RATIO : 0.935

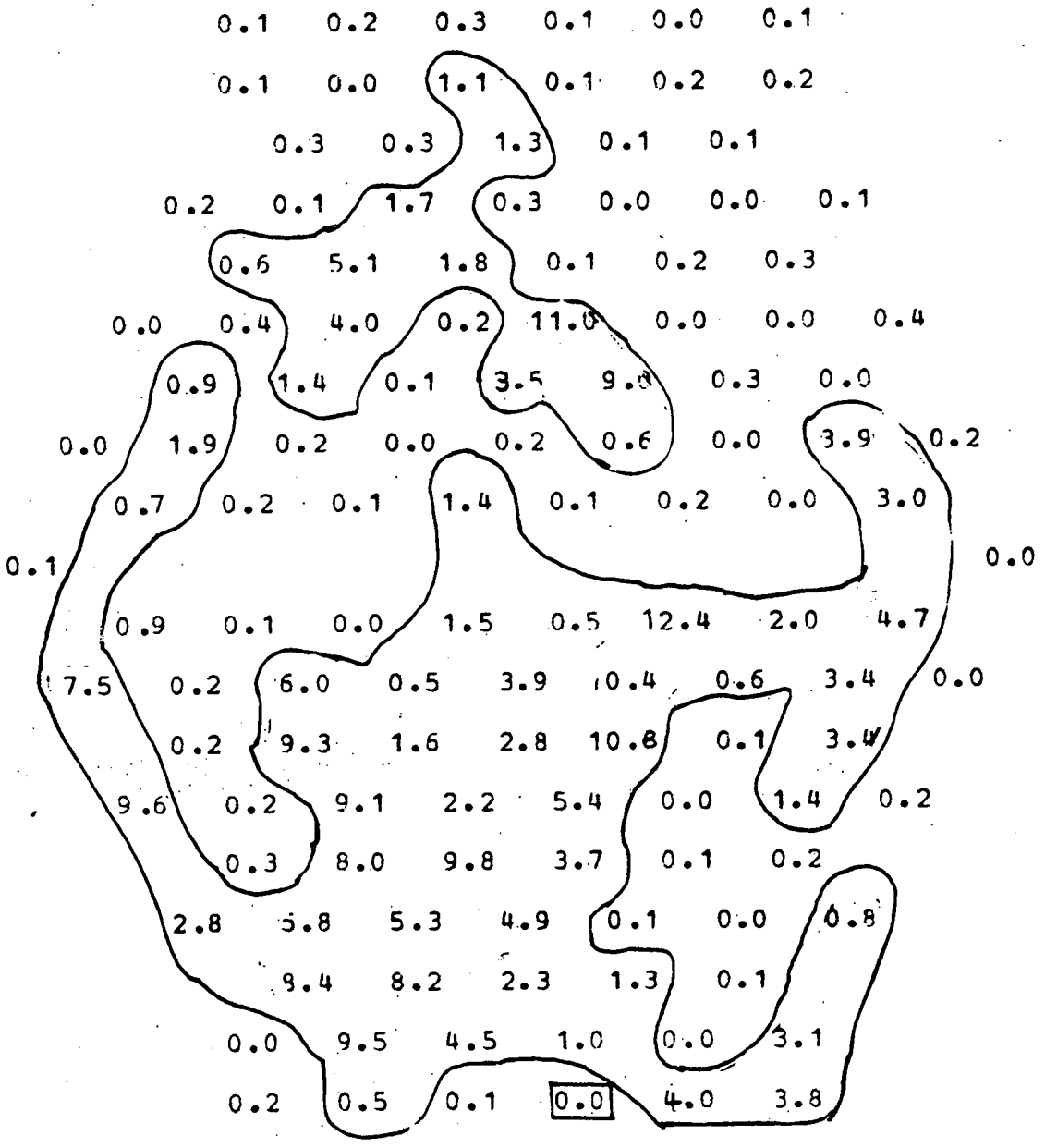

Figure A·48

APPENDIX A.4

DIMENSIONLESS SALT CONCENTRATION MAPS AT DIFFERENT INJECTION DEPTHS FOR INJECTION SUBCHANNEL NO. 3

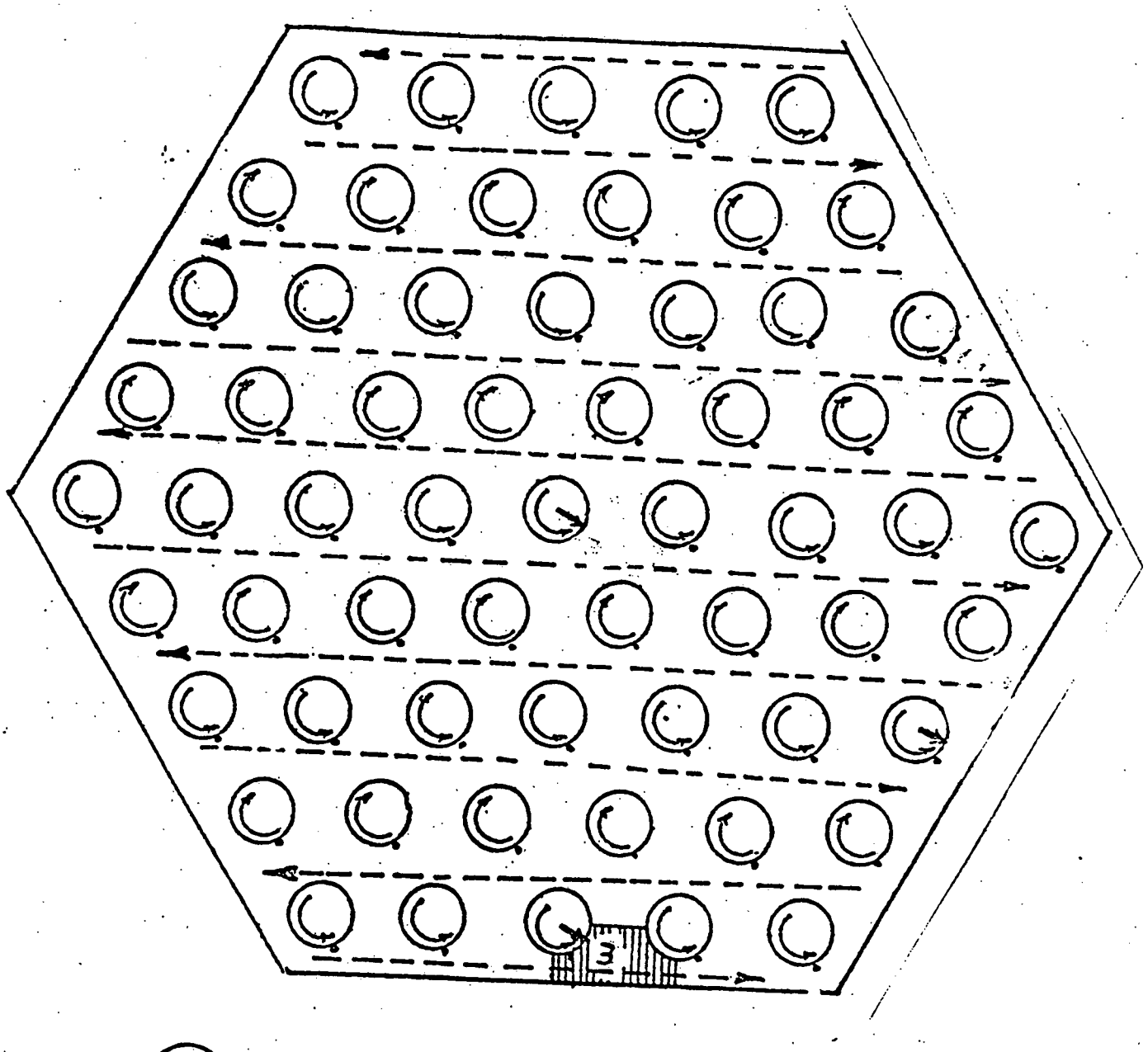

Fuel Pin and Wire Wrap Direction

Flow Preferable Path

Injection Channel

Figure A-49 Injection Positions in the Alternate Wire Wrap Bundle

SALT CONCENTRATION DISTRIBUTTON MAP:

DIMENSIONLESS RATIOS OF SALT CONCENTRATION*0.01
MIX15.01
BUNDLE R.E. : 8822
AXIAL LEVEI (IN.) : 13.50
INJ. SUBCHANNEL : 120
FLOW SPLITS :
X1= 0.8650 X2= 1.2800 X3= 1.2800
MASSBALANCE RATIO : 0.996

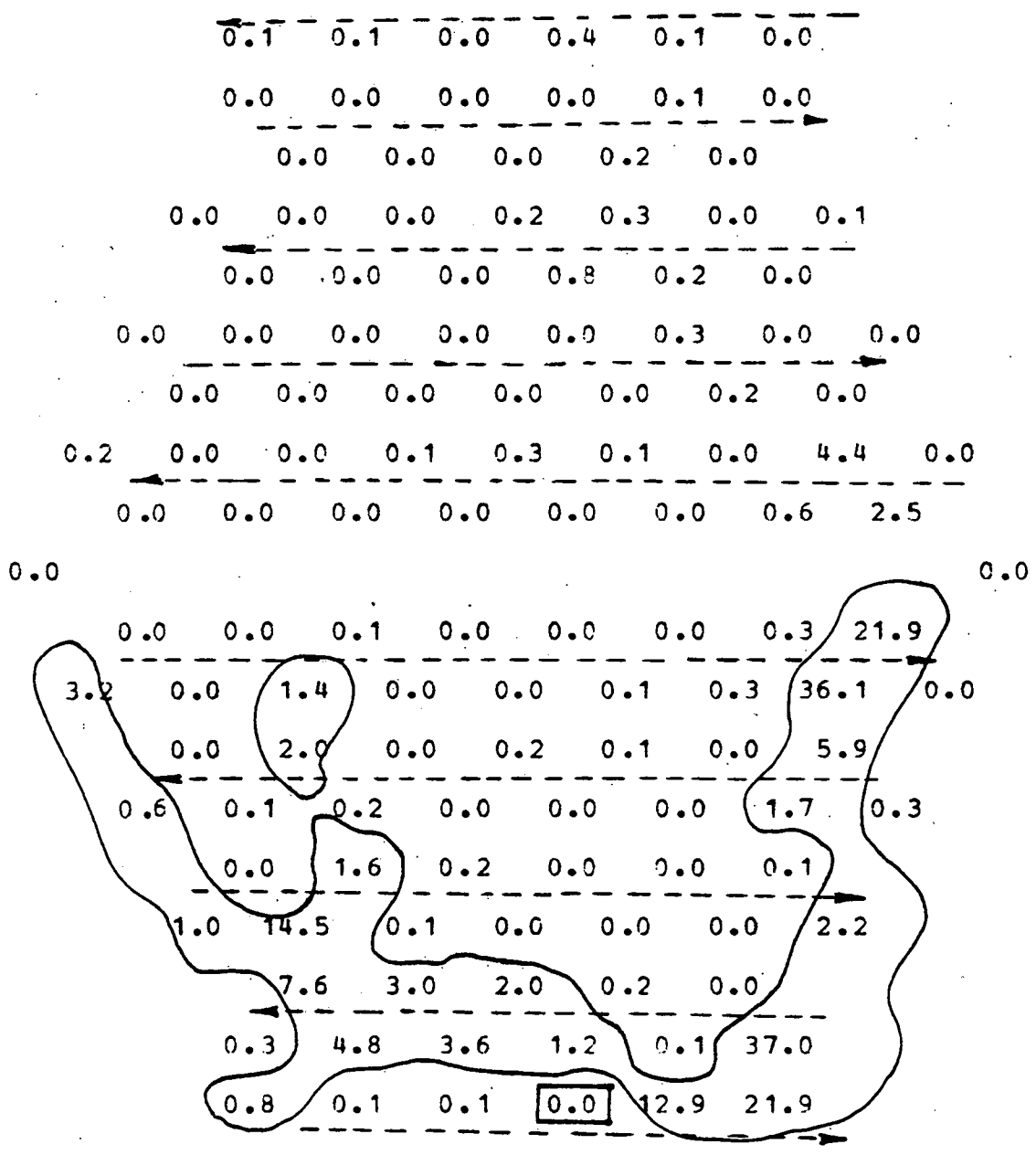

Figure A.50

SALT CONCENTRATION DISTRIBUTION MAP:

DIMENSIONLESS RATIOS OF SALT CONCENTRATION*0.01
MIX15.02
BUNDLE R.E. : 8822
AXIAL LEVEL (IN.) : 14.00
INJ. SUBCHANNEL : 120
FLOW SPLITS :
X1= 0.8650 X2= 1.2800 X3= 1.2800
MASSBALANCE RATIO : 0.991

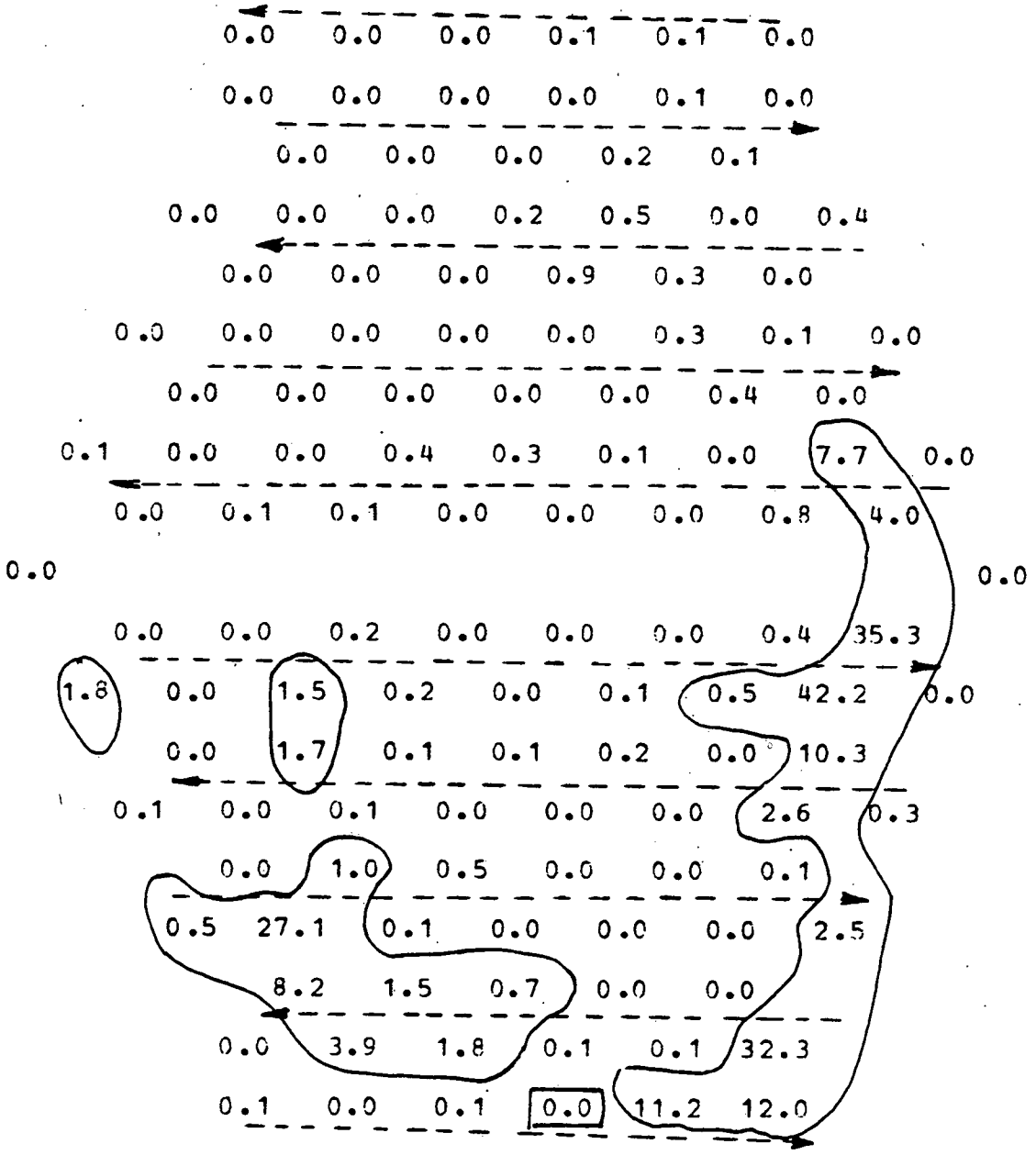

Figure A.51

SALT CONCENTRATION DISTRIBUTION MAP:

DIMENSIONLESS RATIOS OF SALT CONCENTRATION*0.01
MIX15.03
BUNDLE R.E. : 8822
AXIAL LEVEI (IN.) : 14.50
INJ. SUBCHANNEL : 120
FLOW SPLITS :
X1= 0.8650 X2= 1.2800 X3= 1.2800
MASSBALANCE RATIO : 0.973

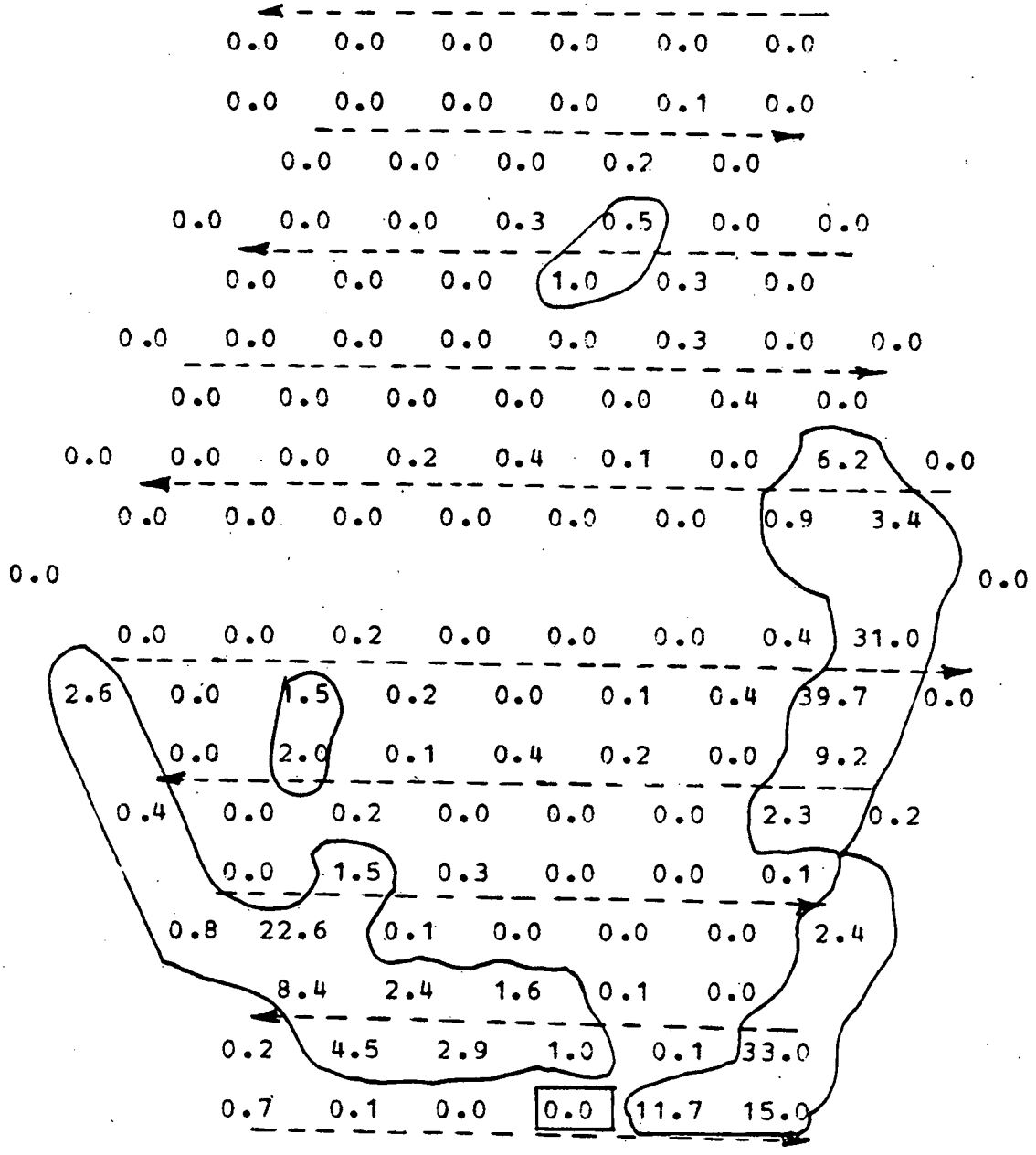

Figure A.52

SALT CONCENTRATION DISTRIBUTION MAP:

DIMENSIONLESS RATIOS OF SALT CONCENTRATION*0.01
MIX15.04
BUNDLE R.E. : 8822
AXIAL LEVEL (IN.) : 15.00
INJ. SUBCHANNEL : 120
FLOW SPLITS :
X1= 0.9650 X2= 1.2800 X3= 1.2800
MASSBALANCE RATIO : 0.977

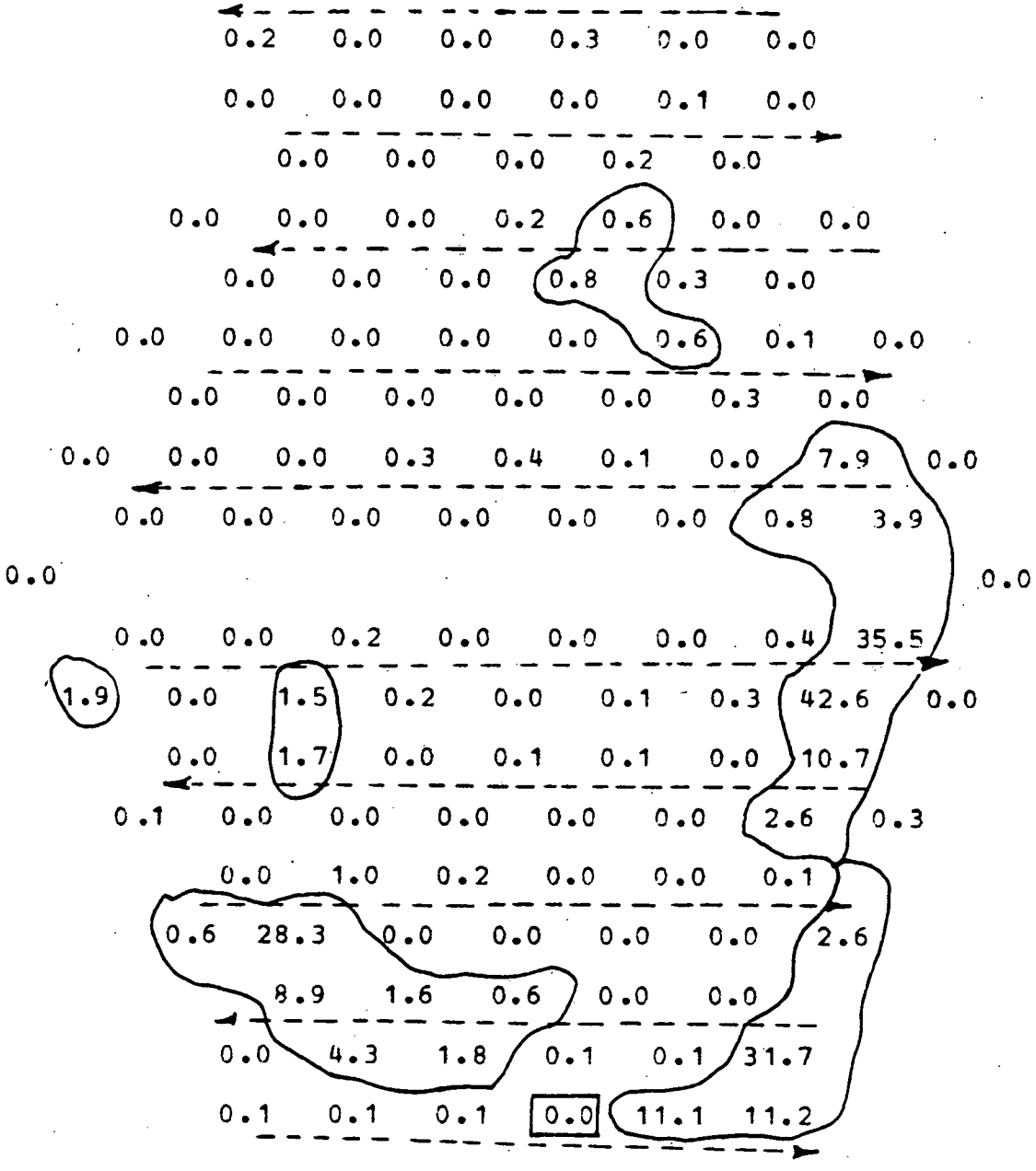

Figure A.53

SALT CONCENTRATION DISTRIBUTION MAP:

DIMENSIONLESS RATIOS OF SALT CONCENTRATION*0.01
MIX16.01
BUNDLE R.E. : 9822
AXIAL LEVEI (IN.) : 15.50
INJ. SUBCHANNEL : 120
FLOW SPLITS :
X1= 0.8650 X2= 1.2800 X3= 1.2800
MASSBALANCE RATIO : 1.011

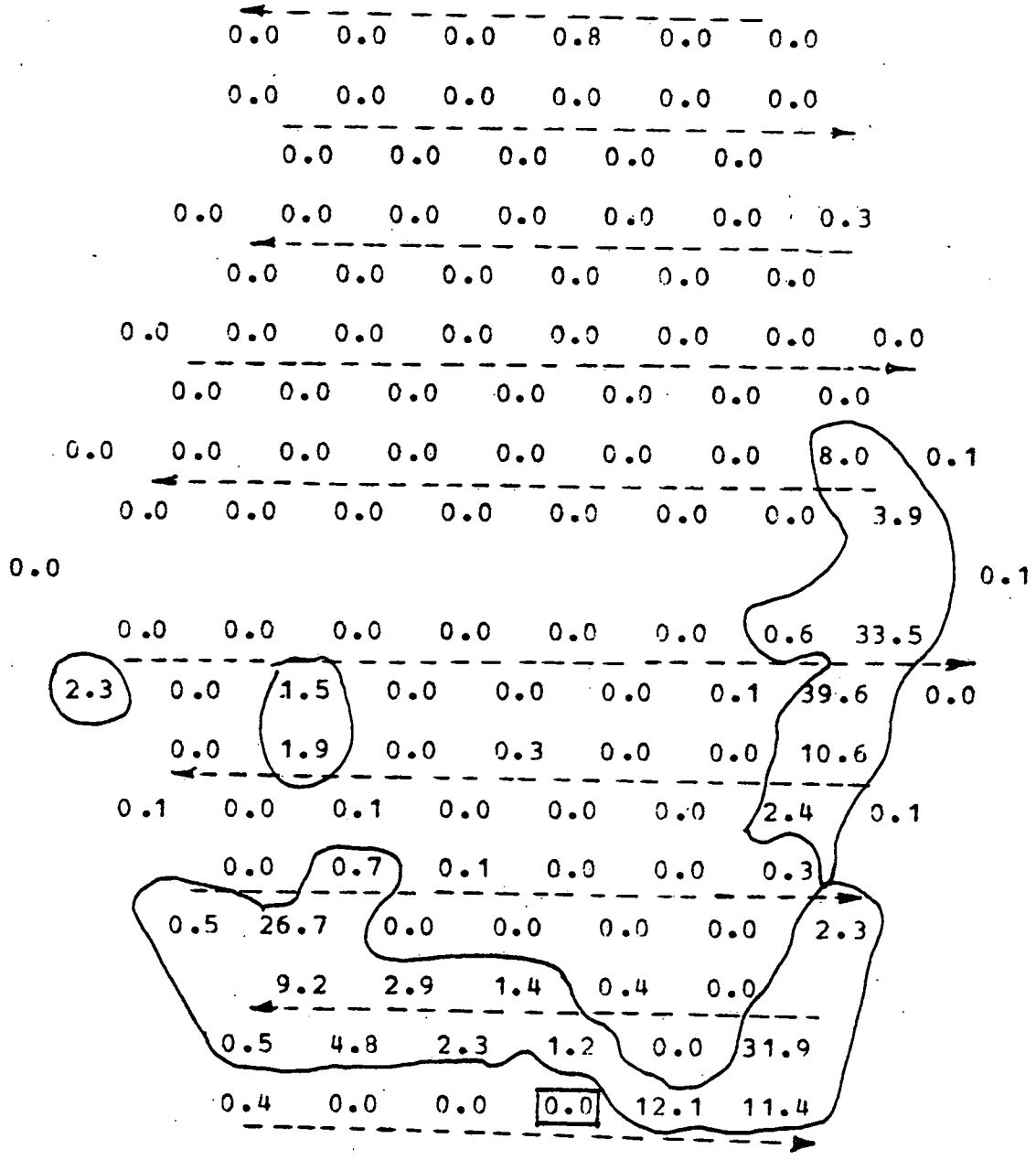

Figure A.54

SALT CONCENTRATION DISTRIBUTION MAP:

DIMENSIONLESS RATIOS OF SALT CONCENTRATION*0.01
MIX16.02
BUNDLE R.E. : 8822
AXIAL LEVEL (IN.) : 16.00
INJ. SUBCHANNEL : 120
FLOW SPLITS :
X1= 0.8650 X2= 1.2800 X3= 1.2800
MASSBALANCE RATIO : 0.995

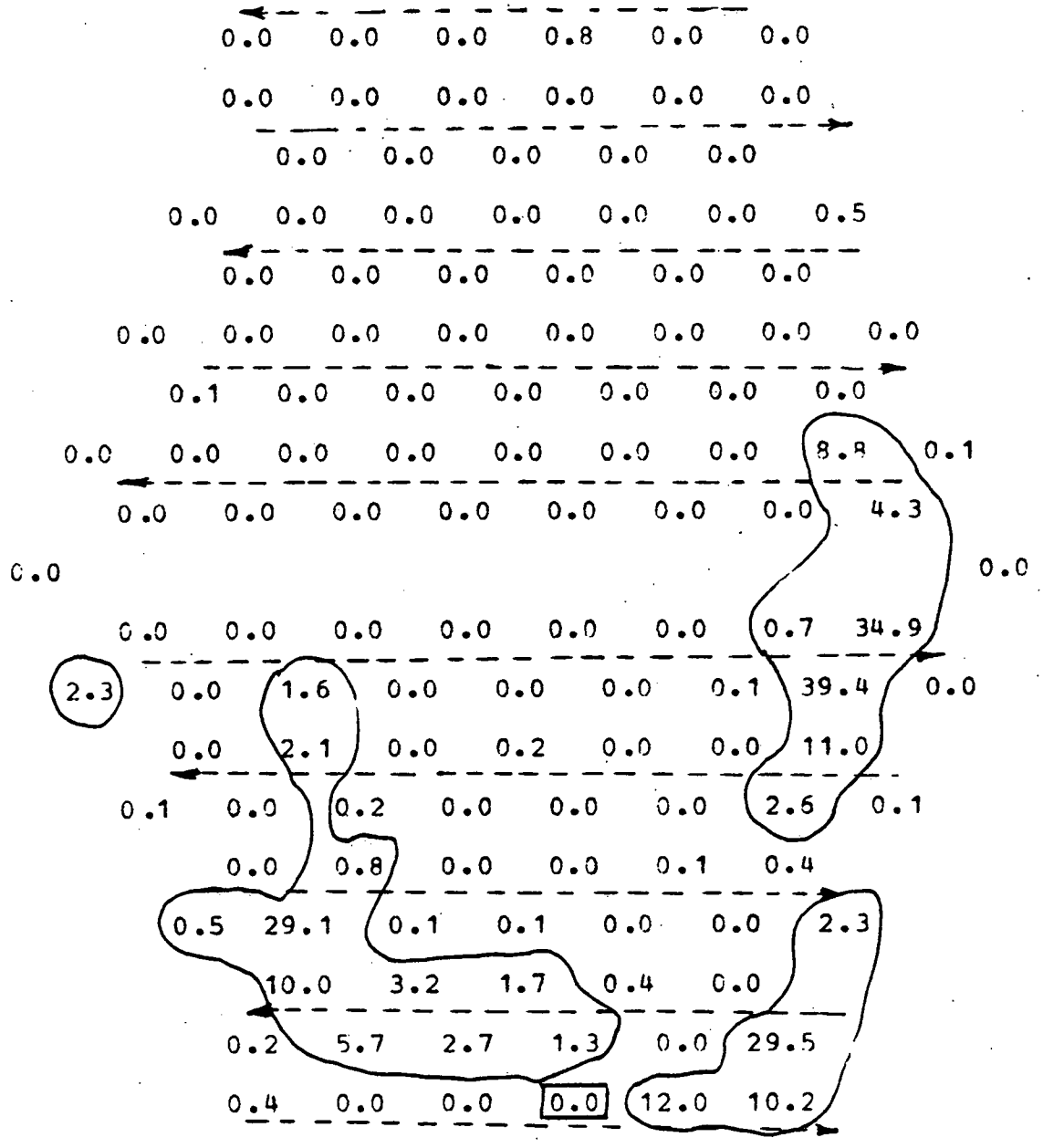

Figure A.55

SALT CONCENTRATION DISTRIBUTION MAP:

DIMENSIONLESS RATIOS OF SALT CONCENTRATION*0.01
MIX16.03
BUNDLE R.E. : 8822
AXIAL LEVEL (IN.) : 16.50
INJ. SUBCHANNEL : 120
FLOW SPLITS :
X1= 0.8650 X2= 1.2800 X3= 1.2800
MASSBALANCE RATIO : 0.987

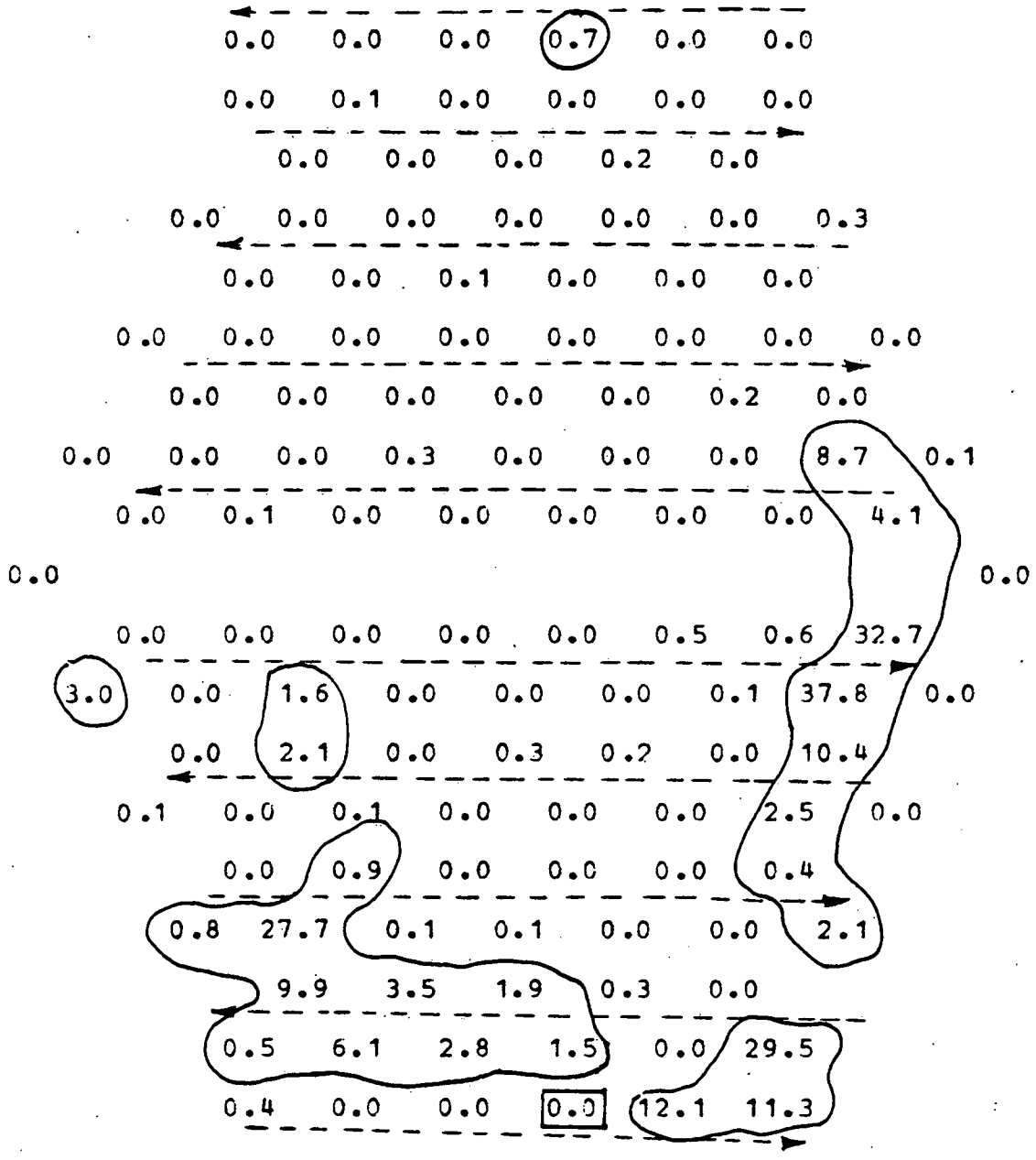

Figure A.56

SALT CONCENTRATION DISTRIBUTION MAP:

DIMENSIONLESS RATIOS OF SALT CONCENTRATION*0.01
MIX16.05
BUNDLE R.E. : 8822
AXIAL LEVEL (IN.) : 17.50
INJ. SUBCHANNEL : 120
FLOW SPLITS :
X1= 0.8650 X2= 1.2800 X3= 1.2800
MASSBALANCE RATIO : 0.989

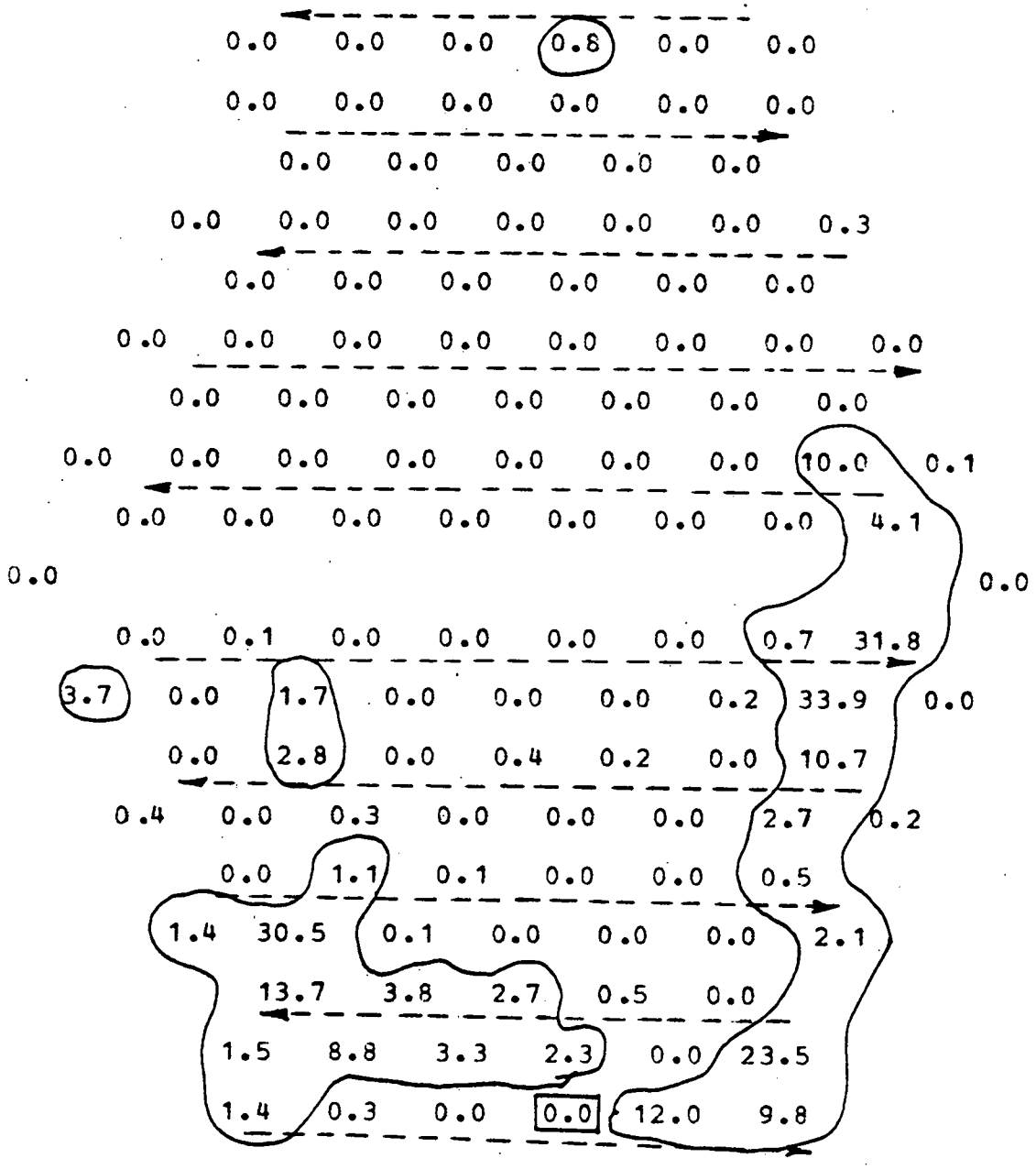

Figure A.57

SALT CONCENTRATION DISTRIBUTION MAP:

DIMENSIONLESS RATIOS OF SALT CONCENTRATION*0.01
MIX17.01
BUNDLE R.E. : 8822
AXIAL LEVEI (IN.) : 18.00
INJ. SUBCHANNEL : 120
FLOW SPLITS :
X1= 0.8650 X2= 1.2800 X3= 1.2800
MASSBALANCE RATIO : 1.019

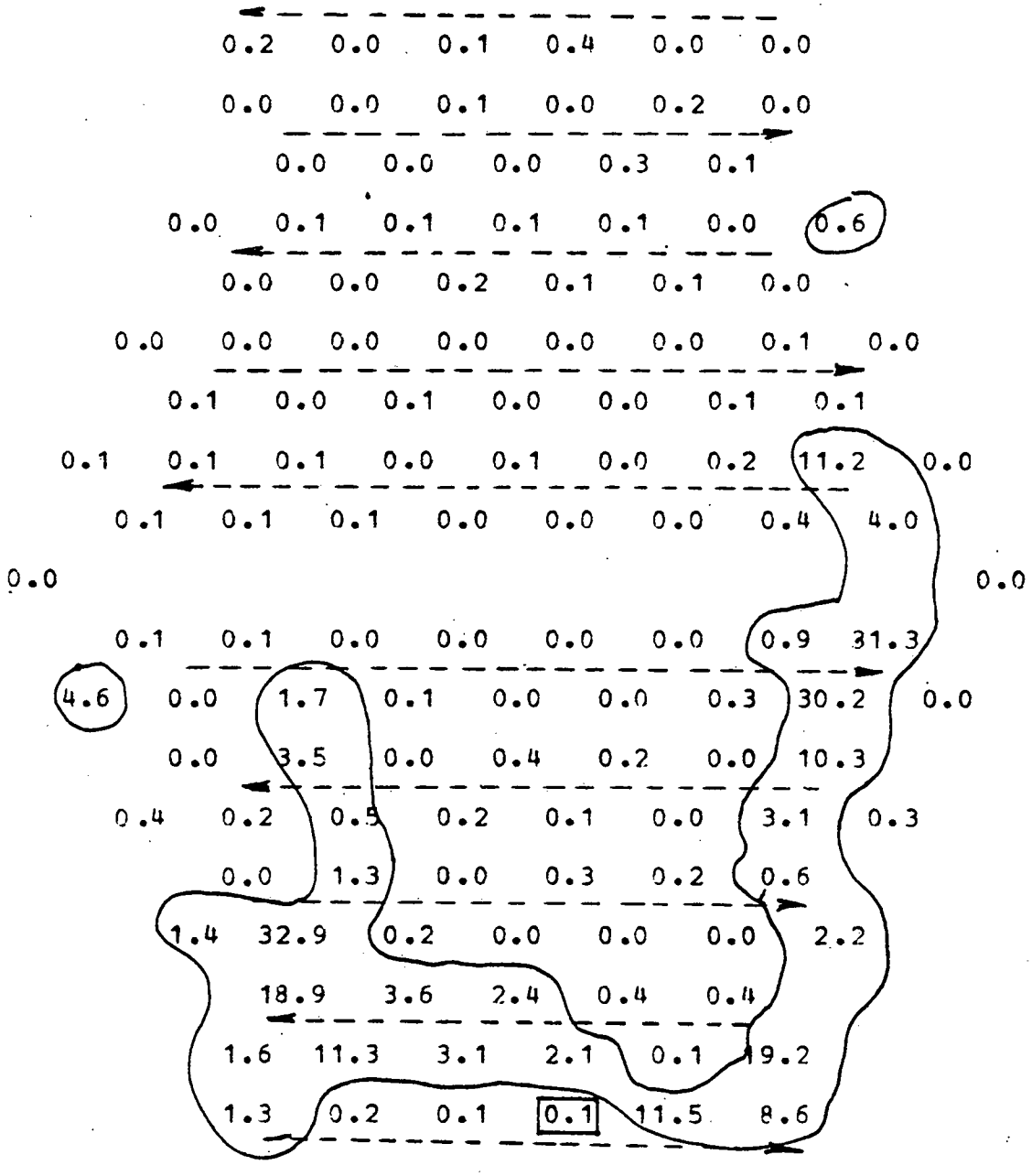

Figure A.58

SALT CONCENTRATION DISTRIBUTION MAP:

DIMENSIONLESS RATIOS OF SALT CONCENTRATION*0.01
MIX17.02
BUNDLE R.E. : 8822
AXIAL LEVEL (IN.) : 18.50
INJ. SUBCHANNEL : 120
FLOW SPLITS :
X1= 0.8650 X2= 1.2800 X3= 1.2800
MASSBALANCE RATIO : 1.021

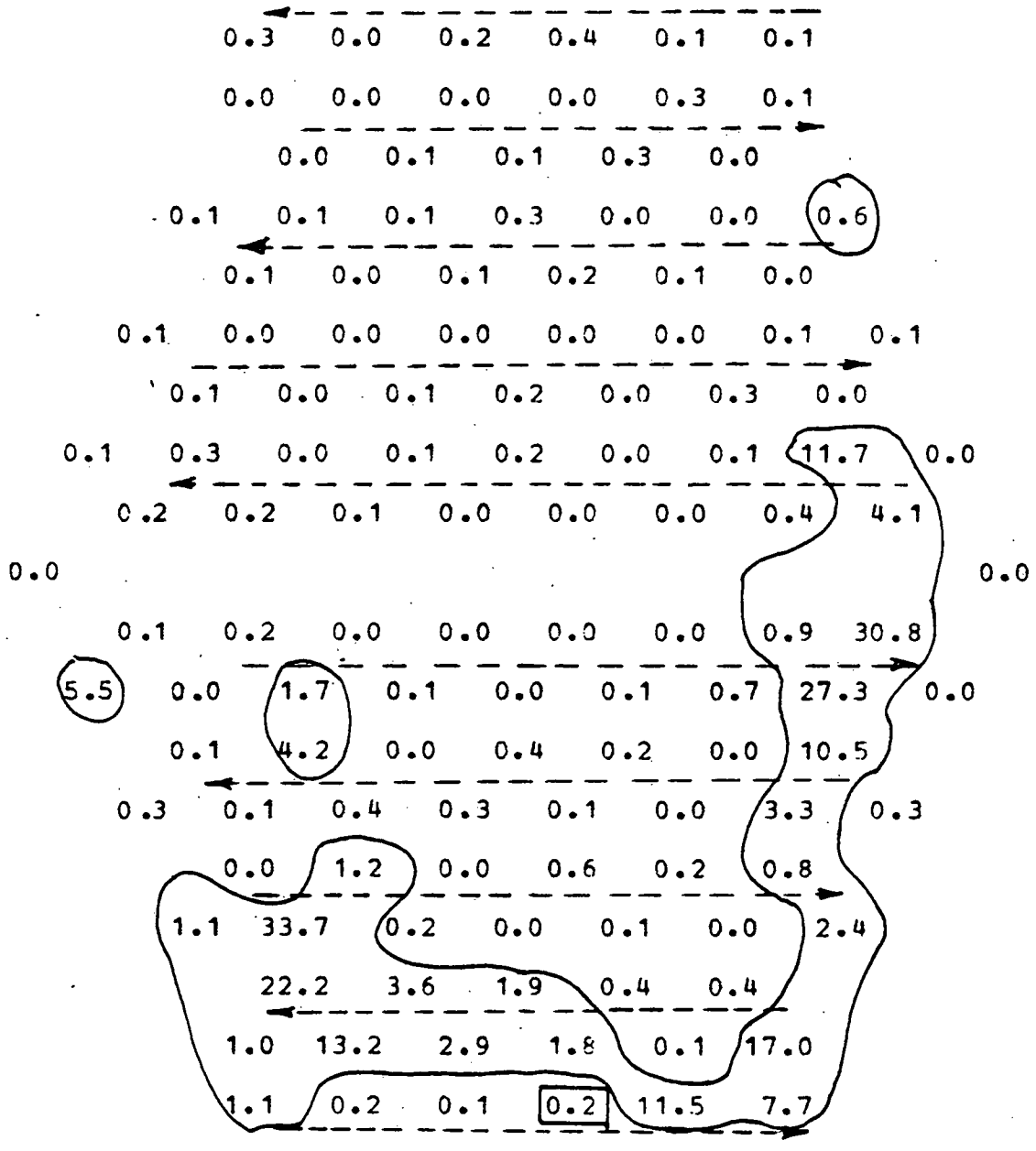

Figure A.59

SALT CONCENTRATION DISTRIBUTION MAP:

DIMENSIONLESS RATIOS OF SALT CONCENTRATION*0.01
MIX17.03
BUNDLE R.E. : 8822
AXIAL LEVEI (IN.) : 19.00
INJ. SUBCHANNEL : 120
FLOW SPLITS :
X1= 0.8650 X2= 1.2800 X3= 1.2800
MASSBALANCE RATIO : 1.015

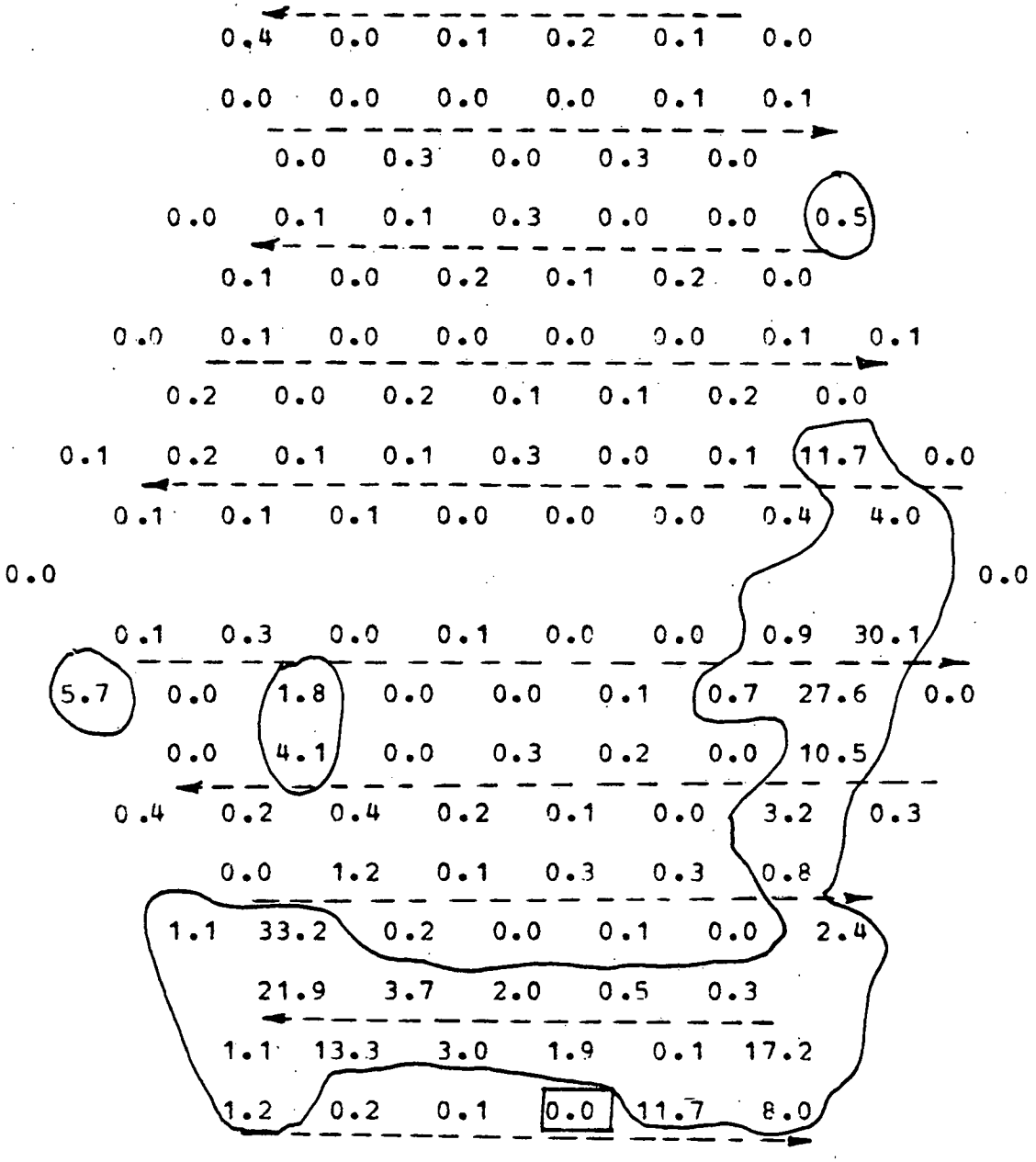

Figure A.60

SALT CONCENTRATION DISTRIBUTION MAP:

DIMENSIONLESS RATIOS OF SALT CONCENTRATION*0.01
MIX17.04
BUNDLE R.E. : 8822
AXIAL LEVEI (IN.) : 19.50
INJ. SUBCHANNEL : 120
FLOW SPLITS :
X1= 0.8650 X2= 1.2800 X3= 1.2800
MASSBALANCE RATIO : 1.022

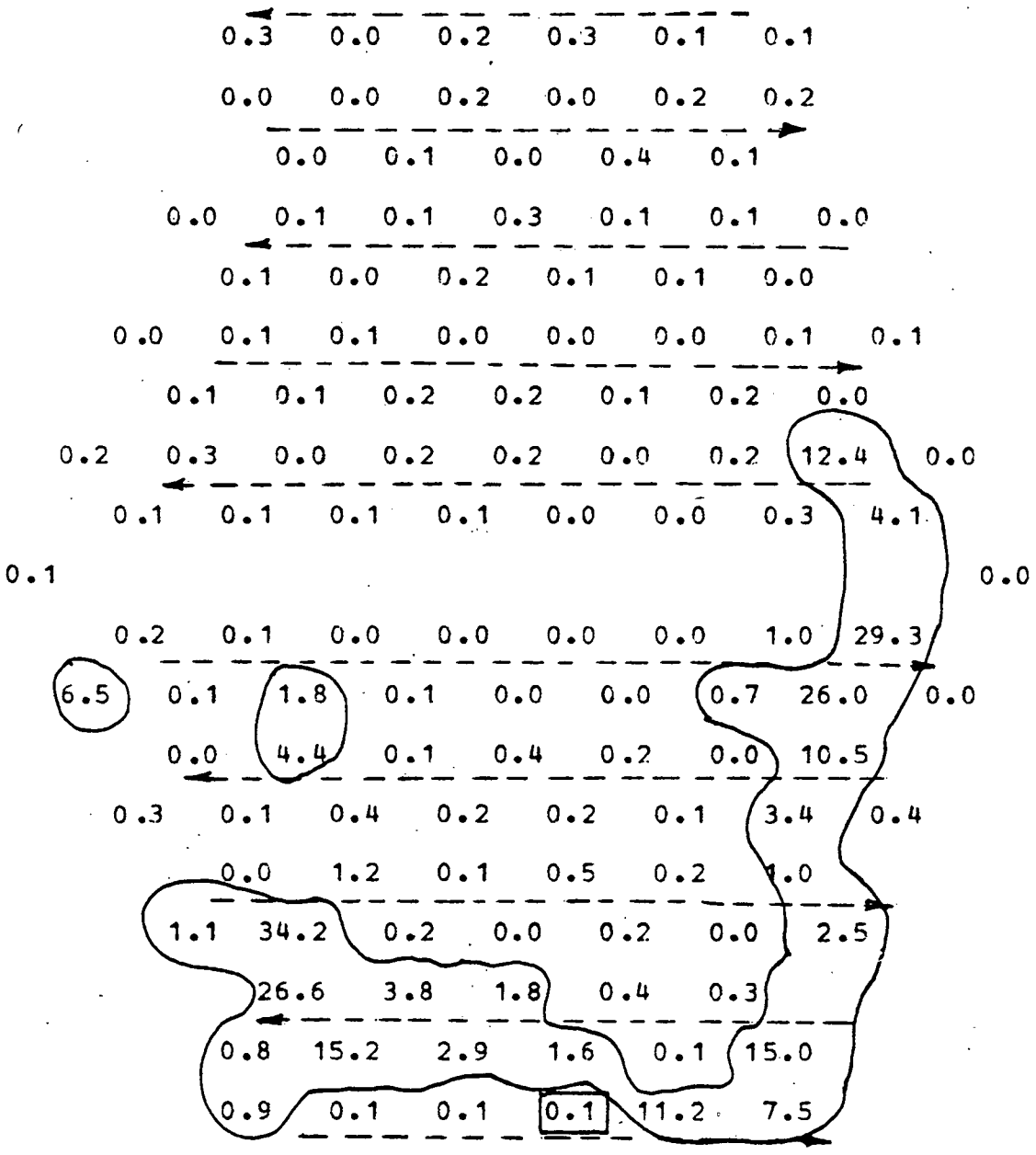

Figure A.61

SALT CONCENTRATION DISTRIBUTION MAP:

DIMENSIONLESS RATIOS OF SALT CONCENTRATION*0.01
MIX17.05
BUNDLE R.E. : 8822
AXIAL LEVEL (IN.) : 20.00
INJ. SUBCHANNEL : 120
FLOW SPLITS :
X1= 0.8650 X2= 1.2800 X3= 1.2800
MASSBALANCE RATIO : 1.021

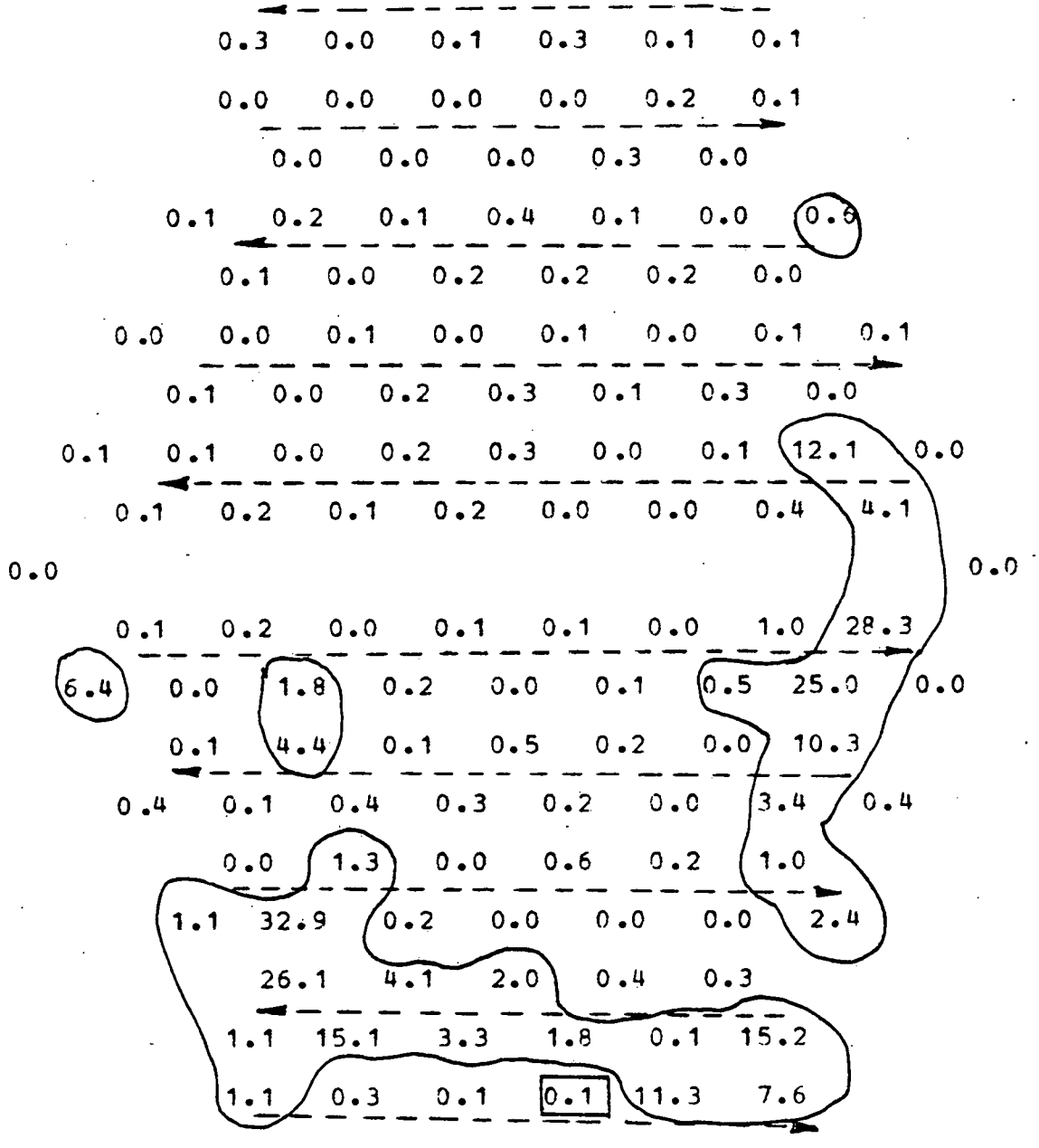

Figure A.62

SALT CONCENTRATION DISTRIBUTION MAP:

DIMENSIONLESS RATIOS OF SALT CONCENTRATION*0.01
MIX18.01
BUNDLE R.E. : 8822
AXIAL LEVEL (IN.) : 20.50
INJ. SUBCHANNEL : 120
FLOW SPLITS :
X1= 0.8650 X2= 1.2800 X3= 1.2800
MASSBALANCE RATIO : 0.981

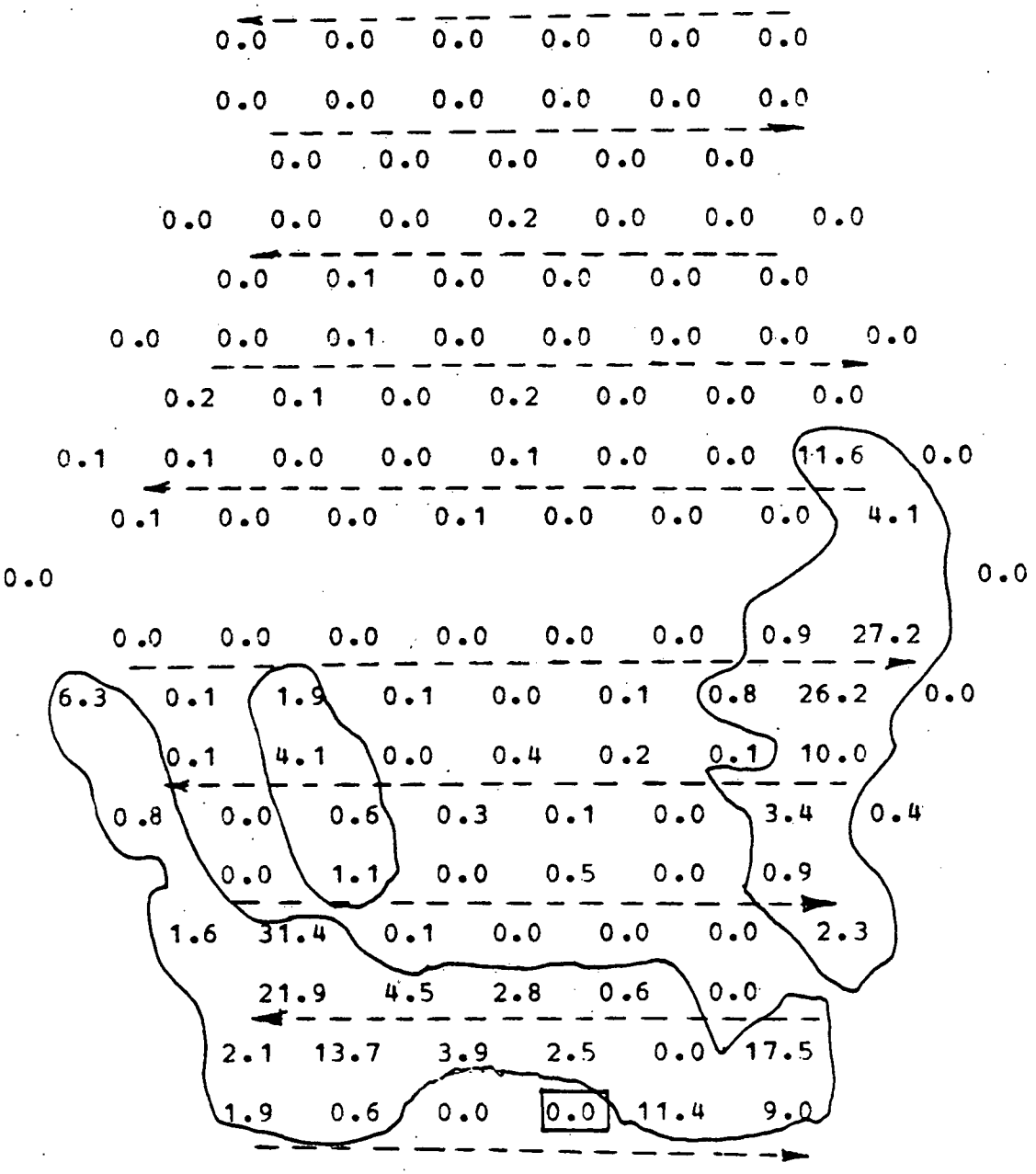

Figure A.63

SALT CONCENTRATION DISTRIBUTION MAP:

DIMENSIONLESS RATIOS OF SALT CONCENTRATION*0.01
MIX18.02
BUNDLE R.E. : 8822
AXIAL LEVEI (IN.) : 21.00
INJ. SUBCHANNEL : 120
FLOW SPLITS :
X1= 0.8650 X2= 1.2800 X3= 1.2800
MASSBALANCE RATIO : 0.991

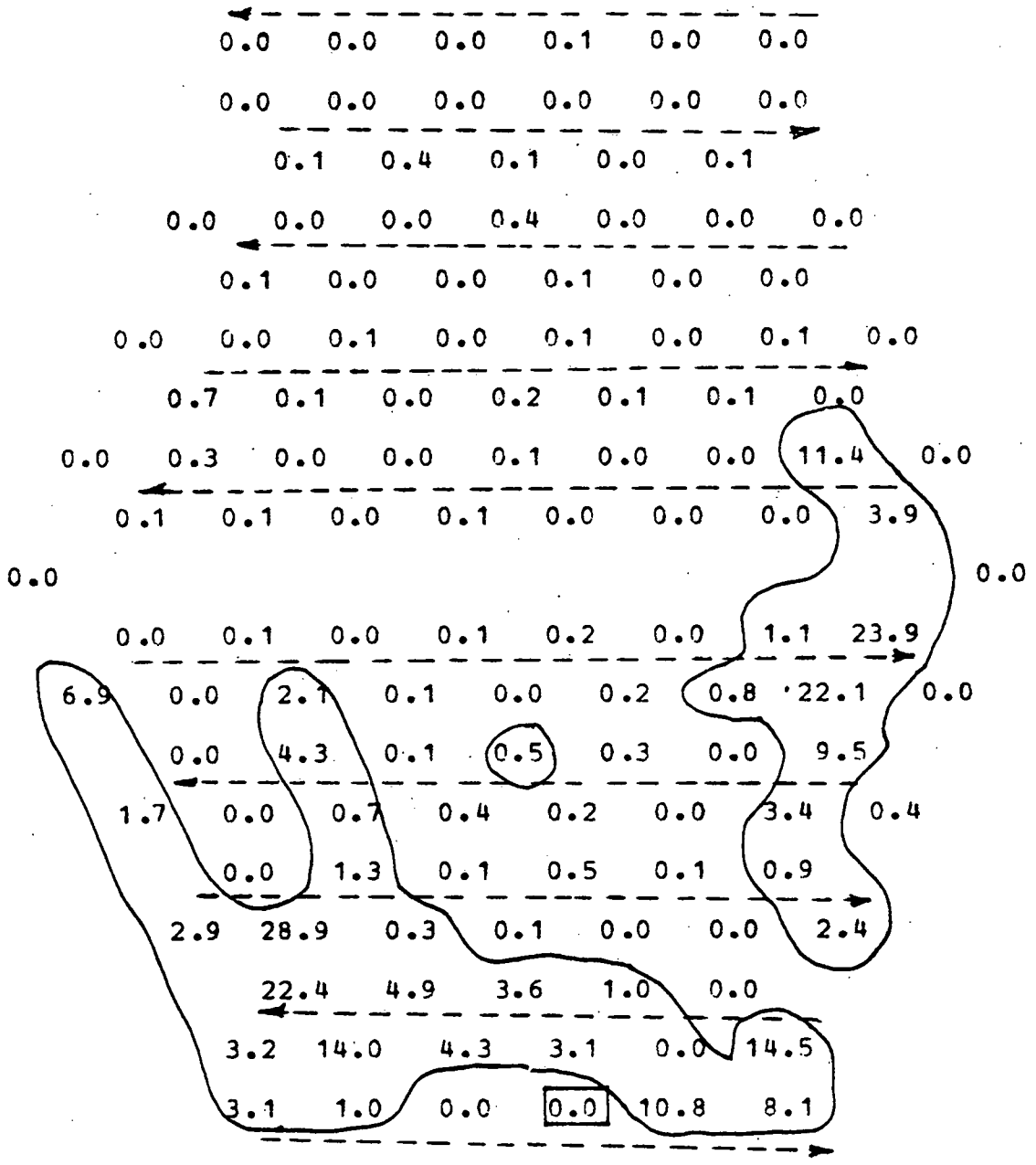

Figure A.64

SALT CONCENTRATION DISTRIBUTION MAP:

DIMENSIONLESS RATIOS OF SALT CONCENTRATION*0.01
MIX18.03
BUNDLE R.E. : 8822
AXIAL LEVEL (IN.) : 21.50
INJ. SUBCHANNEL : 120
FLOW SPLITS :
X1= 0.8650 X2= 1.2800 X3= 1.2800
MASSBALANCE RATIO : 0.976

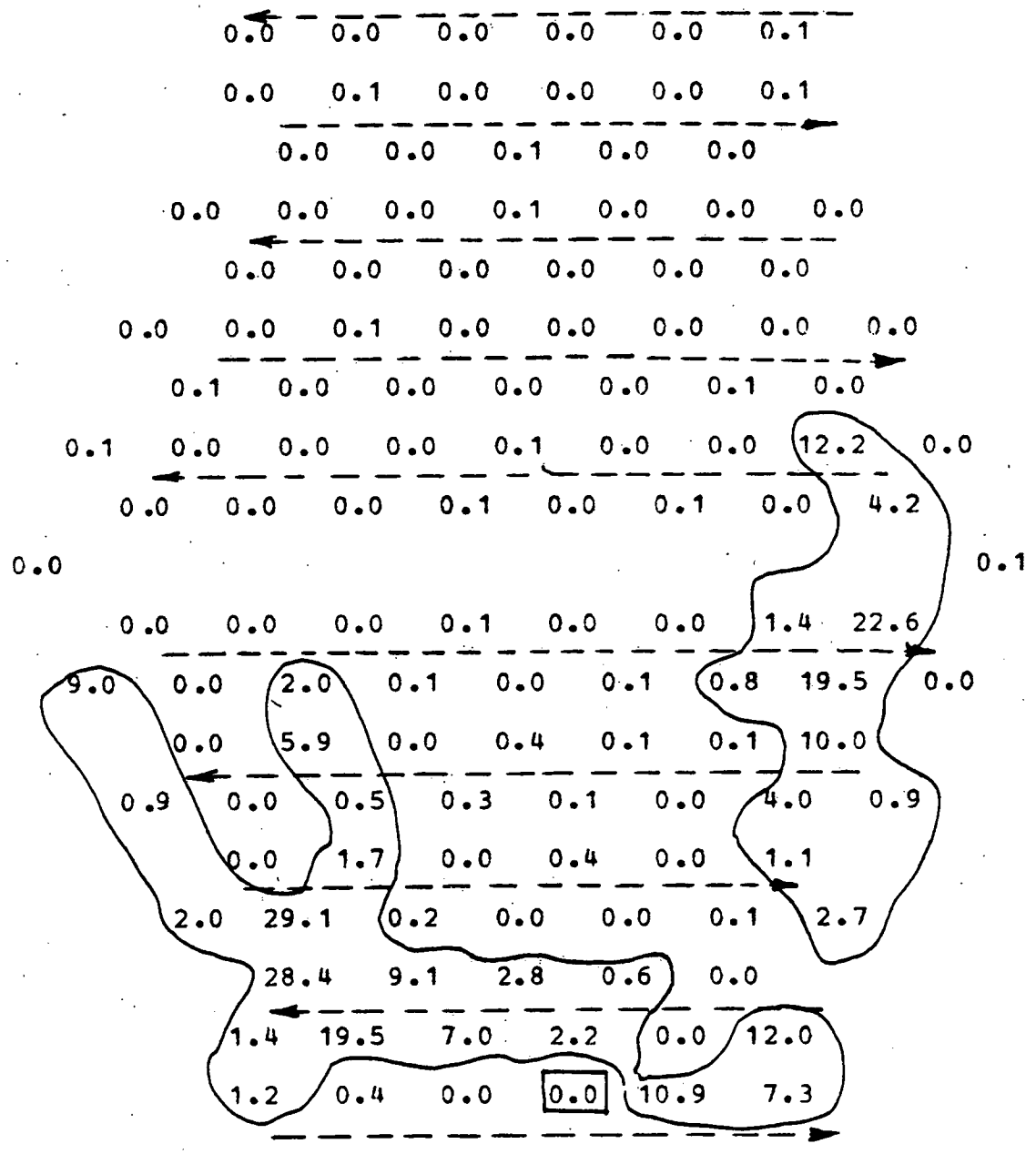

Figure A.65

SALT CONCENTRATION DISTRIBUTION MAP:

DIMENSIONLESS RATIOS OF SALT CONCENTRATION*0.01
MIX18.04
BUNDLE R.E. : 8822
AXIAL LEVEL (IN.) : 22.00
INJ. SUBCHANNEL : 120
FLOW SPLITS :
X1= 0.8650 X2= 1.2800 X3= 1.2800
MASSBALANCE RATIO : 0.972

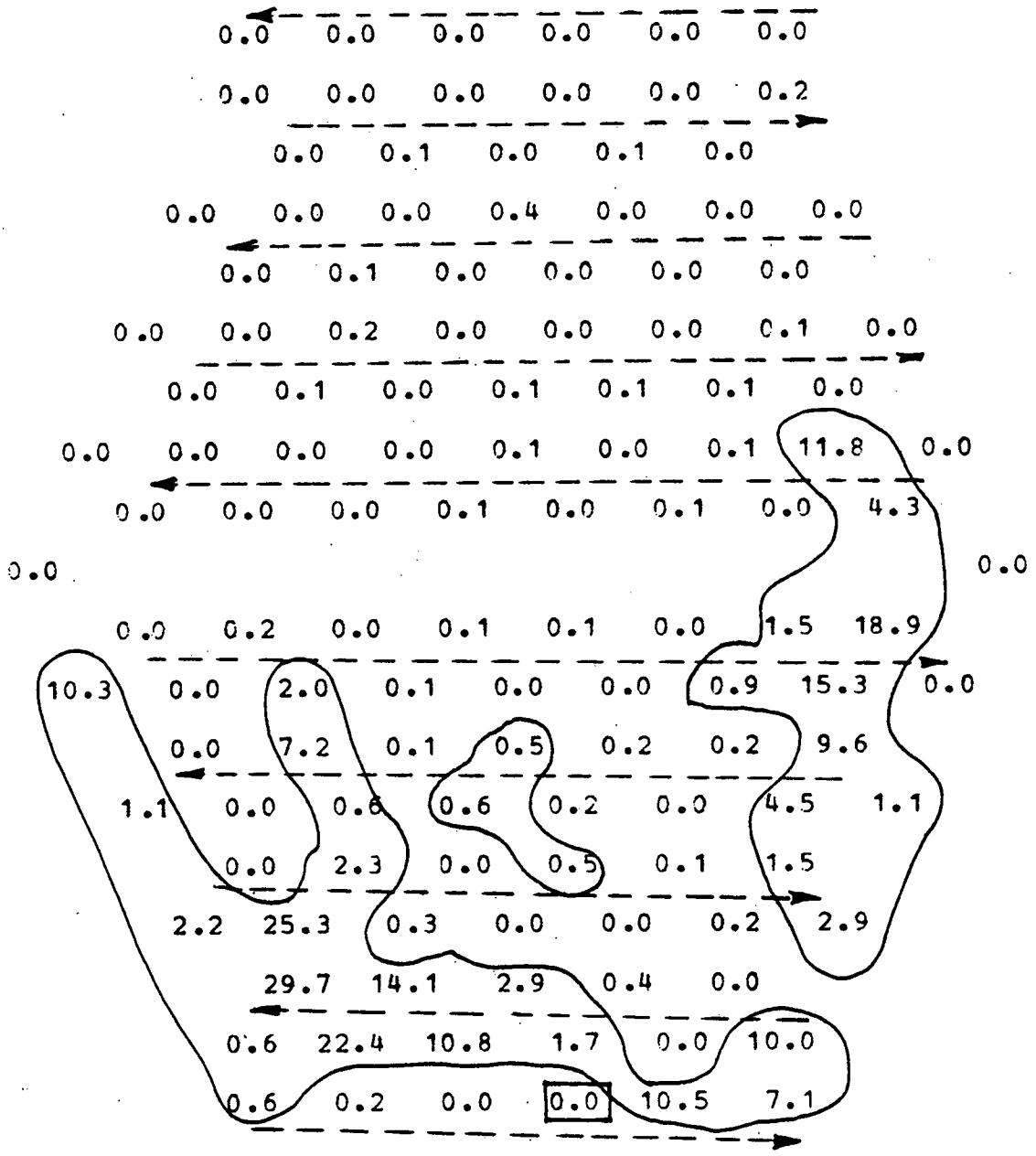

Figure A.66

SALT CONCENTRATION DISTRIBUTION MAP:

DIMENSIONLESS RATIOS OF SALT CONCENTRATION*0.01
MIX18.05
BUNDLE R.E. : 8822
AXIAL LEVEL (IN.) : 22.50
INJ. SUBCHANNEL : 120
FLOW SPLITS :
X1= 0.8650 X2= 1.2800 X3= 1.2800
MASSBALANCE RATIO : 0.974

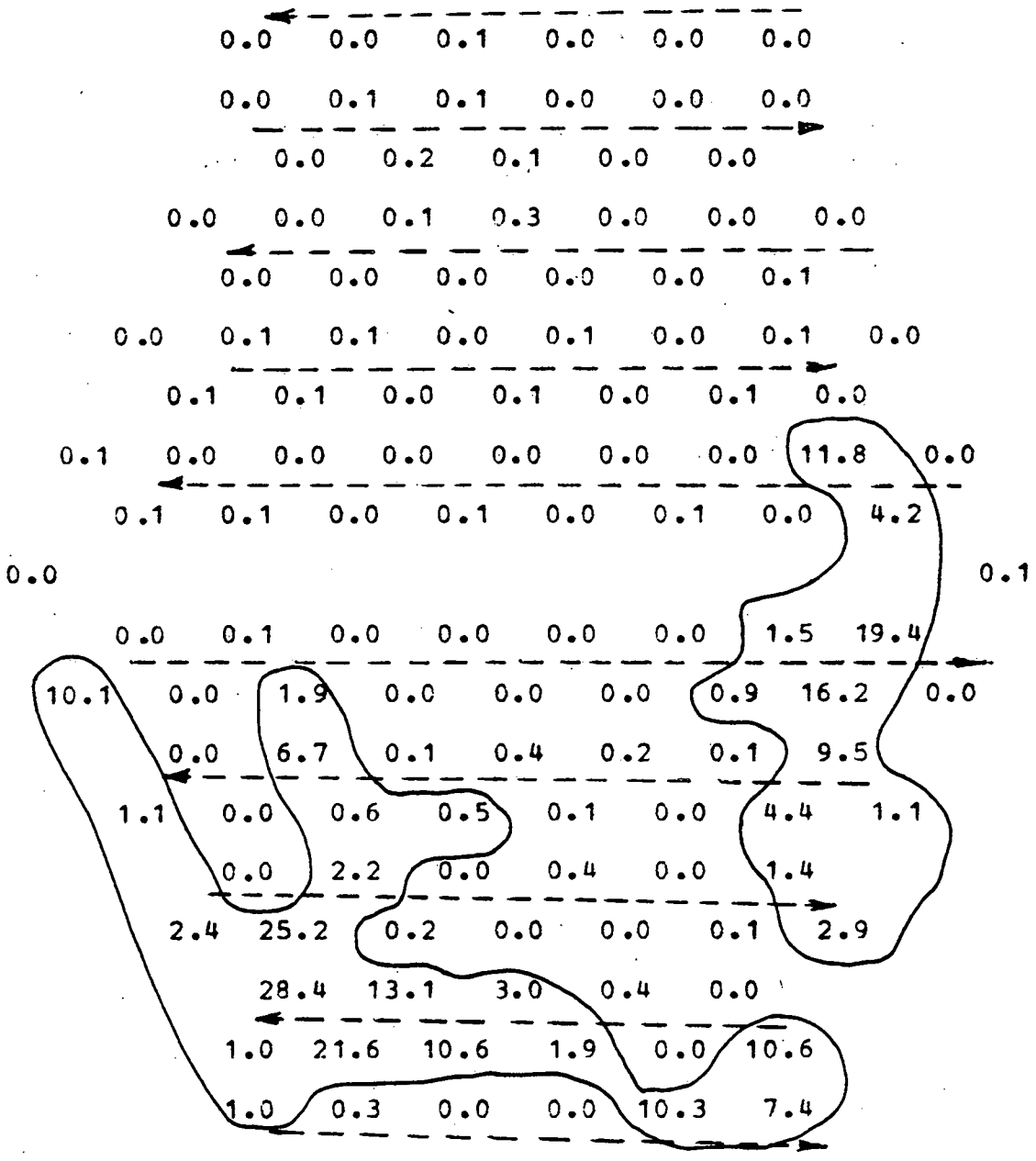

Figure A.67

SALT CONCENTRATION DISTRIBUTION MAP:

DIMENSIONLESS RATIOS OF SALT CONCENTRATION*0.01
MIX19.01
BUNDLE R.E. : 8822
AXIAL LEVEL (IN.) : 23.00
INJ. SUBCHANNEL : 120
FLOW SPLITS :
X1= 0.8650 X2= 1.2800 X3= 1.2800
MASSBALANCE RATIO : 0.984

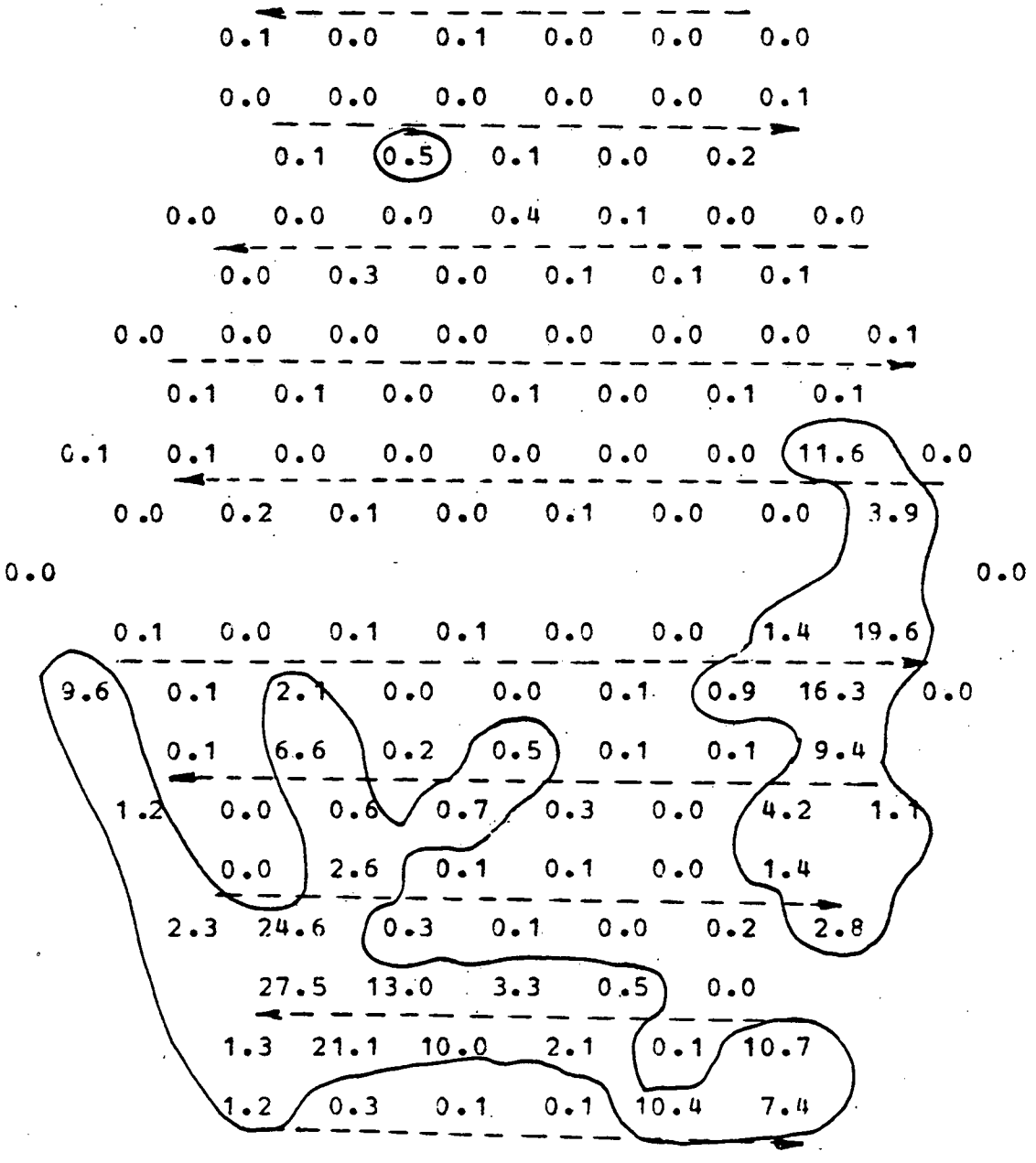

Figure A.68

SALT CONCENTRATION DISTRIBUTION MAP:

DIMENSIONLESS RATIOS OF SALT CONCENTRATION*0.01
MIX19.02
BUNDLE R.E. : 8822
AXIAL LEVEI (IN.) : 24.00
INJ. SUBCHANNEL : 120
FLOW SPLITS :
X1= 0.3650 X2= 1.2800 X3= 1.2800
MASSBALANCE RATIO : 0.986

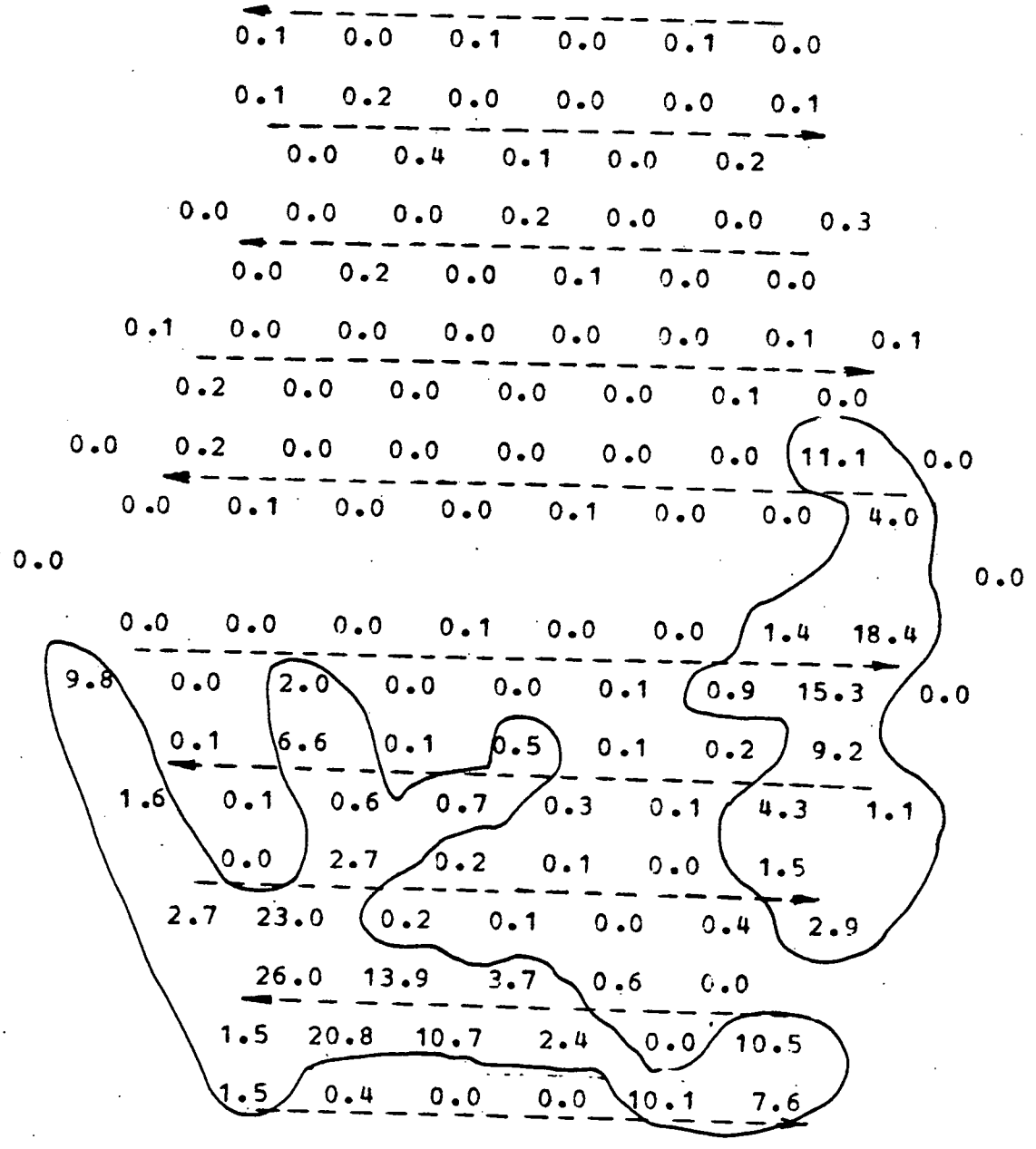

Figure A.69

SALT CONCENTRATION DISTRIBUTION MAP:

DIMENSIONLESS RATIOS OF SALT CONCENTRATION*0.01
MIX19.03
BUNDLE R.E. : 8822
AXIAL LEVEL (IN.) : 25.00
INJ. SUBCHANNEL : 120
FLOW SPLITS :
X1= 0.8650 X2= 1.2800 X3= 1.2800
MASSBALANCE RATIO : 0.973

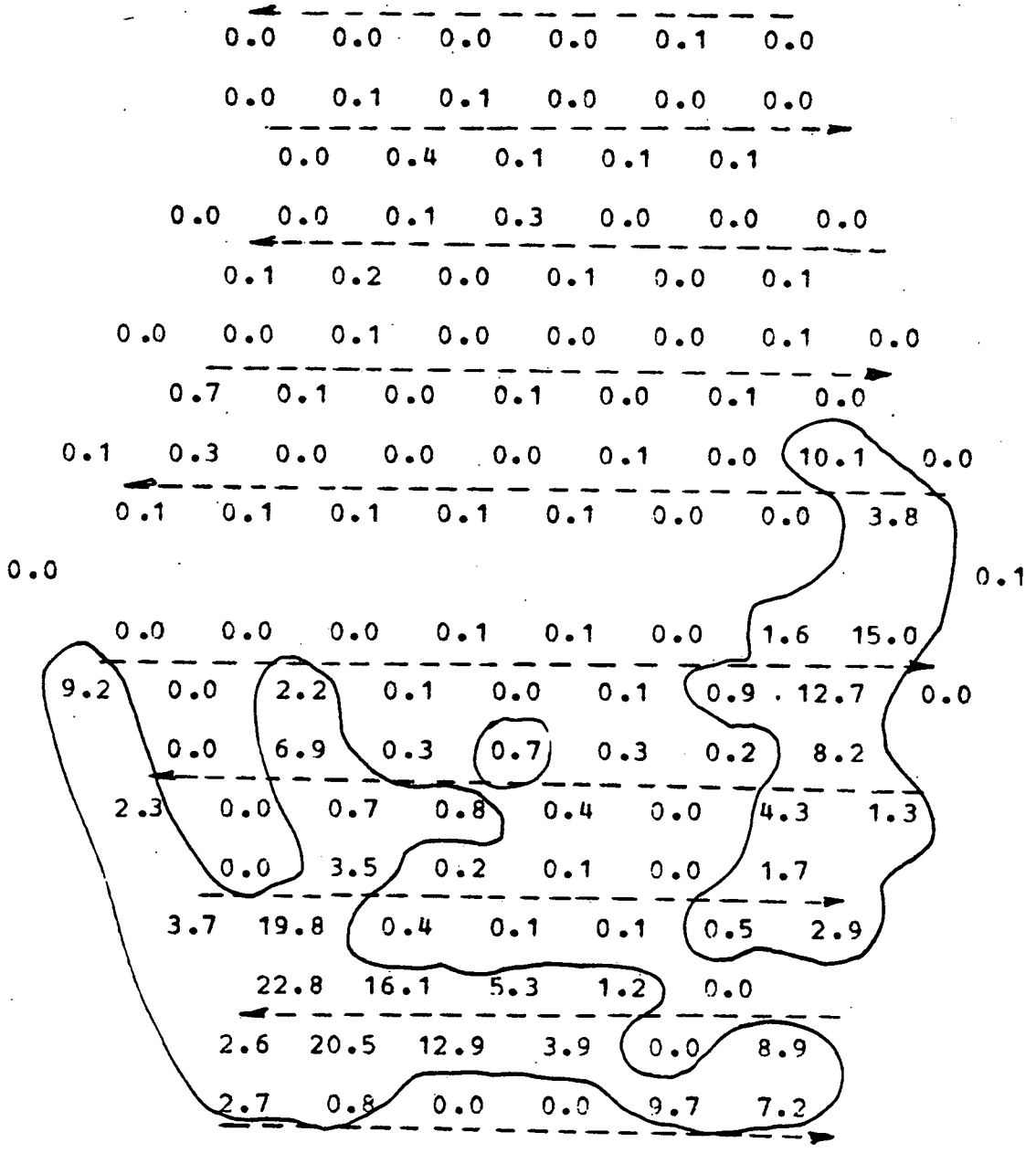

Figure A.70

SALT CONCENTRATION DISTRIBUTION MAP:

DIMENSIONLESS RATIOS OF SALT CONCENTRATION*0.01
MIX19.04
BUNDLE R.E. : 8822
AXIAL LEVEL (IN.) : 26.00
INJ. SUBCHANNEL : 120
FLOW SPLITS :
X1= 0.8650 X2= 1.2800 X3= 1.2800
MASSBALANCE RATIO : 0.978

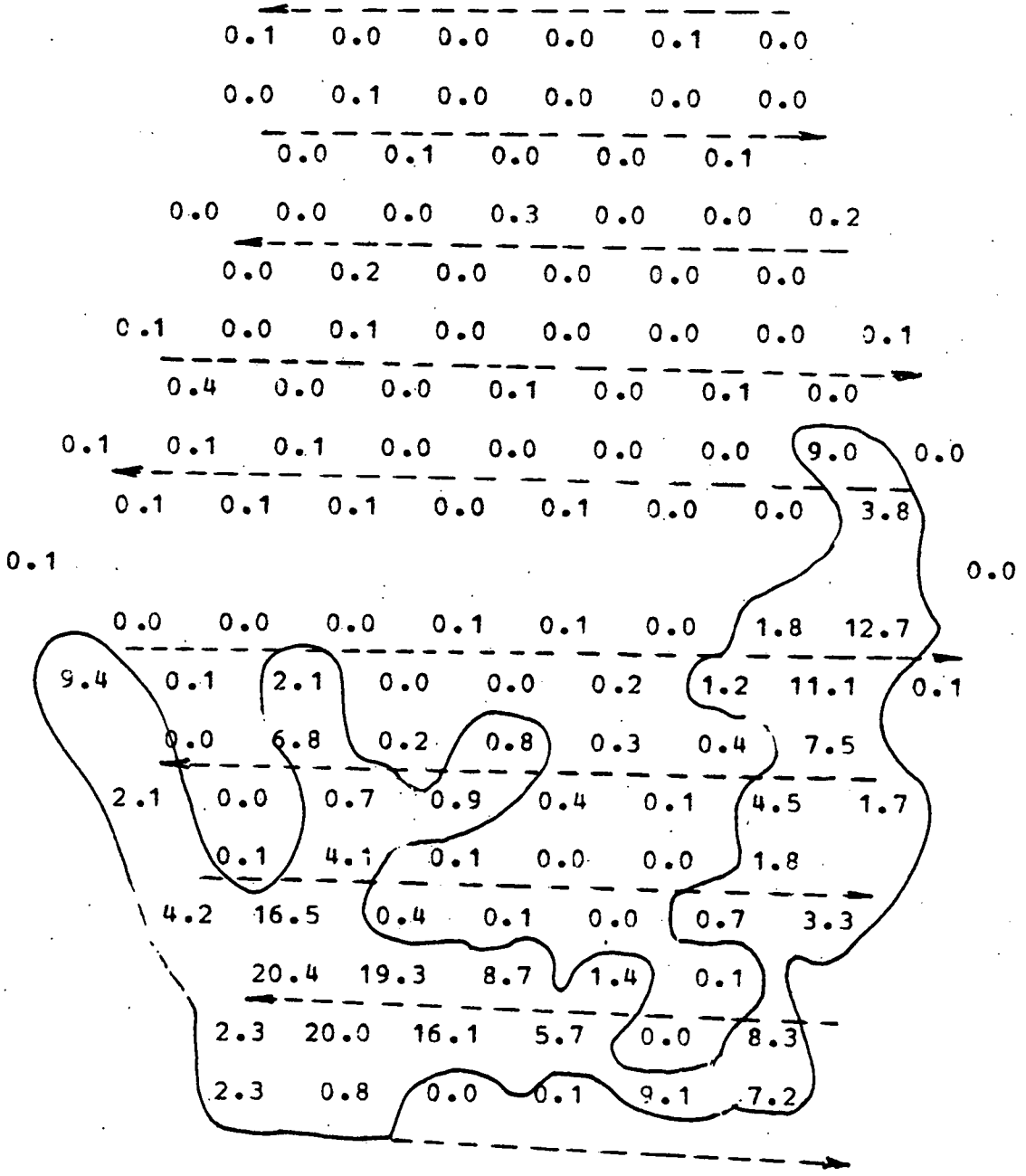

Figure A.71

SALT CONCENTRATION DISTRIBUTION MAP:

DIMENSIONLESS RATIOS OF SALT CONCENTRATION*0.01
MIX19.05
BUNDLE R.E. : 8822
AXIAL LEVEI (IN.) : 27.00
INJ. SUBCHANNEL : 120
FLOW SPLITS :
X1= 0.8650 X2= 1.2800 X3= 1.2800
MASSBALANCE RATIO : 0.986

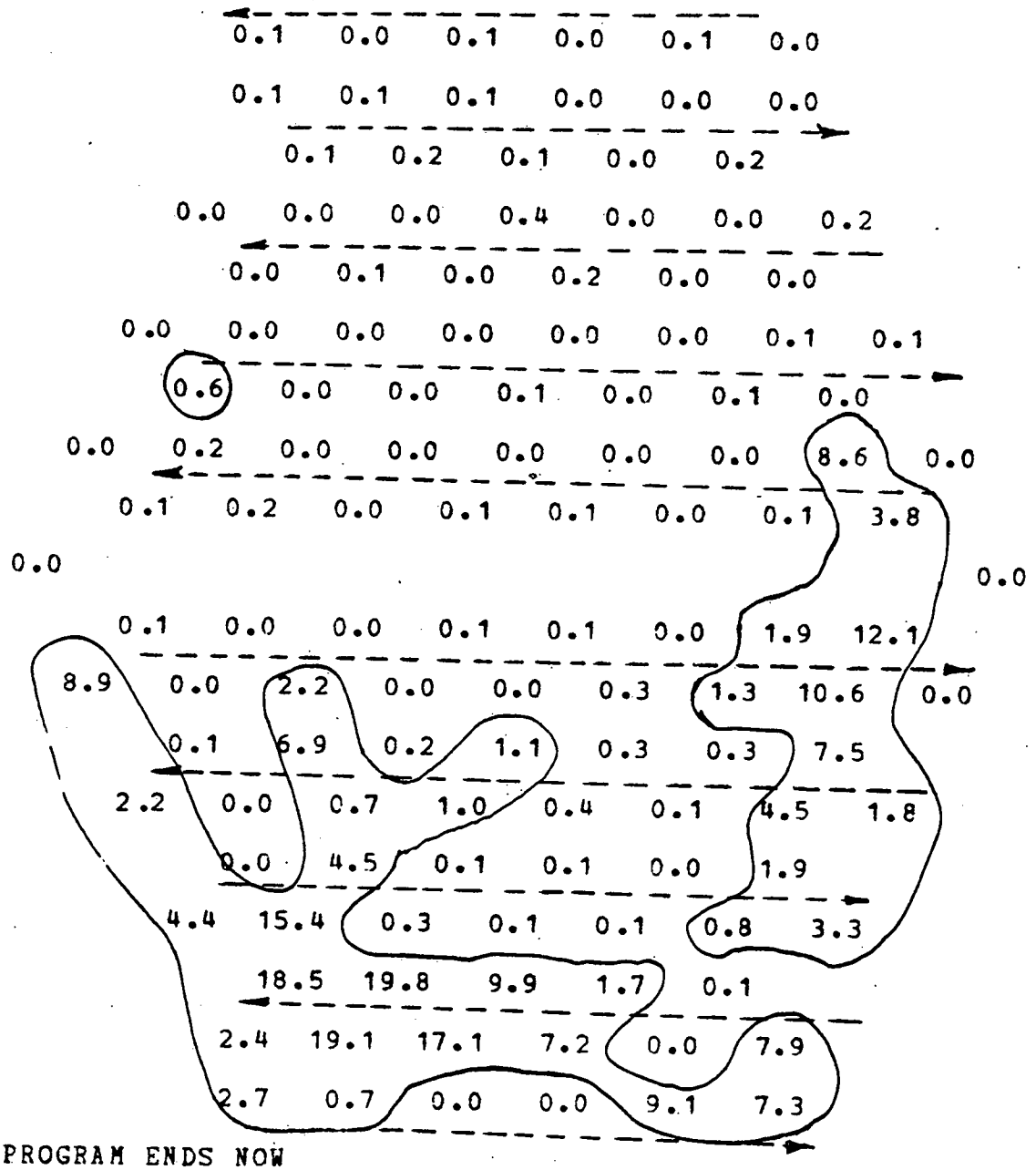

PROGRAM ENDS NOW
// END

Figure A.72

JCF VIO OPERATING SYSTEM VERSION 2 REVISION 222 6/13/76 GENERATED 12/17/7

APPENDIX B

PREDICTION OF DIMENSIONLESS SALT CONCENTRATION FOR THE IN-PHASE WIRE WRAPPED ASSEMBLY

To compare the development of the salt distribution pattern of the alternating wire wrapped assembly with that of the in-phase wire wrapped assembly, SUPERENERGY/DRV is employed. Experimentally calibrated input parameters are used in this code to predict the dimensionless salt concentration maps at the different injection depths used in the experiment for the in-phase wire wrapped assembly. Two injection subchannels are used in the prediction. One of them is the center interior subchannel and the other is an edge subchannel.

Section B.1 contains the dimensionless salt concentration maps for the center interior injection subchannel (marked as a box), and Section B.2 contains the dimensionless salt concentration maps for the edge injection subchannel (also marked as a box), at different injection depths. Two constant dimensionless salt concentration contours, i.e., 0.5 and 3.0, are plotted on all the maps to aid the understanding of the development of the salt distribution pattern versus the subchannel axial length.

APPENDIX B.1

Dimensionless Salt Concentration Maps at Different Injection Depths for a Center Interior Injection Subchannel (In-phase Wire Wrapped Assembly)

SALT CONCENTRATION DISTRIBUTION MAP CALIBRATED BY SUPERENERGY

DIMENSIONLESS RATIOS OF SALT CONCENTRATION * 0.01
AXIAL LEVEL (IN.) = 16.0
INJ. SUBCHANNEL = 5
REYNOLDS NUMBER = 9134.0

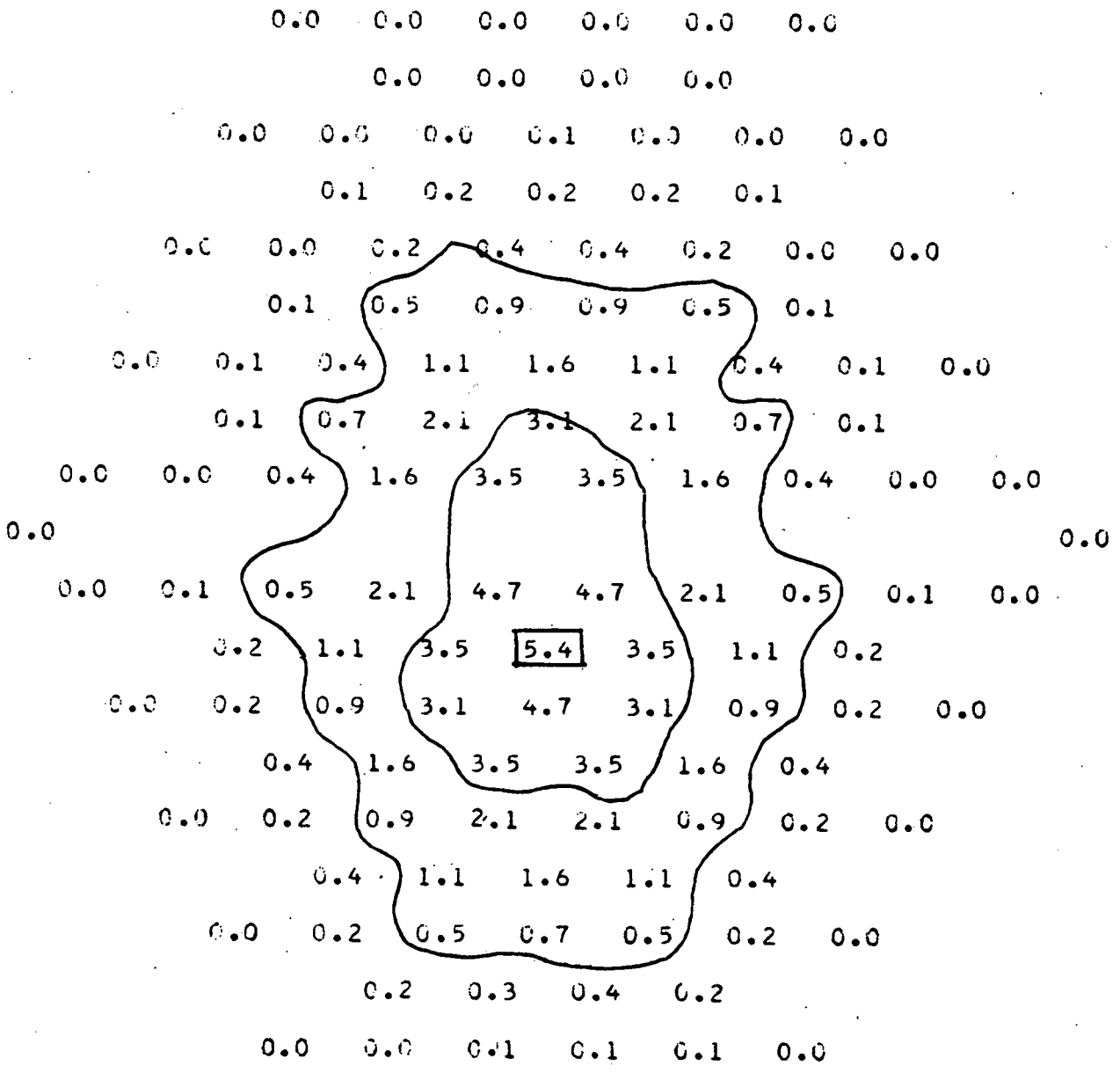

Figure B.1

SALT CONCENTRATION DISTRIBUTION MAP CALIBRATED BY SUPERENERGY

DIMENSIONLESS RATIOS OF SALT CONCENTRATION * 0.01
AXIAL LEVEL (IN.) = 16.5
INJ. SUBCHANNEL = 5
REYNOLDS NUMBER = 9134.0

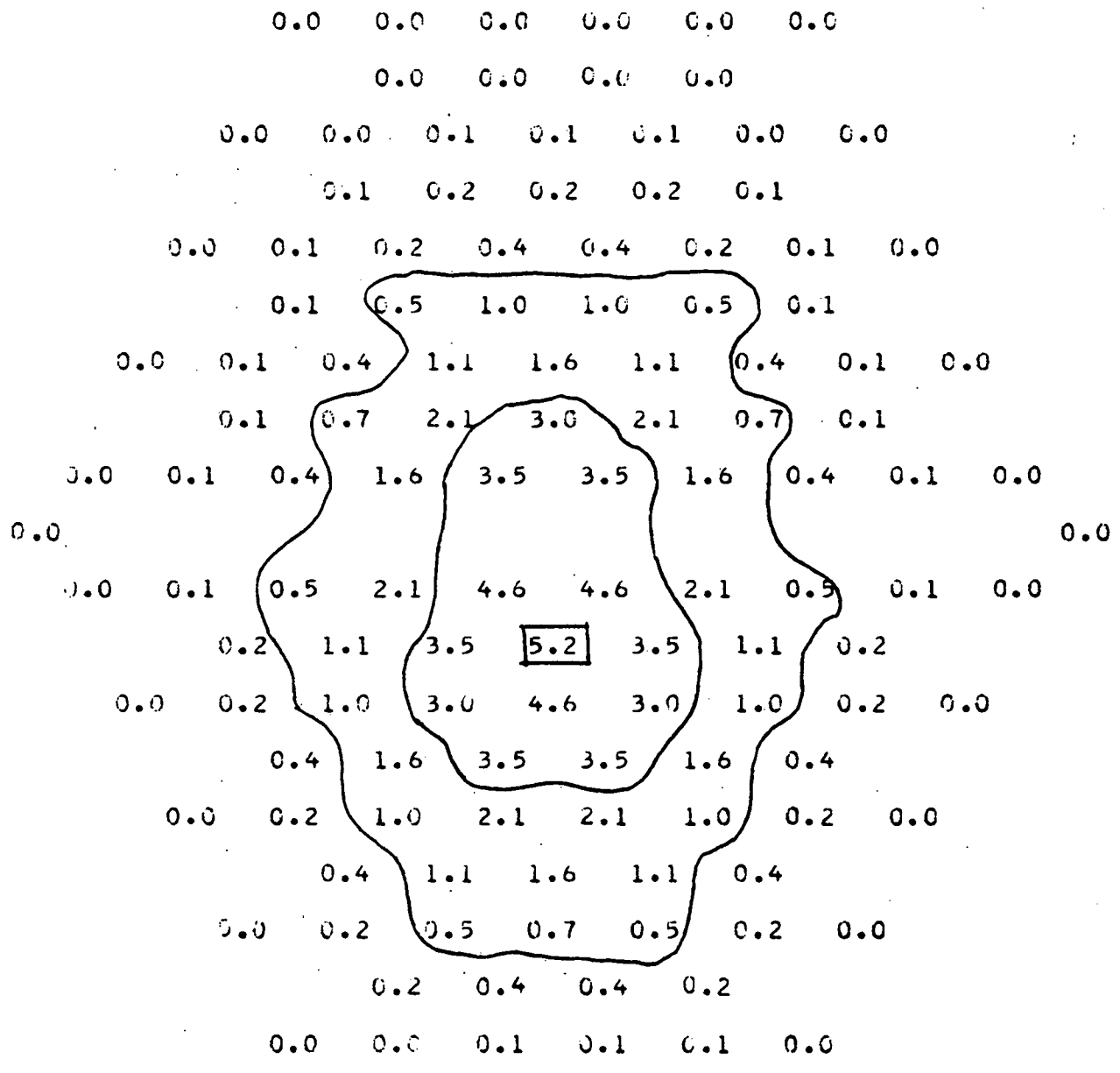

Figure B.2

SALT CONCENTRATION DISTRIBUTION MAP CALIBRATED BY SUPERENERGY

DIMENSIONLESS RATIOS OF SALT CONCENTRATION * 0.01
AXIAL LEVEL (IN.) = 17.0
INJ. SUBCHANNEL = 5
REYNOLDS NUMBER = 9134.0

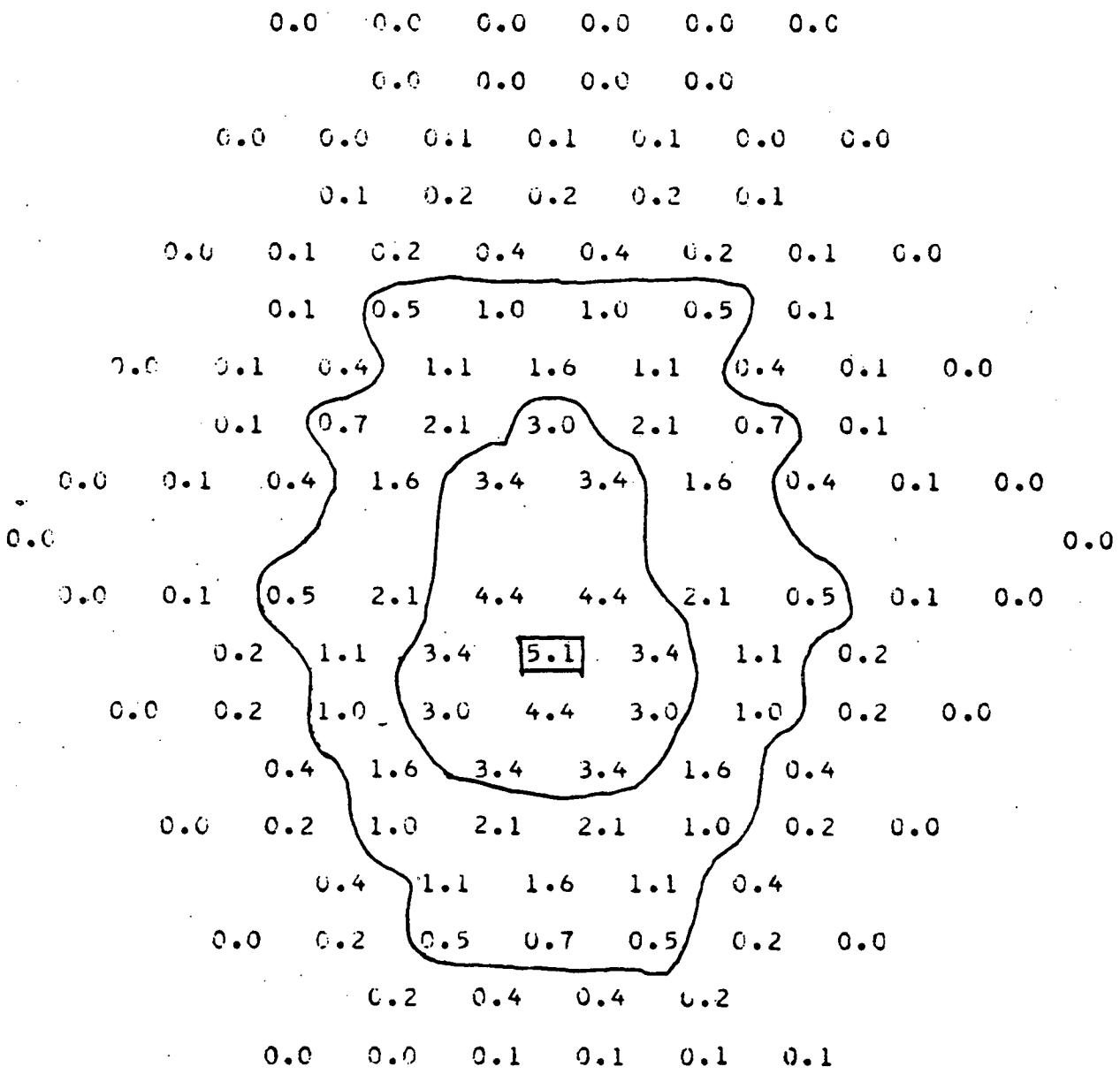

Figure B.3

SALT CONCENTRATION DISTRIBUTION MAP CALIBRATED BY SUPERENERGY

DIMENSIONLESS RATIOS OF SALT CONCENTRATION * 0.01
AXIAL LEVEL (IN.) = 17.5
INJ. SUBCHANNEL = 5
REYNOLDS NUMBER = 9134.0

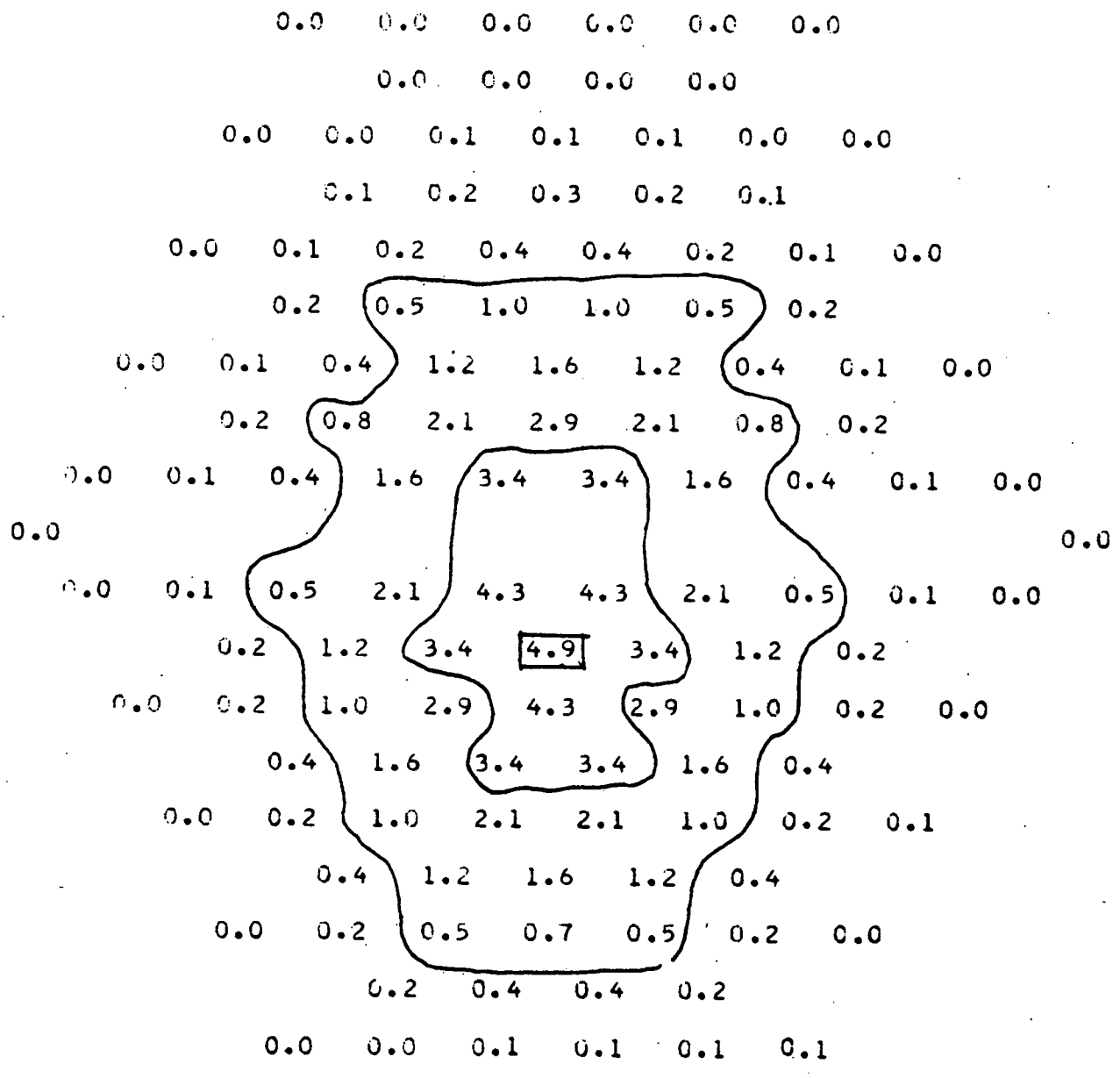

Figure B.4

SALT CONCENTRATION DISTRIBUTION MAP CALIBRATED BY SUPERENERGY

DIMENSIONLESS RATIOS OF SALT CONCENTRATION * 0.01
AXIAL LEVEL (IN.) = 18.0
INJ. SUBCHANNEL = 5
REYNOLDS NUMBER = 9134.0

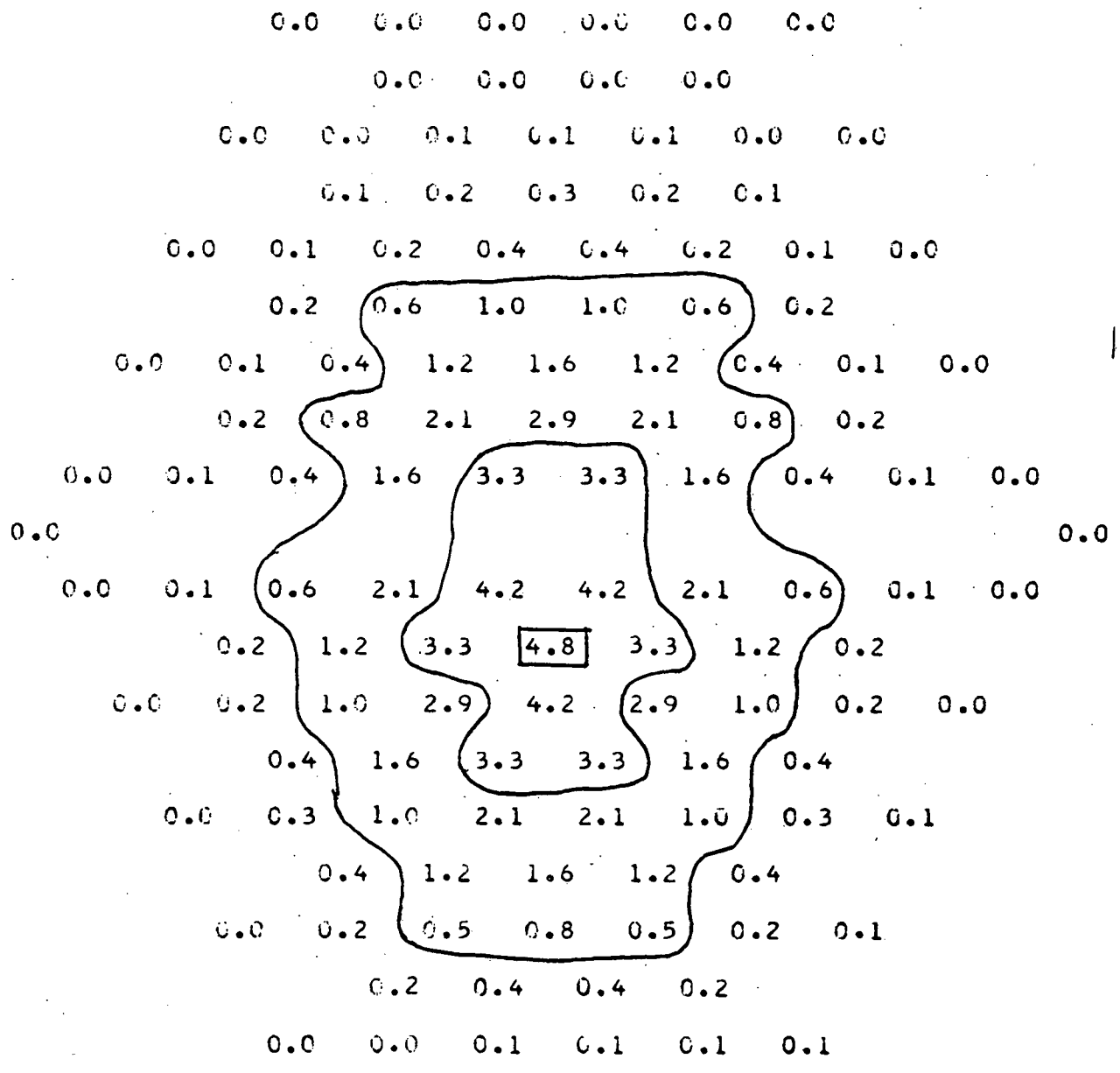

Figure B.5

SALT CONCENTRATION DISTRIBUTION MAP CALIBRATED BY SUPERENERGY

DIMENSIONLESS RATIOS OF SALT CONCENTRATION * 0.01
AXIAL LEVEL (IN.) = 19.0
INJ. SUBCHANNEL = 5
REYNOLDS NUMBER = 9134.0

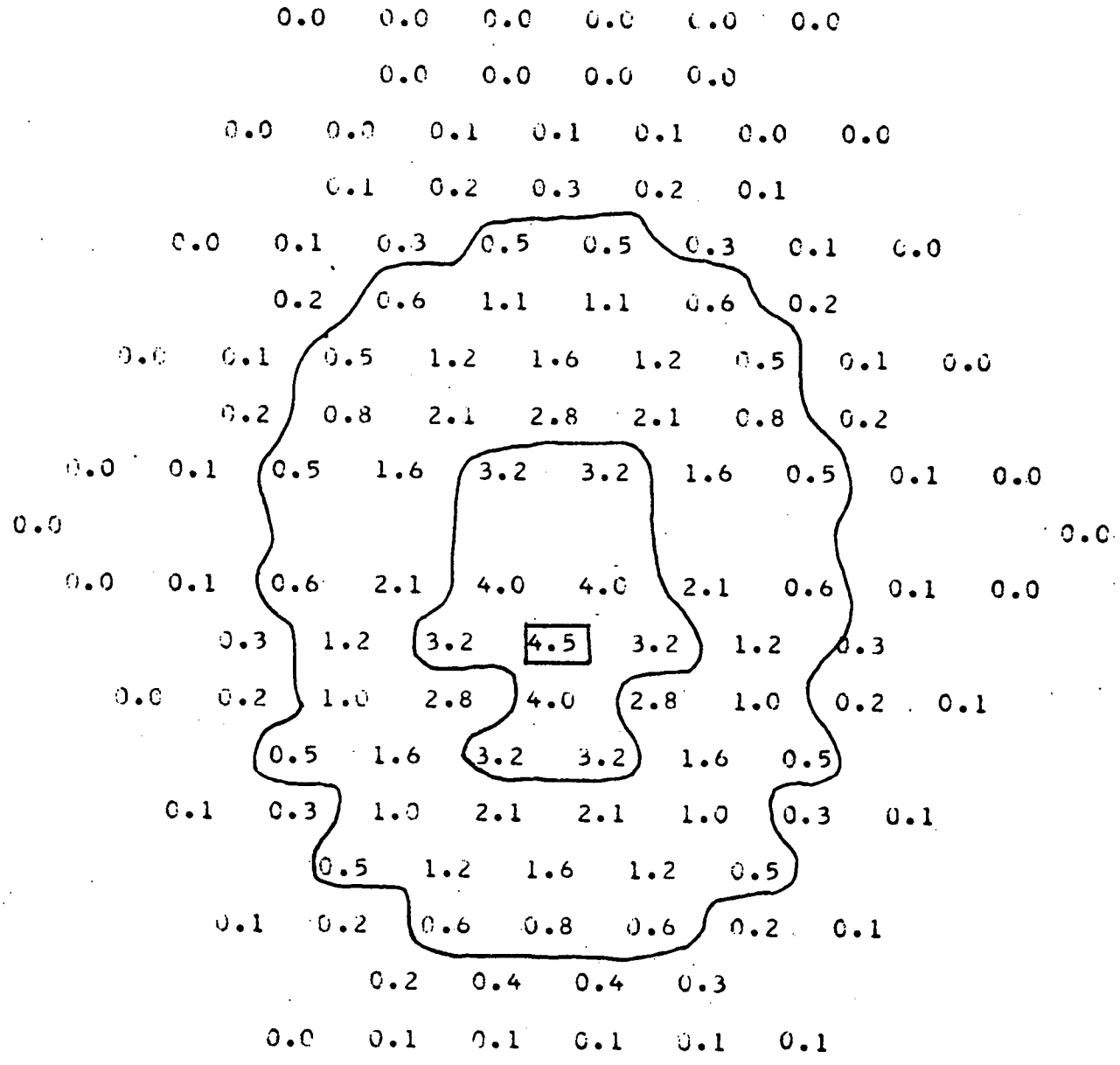

Figure B.6

SALT CONCENTRATION DISTRIBUTION MAP CALIBRATED BY SUPERENERGY

DIMENSIONLESS RATIOS OF SALT CONCENTRATION * 0.01
AXIAL LEVEL (IN.) = 19.5
INJ. SUBCHANNEL = 5
REYNOLDS NUMBER = 9134.0

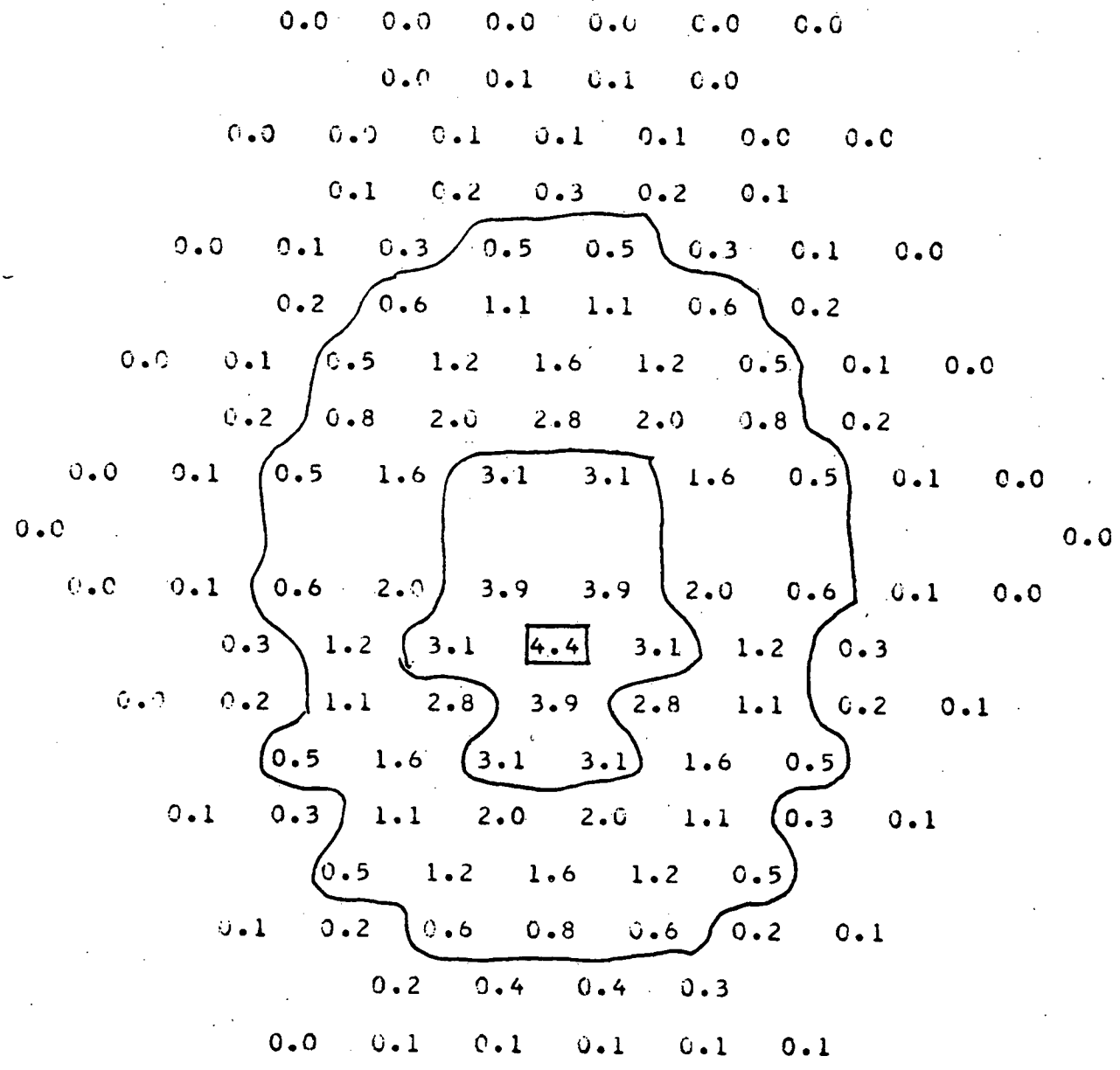

Figure B,7

SALT CONCENTRATION DISTRIBUTION MAP CALIBRATED BY SUPERENERGY

DIMENSIONLESS RATIOS OF SALT CONCENTRATION * 0.01
AXIAL LEVEL (IN.) = 20.0
INJ. SUBCHANNEL = 5
REYNOLDS NUMBER = 9134.0

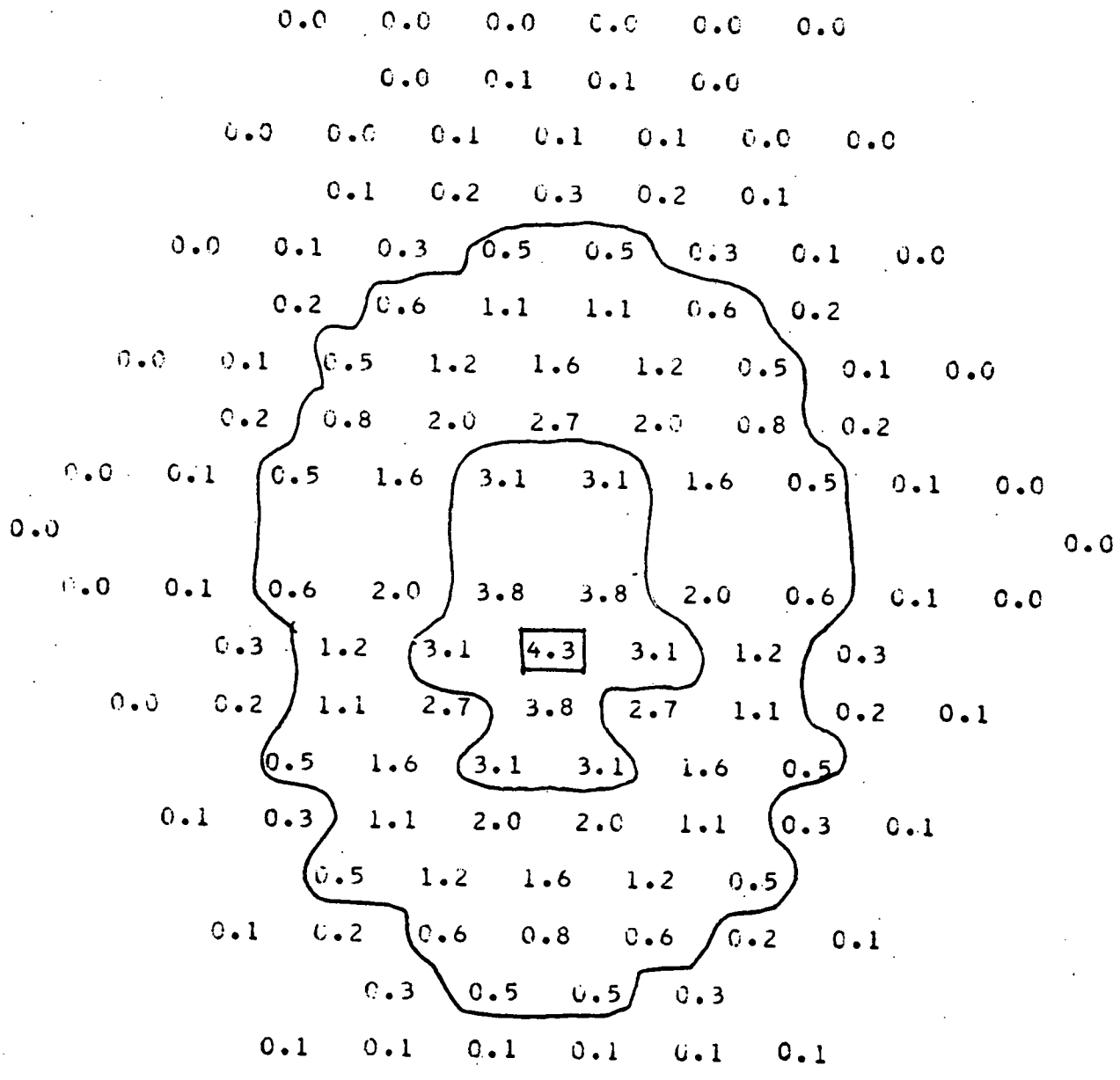

Figure B.8

SALT CONCENTRATION DISTRIBUTION MAP CALIBRATED BY SUPERENERGY

DIMENSIONLESS RATIOS OF SALT CONCENTRATION * 0.01
AXIAL LEVEL (IN.) = 20.5
INJ. SUBCHANNEL = 5
REYNOLDS NUMBER = 9134.0

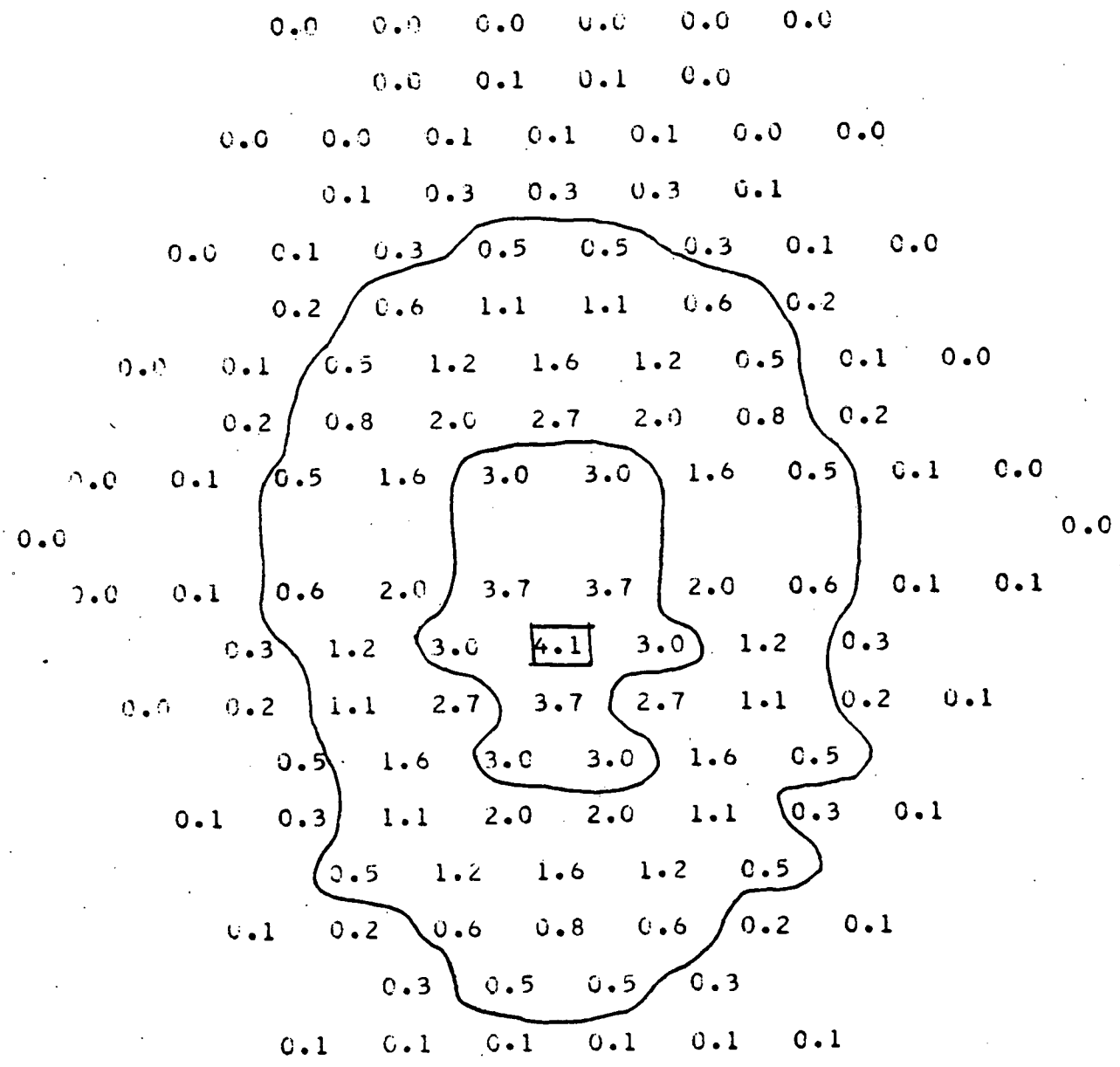

Figure B.9

SALT CONCENTRATION DISTRIBUTION MAP CALIBRATED BY SUPERENERGY

DIMENSIONLESS RATIOS OF SALT CONCENTRATION * 0.01
AXIAL LEVEL (IN.) = 21.0
INJ. SUBCHANNEL = 5
REYNOLDS NUMBER = 9134.0

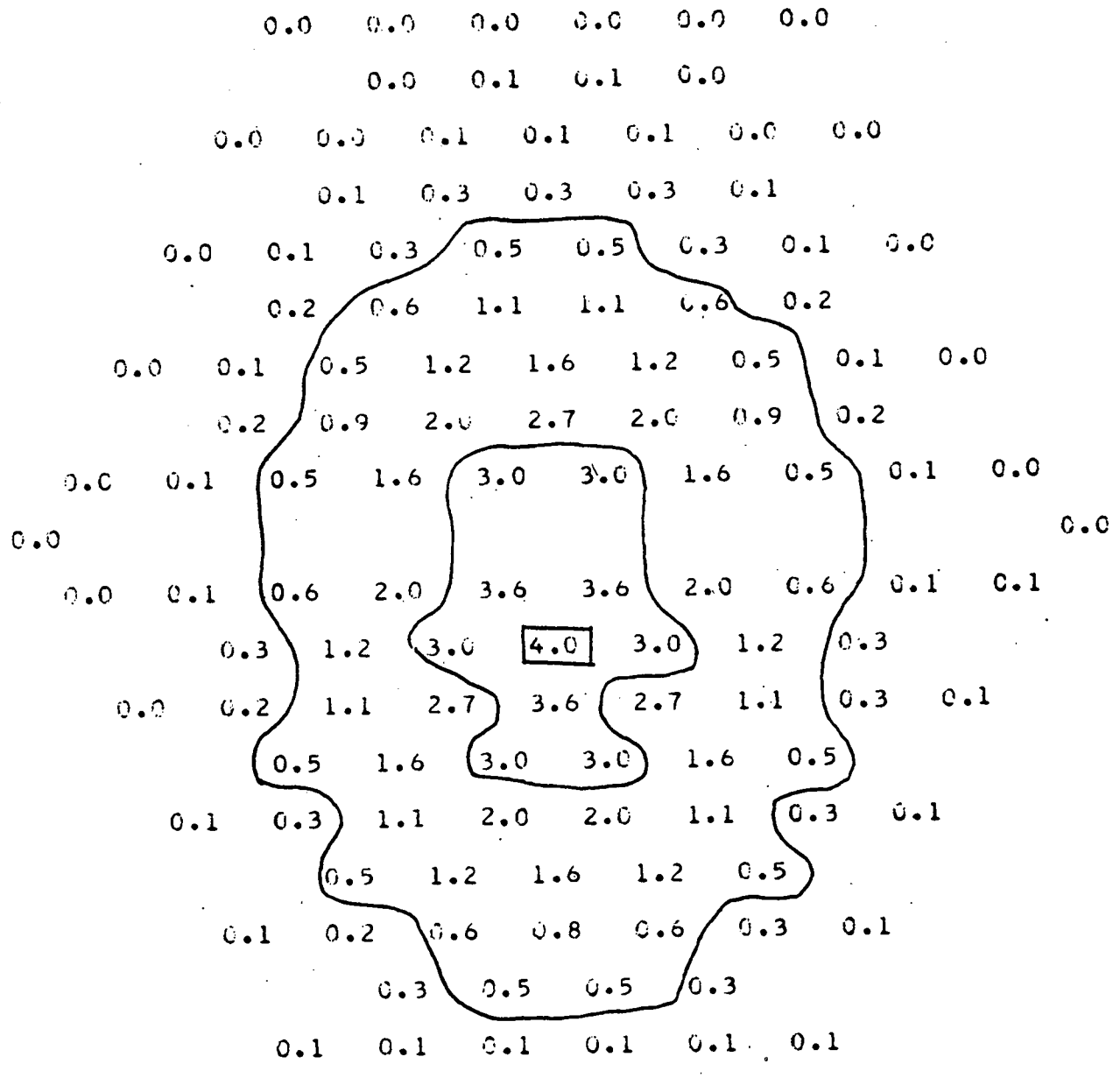

Figure B.10

SALT CONCENTRATION DISTRIBUTION MAP CALIBRATED BY SUPERENERGY

DIMENSIONLESS RATIOS OF SALT CONCENTRATION * 0.01
AXIAL LEVEL (IN.) = 22.0
INJ. SUBCHANNEL = 5
REYNOLDS NUMBER = 9134.0

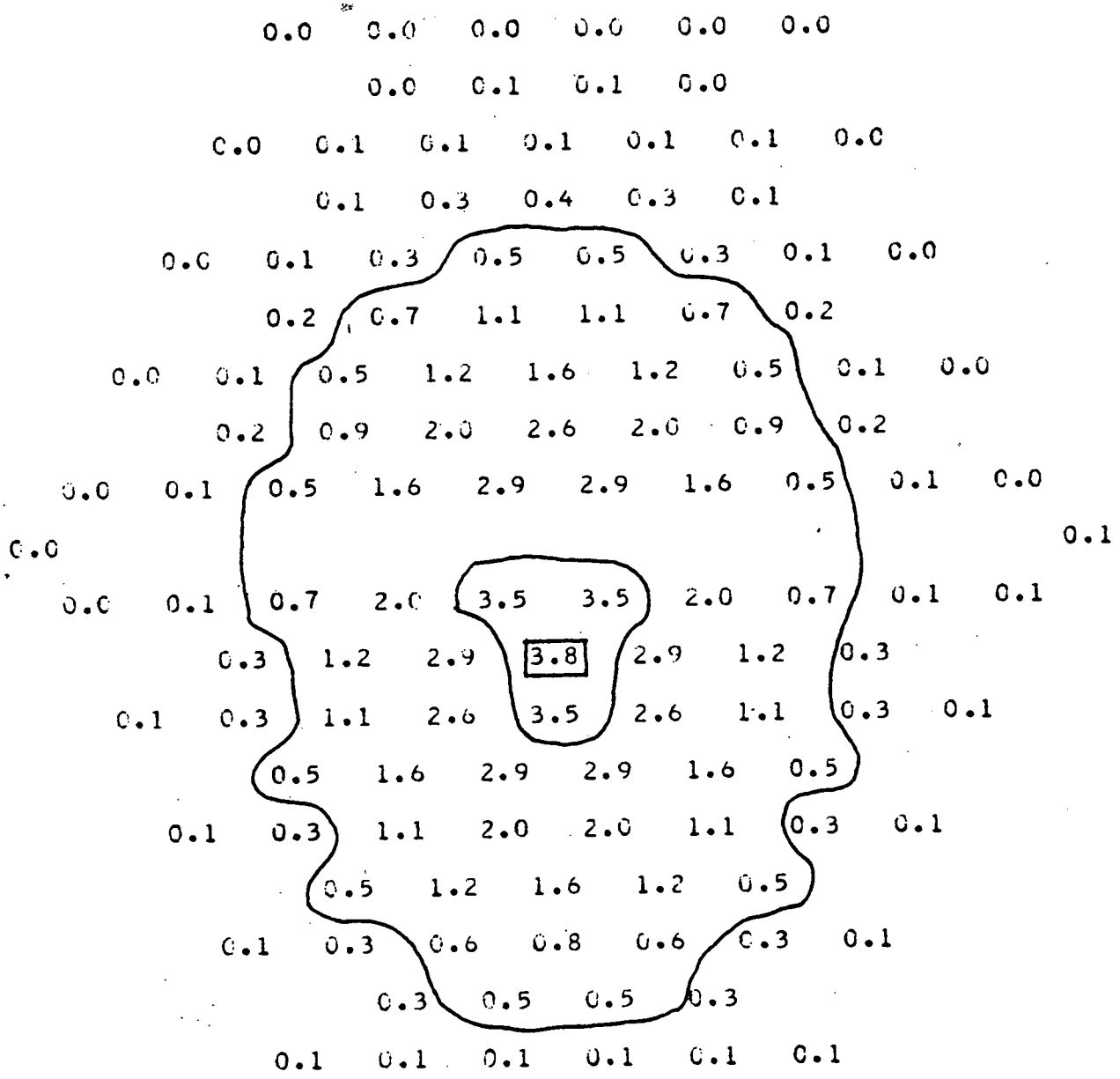

Figure B.11

SALT CONCENTRATION DISTRIBUTION MAP CALIBRATED BY SUPERENERGY

DIMENSIONLESS RATIOS OF SALT CONCENTRATION * 0.01
AXIAL LEVEL (IN.) = 22.5
INJ. SUBCHANNEL = 5
REYNOLDS NUMBER = 9134.0

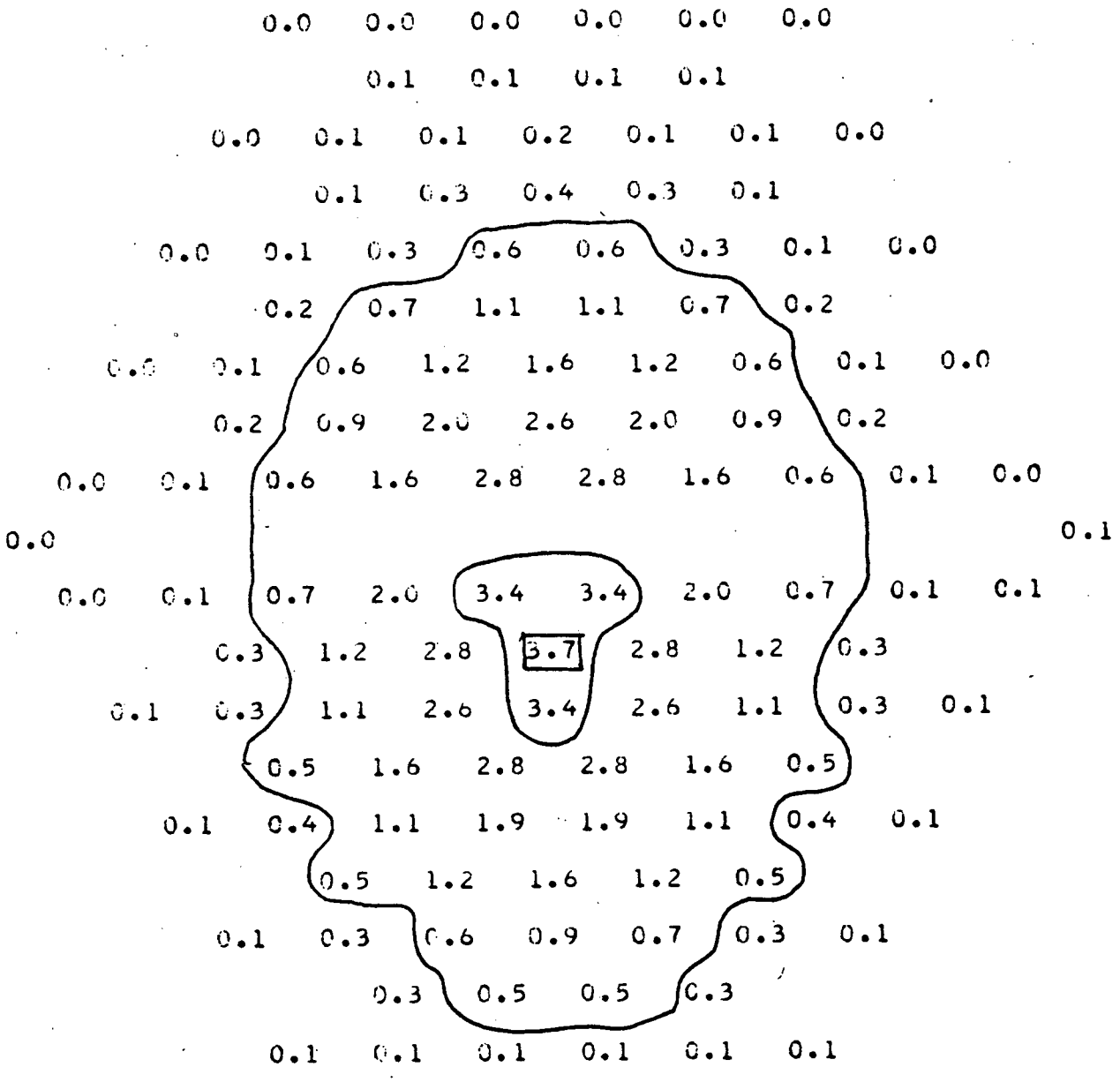

Figure B.12

SALT CONCENTRATION DISTRIBUTION MAP CALIBRATED BY SUPERENERGY

DIMENSIONLESS RATIOS OF SALT CONCENTRATION * 0.01
AXIAL LEVEL (IN.) = 23.0
INJ. SUBCHANNEL = 5
REYNOLDS NUMBER = 9134.0

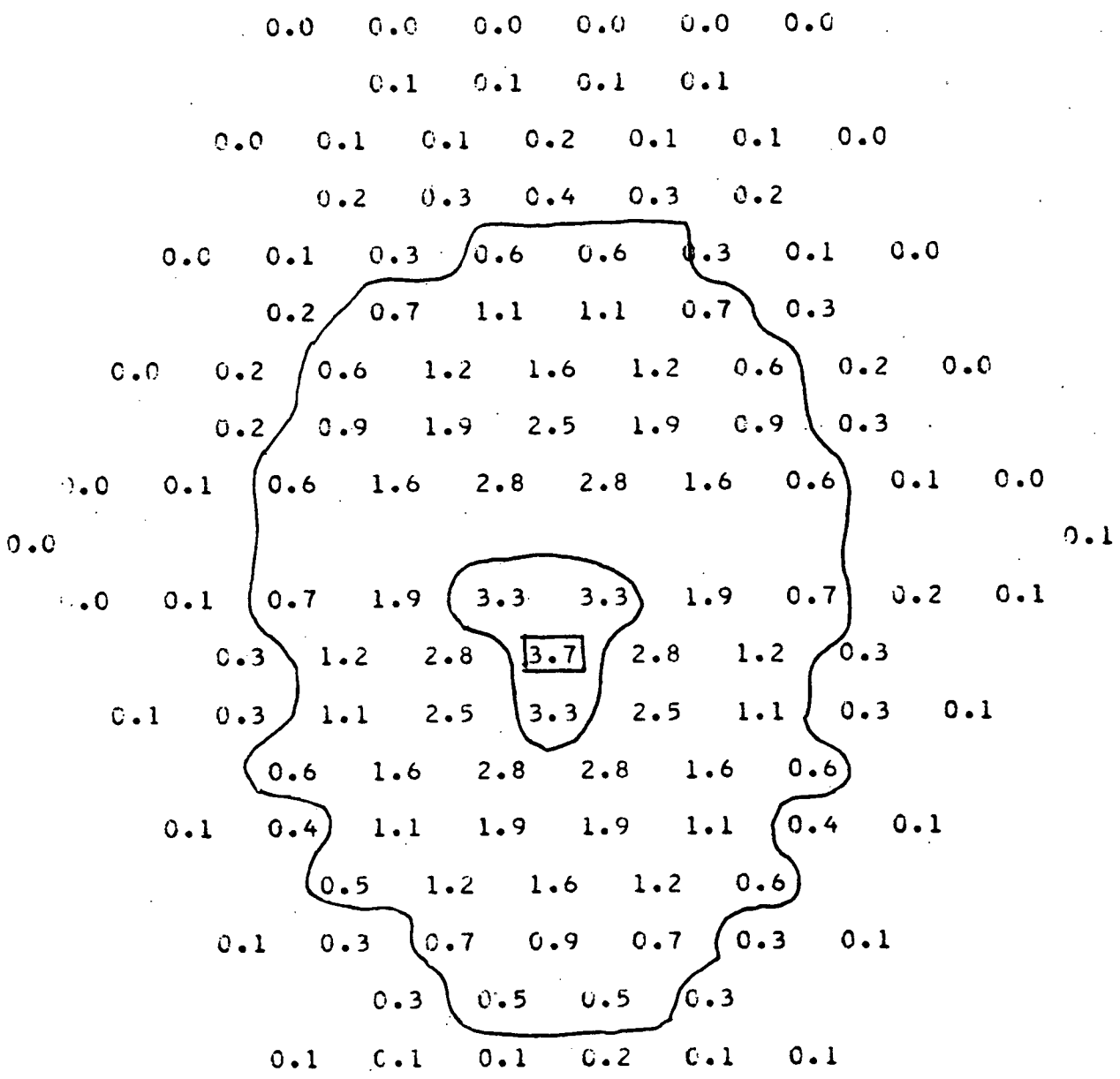

Figure B.13

SALT CONCENTRATION DISTRIBUTION MAP CALIBRATED BY SUPERENERGY

DIMENSIONLESS RATIOS OF SALT CONCENTRATION * 0.01
AXIAL LEVEL (IN.) = 23.5
INJ. SUBCHANNEL = 5
REYNOLDS NUMBER = 9134.0

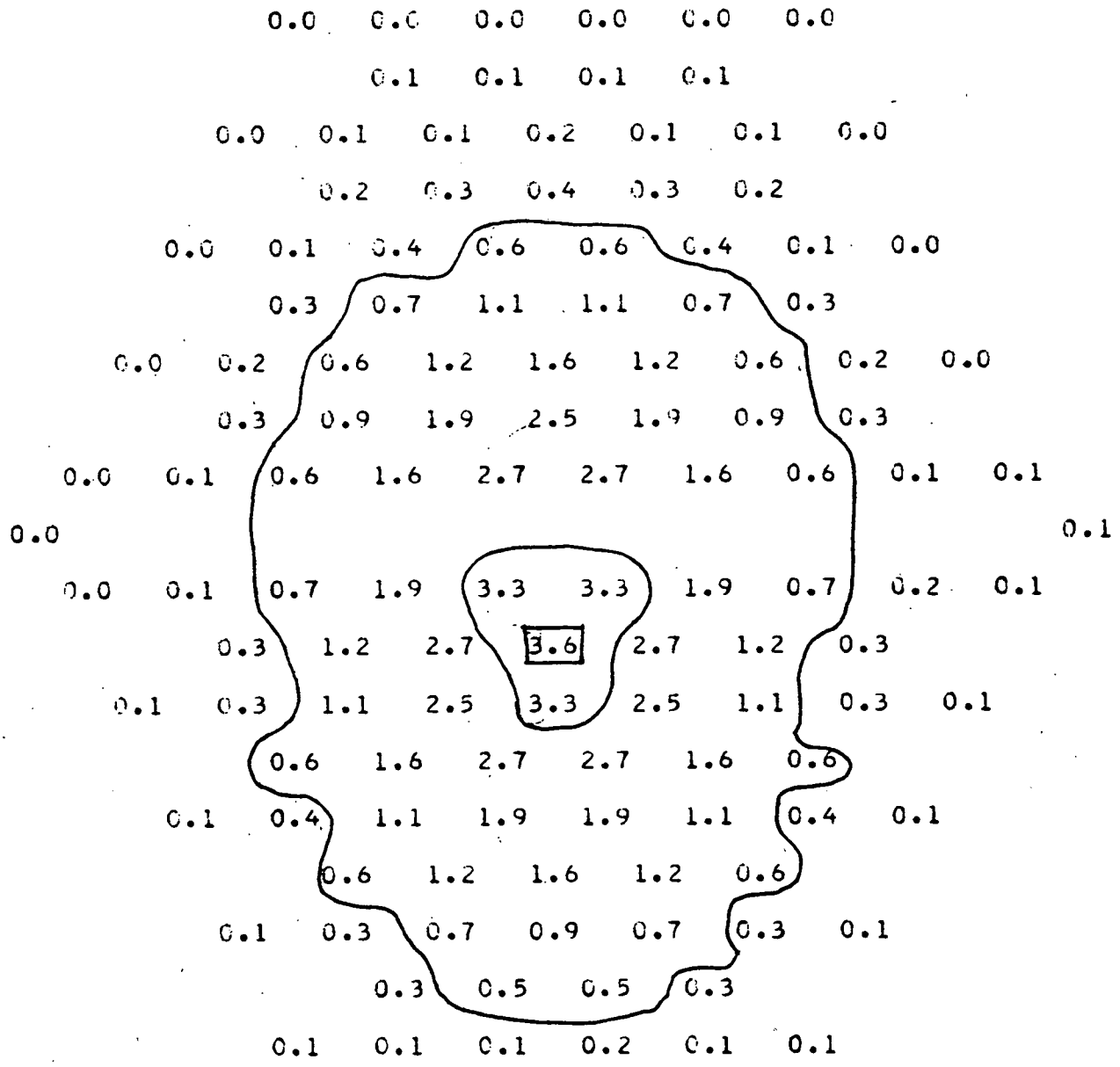

Figure B.14

SALT CONCENTRATION DISTRIBUTION MAP CALIBRATED BY SUPERENERGY

DIMENSIONLESS RATIOS OF SALT CONCENTRATION * 0.01
AXIAL LEVEL (IN.) = 24.5
INJ. SUBCHANNEL = 5
REYNOLDS NUMBER = 9134.0

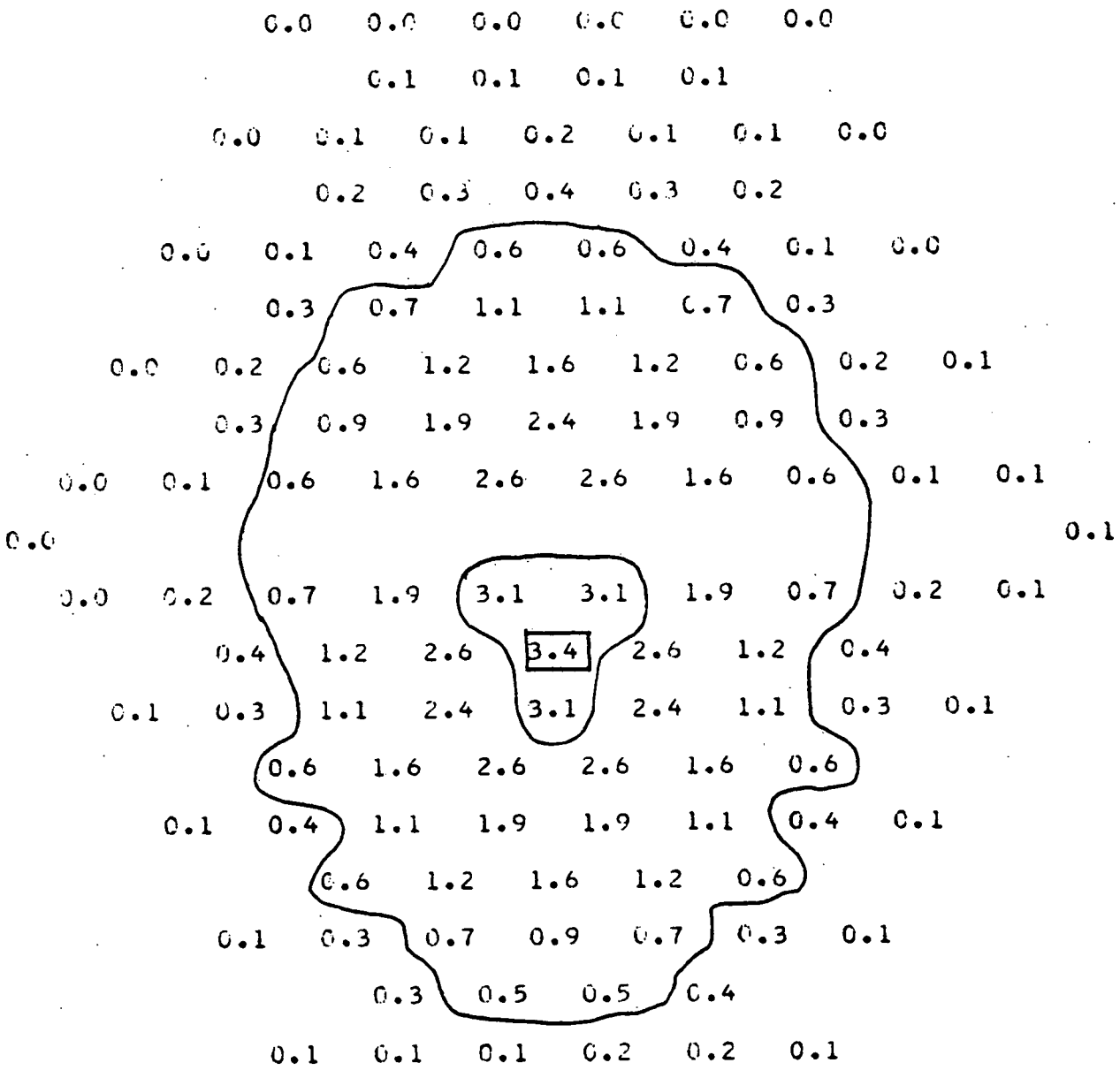

Figure B.15

SALT CONCENTRATION DISTRIBUTION MAP CALIBRATED BY SUPERENERGY

DIMENSIONLESS RATIOS OF SALT CONCENTRATION * 0.01
AXIAL LEVEL (IN.) = 25.5
INJ. SUBCHANNEL = 5
REYNOLDS NUMBER = 9134.0

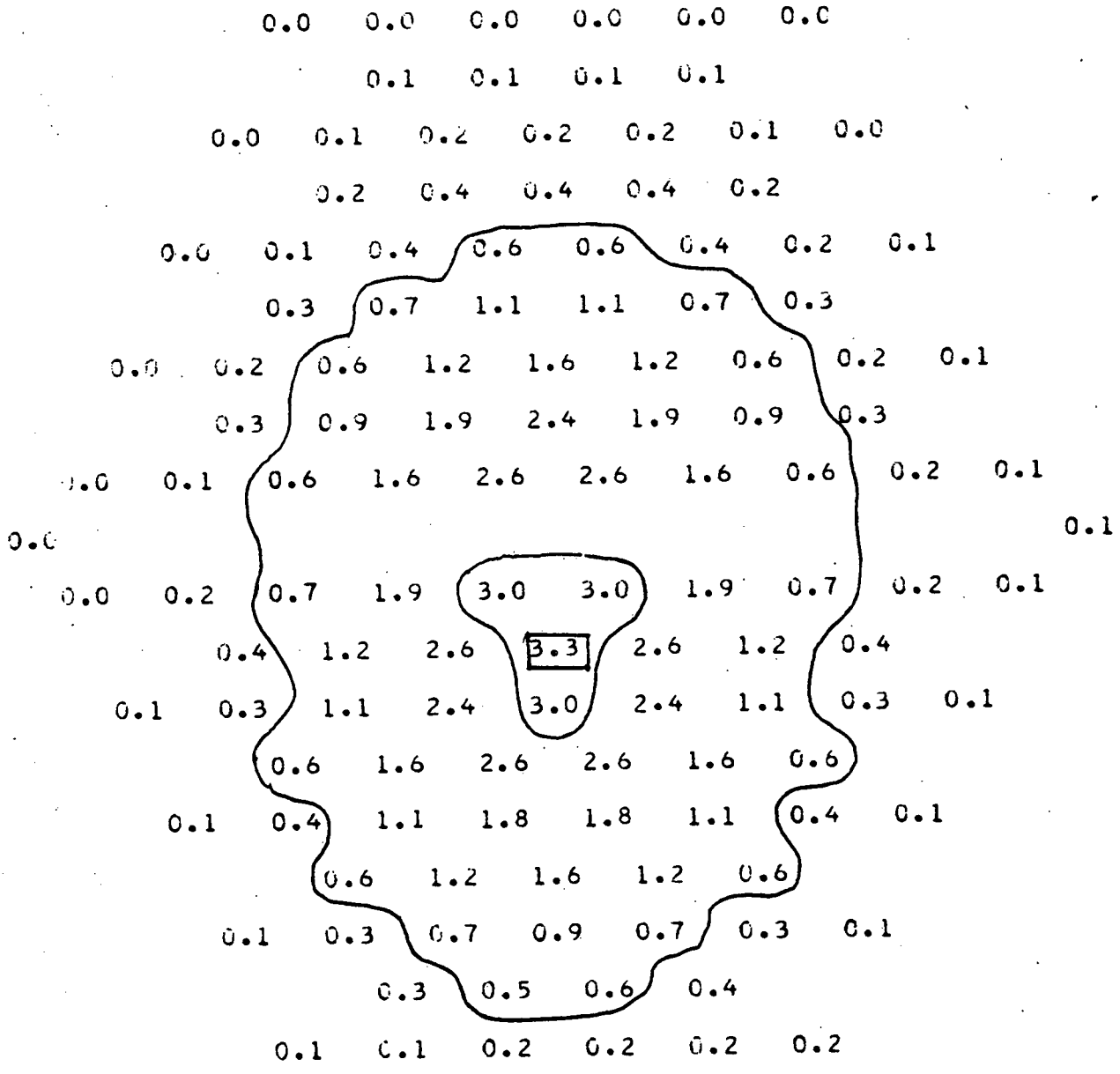

Figure B.16

SALT CONCENTRATION DISTRIBUTION MAP CALIBRATED BY SUPERENERGY

DIMENSIONLESS RATIOS OF SALT CONCENTRATION * 0.01
AXIAL LEVEL (IN.) = 26.5
INJ. SUBCHANNEL = 5
REYNOLDS NUMBER = 9134.0

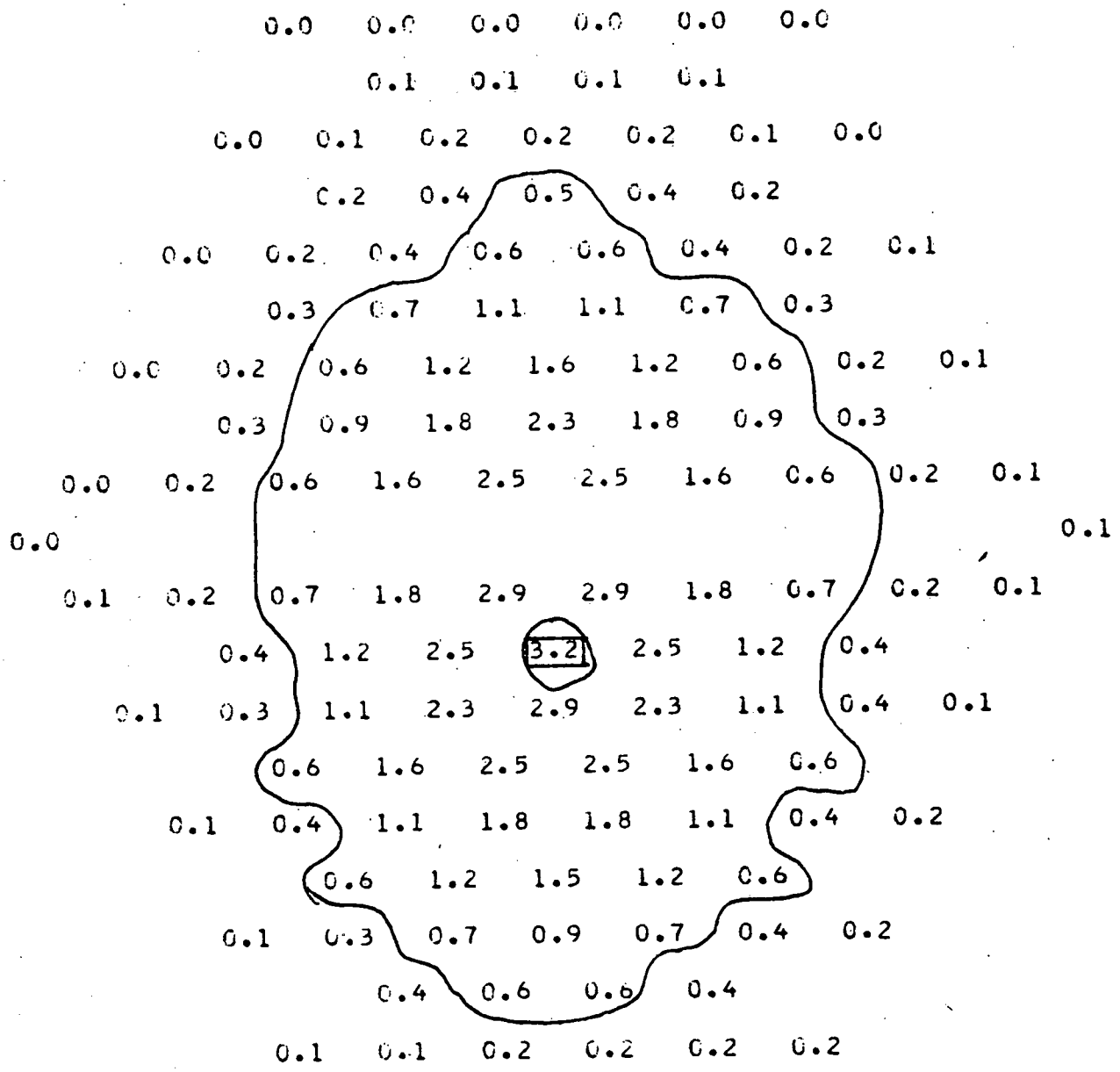

ROD DIA.	WIRE DIA.	LEAD	PITCH	FLATS	LENGTH	DUCT TH.	GAP TH.
0.501	0.031	4.000	0.533	4.275	25.000		

Figure B.17

APPENDIX B.2

Dimensionless Salt Concentration Maps at Different Injection Depths for an Edge Injection Subchannel (In-phase Wire Wrapped Assembly)

SALT CONCENTRATION DISTRIBUTION MAP CALIBRATED BY SUPERENERGY

DIMENSIONLESS RATIOS OF SALT CONCENTRATION * 0.01
AXIAL LEVEL (IN.) = 22.5
INJ. SUBCHANNEL = 115
REYNOLDS NUMBER = 8822.0

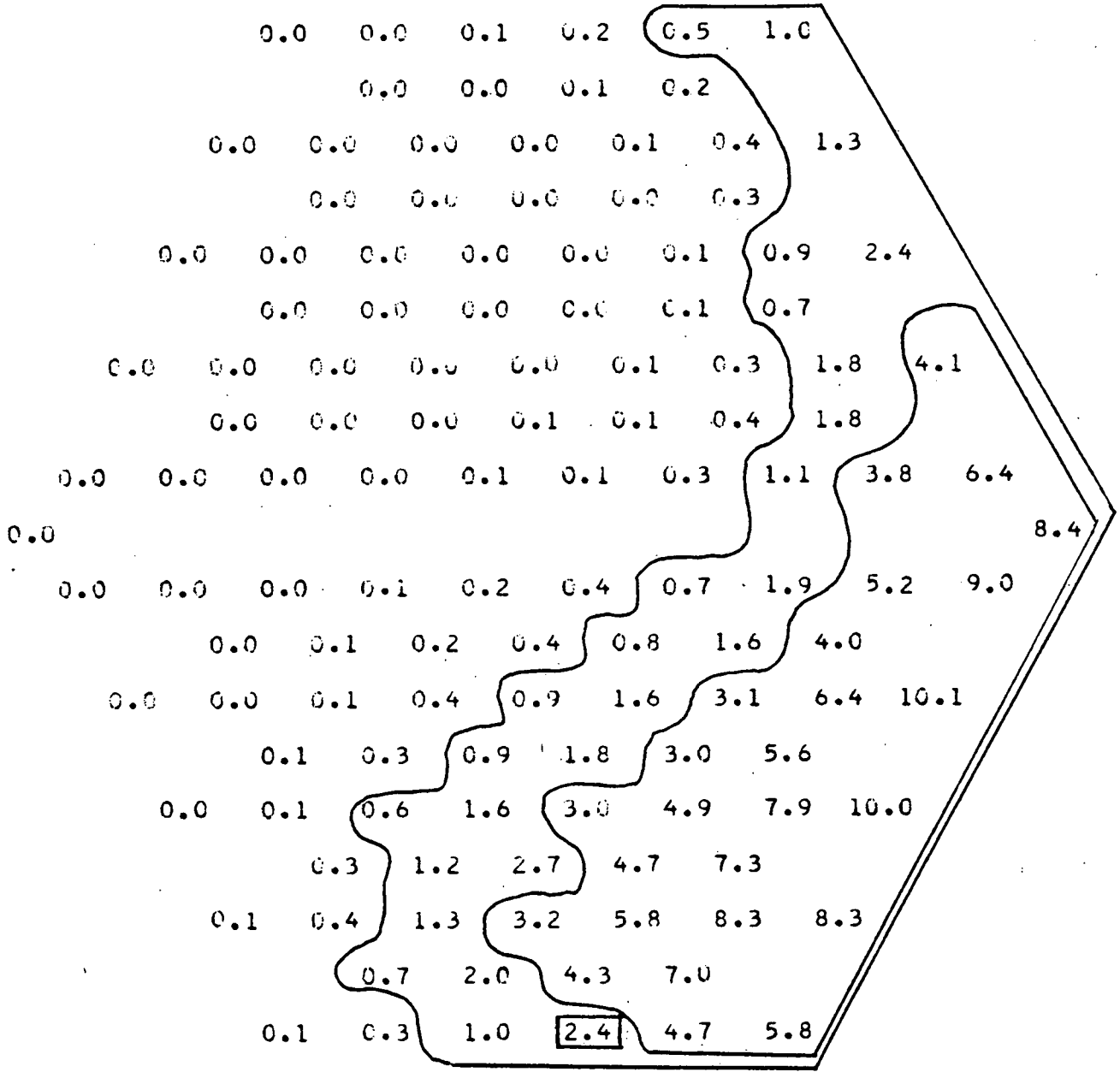

Figure B.18

SALT CONCENTRATION DISTRIBUTION MAP CALIBRATED BY SUPERENERGY

DIMENSIONLESS RATIOS OF SALT CONCENTRATION * 0.01
AXIAL LEVEL (IN.) = 18.5
INJ. SUBCHANNEL = 115
REYNOLDS NUMBER = 9134.0

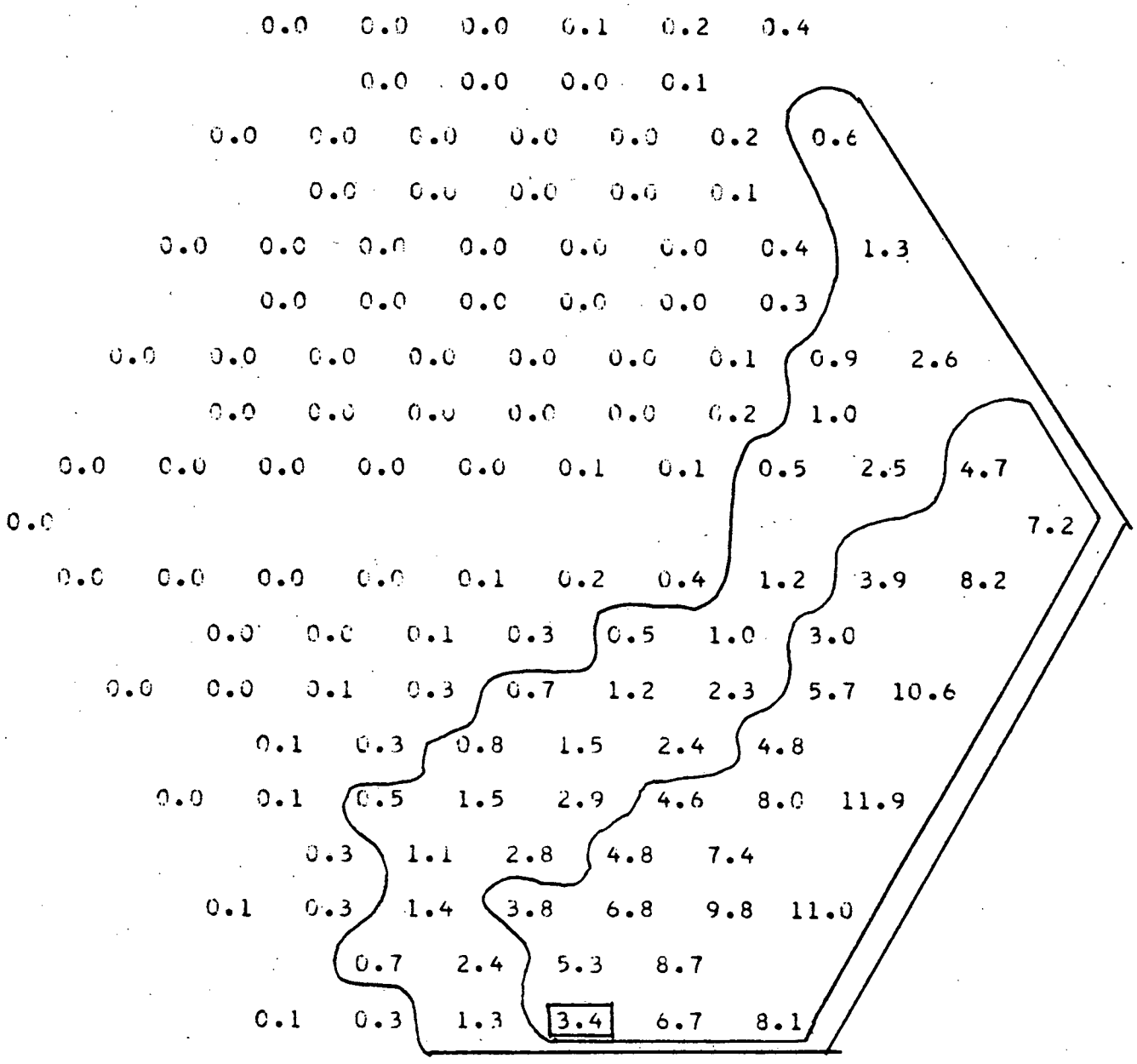

Figure B.19

SALT CONCENTRATION DISTRIBUTION MAP CALIBRATED BY SUPERENERGY

DIMENSIONLESS RATIOS OF SALT CONCENTRATION * 0.01
AXIAL LEVEL (IN.) = 14.5
INJ. SUBCHANNEL = 115
REYNOLDS NUMBER = 9134.0

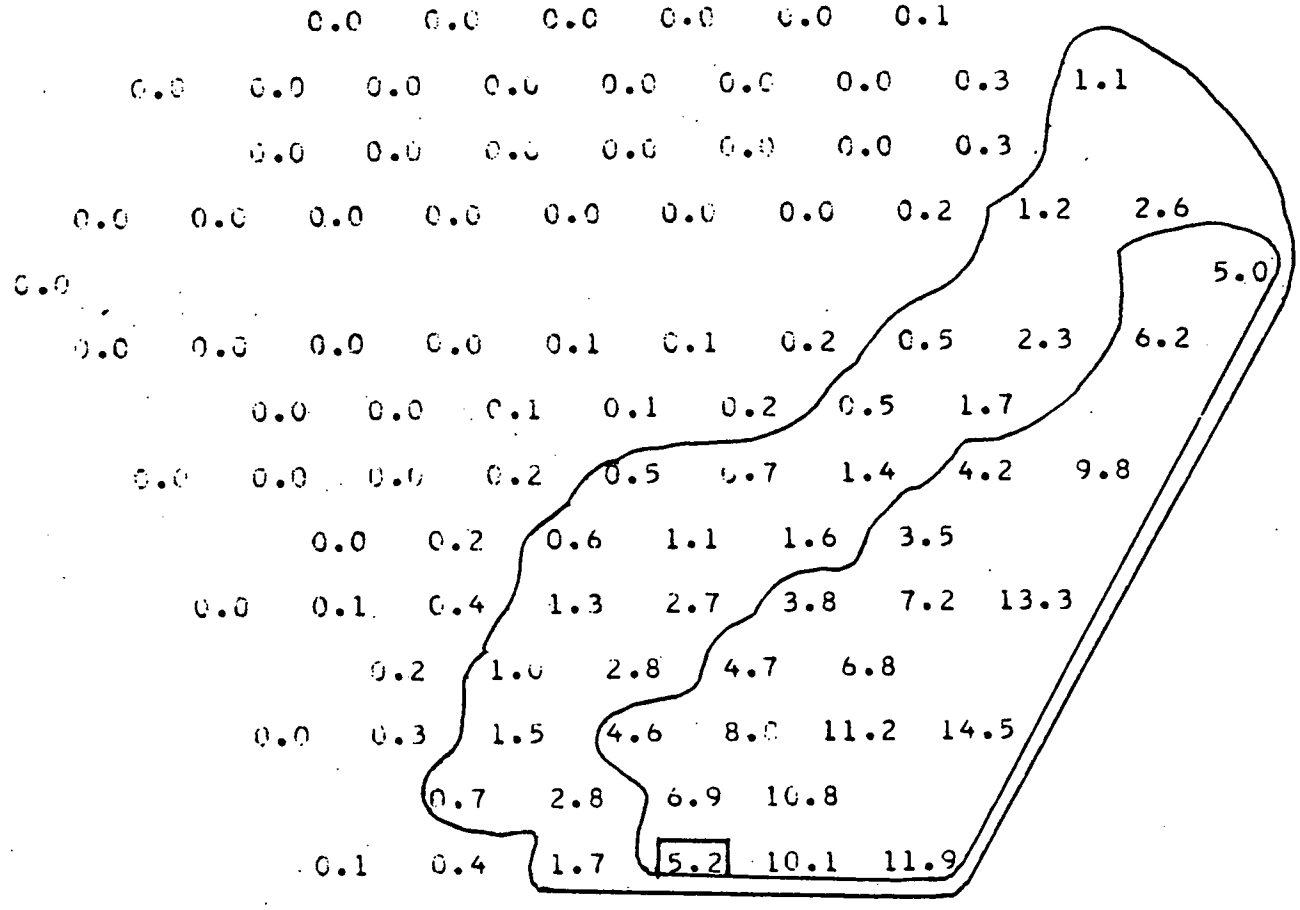

Figure B.20

SALT CONCENTRATION DISTRIBUTION MAP CALIBRATED BY SUPERENERGY

DIMENSIONLESS RATIOS OF SALT CONCENTRATION * 0.01
AXIAL LEVEL (IN.) = 14.0
INJ. SUBCHANNEL = 115
REYNOLDS NUMBER = 8822.0

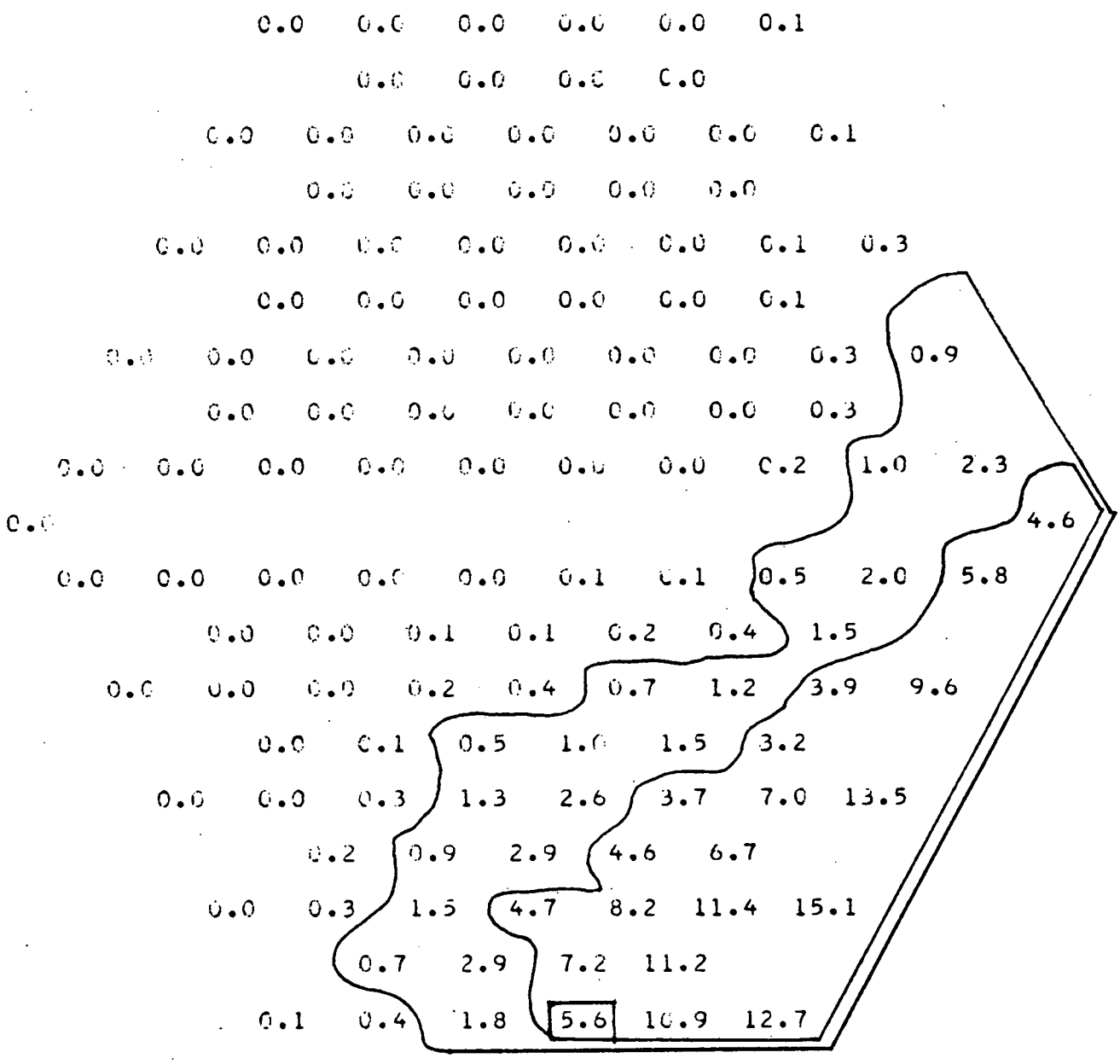

Figure B.21

SALT CONCENTRATION DISTRIBUTION MAP CALIBRATED BY SUPERENERGY

DIMENSIONLESS RATIOS OF SALT CONCENTRATION * 0.01
AXIAL LEVEL (IN.) = 15.0
INJ. SUBCHANNEL = 115
REYNOLDS NUMBER = 8822.0

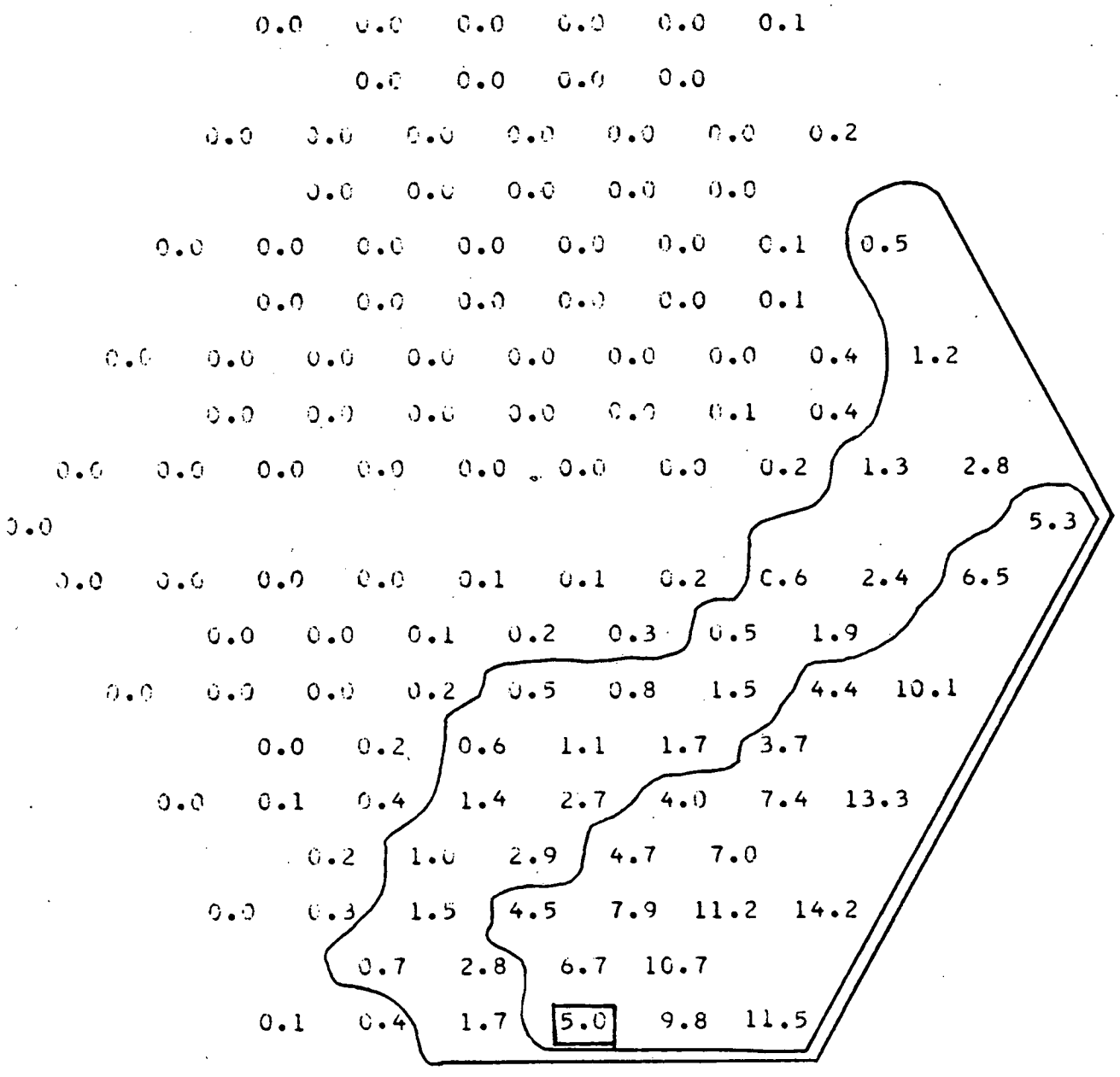

Figure B.22

SALT CONCENTRATION DISTRIBUTION MAP CALIBRATED BY SUPERENERGY

DIMENSIONLESS RATIOS OF SALT CONCENTRATION * 0.01
AXIAL LEVEL (IN.) = 15.5
INJ. SUBCHANNEL = 115
REYNOLDS NUMBER = 9134.0

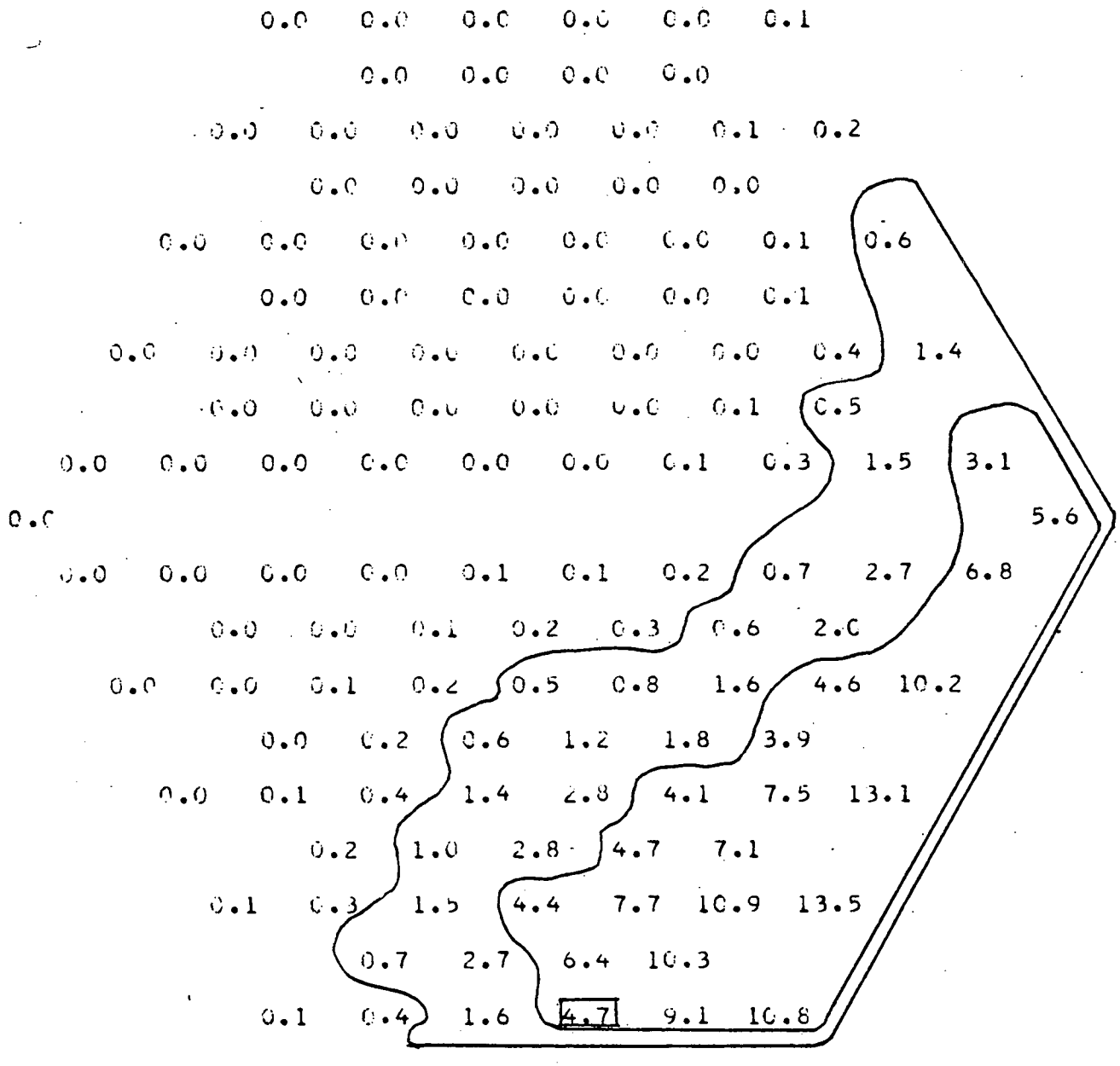

Figure B.23

SALT CONCENTRATION DISTRIBUTION MAP CALIBRATED BY SUPERENERGY

DIMENSIONLESS RATIOS OF SALT CONCENTRATION * 0.01
AXIAL LEVEL (IN.) = 16.5
INJ. SUBCHANNEL = 115
REYNOLDS NUMBER = 9134.0

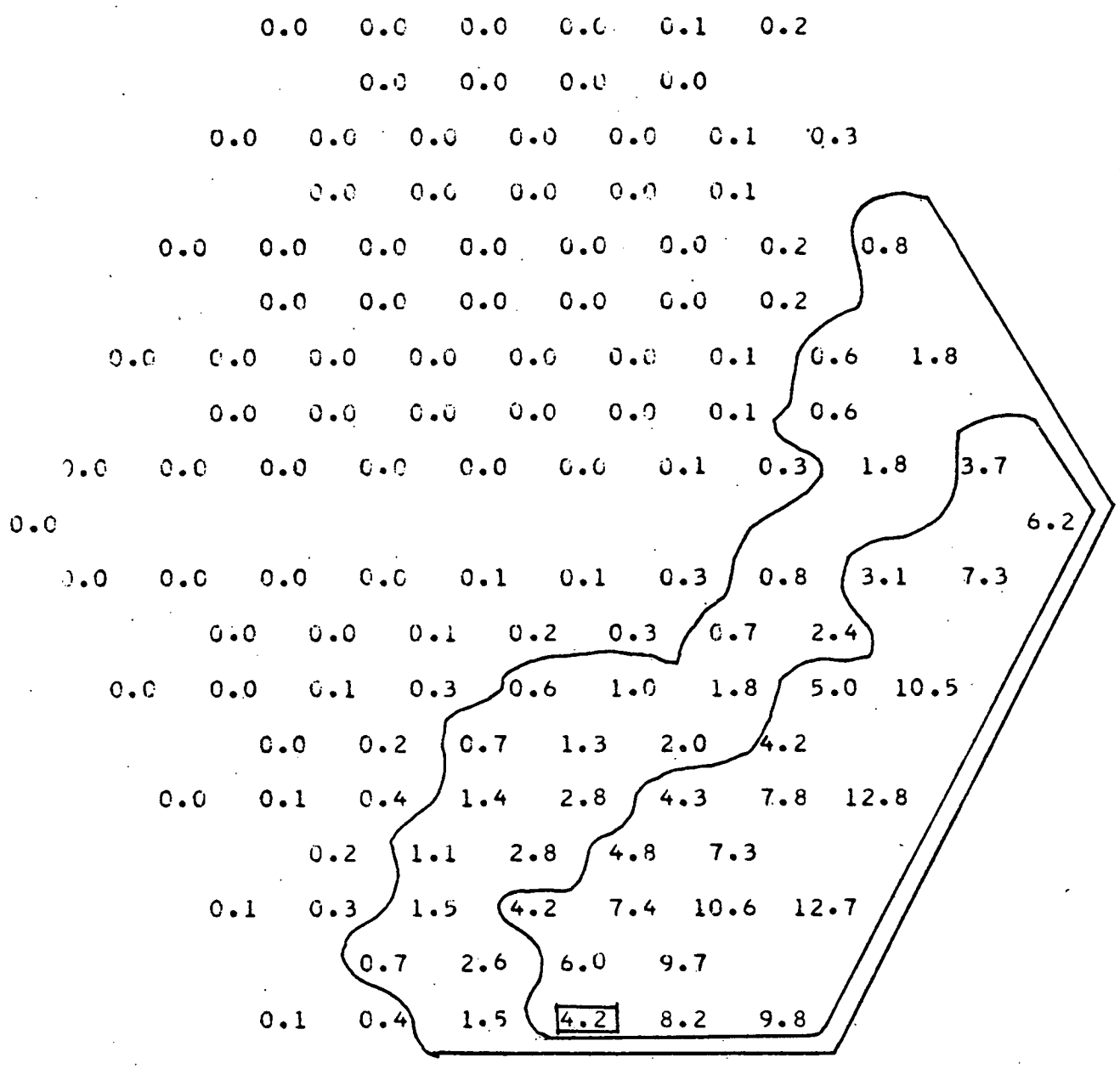

Figure B.24

SALT CONCENTRATION DISTRIBUTION MAP CALIBRATED BY SUPERENERGY

DIMENSIONLESS RATIOS OF SALT CONCENTRATION * 0.01
AXIAL LEVEL (IN.) = 17.5
INJ. SUBCHANNEL = 115
REYNOLDS NUMBER = 9134.0

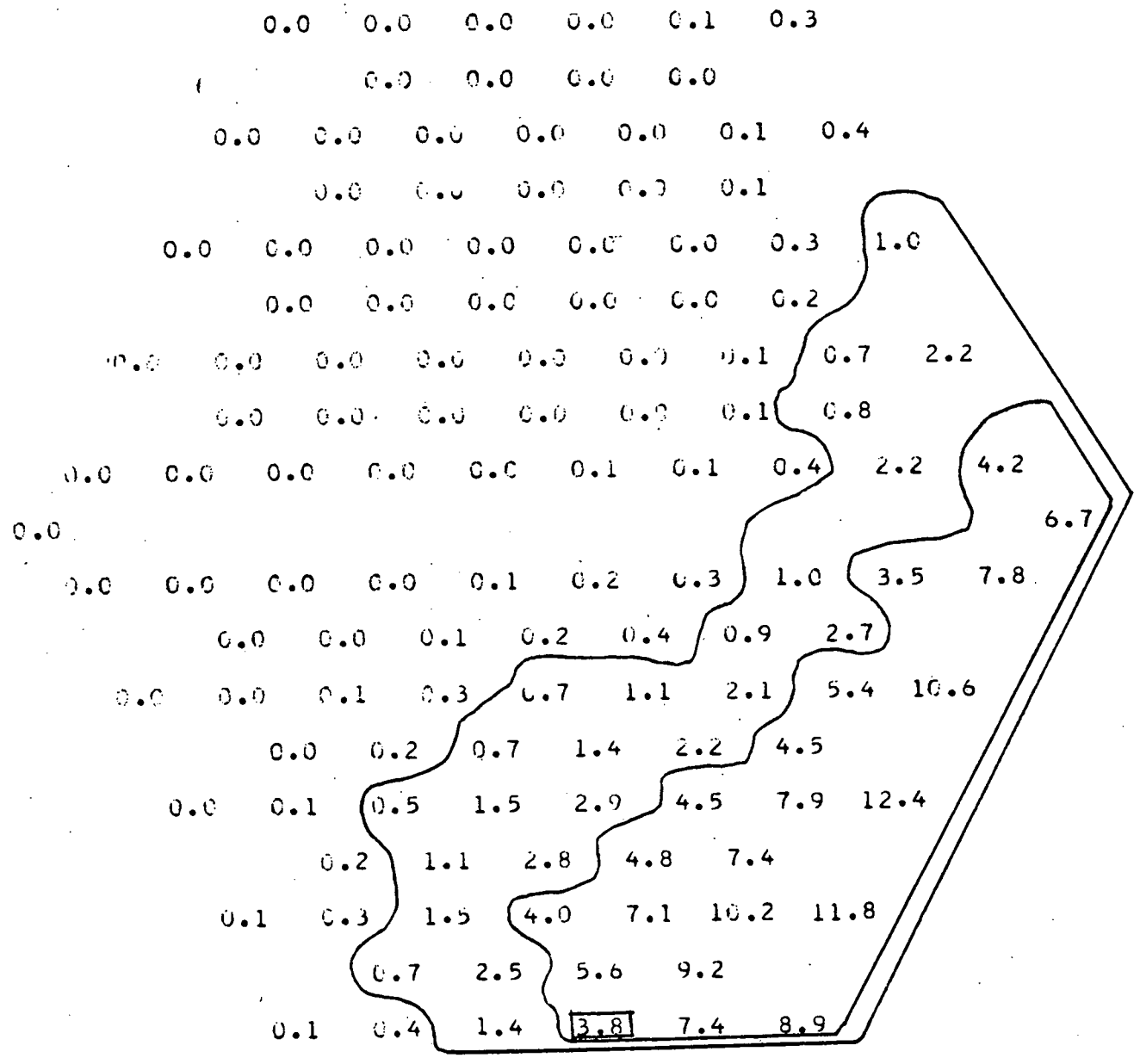

Figure B.25

SALT CONCENTRATION DISTRIBUTION MAP CALIBRATED BY SUPERENERGY

DIMENSIONLESS RATIOS OF SALT CONCENTRATION * 0.01
AXIAL LEVEL (IN.) = 18.0
INJ. SUBCHANNEL = 115
REYNOLDS NUMBER = 9134.0

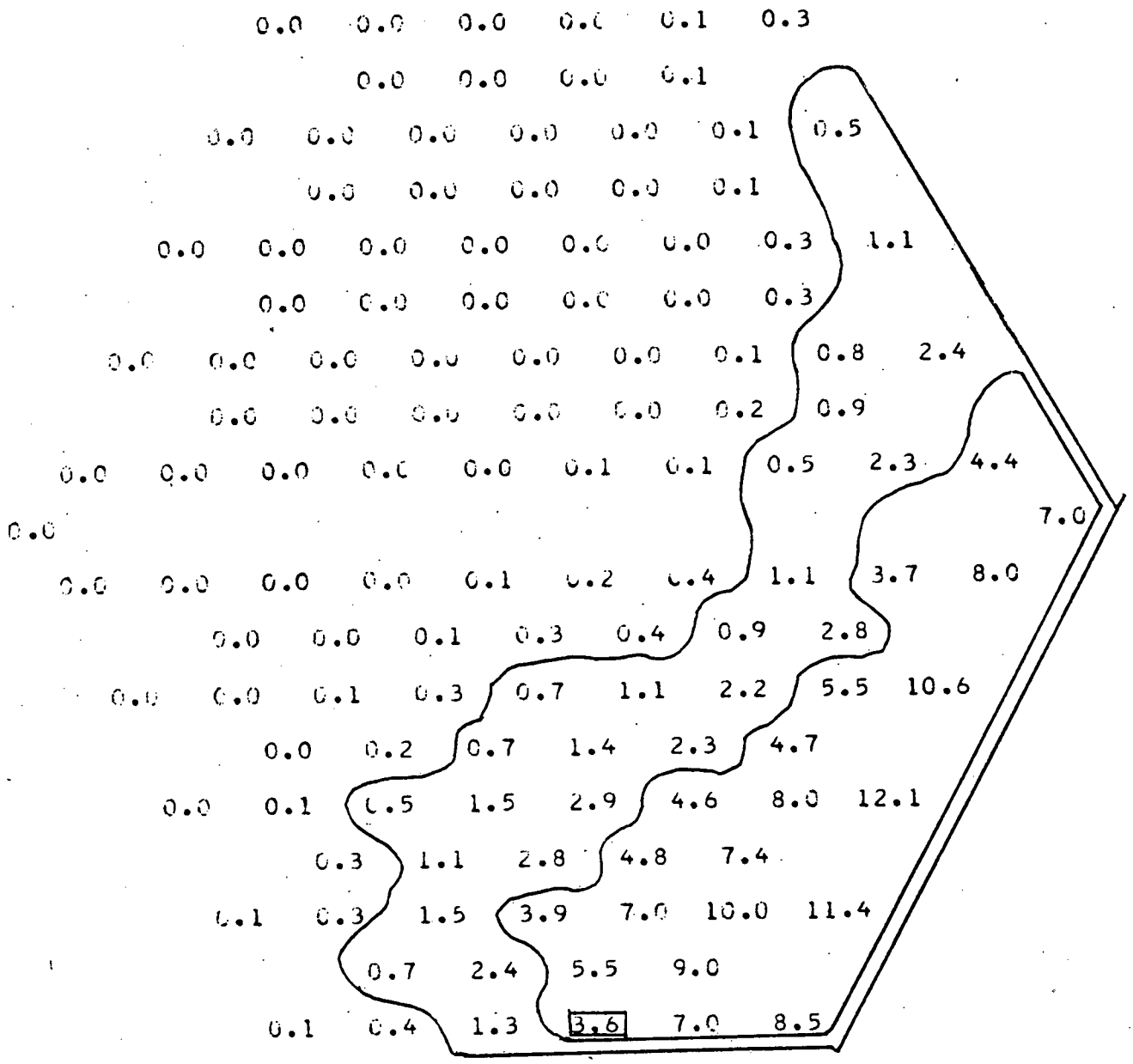

Figure B.26

SALT CONCENTRATION DISTRIBUTION MAP CALIBRATED BY SUPERENERGY

DIMENSIONLESS RATIOS OF SALT CONCENTRATION * 0.01
AXIAL LEVEL (IN.) = 19.0
INJ. SUBCHANNEL = 115
REYNOLDS NUMBER = 9134.0

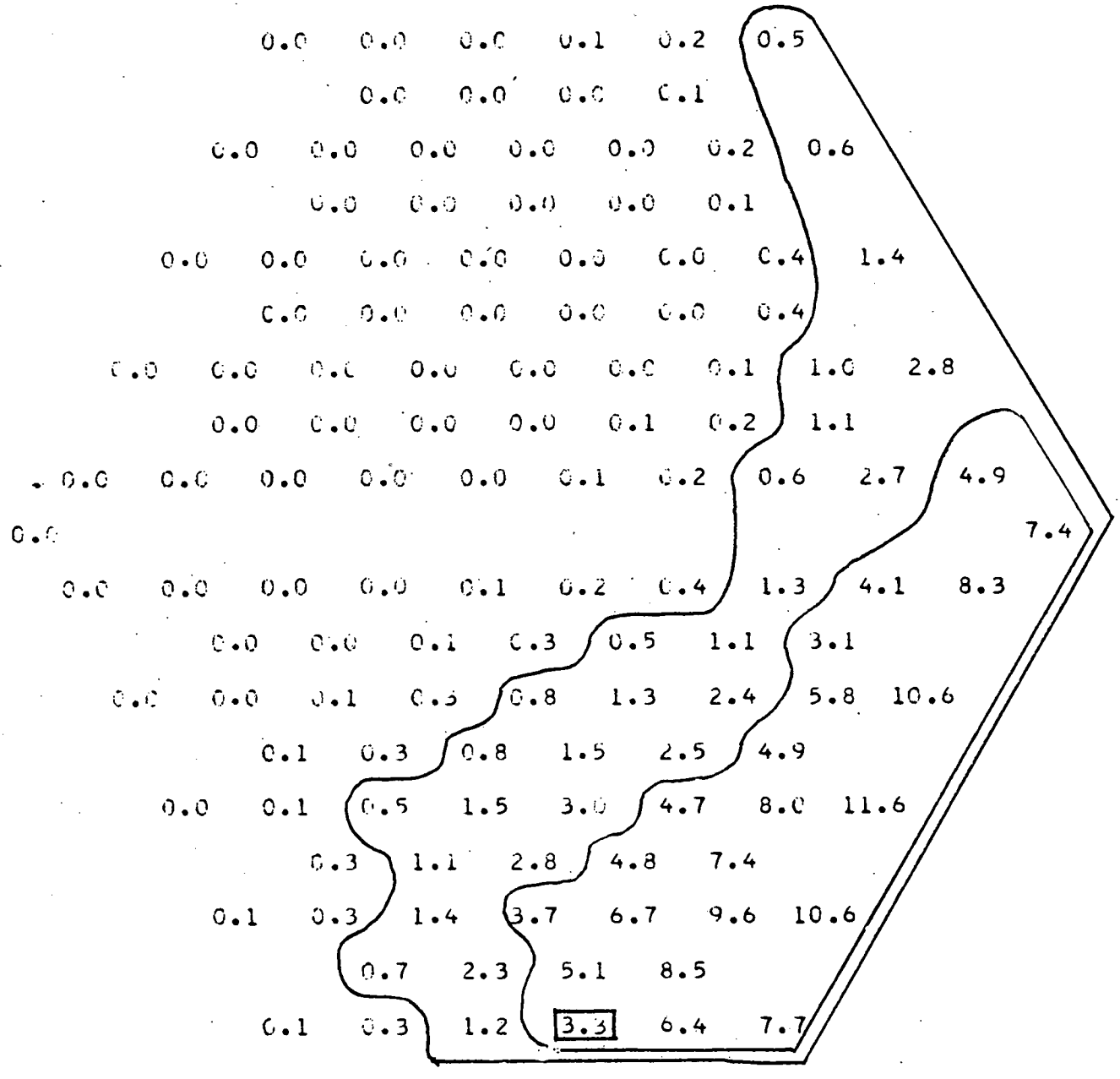

Figure B.27

SALT CONCENTRATION DISTRIBUTION MAP CALIBRATED BY SUPERENERGY

DIMENSIONLESS RATIOS OF SALT CONCENTRATION * 0.01
AXIAL LEVEL (IN.) = 19.5
INJ. SUBCHANNEL = 115
REYNOLDS NUMBER = 9134.0

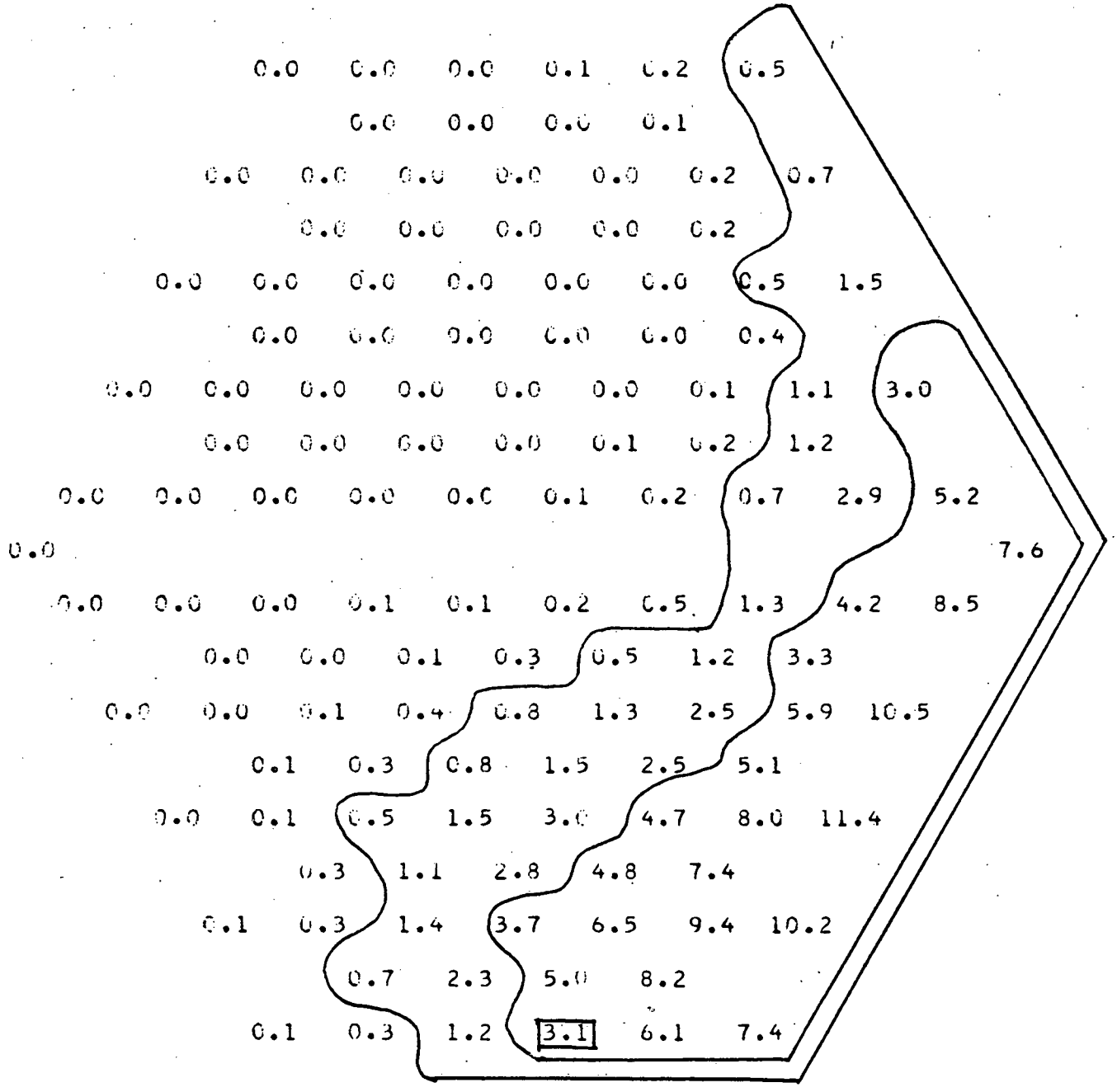

Figure B.28

SALT CONCENTRATION DISTRIBUTION MAP CALIBRATED BY SUPERENERGY

DIMENSIONLESS RATIOS OF SALT CONCENTRATION * 0.01
AXIAL LEVEL (IN.) = 20.0
INJ. SUBCHANNEL = 115
REYNOLDS NUMBER = 9134.0

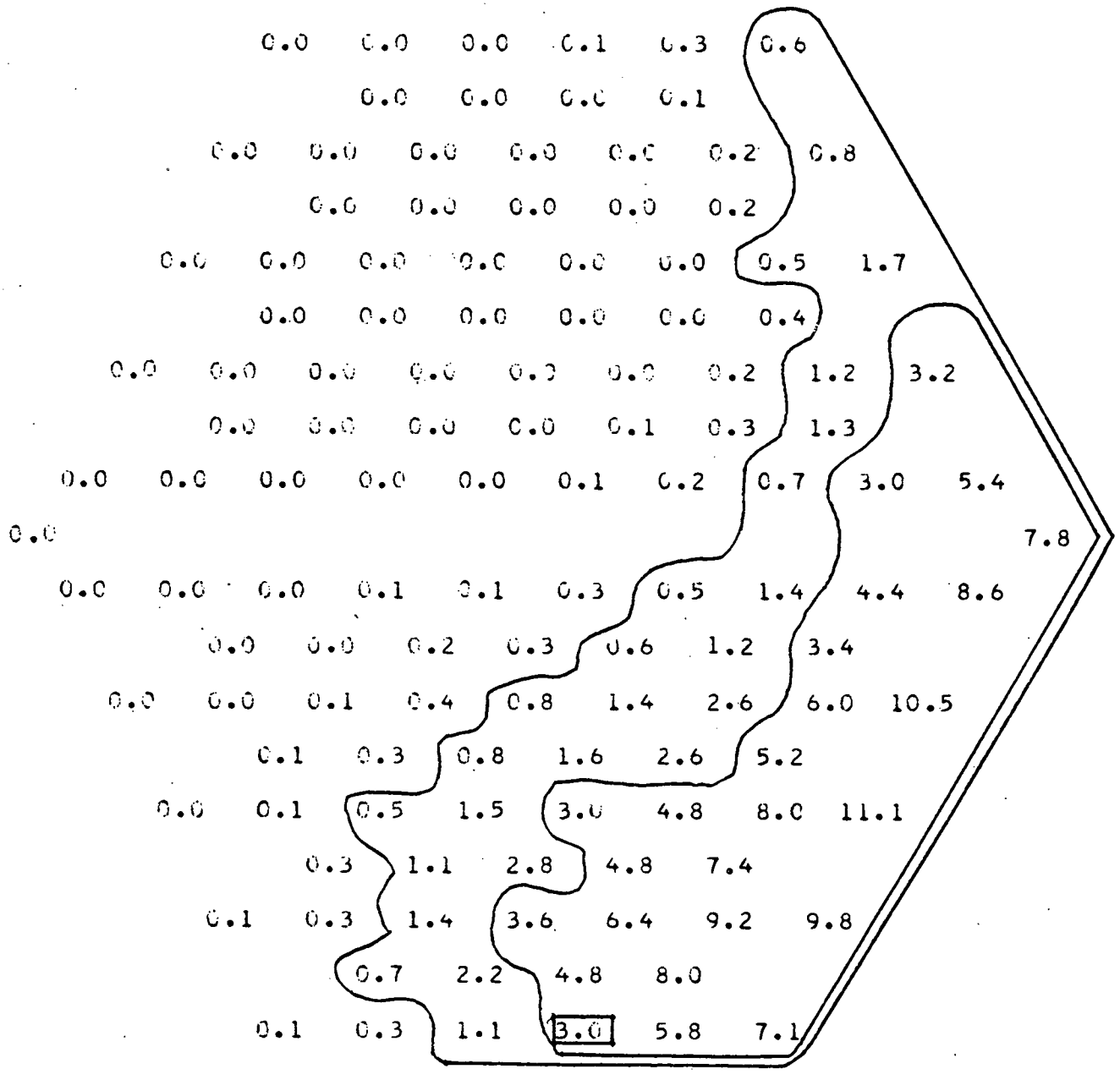

Figure B.29

SALT CONCENTRATION DISTRIBUTION MAP CALIBRATED BY SUPERENERGY

DIMENSIONLESS RATIOS OF SALT CONCENTRATION * 0.01
AXIAL LEVEL (IN.) = 20.5
INJ. SUBCHANNEL = 115
REYNOLDS NUMBER = 8822.0

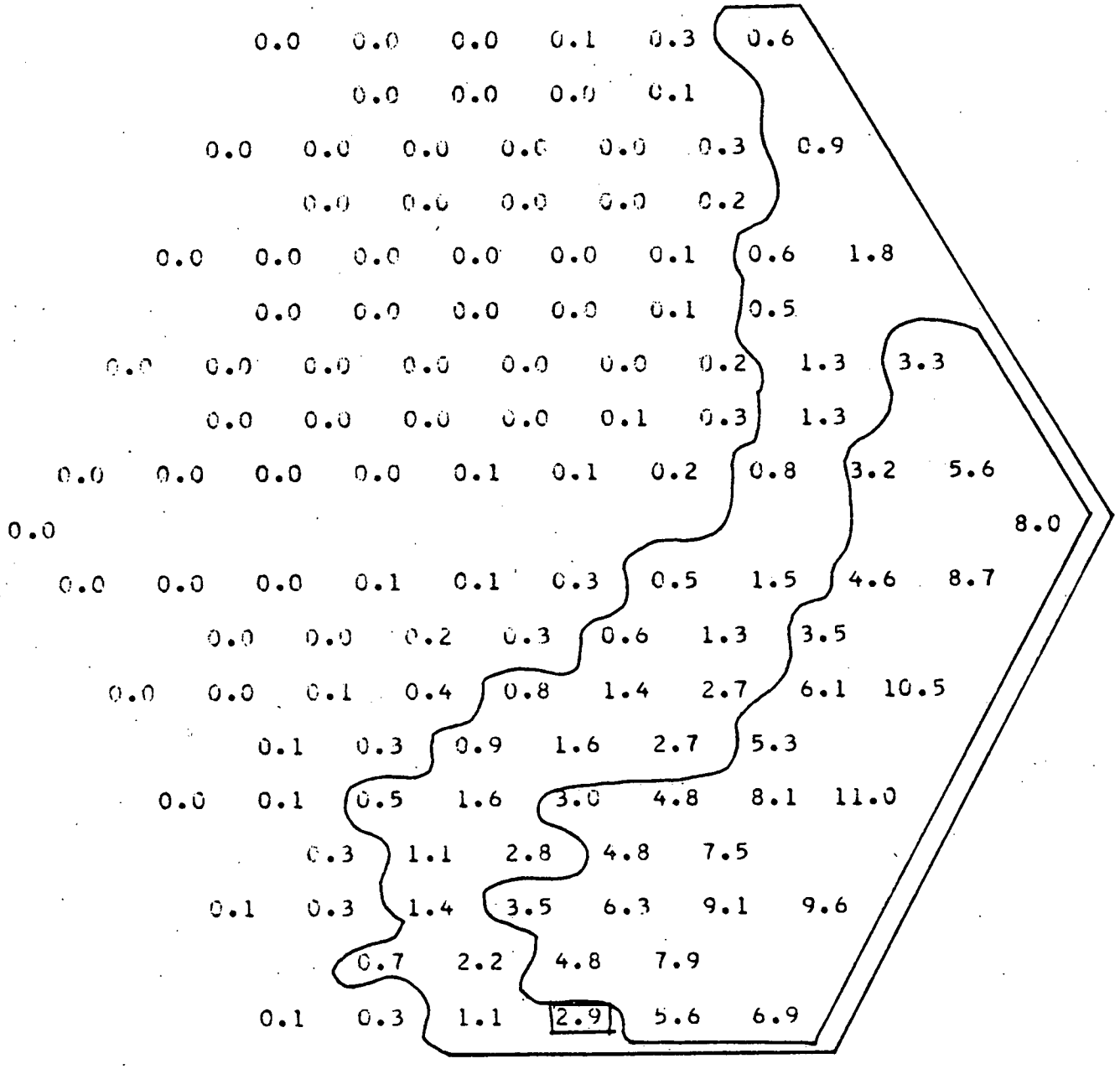

Figure B.30

SALT CONCENTRATION DISTRIBUTION MAP CALIBRATED BY SUPERENERGY

DIMENSIONLESS RATIOS OF SALT CONCENTRATION * 0.01
AXIAL LEVEL (IN.) = 21.0
INJ. SUBCHANNEL = 115
REYNOLDS NUMBER = 8822.0

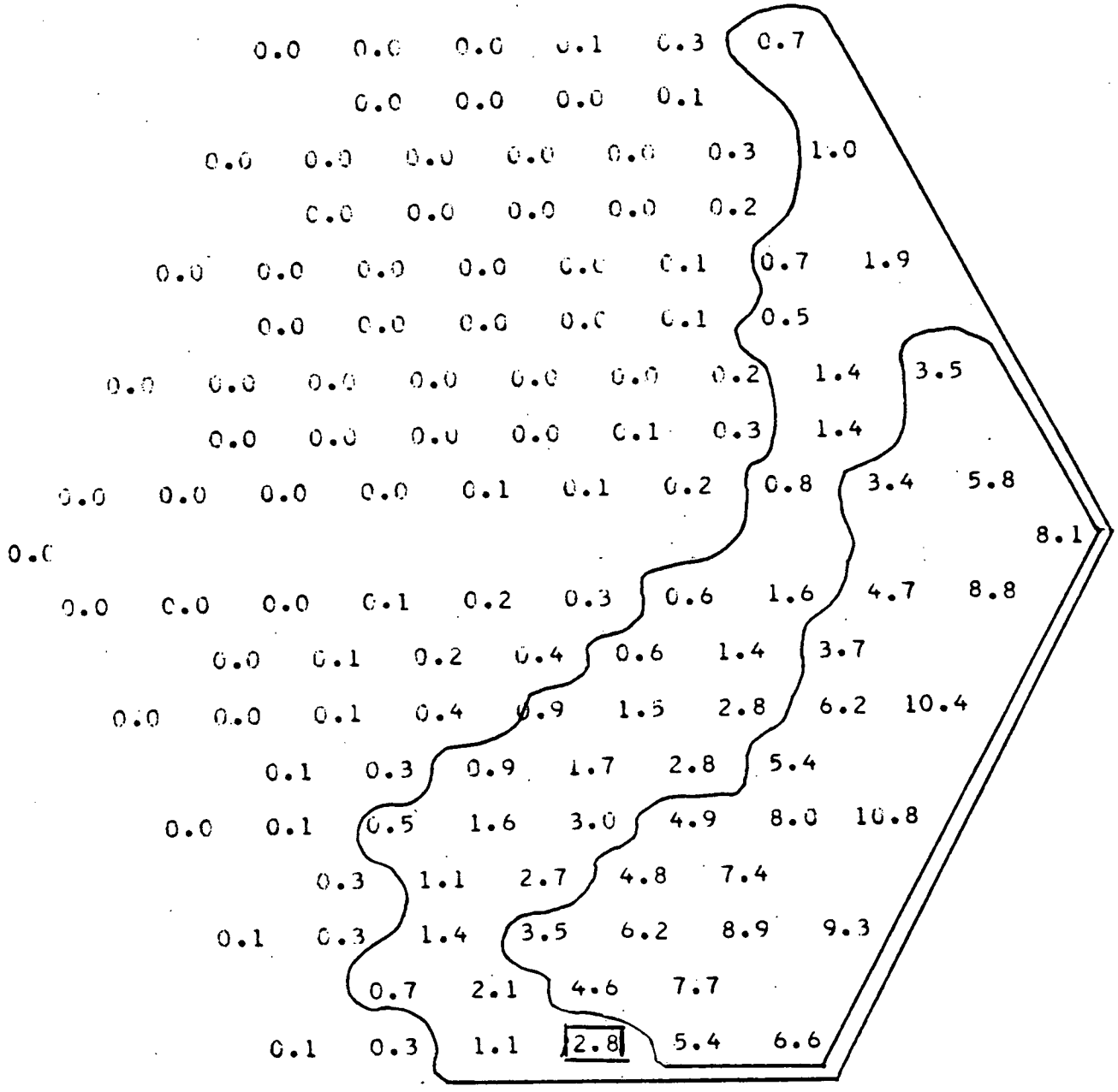

Figure B.31

SALT CONCENTRATION DISTRIBUTION MAP CALIBRATED BY SUPERENERGY

DIMENSIONLESS RATIOS OF SALT CONCENTRATION * 0.01
AXIAL LEVEL (IN.) = 21.5
INJ. SUBCHANNEL = 115
REYNOLDS NUMBER = 8822.0

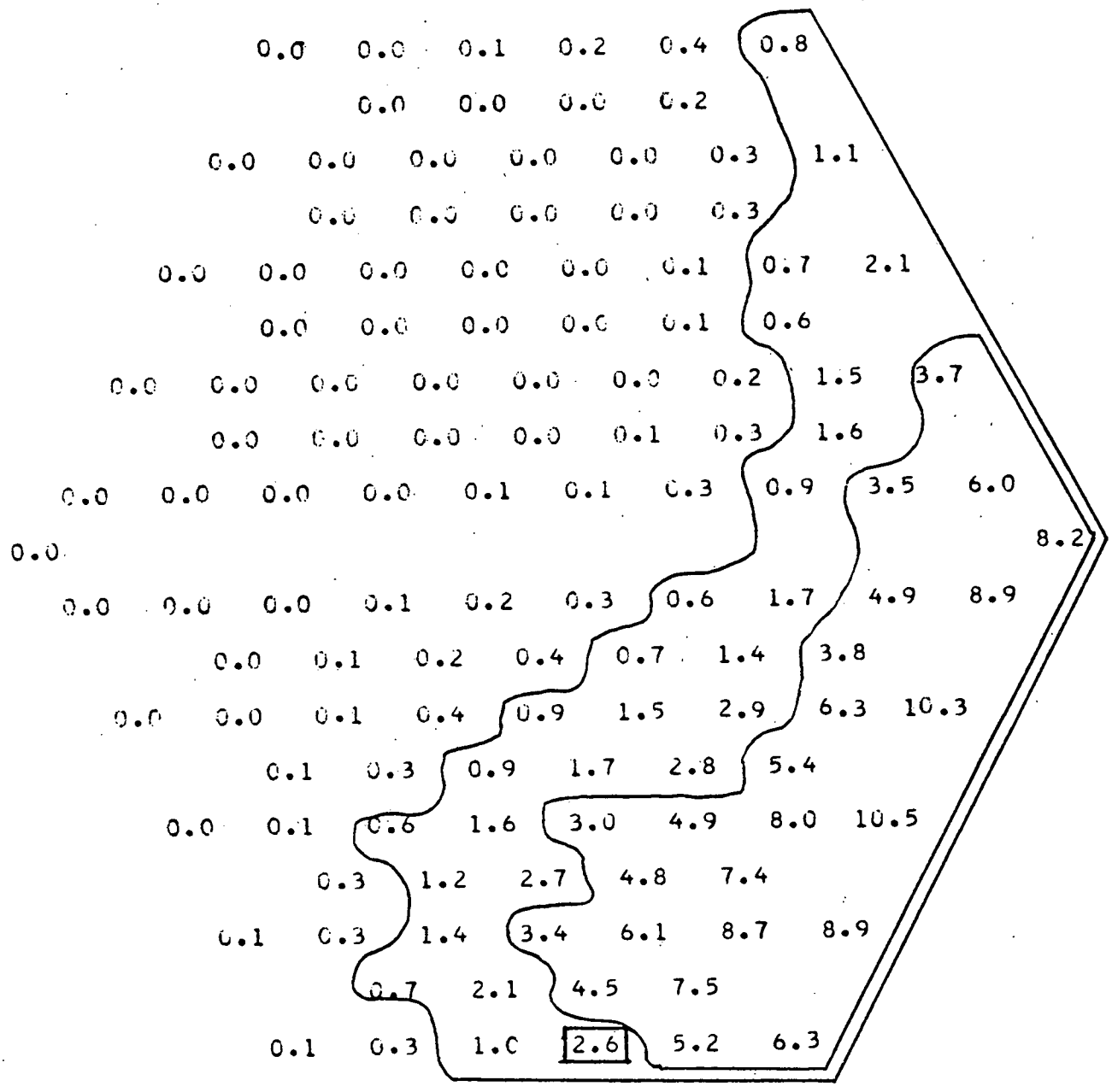

Figure B.32

SALT CONCENTRATION DISTRIBUTION MAP CALIBRATED BY SUPERENERGY

DIMENSIONLESS RATIOS OF SALT CONCENTRATION * 0.01
AXIAL LEVEL (IN.) = 22.0
INJ. SUBCHANNEL = 115
REYNOLDS NUMBER = 8822.0

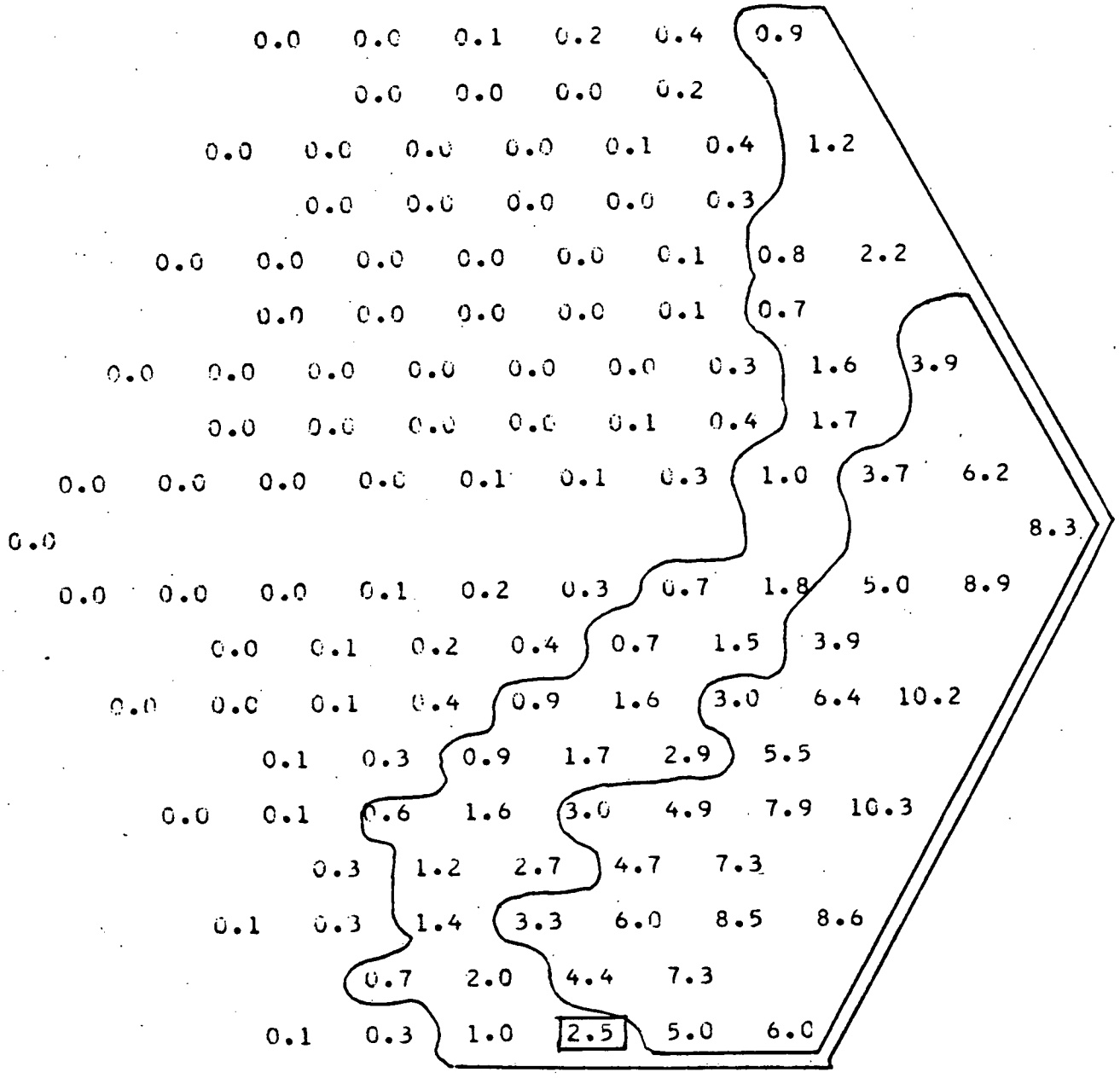

Figure B.33

SALT CONCENTRATION DISTRIBUTION MAP CALIBRATED BY SUPERENERGY

DIMENSIONLESS RATIUS OF SALT CONCENTRATION * 0.01
AXIAL LEVEL (IN.) = 23.0
INJ. SUBCHANNEL = 115
REYNOLDS NUMBER = 9134.0

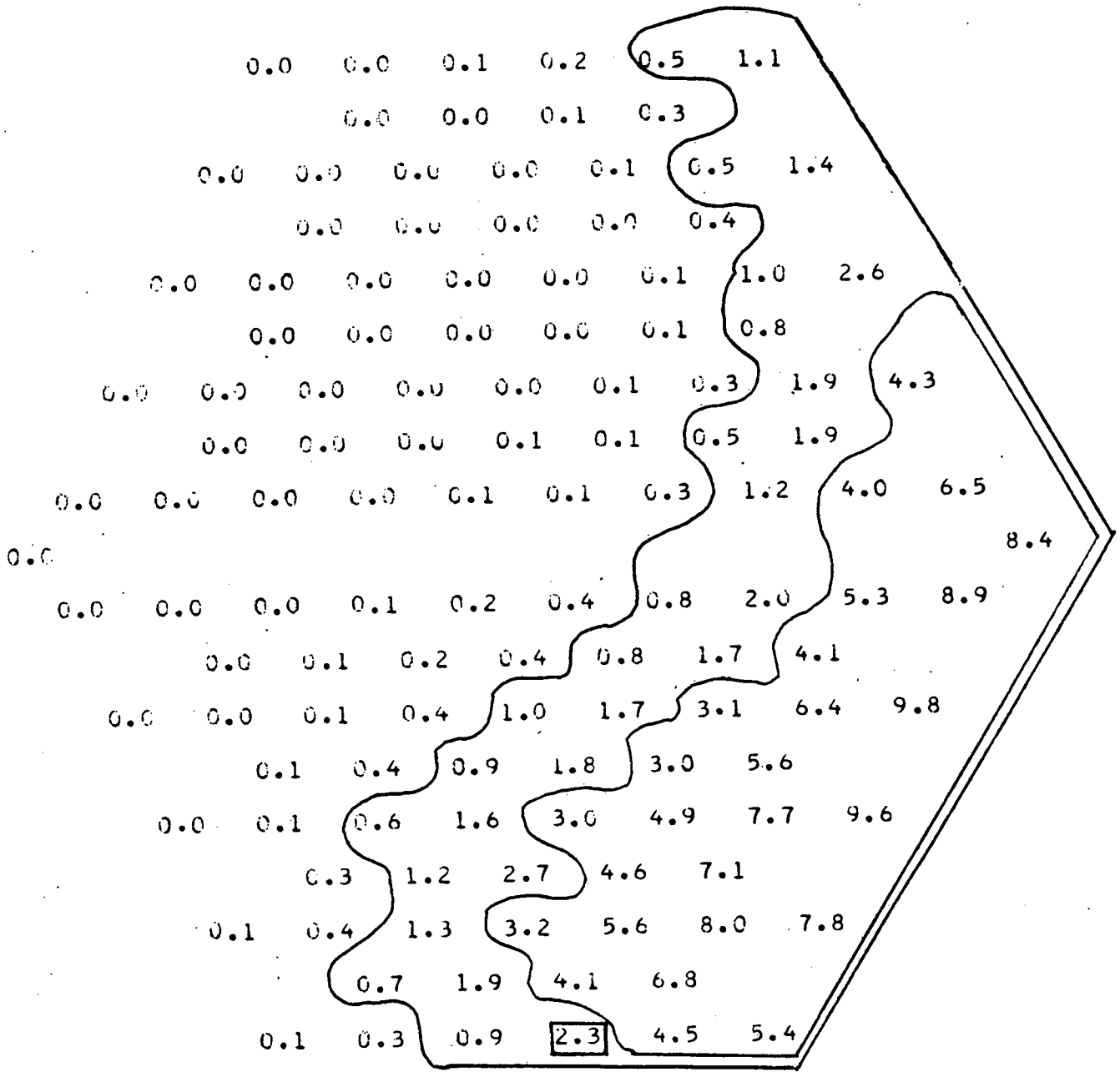

Figure B.34

SALT CONCENTRATION DISTRIBUTION MAP CALIBRATED BY SUPERENERGY

DIMENSIONLESS RATIOS OF SALT CONCENTRATION * 0.01
AXIAL LEVEL (IN.) = 23.5
INJ. SUBCHANNEL = 115
REYNOLDS NUMBER = 9134.0

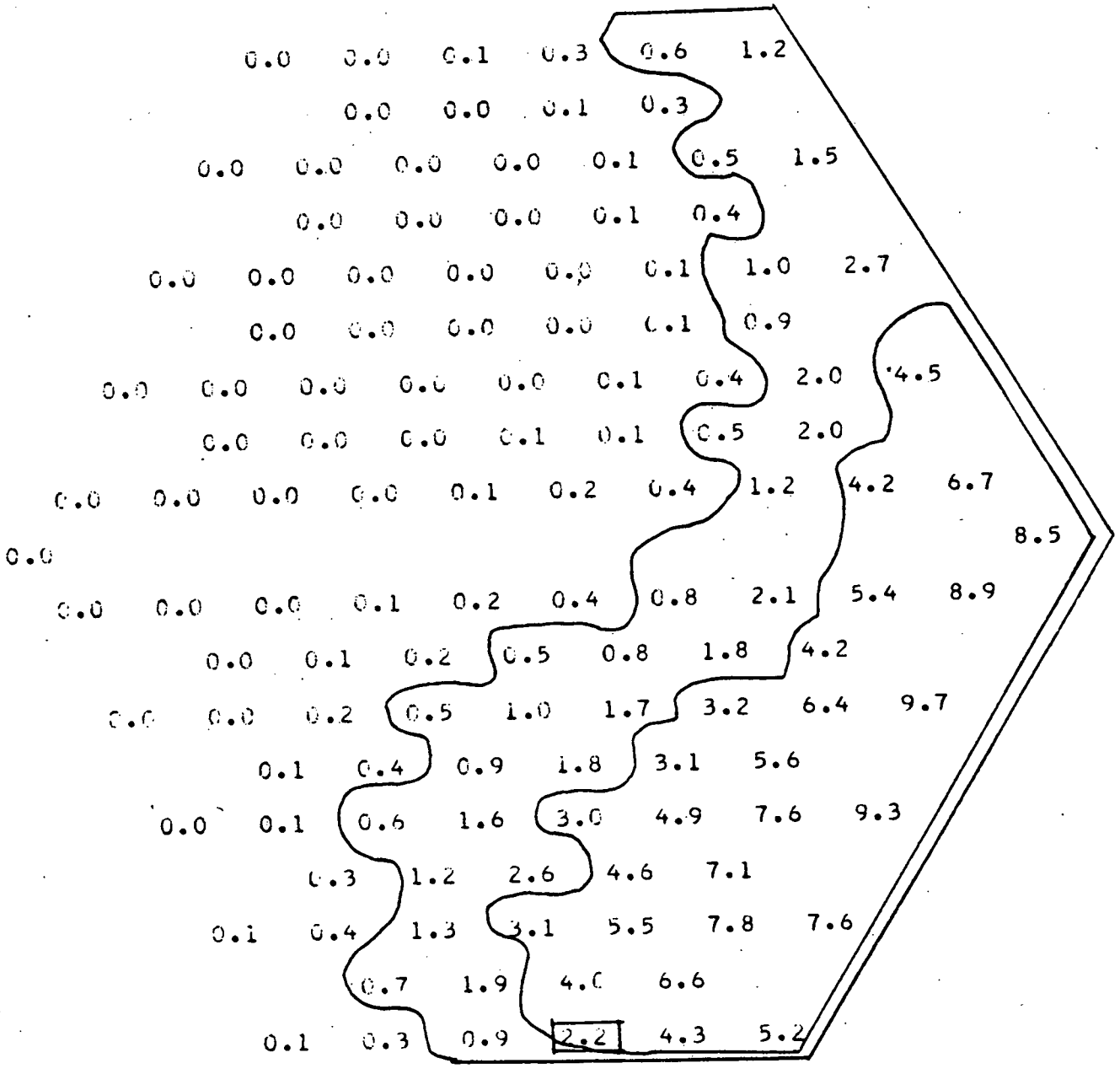

Figure B.35

SALT CONCENTRATION DISTRIBUTION MAP CALIBRATED BY SUPERENERGY

DIMENSIONLESS RATIOS OF SALT CONCENTRATION * 0.01
AXIAL LEVEL (IN.) = 24.0
INJ. SUBCHANNEL = 115
REYNOLDS NUMBER = 9134.0

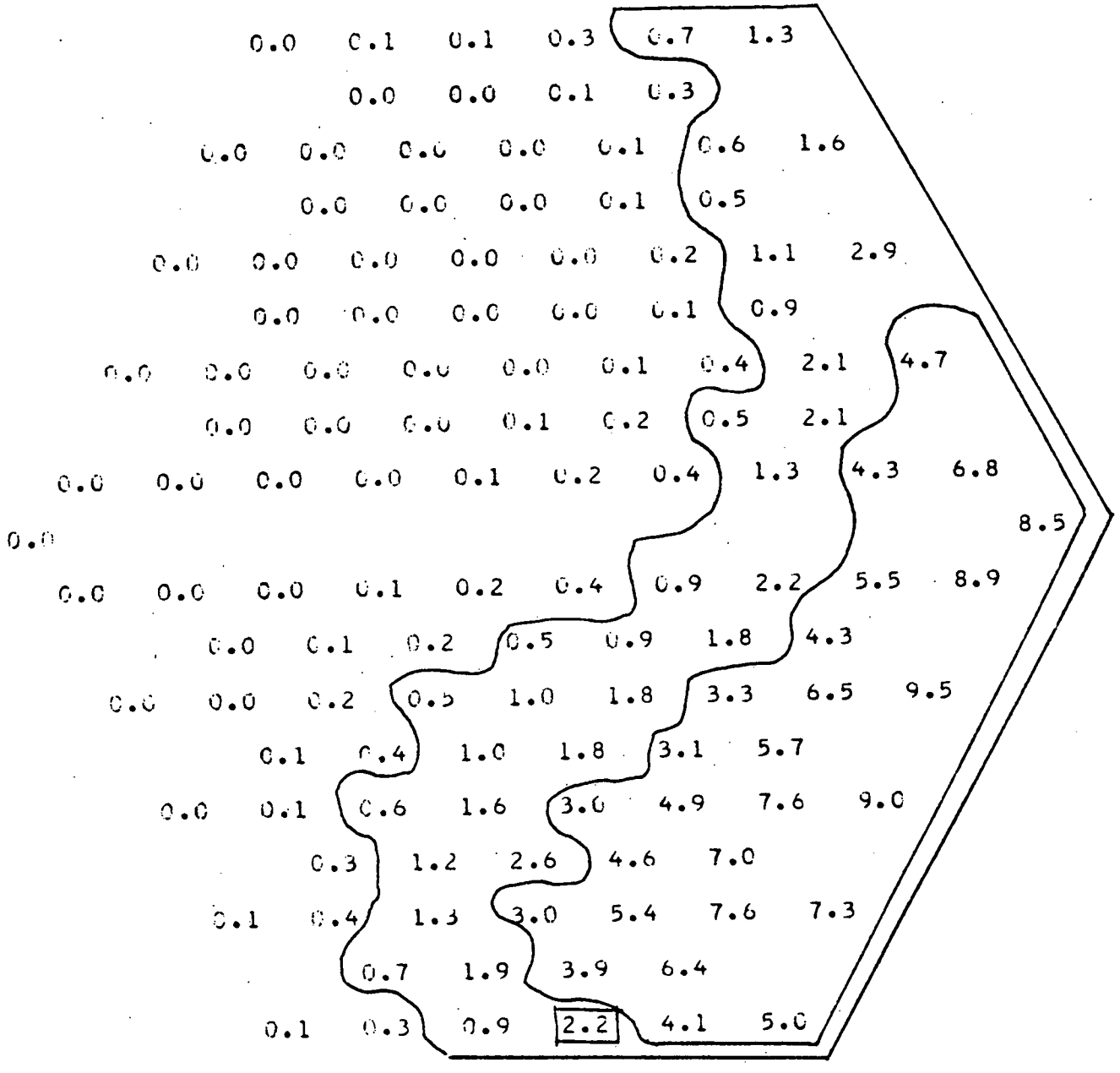

Figure B.36

SALT CONCENTRATION DISTRIBUTION MAP CALIBRATED BY SUPERENERGY

DIMENSIONLESS RATIOS OF SALT CONCENTRATION * 0.01
AXIAL LEVEL (IN.) = 25.0
INJ. SUBCHANNEL = 115
REYNOLDS NUMBER = 9134.0

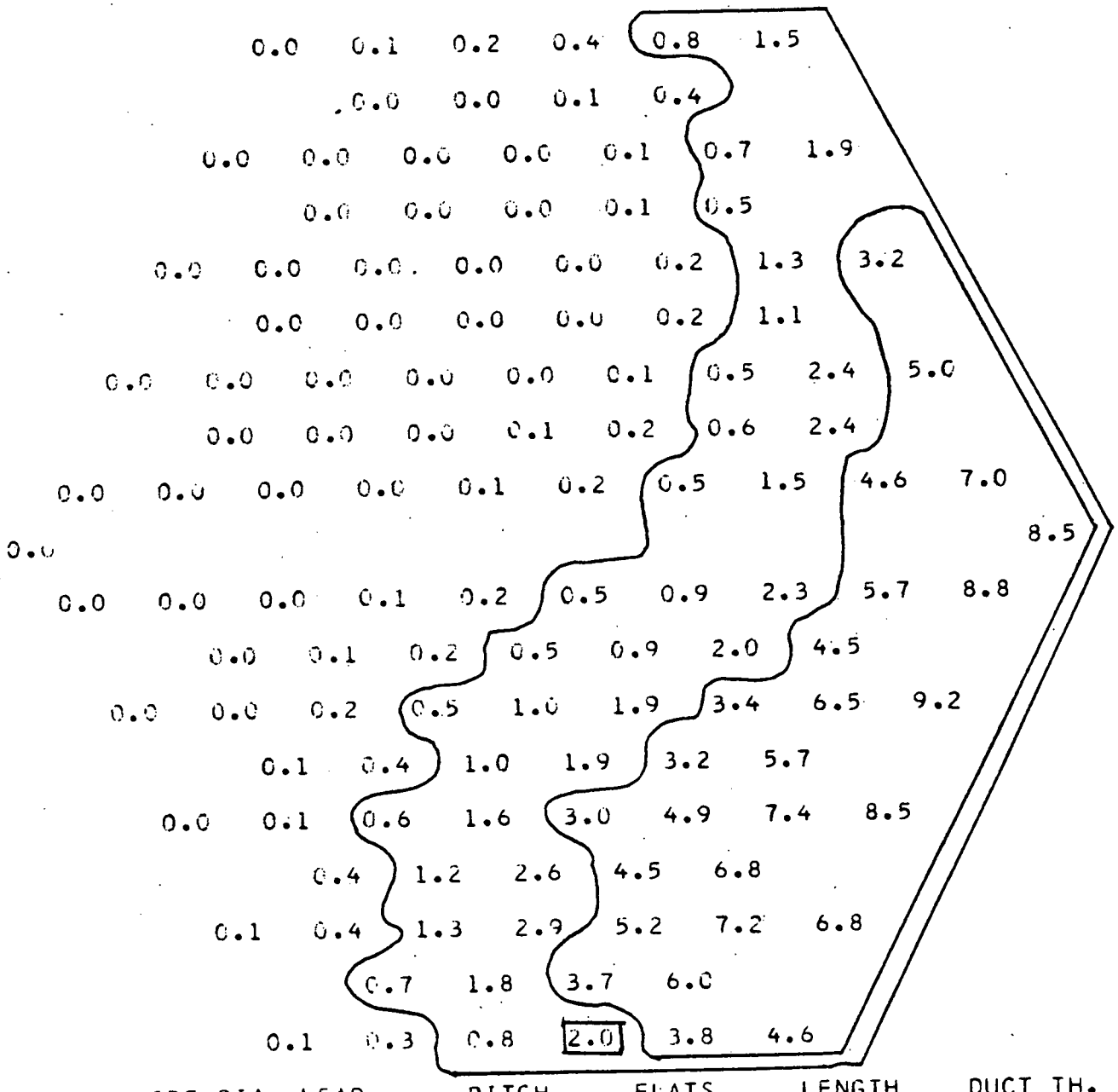

ROD DIA.	WIRE DIA.	LEAD	PITCH	FLATS	LENGTH	DUCT TH.	GAP TH.
0.501	0.031	4.000	0.533	4.275	27.000		

Figure B.37

SALT CONCENTRATION DISTRIBUTION MAP CALIBRATED BY SUPERENERGY

DIMENSIONLESS RATIOS OF SALT CONCENTRATION * 0.01
AXIAL LEVEL (IN.) = 26.0
INJ. SUBCHANNEL = 115
REYNOLDS NUMBER = 8822.0

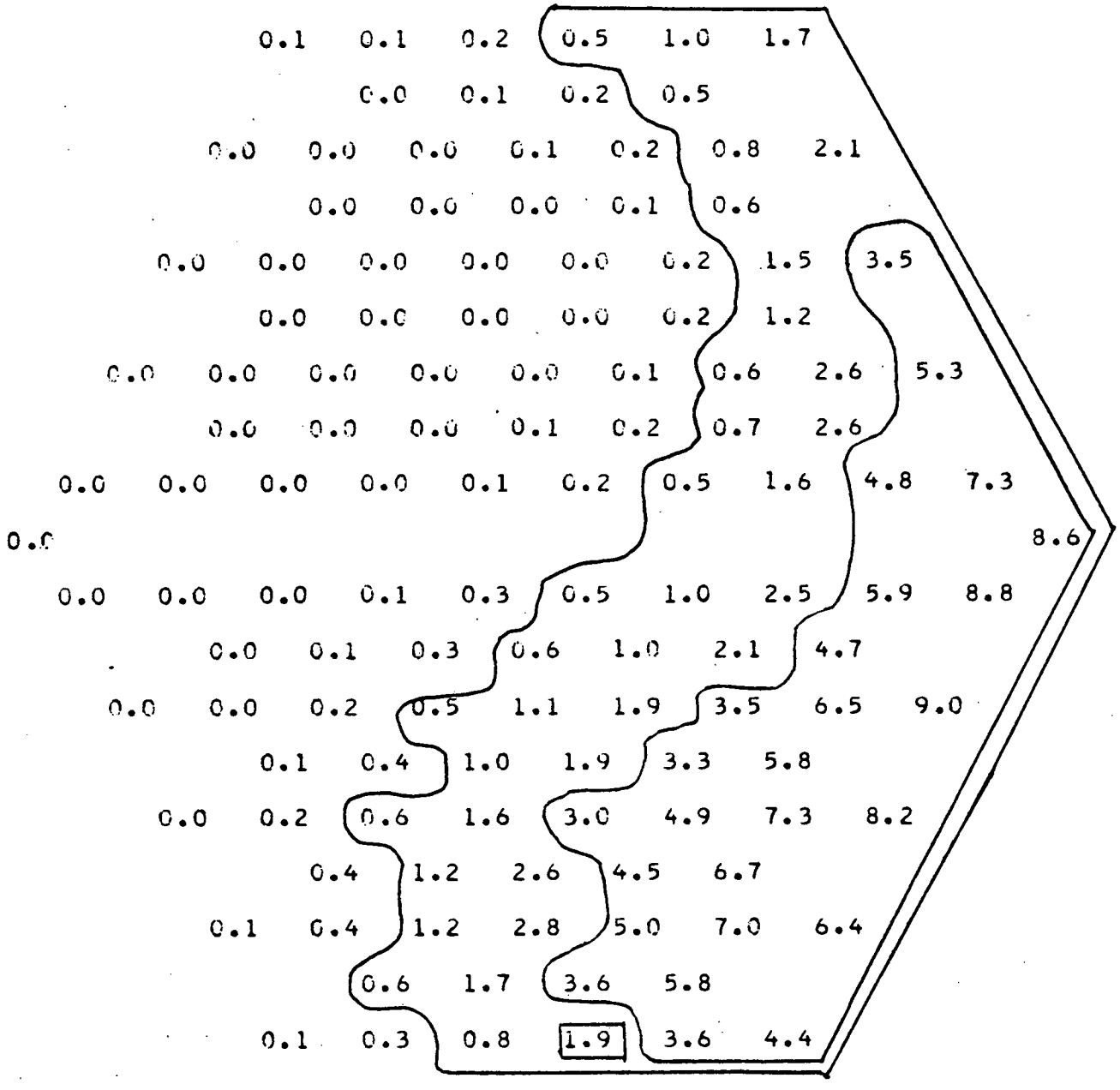

Figure B.38

SALT CONCENTRATION DISTRIBUTION MAP CALIBRATED BY SUPERENERGY

DIMENSIONLESS RATIOS OF SALT CONCENTRATION * 0.01
AXIAL LEVEL (IN.) = 27.0
INJ. SUBCHANNEL = 115
REYNOLDS NUMBER = 8822.0

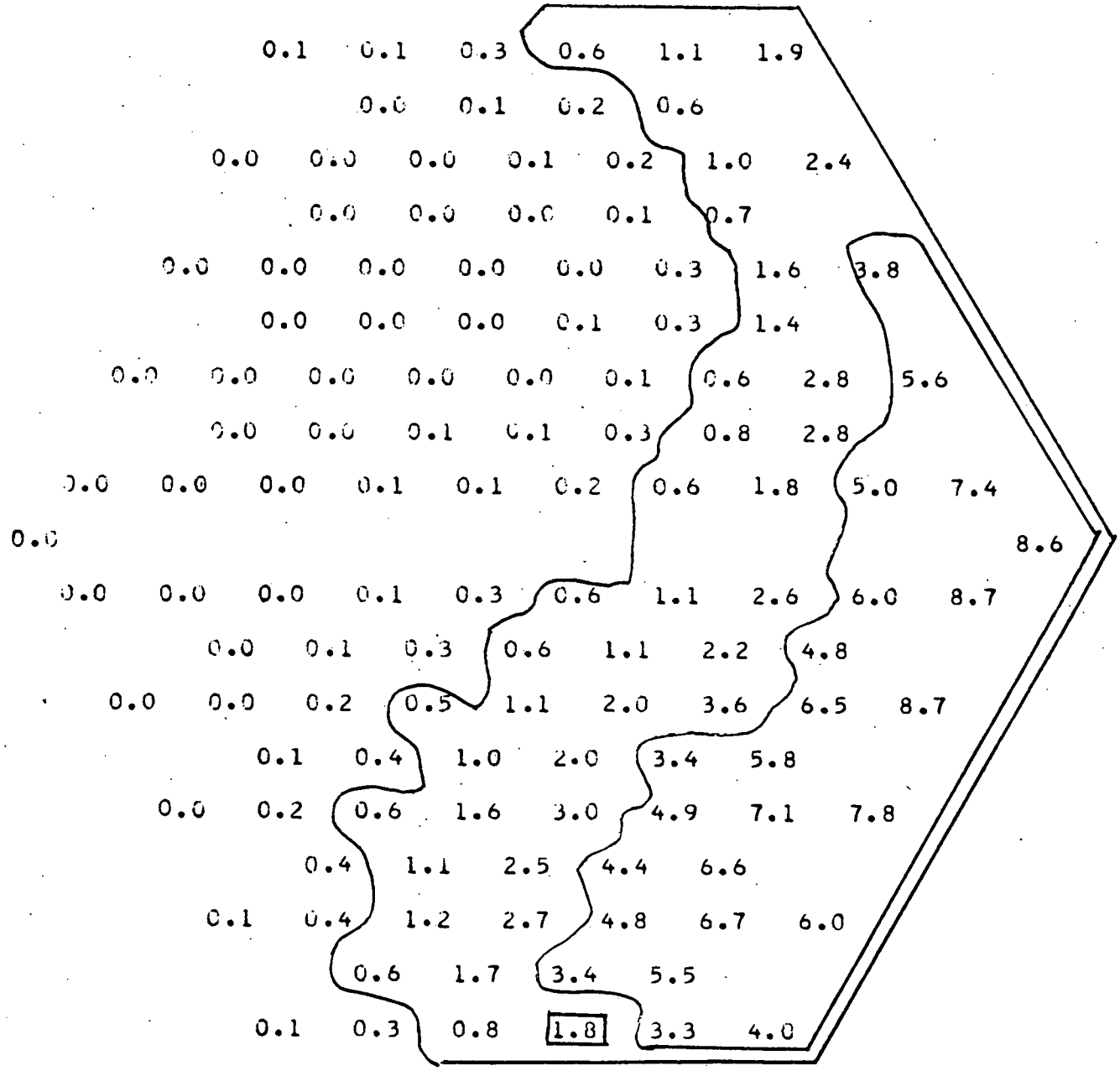

Figure B.39

REFERENCES

[1] Markley, R.A., "Radial Blanket Water Table Tests", LMFBR Rod Bundle T & H Working Group First Meeting, Pittsburgh, December, 1975.

[2] Personal Communication with C.E. Ockert, Department of Energy, December, 1975.

[3] Robert Bowring and Pablo Moreno, "COBRA-IIIC/M.I.T. Computer and Code Manual", to be issued as an EPRI Report.

[4] C. Chiu and N.E. Todreas, "Flow Split Measurements in LMFBR Blanket Assemblies", C00-2245-TR41, Nuclear Engineering Department, M.I.T., April, 1978.

[5] C. Chiu, N.E. Todreas, W.M. Rohsenow, "Turbulent Sweeping Flow Model for Wire Wrapped LMFBR Assemblies", C00-2245-55TR, Department of Nuclear Engineering, M.I.T., April 1978.

[6] S. Glazer, C. Chiu and N.E. Todreas, "Collection and Evaluation of Salt Mixing Data with the Real Time Data Acquisition System", C00-2245-36TR, M.I.T., April, 1977.

[7] C. Chiu and N.E. Todreas, "Flow Split Measurement of an LMFBR Blanket Assembly", ANS Annual Meeting Transaction, Vol. 26, June 1977, pp. 455-456.

[8] C. Chiu and N.E. Todreas, "Mixing Experiments in LMFBR Wire Wrapped Blanket Assemblies", C00-2245-TR45, Nuclear Engineering Department, M.I.T., April, 1978.

[9] B. Chen and N.E. Todreas, "Prediction of the Coolant Temperature Field in a Breeder Reactor Including Interassembly Heat Transfer", Nuclear Engineering and Design 35, (1975), pp. 423-440.

[10] P.W. Dickson, "Clinch River Breeder Reactor Plant; Core Assemblies Data for SUPERENERGY Analysis", LRA-77-557, May, 1977.

[11] W.E. Pennel, "LMFBR Core Restraint System Design", Nuclear Reactor Safety Course, Nuclear Engineering Department, M.I.T., 1976.

NOTICE

Printed in the United States of America

Available from

National Technical Information Service
U.S. Department of Commerce
5285 Port Royal Road
Springfield, VA 22161

Price: Printed Copy ; Microfiche $3.00